DEVELOPMENT OF CONDUCTING POLYMER-BASED FLUORESCENCE ON/OFF BIOSENSOR FOR BIOMOLECULE ANALYSIS

A Thesis Submitted to
the Graduate School of Engineering and Sciences of
İzmir Institute of Technology
in Partial Fulfillment of the Requirements for the Degree of
DOCTOR OF PHILOSOPHY
in Bioengineering

by
Duygu ARSLANTAŞ

November 2022
İZMİR

ACKNOWLEDGMENTS

First of all, I would like to thank my supervisor, Assoc. Prof. Dr. Ahu Arslan Yıldız for her professional guidance and encouragement throughout my Ph.D., and her humanity and patience during my tough times. I want to thank her for everything I learned, both scientifically, and socially.

I also would like to express my thankfulness to Assoc. Prof. Dr. Ümit Hakan Yıldız for conveying his scientific enthusiasm to me. He also allowed me to use all laboratory facilities to carry out my studies. I conducted my studies thanks to these two academically and humanely valuable people, Assoc. Prof. Dr. Ahu Arslan Yıldız and Assoc. Prof. Dr. Ümit Hakan Yıldız. I will always be honored to be their student.

I appreciate to my committe members, Prof. Dr. Semra Koçtürk, and Prof. Dr. Mustafa Emrullahoğlu for their valuable comments and advices during my studies.

I want to thank my dear husband, Guidance Counselor Fethi Arslantaş, with my heart. He showed never–ending patience and tolerance throughout all my Ph.D. studies. I would never have been able to finish my Ph.D. without her support.

I am very grateful to all members of the Bioinspired Engineering & Biomimetics Research Group. They shared their knowledge and experience with me to improve my work. We shared lots of things during this journey.

I want to express my sincere thanks to all members of the BioSens & BioApps groups. I would especially like to thank Soner Karabacak for providing me essential materials throughout my Ph.D. studies.

I am thankful to specialists at Biotechnology and Bioengineering Application and Research Center for their help during my experimental studies.

I dedicate this thesis to the best parents, Yunus Aybay, and Şükran Aybay.

This thesis is supported by Scientific Research Projects of İzmir Institute of Technology (BAP–20l91YTE0250)

ABSTRACT

DEVELOPMENT OF CONDUCTING POLYMER–BASED FLUORESCENCE ON/OFF BIOSENSOR FOR BIOMOLECULE ANALYSIS

Sensitive and selective detection of biomolecules and cells is essential for early diagnosis of diseases, prognosis monitoring, and effective therapy. This thesis aimed to develop a novel fluorescence ‘‘turn-on/off’’ biosensor for biomolecules and cells detection. In this study, cationic polythiophene derivative poly(1,4-dimethyl-1-(3-((4-methylthiophen-3-yl)oxy)propyl)piperazin-1-ium bromide) (PT–Pip) was used as an efficient fluorescence transduction element to discriminate proteins, mammalian cells, and amino acids for the first time. Initially, pH–dependent spectroscopic characterization of the PT–Pip was performed to monitor the conformational and optical changes. The pH sensitivity of the PT–Pip was demonstrated for the first time. Afterwards, the fluorescence ‘‘turn–off’’ phenomena were investigated in detail using citrate–capped gold nanoparticles as an efficient fluorescence quencher. Further, the interaction of target analytes such as proteins, mammalian cells, and amino acids with pre–quenched non–covalent PT–Pip–AuNP complexes was examined. Disruption of the binding equilibrium between PT–Pip and AuNP by analytes resulted in the selective displacement of PT–Pip, which generated signal output as a fluorescence ‘‘turn–on’’ mode. Consequently, for the sensitive detection of biomolecules and cells, chemical tongue sensor arrays were developed utilizing differential sensing approaches. PCA was used for the statistical evaluation of the multi–dimentional fluorescence response patterns. As a result, unique fingerprints were rapidly obtained by the direct sensing of proteins, ratiometric sensing of mammalian cells, and indirect sensing of amino acids. The combination of a differential sensing strategy with an appropriate multivariate statistical technique enabled the selective and sensitive detection and identification of proteins, mammalian cells, and amino acids.

Keywords: *Biosensors, Conjugated Polythiophene, Protein Detection, Mammalian Cell Detection, Amino Acid Detection*

ÖZET

BİYOMOLEKÜL ANALİZİ İÇİN İLETKEN POLİMER–TEMELLİ FLORESANS AÇIK/KAPALI BİYOSENSÖR GELİŞTİRİLMESİ

Biyomoleküllerin ve hücrelerin duyarlı ve seçici tespiti hastalıkların erken teşhisi, prognozunun izlenmesi ve etkili tedavi için önemlidir. Bu tez, biyomoleküller ve hücrelerin tespiti için yeni bir floresan 'açma/kapama' biyosensörü geliştirmeyi amaçlamıştır. Bu çalışmada ilk kez, bir katyonik politiyofen türevi olan poly(1,4-dimethyl-1-(3-((4-methylthiophen-3-yl)oxy)propyl)piperazin-1-ium bromide) (PT–Pip), proteinleri, memeli hücrelerini ve amino asitleri ayırt etmek için etkili bir floresan transdüksiyon elemanı olarak kullanıldı. Başlangıçta, konformasyonel ve optik değişiklikleri izlemek için PT–Pip'in pH'a bağlı spektroskopik karakterizasyonu yapıldı. PT–Pip'in pH duyarlılığı ilk kez gösterildi. Daha sonra, floresan ''kapanma'' fenomeni, verimli bir floresan söndürücü olarak sitrat–başlıklı altın nanoparçacıklar kullanılarak ayrıntılı olarak araştırıldı. Ayrıca, proteinler, memeli hücreleri ve amino asitler gibi hedef analitlerin önceden–söndürülmüş kovalent olmayan PT–Pip–AuNP kompleksleri ile etkileşimi incelendi. Analitler tarafından PT–Pip ve AuNP arasındaki bağlanma dengesinin bozulması, bir floresan ''açma'' modu olarak sinyal çıktısı üreten PT–Pip'in seçici yer değiştirmesiyle sonuçlandı. Sonuç olarak, biyomoleküülerin ve hücrelerin hassas tespiti için diferansiyel algılama yaklaşımlarını kullanan kimyasal burun/dil sensör dizileri geliştirilmiştir. Çok boyutlu floresan yanıt paternlerinin istatistiksel olarak değerlendirilmesi için PCA kullanıldı. Sonuç olarak, proteinin doğrudan algılanması, memeli hücrelerinin oransal algılanması ve amino asitlerin dolaylı olarak algılanmasıyla benzersiz parmak izleri hızla elde edildi. Diferansiyel algılama stratejisinin uygun bir çok değişkenli istatistiksel teknikle kombinasyonu, proteinlerin, memeli hücrelerinin ve amino asitlerin seçici ve hassas tespiti ve tanımlanmasını sağladı.

Anahtar Kelimeler: *Biyosensorler, Konjuge Politiyofen, Protein Deteksiyonu, Memeli Hücre Deteksiyonu, Amino asit Deteksiyonu*

TABLE OF CONTENTS

LIST OF FIGURES

Figure **Page**

Figure **Page**

Figure **Page**

Figure **Page**

Figure **Page**

Figure **Page**

Figure **Page**

Figure **Page**

Figure **Page**

LIST OF TABLES

Table **Page**

CHAPTER 1

INTRODUCTION

1.1. Sensors

The most commonly used and generalized definition of a sensor is "A device that receives a stimulus and responds with an electrical signal".[1] The transducer and analog to digital converter (A/D converter) are two primary components of typical sensors. Sensors detect physical variables such as temperature, pressure, mass, light, etc. Transducers are responsible for converting these variables into analog signals.[2] The analog signals should be converted to digital signals by the A/D converter before transferring to a computer.[3] The essential components of typical sensors are summarized in Figure 1.

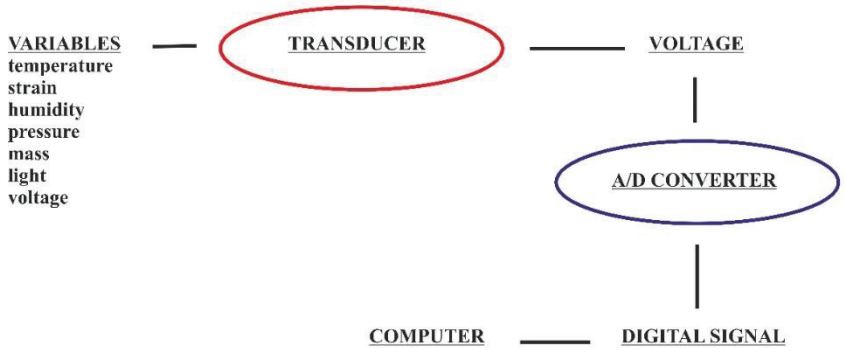

Figure 1. Basic components of a typical sensor.[3]

Many sensor classification criteria have been given in the literature. Based on the recognition elements, one can divide sensors into two subclasses. The first class is chemosensors, which have recognition molecules of non–biological origin that respond to target analytes.[4] The second class is biosensors with a sensing element of biological origin or biomimetic materials that respond to target analytes.[5] Among these sensor classes, biosensors are of great interest especially in medical diagnostics, drug

development, environmental monitoring, chemical and biological terrorism, and food quality control applications.[6]

1.2. Biosensors

A general definition of a biosensor is ‘‘a device that measures biological or chemical reactions by generating signals proportional to the concentration of an analyte in the reaction’’.[7]

Biosensors are mainly used for drug discovery; clinical diagnostics; soil, air, and water monitoring; food quality control; prosthetic devices; etc.[7] Bioreceptors, transducers, electronics, and display parts are the main components of biosensors as given in Figure 2.

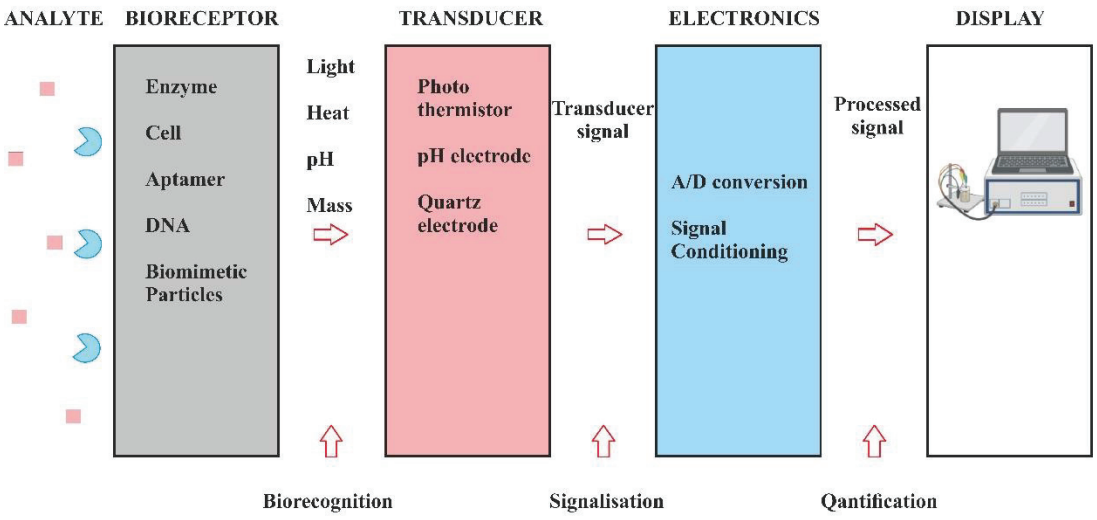

Figure 2. Main components of biosensors.[7]

The recognition element and transducer are two essential components for sensing. Recognition elements can be of biological origin, such as cells, tissues, enzymes, nucleic acids, etc.[8]; of biologically derived origin, such as aptamers and recombinant proteins; or biomimetic materials, such as molecularly imprinted polymers or synthetic receptors, etc.[9] These recognition elements are integrated within a transducer element[5] and are utilized to detect simple biochemical compounds, such as glucose or ammonia, or complex biological microorganisms such as viruses, bacteria, and mammalian cells.[6,10]

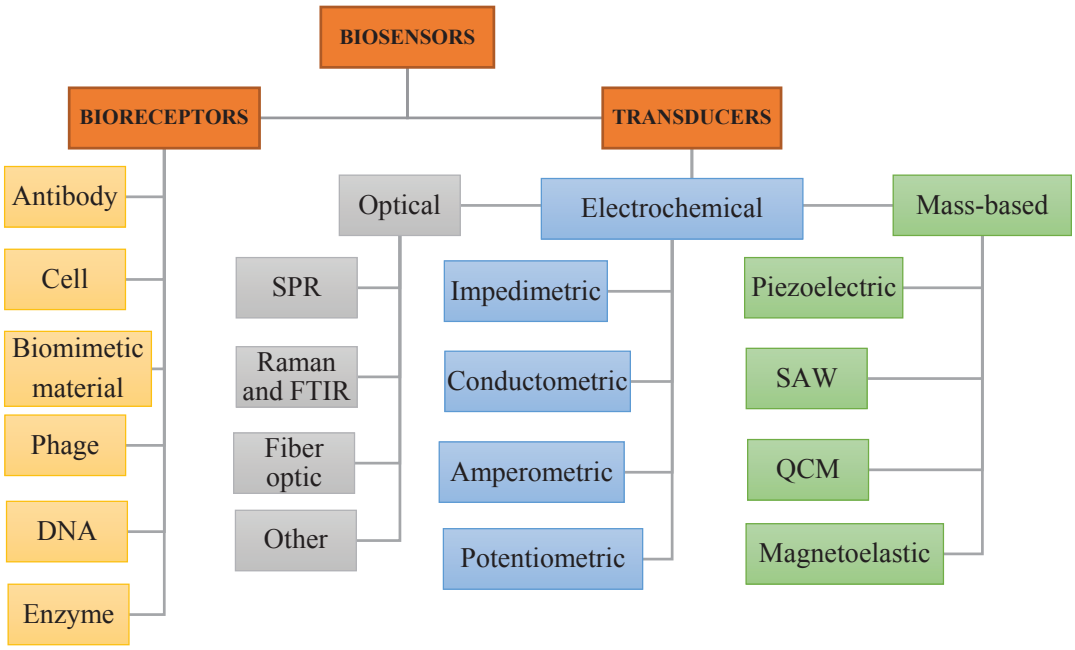

Figure 3. Classification of biosensors based on transducing and biorecognition elements.[10]

In recent years, nanomaterials were commonly classified under the class of bioreceptors due to their outstanding signal transducing properties and increasing usage in biosensing applications.[11]

The second important component of biosensors is the transducing element, called the ‘‘transducer’’, which converts the energy of the signal from one form to another. Based on transducing elements, biosensors can be divided into three subgroups: optical biosensors, mass–based biosensors, and electrochemical biosensors, as shown in Figure 3.

1.2.1. Biorecognition Elements (Bioreceptors)

A biorecognition element is a receptor utilizing biochemical interactions to detect analytes. The most commonly used bioreceptors in biosensors are cells, DNA, enzymes, and antibodies.[12]

The living cells used as biorecognition elements can qualitatively and quantitatively analyze multiple analytes simultaneously without effort and expense. The required enzymes and other biomolecules are readily present in the native surroundings of these cells. Therefore, cell bioreceptors recognize analytes of interest with optimal activity and high specificity.[13] Various cells with different origins can be used as

bioreceptors, such as microbial cells (bacteria, fungi, algae, and yeast) and higher eukaryotic cells (fish, rat, and human cells).[13] While biosensors utilizing microbial cells are commonly used to monitor water quality, higher eukaryotic cells are generally used to monitor cellular functions, and disease development.

Nucleic acids can also be used as biorecognition elements. For instance, DNA with specific genomic sequences was immobilized in the biologically active layer of biosensors and used as a nucleic acid–based biorecognition element.[14] DNA–based biosensors (genosensors) are utilized for analyzing genomic sequences, investigating oxidative damage on DNA, and revealing specific interactions between DNA and molecules or ions. The application areas of DNA–based biosensors have expanded considerably, now including clinical diagnosis, medical research, food safety analysis, and environmental monitoring. Reliable results can be obtained quickly without high cost.[15]

Meanwhile, enzymes' catalytic activity and specific binding properties make them useful biorecognition elements for enzyme–based biosensors. To detect target molecules, appropriate enzymes are utilized to develop robust biosensors, such as fructose dehydrogenase for fructose detection or glucose dehydrogenase for glucose detection. Although high specificity can be obtained by enzyme–based biosensors, the short lifetime of enzyme receptors is these biosensors' main drawback.[16]

Antibodies are widely used as bioreceptors due to their excellent selectivity to antigens. In antibody–based biosensors (immunosensors), antibodies are immobilized onto transducer surfaces to allow highly sensitive and selective detection of target analytes such as diagnostic biomarkers, harmful substances in food, environmental contaminants, biological terrorism agents, illicit drugs such as cocaine and heroin, etc.[17] Besides, the integration of antibodies into biosensors enables the development of *in vivo* biosensors, which are used for monitoring analytes continuously in biological media.[18]

In recent years, many biosensors have utilized ‘‘biomimetic’’ components as recognition elements imitating their biological analogues. These biomimetic components detect specific analytes via host–guest chemistry.[19] Biomimetic receptors provide highly selective and sensitive recognition of target molecules due to their well–characterized biomolecular mechanisms, such as enzyme–substrate interactions. Molecularly and ion–imprinted polymers and synthetic polymers are the most commonly used biomimetic materials due to their ease of synthesis and ability to be integrated within many different sensing strategies.[20]

1.2.2. Transducing Elements (Transducer)

Transducers are essential components of biosensors that convert the interaction between the analyte and the bioreceptor into a measurable signal. The signal is proportional to the biorecognition events. This energy convertion is known as ‘‘signalization’’.[7] Based on transducing elements, biosensors can be classified into three subgroups, as seen in Figure 3. The first group is mass–based biosensors, including piezoelectric, magneto–elastic, quartz crystal microbalance (QCM), and surface acoustic wave (SAW) biosensors. The second group is electrochemical biosensors, including amperometric, potentiometric, impedimetric, and conductometric measurements. The third group is optical biosensors, such as surface plasmon resonance (SPR), fiber optic, raman, and fourier transform infrared spectrophotometers (FTIR). The following section explains optical biosensors in detail.

1.3. Optical Biosensors

An optical biosensor is an analytical device containing biosensing elements integrated with an optical transducer. It is the most commonly preferred tool for the analysis of biomolecular interactions.[11] Bioreceptors identify chemical and biological analytes by creating optically measurable signals, as shown in Figure 4.

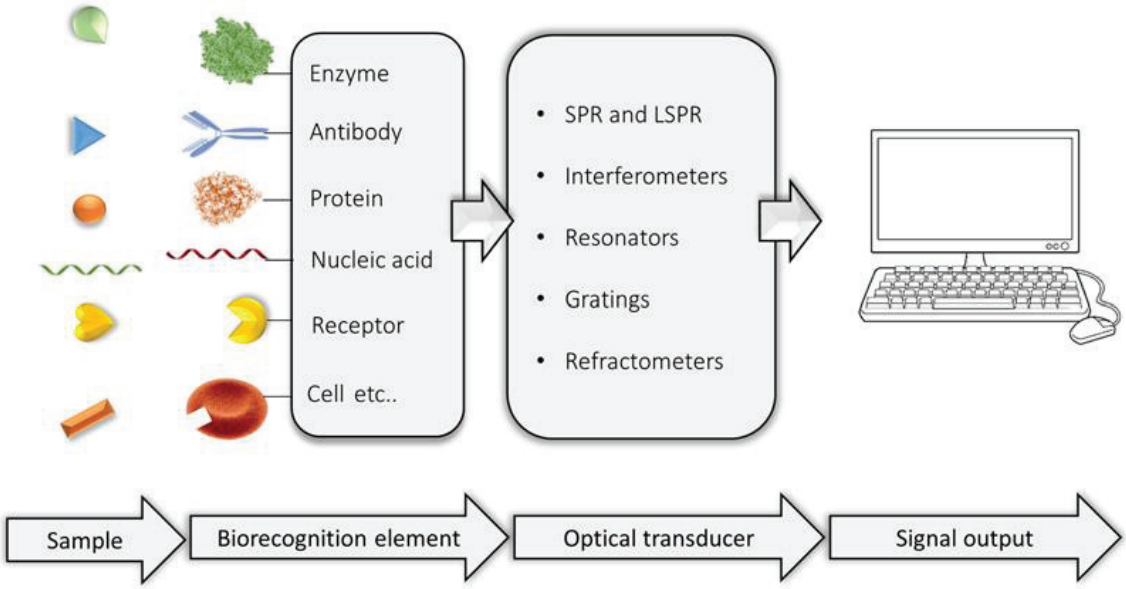

Figure 4. Main components of optical biosensors.[11]

Optically measurable signals can be obtained by the change of phase, intensity, and frequency or polarization of the incident light. These alterations result from the physiological or chemical interactions between the biorecognition element and the analyte. Differences in the absorption or reflection cause amplitude variation, which then affects the intensity of light. Frequency changes in biological sensing events utilize fluorescence, Raman scattering, or frequency shift[6], as shown in Figure 5.

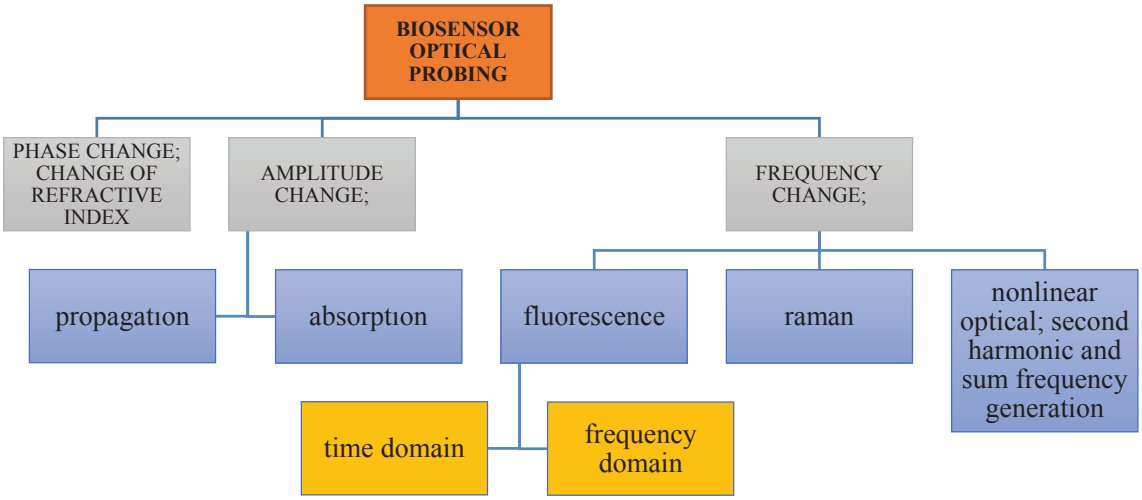

Figure 5. Optical changes used in biosensing applications.[6]

Optical biosensors utilize two modes: label–based and label–free. In label–based modes, label molecules permanently or temporarily interact with analytes. These interactions change their intrinsic properties. Conversely, in label–free modes, physicochemical properties such as charge, refractive index, and molecular weight (MW) are utilized for the detection of analytes.[21] In label–free biosensors, the molecular interactions between the biorecognition element and the analyte are converted into an optical, mechanical, or electrical signal. These signals can be detected without labels.

Optical biosensors have some advantages over conventional analytical methods. For instance, optical biosensors allow selective, specific, fast, and real–time measurement with remote sensing features. Optical components of these biosensors can be chosen for biocompatibility requirements as well. These biosensors also have compact designs and minimal invasiveness for *in –vivo* measurement.[6]

1.4. Sensing Approaches In Biosensors

Based on sensing techniques, biosensors can be divided into two categories: The first one is the ‘‘lock–and–key’’ methodology utilizing classical chemosensing approaches. The second one is the differential sensing method, which is an alternative method to classical chemosensing techniques.[22]

1.4.1. Lock And Key Models

The lock–and–key model is long–established method depending on the detection of the target molecules by receptors. These detections are highly specific and selective to a single analyte and identify no other species (one sensor–one analyte technique)[23,24], as shown in Figure 6. This conventional analogy explains the specific enzymatic reactions (enzyme–substrate interaction). Scientists also have used this principle to design synthetic biosensors for many years.

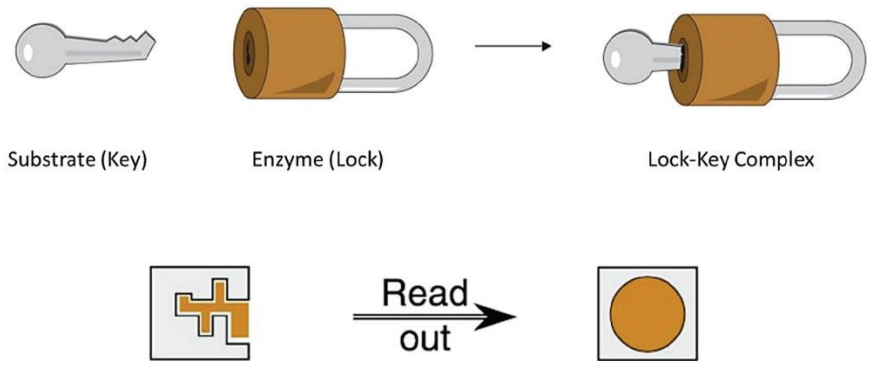

Figure 6. Classical chemosensing ‘‘lock–and–key’’ principle.[22]

The most common biosensors that utilize the one sensor–one analyte technique are blood glucose meters used by diabetics[25] and pregnancy tests[26]. Although lock–and–key methods are beneficial and advanced, they cannot be useful for simultaneous detection of multiple analytes. In recent years, researchers have focused on differential sensing techniques that mimic the nature of the biological olfactory and gustation systems for molecular recognition.[27] These sensing models allow monitoring of multiple

biomarkers simultaneously by an array of recognition elements and create a multidimensional response for each biomarker.[23]

1.4.2. Differential Sensing Models

Differential sensing is a universal technique that is an alternative to the classical ‘‘lock and key’’ analogy. In differential sensing models, a single biorecognition element does not have to bind to a single target specifically. In contrast, the biorecognition element is supposed to interact with multiple analytes with different affinities, as this element is "generalized" rather than "specialized".[27] This multiple analyte sensing method mimics the mammalian olfactory and gustatory systems by using cross–reactive receptors that interact unselectively and differentially with target analytes.[23] Therefore, this sensing architecture is called a ‘‘chemical nose/tongue strategy’’.[22] As a result, multi dimensional sensor outputs give a unique fingerprint for a single analyte or multiple analytes [28] , as shown in Figure 7. The multi–dimensional sensor results of cross–reactive sensor elements can be analyzed by multivariate statistical techniques, such as linear discriminant analysis (LDA) and principal component analysis (PCA).[22] The combination of differential sensing methods with an appropriate statistical analysis allows the identification of biological analytes such as proteins[29], carbohydrates[30], amino acids[31] , microorganisms[32], mammalian cells[33], etc.

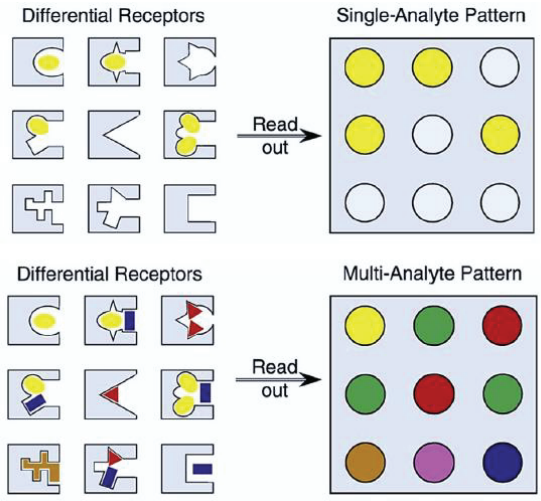

Figure 7. Schematic representation of differential sensing methods for single– or multiple–analyte detection by multiple sensor elements.[22,34]

1.5. Biomolecule and Cell Identification

The term ‘‘biomolecules’’ refers to macromolecules and small molecules found in living organisms, as shown in Figure 8. The macromolecules can be proteins, lipids, carbohydrates, and nucleic acids. Small molecules can be primary metabolites and natural products. Analysis of biomolecules is an essential issue, as some biomolecules are used as biomarkers in various applications.[35]

In literature, the general definition of a biomarker is "a characteristic that is objectively measured and evaluated as an indicator of normal biological processes, pathogenic processes, or pharmacologic responses to a therapeutic intervention".[36] Biomarkers are utilized in many fields, such as environmental monitoring[37], drug development[38], food safety analysis[39], and diagnostic purposes[40]. Macromolecules such as nucleic acids[2,41], proteins[42], and carbohydrates[43]; pathogens such as viruses and bacteria[44]; and mammalian cells[45] are used as promising biomarkers for disease detection and treatment.[46]

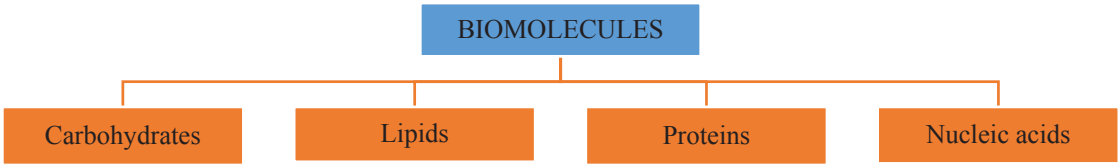

Figure 8. Classification of biomolecules found in living organisms

1.5.1. Protein Detection and Identification

Several biomarkers are used for environmental monitoring, drug development, food safety analysis, and medical purposes. Figure 9. shows the biomarkers’ classification. Among these biomarkers, proteins are of great interest. These biomarkers influence the molecular pathways in cells and are more relevant to disease initiation and progression than nucleic acid–based biomarkers.[36]

Figure 9. Biomarker classification

The presence and absence of proteins, the concentration fluctuations in biological samples, and the misfolding and aggregation occurring in protein structures are used as protein–based biological indicators for human health. Sensitive, accurate, and precise protein detection methods, especially with low concentrations in biological samples, are crucial for the early detection of several diseases and successful treatment of patients. However, proteins have complex 3D structures and exist in low concentrations in biological media. Therefore, the detection of protein biomarkers becomes challenging.

For many years, the detection and identification of proteins have been achieved by conventional assays:[47] such as Coomassie, Bradford[48], biuret[49], Lowry[50], and ELISA[51]. These methods have their own advantages and drawbacks. The common obstacles of these conventional methods are the need for calibration, structural variety, impurities, and the requirement of technicians.[52] In recent years, apart from these conventional methods, researchers developed various biosensors for protein detection that offer more advantages, such as measurement speed, cost–effectiveness, portability, ease of usage, and serial fabrication.[53]

1.5.2. Mammalian Cell Detection and Identification

The cell is the fundamental unit of a living organism. Distinguishing diseased cells from normal cells is crucial for the early diagnosis of some deadly diseases, such as cancer.[54] In recent years, early detection of cancerous or metastatic cells has become the center of cancer research. Cancer became the second–leading cause of death[55,56] and 10.0 million people died because of cancer in 2020.[57]

For early diagnosis, numerous invasive and non–invasive methods are used as standard procedures, such as electrocardiograms, bronchoscopy, and tissue biopsy. Although these procedures are widely used in the early detection of diseases, they are also painful and dangerous for patients.[58] Besides these operational techniques, laboratory diagnosis techniques such as cell culture methods (histopathology), analytical biochemistry assays (ELISA), parallel and deep sequencing approaches (next–generation sequencing), and amplification techniques (PCR) are also utilized for biomarker detection. Although these laboratory methods can be used to examine multiple samples simultaneously, they require multi–step and complex protocols, time–

consuming experimental steps, high sample volumes, equipped laboratories, and technicians.[59] Moreover, the detection of the intracellular and extracellular biomarkers used in these requires previous knowledge.[45,51] Unfortunately, not all cancer cells express apparent biomarkers to enable the detection of the subtle changes between normal and cancerous cells.[33] Therefore, investigation of cellular signatures by differential analysis[45,60] displays the properties of cells more precisely than target–specific approaches.[61] Polymerase chain reaction PCR[62], two–dimensional electrophoresis (2–DE) with mass spectrometry (MS) [63], and Raman spectroscopy [64] have also been used to obtain the cellular fingerprints arising from altered physicochemical features of cells. However, instrumentation complexity and time–consuming experimental procedures limit their usage for clinical purposes.

The electrical charge of cell surfaces and potential differences between the biological membrane and surrounding solution are essential markers for monitoring the cellular state. The phospholipid and receptor profiles of the cell membrane significantly influence the charge of the plasma membrane. The inner leaflet of healthy cells has a negative net charge due to the presence of anionic phospholipids. The outer leaflet of the membrane only consists of zwitterionic phospholipids, neutral phospholipids[65], and membrane cholesterols. Phospholipids asymmetrically localize between the two leaflets in healthy cells.[66–68] Contrarily, cancer cells cannot maintain the asymmetric distribution of phosphatidylserine, an anionic phospholipid.[69] Therefore, compared to normal eukaryotic cells, the membrane of cancer cells has more negatively charged components exposed on the outer membrane leaflet[70,71], as shown in Figure 10. Moreover, lipid composition differs not only between healthy cells and cancer cells but also between different types of cells. The phospholipid compositions are characteristics of specific cell types.

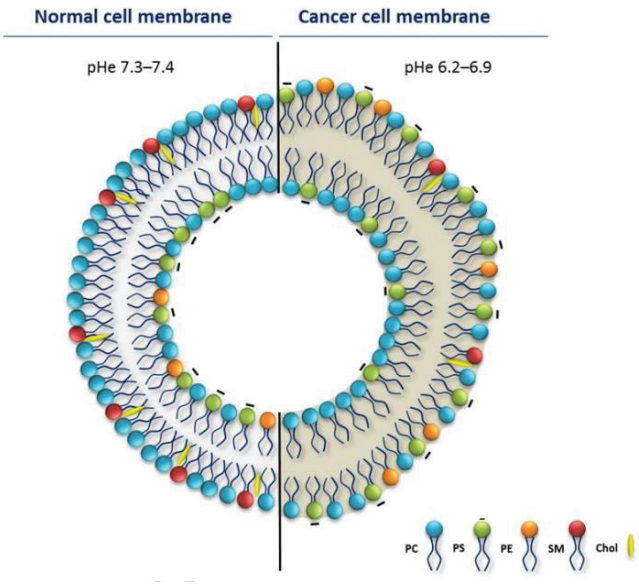

Figure 10. Lipid composition and extracellular pH of normal cell membrane and cancer cell membrane.[72]

The high concentration of sialic acid in the membrane of cancer cells and increased lactic acid secretion due to high–speed glycolysis are other reasons explaining the enhanced negative charges of the cancer cell membrane.[73–75]

Cell surface phenotypic and physicochemical signatures arise from the differences of cell membrane surfaces. These differences allow rapid and simple detection and identification of cancer types compared to intracellular signatures. The phenotyping investigations do not need any additional experimental steps, such as extraction of some specific macromolecules, etc.[76] Therefore, studies are focusing on phenotyping surface properties to distinguish normal cells from diseased ones.[33,45,77]

Among biosensors that offer rapid, stable, selective, and sensitive detection[78], optical biosensors are widely used due to their sensitive and quick response.[79] Various optical biosensors have been developed to sense overall cell surface physicochemical properties to distinguish cancerous cells from healthy cells.[33,45,80]

1.5.3. Amino Acid Detection and Identification

An amino acid is defined as an organic compound consisting of an amino and carboxylic acid group attached to an α–carbon (central carbon) and a distinctive R (radical) group (also called pendant groups) in the side chain. Peptides, proteins, enzymes, and hormones are polymerized forms of these essential substrates.[81,82]

Moreover, amino acids are fundamental bioactive molecules that play crucial roles in energy regulation, metabolic processes, and signaling pathways.[83] Among 500 naturally occurring amino acids identified to date[84], only 22 of them are proteinogenic (natural) amino acids. The proteinogenic amino acids are incorporated into protein formation in the translation process. Except for selenocysteine and pyrrolysine, the other 20 proteinogenic amino acids are encoded by a universal genetic code on DNA.

The 20 proteinogenic amino acids are classified according to their side chains attached to the α–carbon. These side chains have unique structures according to their sizes and shapes, hydrophobic and hydrophilic properties, and reactivity.[85] According to the form, side chains can be classified as cyclic (such as L–proline), non–cyclic (such as L–valine), branched (such as L–leucine), and non–branched (such as L–alanine). According to their atomic composition, amino acids can be clustered in to two subgroups: aliphatic amino acids and non–aliphatic amino acids. The side chains of aliphatic amino acids consist of hydrogen and carbon atoms. Non–aliphatic amino acids can contain either nitrogen, oxygen, or sulfur in their pendant chains.[86] In Figure 11, these 20 proteinogenic amino acids are classified in detail according to their side chains.

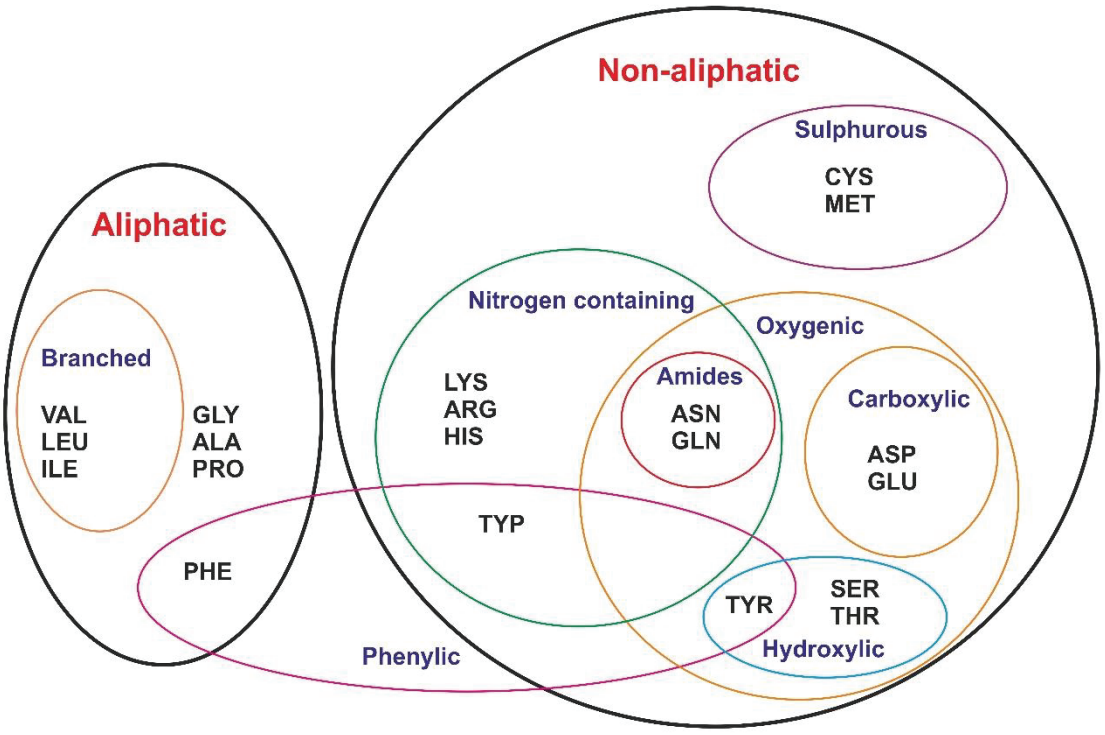

Figure 11. Classification of 20 proteinogenic amino acids via Venn diagram

Amino acids in bodily fluids are used as essential biomarkers for various diseases, such as Alzheimer's disease and pancreatitis.[87,88] Moreover, amino acid sensing also plays a crucial role in nutritional analysis.[87]

Generally, the detection and identification of natural amino acids are difficult to achieve. They have similar molecular structures as the only difference between amino acids is in the –R group. There are numerous conventional methods for amino acid detection, such as chromatographic, electrochemical and spectrophotometric methods. These traditional techniques are not cost–effective and require technicians.[87] Besides, these methods are specific to certain amino acids, as they only recognize amino acids with specific –R groups such as L–cysteine, L–histidine, and L–aspartic acid.[89] The detection and identification of amino acids that do not have particular –R groups such as L–alanine and L–valine are still challenging.[90] Moreover, a single amino acid level is insufficient for diagnosis. To enhance the accuracy of diagnostic tools, simultaneous analysis of multiple amino acids, especially the detection of the 20 amino acids in one test–bed, is required.[88] Therefore, studies are focused on developing biosensors that use cross–reactive sensor elements to detect and identify the 20 amino acids simultaneously.[31,88,89]

1.6. Conjugated Polymers in Sensor Applications

Conjugated polymers have attracted great attention in sensor studies as they have unique and unusual optical and electrical properties.[91] Alternating single and double bonds exist along the polymeric chain axis. The conjugation on the polymeric backbone provides a delocalized electronic structure over the entire chain.[92] The delocalized π–electrons generate π–bands and are responsible for the strong light absorption in the UV–visible region.[93] The polymers exhibit excellent light harvesting and semiconducting natures due to the energy gap between empty and filled π–bands. Conjugated polymers have two necessary compartments: the first one is the polymeric backbone, and the second one is functional side chains.[94] Different types of polymeric backbones are shown in Figure 12. Modifications of the conjugated polymer's side chain by various functional groups enhance the sensitivity of these polymers to target analytes, which is very desirable for sensing applications.

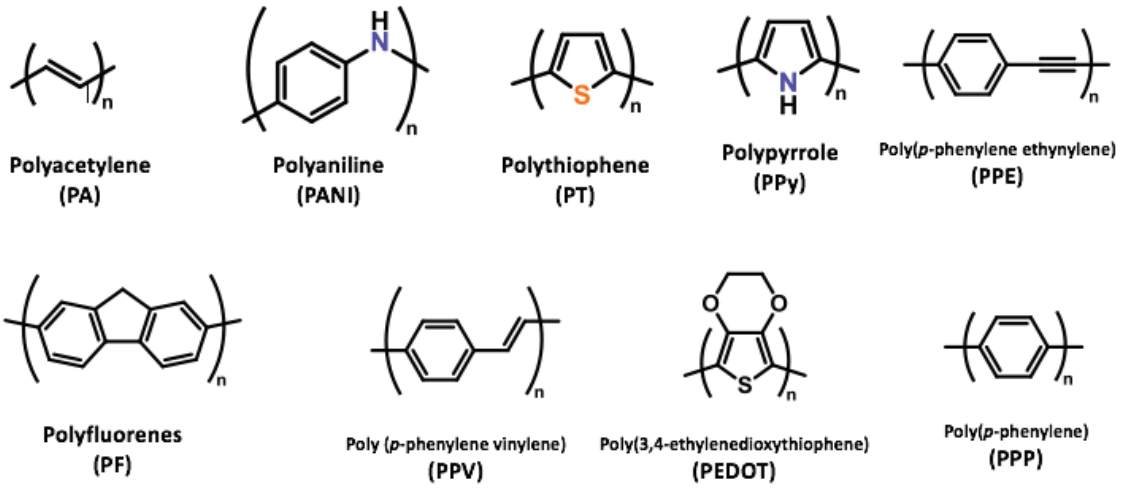

Figure 12. Structures of certain conjugated polymers.[95]

Conjugated polymers have become research hotspots in various fields such as photovoltaic cells[96], optoelectronic devices[97], and chemical[98] and biological sensing applications[99] due to their outstanding optical and electronic properties.[100,101] The use of conjugated polymers in biosensor development is an emerging field, as the detection of small quantities of molecules can be achieved by these stimuli–responsive polymers.[102] Conjugated polymers can be utilized as an optical probe in colorimetric, fluorometric, and fluorescence quenching–based assays.[98] Multiple recognition units can be introduced on a polymer backbone or pendant groups due to the molecular wire effect of conjugated polymers.[103] An analyte binding to single recognition unit creates collective responses from multiple sensor sites, as shown in Figure 13. This signal amplification leads to more sensitive detection of target analytes compared to single–molecule counterparts.

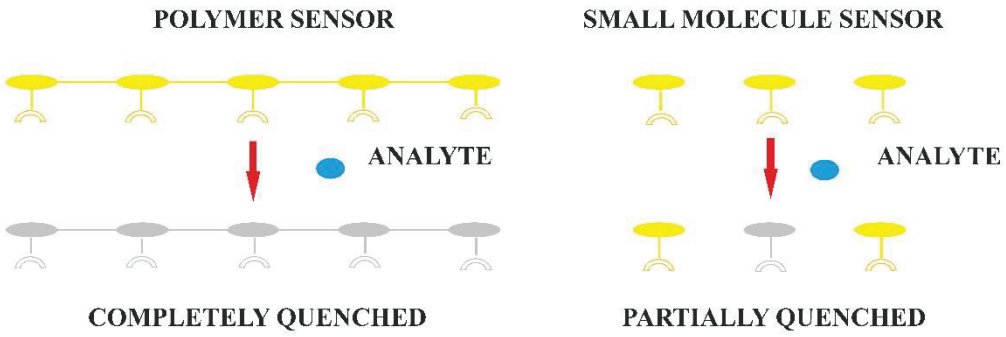

Figure 13. Characteristic responses of conjugated polymer and small molecule to target analyte

1.7. Conjugated Polythiophene

Polythiophene (PT) is a polymerized form of thiophene's heterocycles and has a conjugated sp^2 hybridized backbone.[104] The electrical and chemical structures of PT significantly affect its optical properties. Overlapping bonding molecular orbitals (π) with lower energy–forming valence bands are called the highest occupied molecular orbital (HOMO). Overlapping antibonding molecular orbitals (π^*) with higher energy–forming conduction bands are called the lowest unoccupied molecular orbital (LUMO). These orbitals create an energy gap that is defined by the energy differences between HOMO and LUMO. The monomer number of PT significantly influences the conjugation length of the polymer, the delocalized electronic structure, and the band gaps. For instance, when the number of monomers increases, the conjugation length increases concomitantly. This results in the formation of a delocalized electronic structure with lower band gaps and enhanced conductivity,[105] as shown in Figure 14.

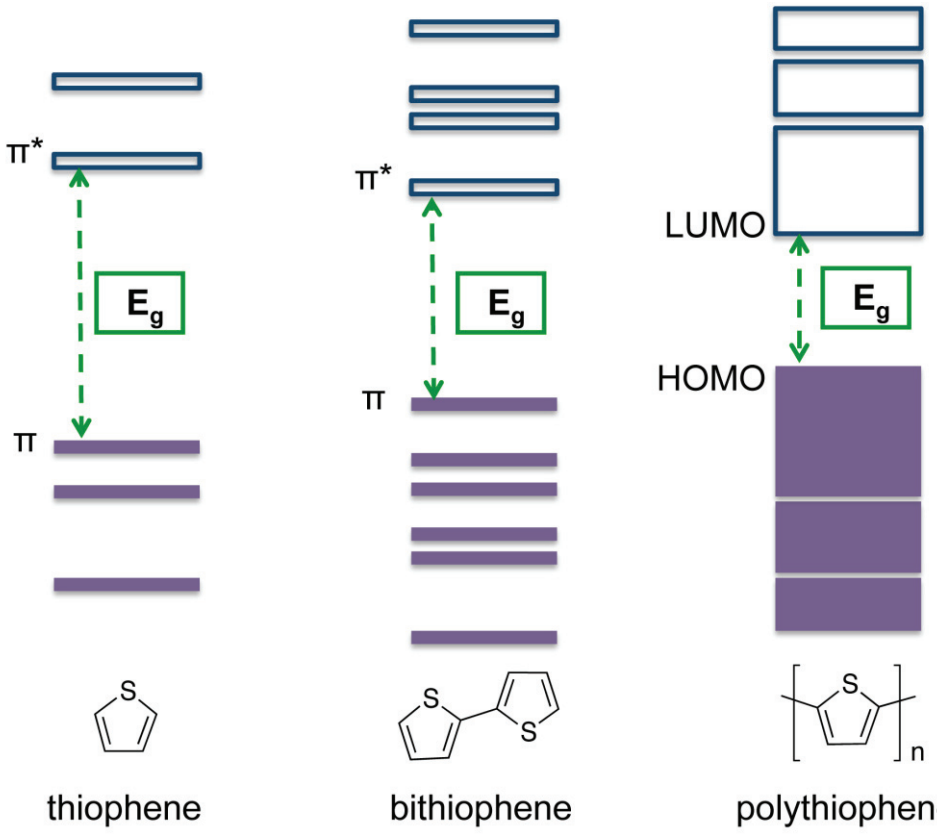

Figure 14. Band structure diagram of PT as a function of monomer units.[106]

Besides the number of monomers, the optoelectronic properties of PT can be tuned by doping. Doping decreases band gap and increases conductivity.[104] The light absorption of PT in the UV–visible region is strongly influenced by the π–π* transition from HOMO to LUMO and the stabilization and transportation of charge carriers by doping.[93] Therefore, the π electrons determining the band structure strongly influence the optical properties of PT. These tunable optical properties of PT have made this polymer an essential material for various applications.

The conformation of the polymeric backbone and the photo physical properties of PT are sensitive to external stimuli, such as temperature, pH values, electric field, solvent types, and introduction of target molecules which are essential for sensing applications.[107] Moreover, PTs are highly desirable and widely used materials[108] due to their thermal, chemical, and electrochemical stability and low–cost synthesis as well.[101]

Neutral conjugated polymers have some drawbacks in processing, such as insolubility and infusibility. Large counter–ions' incorporation or side chain attachment can overcome these limitations.[93] Besides these advantages, side chain attachment to the backbone of PT also lead to the production of PT derivatives and provides specific recognition units for sensing applications.[104]

Maynor et al. developed a sensor array using carboxylate functionalised PT derivative as a cross–reactive sensor element to detect soft divalent metal ions (Co^{2+}, Cu^{2+} and Ni^{2+}).[109] This anionic PT derivative was aggregated upon addition of polyvalent metal ions. Competitive ligand addition (α,ω–diamines) caused disaggregation of the polymer. PT derivative that was aggregated by different metal ions displayed different dissociation behavior upon addition of ligands. After the PT–metal aggregates were dissociated by a competitive ligand, unique colorimetric fingerprints were obtained for each PT–metal–ligand complex, which allowed sensitive and selective detection of metal ions.

In recent years, the superior optical, electronic and solubility properties of water–soluble cationic PT derivatives have drawn much attention[107] in biosensor development to detect and identify small molecules and anionic biomolecules, such as DNA, RNA, proteins, etc.[110,111] Introducing negatively charged macromolecules or anions to water–soluble cationic PT derivatives induces conformational changes on the polymer backbone and significantly affects interchain or intrachain interactions. These alterations can be monitored by the naked eye with UV–irradiation or under sunlight.[112]

The optical detection of iodine, a biologically important anions, via water soluble cationic poly(3–alkoxy–4–methylthiophene) was achieved by Ho et al.[113] This polymer showed high selectivity for I^- among various anions such as F^-, Cl^-, Br^-, CO_3^{2-}, HCO_3^-, $H_2PO_4^-$, HPO_4^{2-}, CH_3COO^-, $EDTA^{4-}$, SO_4^{2-}, and $(C_6H_5)_4B^-$. The fluorescence of PT derivative was decreased gradually by I^- addition. This fluorescence decrement was more distinct than that of other anions. Electrostatic interaction between cationic PT derivative and iodine enables selective fluorometric and colorimetric determination of I^-, as shown in Figure 15.

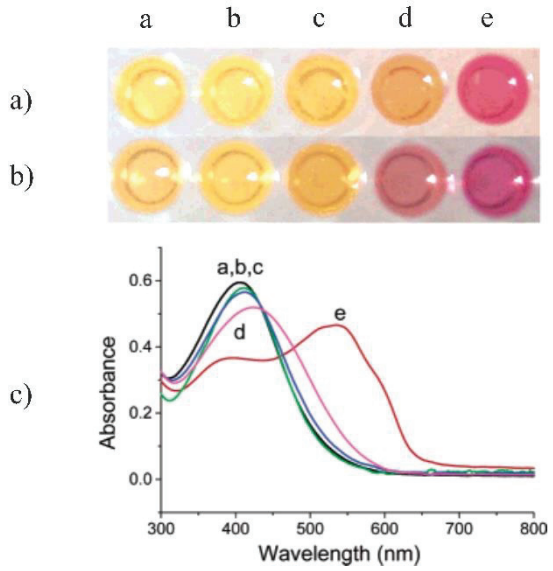

Figure 15. (a) Photograph of PT solutions of PT, PT + NaF, PT + NaCl, PT + NaBr and PT+ NaI; (b) photograph of PT solutions after 4 days; (c) absorbance spectra of PT solution in photograph.[113]

A facile method for the aluminum ion (Al^{3+}) detection in drinking water has been proposed by Tu et al.[114] A water soluble cationic PT copolymer was utilized as a fluorescence source. Complexation between PT copolymer with the charge complementary ATP resulted in the fluorescence quenching (15 % of initial fluorescence intensity) and color transition (from yellow to purple). This electrostatic self–assembly was disrupted by aluminum ion (Al^{3+}) a trivalent metal ion, due to the strong affinity between Al^{3+} and negatively charged ATP. The complexation between Al^{3+} and ATP liberated PT copolymer, induced the fluorescence recovery and color transition (from purple to yellow). The visual color change was evidence for 4 μM Al^{3+} in tap water, which is below the threshold according to European Economic Community (EEC) standards. This colorimetric naked-eye assay enables the sensitive and selective indirect detection of Al^{3+}in tap water.

Determination of biocompounds was also achieved by cationic PT derivatives. Liu et al. presented a colorimetric assay for thrombin detection.[115] The cationic PT derivative poly[3–(3′–N,N,N–triethylamino–1′–propyloxy)–4–methyl–2,5–thiophene hydrochloride] was used as a catalyzer of the oxidation reaction between 3,3′,5,5′–tetramethylbenzidine (TMB) and H_2O_2. After oxidation, the color of the solution became blue. The addition of thrombin–binding aptamer (TBA) enhanced the absorbance of TMB–H_2O_2. Introducing thrombin decreased the catalytic activity of PT derivative and reduced the absorbance by interacting with TBA. This colorimetric sensing mechanism detected thrombin with high selectivity in the presence of other proteins.

In another study, the water soluble cationic PT derivative (PTQ) was used as a fluorescence reporter for real–time determination of p97/VCP (a member of AAA–ATPase family) activity by Yildiz et al.[116] Initially, complexation between poly PTQ and ATP induced planarization of polymeric backbone, which triggers the aggregation of poly PTQ chains leading to fluorescence quenching. In contrast to ATP, ADP caused less planarization, less aggregation, and less fluorescence quenching. These two different fluorogenic responses were utilized to monitor the ATP–ADP conversion. In this assay, the upon addition of p97/VCP to the pre–quenched poly PTQ–ATP complex florescence recovery was observed due to the consumption of ATP by the p97/VCP. These fluorescence alterations were directly proportional to the conversion of ATP to ADP, which enabled real–time monitoring of the ATP hydrolysis by ATPase. Moreover, the convertion of ATP to ADP was detectable by naked eye due to the color transition from pink–red to yellow.

Cationic PT derivatives are also essential for nucleic acid sensing approaches. Rubio Magnieto et al. developed DNA hybridization biosensor using cationic poly[3–(60–(trimethylphosphonium)hexyl)thiophene–2,5–diyl] (PP).[117] The self–assembly of DNA and PP was studied. The ssDNA–PP constructs have chiroptical signatures in the absorption region of the PP derivative. These signatures were highly influenced by various ssDNA sequences due to the different interactions between individual thiophene monomers and nucleobases and were specific to DNA sequence, length, and topology. This study indicated that the cationic PP could be used in DNA hybridization biosensors.

Rajwar et al. developed a colorimetric assay for the detetction of microRNA (miRNA) in human plasma by using water–soluble cationic thiophene copolymers as

reporters.[118] The mir21, a miRNA sequence related to the lung cancer, was utilized as a target sequence (Tseq). Following the complexation of PT with the peptide nucleic acid sequence (PNA), which was complementary to the mir21, PT–PNA complex produce distinguishable colorimetric response due to the PT–PNA–Tseq triplexes formation. This colorimetric responses were more pronounced compared to that of PT−PNA−NCseq (noncomplementary sequence) or PT−Tseq/NCseq complexes. This colorimetric assay depended on the color transition of PT upon introducing Tseq or NCseq in the absence or presence of PNA. In the absence of PNA, weak fluorescent PT–Tseq/NCseq complexes were observed. In the presence of PNA, the PT–PNA–Tseq complex produced high fluorescence signal. These different signals enabled the detection of mir21 in human plasma, with a detection limit of 10 nM.

Ammanath et al. evolved this colorimetric nucleic acid detection method from solution–based assay to membrane–based assay to detect mir21 and hepatitis B virüs DNA in plasma.[119] In this flow–through colorimetric assay, poly–(vinylidene fluoride) (PVDF) was used as a membrane and cationic poly (3–alkoxy–4–methylthiophene) was used as an optical transducing element. Similar nucleic acid sensing strategy was utilized, and the two biomarkers; mir21 and hepatitis B virus DNA were succesfully detected in DI water and plasma at nanomolar concentration.

Yucel et al. combined a nonamplification–based nucleic acid assay with the polymerase chain reaction (PCR) for the detection of SNP biomarker of Familial Mediterranean Fever (FMF).[120] This sensing arthitecture relied on the hybridization of primer to the complementary sequences of DNA and a fluorometric method. In this methodolgy, the wild–type (WT) and mutant–type (MT) primers were introduced to the DNA individually at their melting temperatures. While the wild–type primer was strongly bind to the homozygous wild DNA, the mutant–type primer could not hybridize to the homozygous wild DNA. After precipitation of DNA, the supernatants were obtained for fluorometric examination. The supernatant of the former sample contained less amount of wild–type primer while the supernatant of the latter sample had more mutant–type primer. The fluorescence study revealed that in the presence of unbound primers, the significant bathochromic shift of fluorescence maximum was observed (from 525 to 580nm) due to the conformational change in the polymeric backbone, which is correlated with the binding affinity of primers to the DNA. The diagnostic potential of this assay was demonstrated for FMF, and provided distinct separation of healthy and patient individuals.

In recent years, biosensors have utilized fluorescence "turn on/off" approaches, as the fluorescence ‘‘turn on’’ mechanism is more sensitive than the ‘‘turn off’’ mechanism due to its high signal–to–background ratio, low LOD, and enhanced sensitivity.[121] In these turn "on/off" approaches, initial fluorescence can be reduced by quencher molecules and recovered by adding analyte. This sensing mechanism using the conjugated polymers is explained in the following section.

1.8. Fluorescence Quenching by Gold Nanoparticles

In the last decade, nanoscience has been developed as an alternative to traditional methods. It has been widely used in drug delivery, bio imaging and biosensing applications. Metals such as gold, silver, and copper are valuable candidates for nano probes. The unique optical properties, large surface–to–volume ratio, variable surface functionalities, and size– and shape–dependent optoelectrical properties make AuNPs (gold nanoparticles) an essential material for biosensing, drug delivery, and bioimaging applications, as shown in Figure 16.

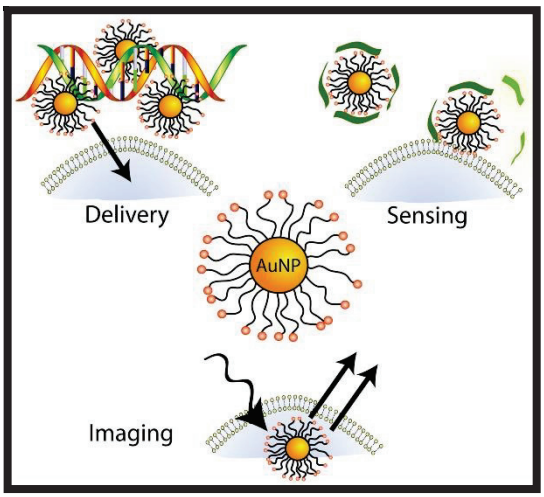

Figure 16. Common applications of AuNPs.[122]

In biosensing applications, two important properties of gold nanoparticles are utilized: the first one is SPR, and the second one is its fluorescence quenching ability. The SPR band results from the oscillation of the surface conduction electron of gold nanoparticles, which arises from resonant excitation by the electromagnetic radiation of incident light as[123], , shown in Figure 17.

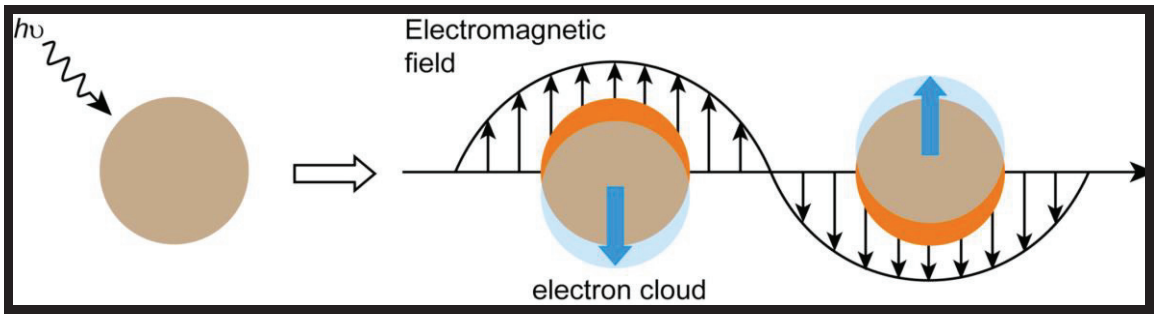

Figure 17. Oscillation of conduction electrons of AuNPs by incident light.[122]

Depending on the size of the spherical gold nanoparticles, the color and SPR peaks can vary from brown to purple and from 500 nm to 550 nm, respectively. Aggregation of colloidal gold nanoparticles causes red shifts in the SPR peak and changes the color of the solution from red to purple, which arises from interparticle plasmon coupling.[122] The aggregation and disaggregation of gold nanoparticles are mainly utilized for colorimetric sensing of molecules. Introducing molecules to gold nanoparticle solution induces aggregation/disaggregation and changes the color of the solution which are detectable by the naked eyes.

Gold nanoparticles possess an excellent fluorescence quenching ability which is very useful for sensing applications requiring fluorescence manipulation. Fluorescence resonance energy transfer (FRET) occurs when the emission of fluorophores and the SPR band of gold nanoparticles overlapp. This spectral overlap results in fluorescence quenching of fluorophores. The non–covalent conjugation of gold nanoparticles and fluorophores is widely used in fluorescence ‘‘turn on/off’’–based sensing applications. This pre–quenched complex is selectively disrupted by analyte addition.

1.9. Literature Survey of Fluorescence Turn on/off Sensing

Conjugated polymers are able to couple to more than one analyte with different affinities due to electrostatic, hydrophobic, or hydrophilic interaction. Therefore, these polymers become excellent recognition elements in differential sensing applications. Fluorescence conjugated polymers can be used individually as sensor elements[51] or together with the quencher molecules.[32] In the literature, polymer–quencher constructs

have been widely used to develop chemical nose/tongue sensor arrays using a fluorescence ‘‘turn on/off’’ sensing mechanism. In these sensor arrays, fluorescence quenchers are utilized to reduce the fluorescence of the polymer, which is called the fluorescence ‘‘turn off’’ mode.[124] Adding analytes disrupts this polymer–quencher complexation through competitive binding. Selective displacement of the polymer results in complete or partial fluorescence recovery, which is called fluorescence ‘‘turn on’’ mode. Fluorescence response patterns for each analyte were analyzed via multivariate statistical techniques such as PCA and LDA.

Kong et al. developed a nanomaterial–assisted chemiluminescence–based sensor to identify 12 common proteins with three different concentrations and 12 types of human cell lines containing healty, cancerous, and metastatic cells.[125] The collective responses obtained by this sensor array created a unique pattern for each analyte. Statistical analysis of these patterns was carried out by LDA. Twelve proteins could be classified successfully.

You et al. created a chemical ‘‘nose’’ sensor array to identify seven proteins by using six differently functionalized cationic nanoparticles as fluorescence quencher molecules and an anionic poly(p–phenyleneethynylene) (PPE) as a fluorescence source.[126] Initially, the fluorescence of polymer was quenched by the nanoparticles. The addition of protein analyte disrupted the pre–quenched nanoparticle–polymer complexation. The fluorescence polymer was released to the solution phase and regained its fluorescence. The interaction between proteins and nanoparticles depends on the MW and isoelectric point (pI) of proteins. The competitive binding of polymer and proteins to the nanoparticles created distinct fluorescence patterns for each protein, as shown in Figure 18. These multidimentional fluorogenic responses were statistically evaluated by linear discriminant analysis (LDA). Seven proteins were successfully identified by this fluorescence–based sensor array.

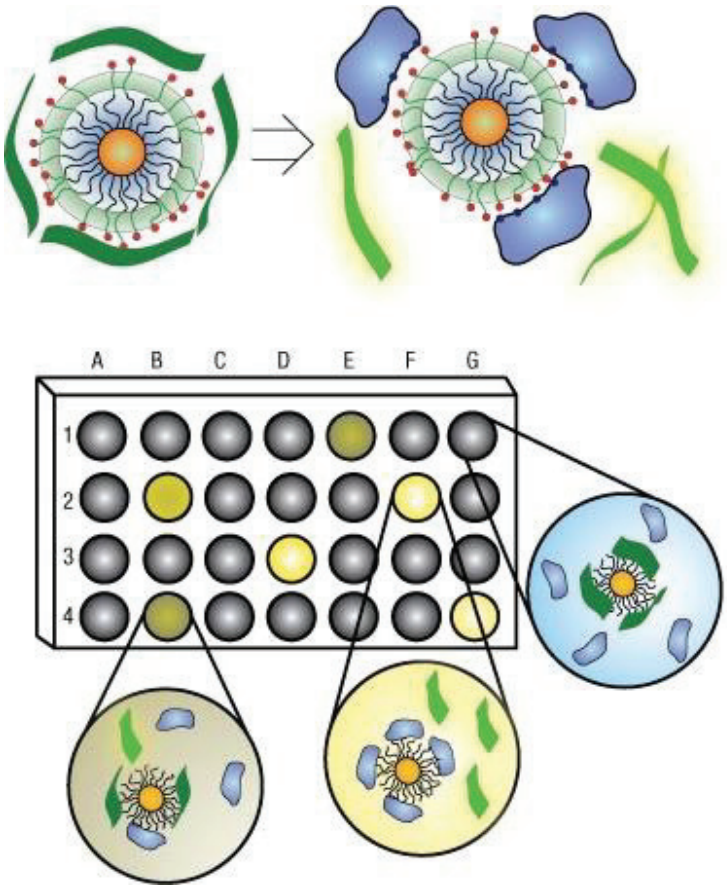

Figure 18. Fluorophore displacement of sensor array; fluorescence turn on/off behavior as a result of competitive binding of polymer and protein to nanoparticles.[126]

De et al. created a sensor array using similar sensing mechanism to the previously developed by the You et al. to discriminate 5 human serum protein (human serum albumin, immunoglobulin G, transferrin, fibrinogen and a–antitrypsin) in buffer and in human serum.[127] Green fluorescent protein (GFP) was used instead of fluorescence polymer. Initially, the fluorescence of anionic GFP was quenched by the cationic AuNP. In the presence of analyte, the fluorescence of GFP was modulated depending on the binding affinity of analyte towards AuNP and GFP. In these sensor array, proteins were detected according to their physicochemical properties, such as MW and pI. The fluorogenic responses of proteins were statistically evaluated by LDA. The combination of sensor array and LDA enabled the identification of five human serum proteins with various concentration, as shown in Figure 19.

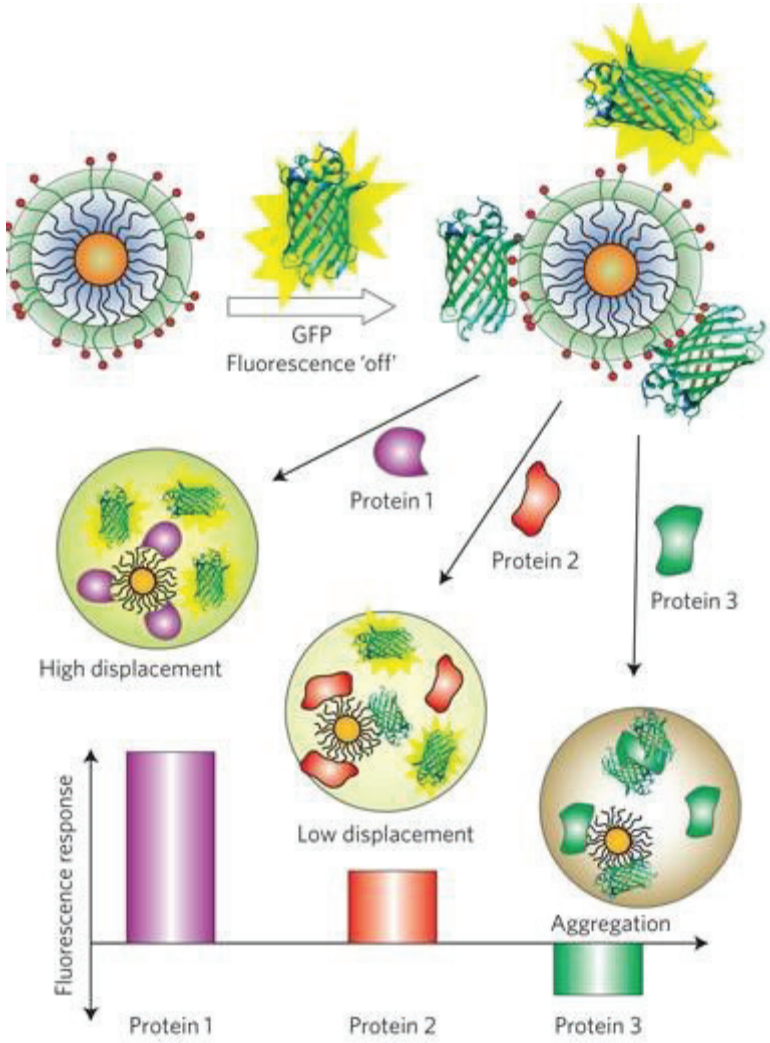

Figure 19. Fluorescence–based sensor array; fluorescence turn on/off approach and fluorescence response pattern created by protein addition.[127]

Bajaj et al. developed an array–based sensing system with a nanoparticle–fluorescence polymer to differentiate normal, cancerous, and metastatic cells as well as isogenic cells.[45] Initially, the fluorescence of the anionic polymer (PPE–CO_2) was quenched by cationic nanoparticles. Upon addition of analyte, the competitive binding of cell surfaces and the polymer to nanoparticles disrupted the polymer–nanoparticle conjugation. The polymer regained fluorescence after being released into the solution. Differential interaction of different cell lines created a unique florescence response for each cell line. These fluorogenic responses were then analyzed by LDA, and unique fingerprint for each analyte was obtained. Therefore, different cell types; normal, cancerous, and metastatic human breast cells; and isogenic normal, cancerous and metastatic murine epithelial cell lines were successfully discriminated.

The same group developed a sensor array utilizing similar sensing mechanism to the previously developed sensor array. However, GFP was used instead of conjugated polymers to decrease the sensor array's detection limit (LoD). This sensor array creates multidimensional data for cells, which are normal, cancerous, and metastatic, as well as isogenic, as shown in Figure 20. Four–fold sensitivity enhancement was obtained by this sensor array relative to the nanoparticle–polymer sensor array developed by the same group.[33]

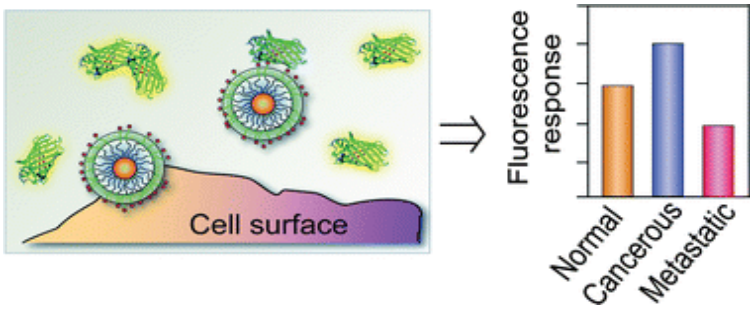

Figure 20. Schematic representation of competitive binding of GFP and cell surface to nanoparticles and fluorescence responses of normal, cancerous, and metastatic cells.[33]

Shang et al. reported a fluorescence detection method utilizing a fluorescence polymer–nanoparticle conjugate to detect L–cysteine.[128] The fluorescence of the anionic polymer was quenched by FRET occurring between the cationic quencher and fluorophores. L–cysteine modulated this energy transfer. This approach allowed sensitive detection of L–cysteine with LoD of 25 nM.

Wang et al. developed an optoelectronic tongue that contained a poly(para–phenyleneethynylene) (PPE) and green fluorescent protein (GFP) and three metal ions((Fe^{2+}, Co^{2+}, and Cu^{2+}) at three pH values (7, 10, and 13) to discriminate 20 natural amino acids.[31] The fluorescence of PPE and GFP were significantly quenched by these metal ions. 20 amino acids introduced to the pre–quenched PPE/GFP–metal complexes created distinct fluorogenic responses. Statistical analysis of fluorescence response patterns was carried out by LDA. This sensor array successfully clustered 20 amino acids into 5 classes which were hydrophobic, polar, aromatic, positively charged, and negatively charged groups.

Wang et al fabricated a sensor assay based on fluorescence quenching and recovery mechanism for the detection of Cr(VI) and Fe(III).[129] Formaldehyde–modified, hyperbranched polyethyleneimine (F–hPEI–) capped AuNPs were used as a

fluorescence sensor element. Initially, the fluorescence of sensor was quenched by Cr(VI) due to the combined effects of internal charge transfer (ICT) and the inner filter effect (IFE). The limit of detection was calculated as 0.63 μM for Cr(VI). Moreover, this sensor could distinguish between Cr(III) and Cr(VI). Upon addition of Fe(II), the fluorescence of sensor was recovered as a result of redox reaction between Cr(VI) and Fe(II). The successfull discrimination between Cr(III) and Cr(VI), and Fe(II) and Fe(III) could be achieved by this sensor.

Qin et al. developed a new bifunctional nanosensor for the detection of Cu^{2+} and bithiols.[130] Polyethyleneimine nanoparticles (PEIN) were utilized as a fluorescence source. Among thirteen common metal ions, the strong fluorescence of PEIN was effectively quenched only by Cu^{2+} via static quenching. The fluorescence of PEIN–Cu^{2+} was recovered upon addition of bithiols such as Cys or GSH. Therefore this system had two sensory events; Cu^{2+} sensing was achieved by fluorescence turn–off mode, and bithiol sensing was performed by subsequent addition of bithiols to the pre–quenched PEIN–Cu^{2+} complex, which resulted in fluorescence turn–on mode.

In another work, Zhang et al. reported a complementary approach to the classical chromatography methods to determine Edman degradation of amino acids.[131] A sensor array had complexes of three anionic poly(pphenyleneethynylene) (PPE) derivatives and metal ions such as Fe^{2+}, Cu^{2+}, Co^{2+}. In this study, metal ions were used to construct a more discriminative array. Addition of degradation products of the Edman process (phenylhydantoin–derivatives of amino acids) created fluorescence alteration; such as fluorescence quenching or fluorescence turn–on. These fluorogenic responses were statistically evaluated by linear discriminant analysis (LDA) to obtain unique fingerprint for each analyte. This sensor array enabled the dicrimination of phenylhydantoin–derivatives of amino acids degraded from oligopeptides during Edman sequencing.

Recently, Tawfik et al. presented a new monitoring technique for the environmental pollutants.[132] The fluorescence on–off sensor consisted of conjugated PT derivative and quantum dots to detect Hg^{2+} and triacetone triperoxide (TATP). Initially, the fluorescence of polymer–quantum dot complex was quenched by Hg^{2+} addition via electron transfer. Addition of TATP induced significant fluorescence recovery due to the strong interaction between TATP and Hg^{2+}. This sensor displayed high sensitivity for TATP and Hg^{2+} with a detection limits of 0.055 mg L^{-1} and 7.4 nM in water, respectively.

CHAPTER 2

MATERIALS & METHODS

2.1. PH–dependent Spectroscopic Characterization of PT-Pip

Cationic water–soluble poly(1,4–dimethyl–1–(3–((4–methylthiophen–3–yl)oxy)propyl)piperazine–1–ium bromide) (PT–Pip) was synthesized at the Biosens & Bioapps Laboratory (İzmir Institute of Technology) according to the procedure reported previously.[133] Sodium hydroxide (98%) were purchased from Sigma–Aldrich (St. Louis, USA). Hydrochloric acid (37% concentrated fuming HCl) were provided from Merck (Darmstadt, Germany). The chemical structure of the PT–Pip are shown in Figure 21.

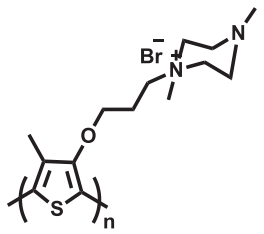

Figure 21. Chemical structure of PT–Pip.[133]

2.1.1. UV–visible and Fluorescence Spectroscopy Analysis of PT-Pip

PH–dependent spectroscopic analyses of PT–Pip were carried out by UV–visible and fluorescence spectroscopy. Scanning of the fluorescence and absorbance intensity for all samples were recorded using a Varioskan™ flash multimode reader (Thermo Scientific). The excitation wavelength was fixed at 405 nm, step size 2 nm, excitation bandwidth 5 nm, and measurement time 100 ms at room temperature. According to the excitation and emission maxima of PT–Pip [133], the fluorescence spectra were obtained between 450–700 nm. The absorbance spectra were obtained between 300–700 nm.

200 µL PT–Pip (1.4 mM (monomer based)) solution was placed in a well plate. PT–Pip was titrated by HCl and NaOH sequentially with the final concentration of 56.6

mM and 52.9 mM, respectively. The UV–visible absorption and fluorescence spectra were recorded after all titration steps.

2.2. Direct Sensing of Proteins

To develop a sensitive and selective fluorescence ‘‘turn on/off’’ mode, the fluorescence quenching mechanism was initially optimized for buffer and pH. After fluorescence quenching, proteins were introduced to the pre–quenched supramolecular PT–Pip–AuNP complexes. As a result of the self–assembly between the PT–Pip–AuNP complex and protein, fluorescence responses were investigated in detail by fluorescence spectroscopy. The schematic represantation of the fluorescence ‘‘turn–on/off’’ sensing mechanism is illustrated in Figure 22.

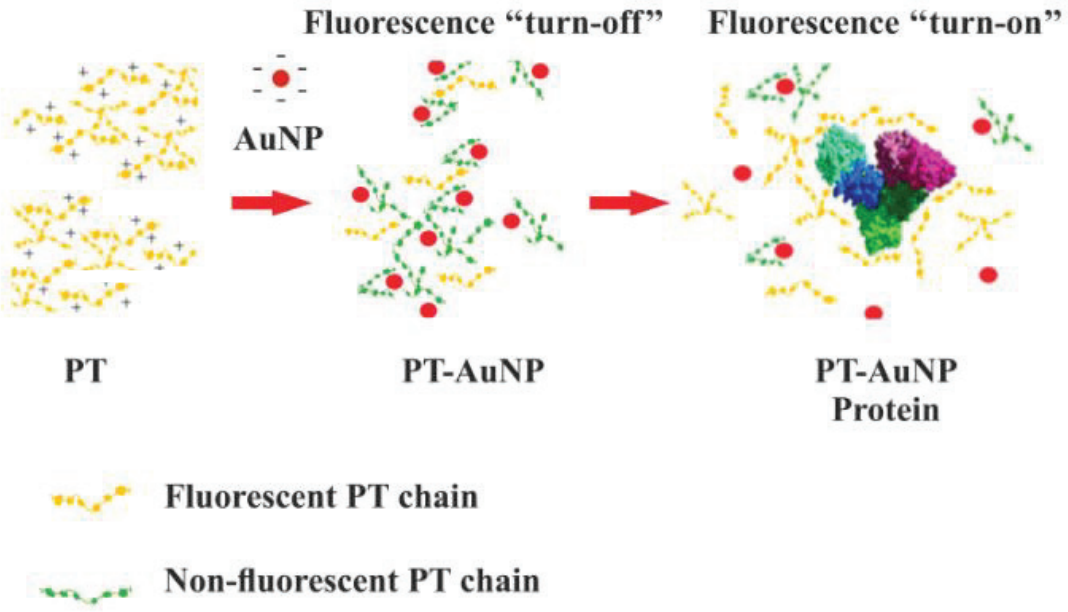

Figure 22. Schematic representation of fluorescence ‘‘ turn–on/off’’ sensing mechanism

2.2.1. Spectroscopic Analysis of Gold Nanoparticle

A negatively charged AuNPs were synthesized by Turkevic Method[134] as shown in Figure 23. The chloroauric acid solution (0.5 mM) was prepared by dissolving 0,01g gold (III) chloride hydrate (purchased from Sigma–Aldrich Company) in 60ml MQ water. 38,8 mM sodium citrate solution was prepared by dissolving 0,069g sodium citrate (purchased from Sigma–Aldrich Company) in 6ml MQ water. Initially, the chloroauric acid solution was heated to 100 ºC, then cooled to 75 ºC. The chloroauric acid solution was then treated with sodium citrate and constantly stirred until the color of the solution became wine red. This solution was stored at +4 ºC.

Citrate ions acted as reducing and capping agents. The production of colloidal gold was detectable by naked eyes (yellow to red color transition). The UV–visible spectroscopy and zeta size analysis were carried out to detect the intensity and the diameter of the AuNP. Scanning of the absorbance intensity of the colloidal AuNPs was carried out by a Varioskan™ flash multipurpose plate reader using a step size of 2 nm and a measurement time of 100 ms at room temperature. Absorbance spectra were obtained between 300–800 nm.

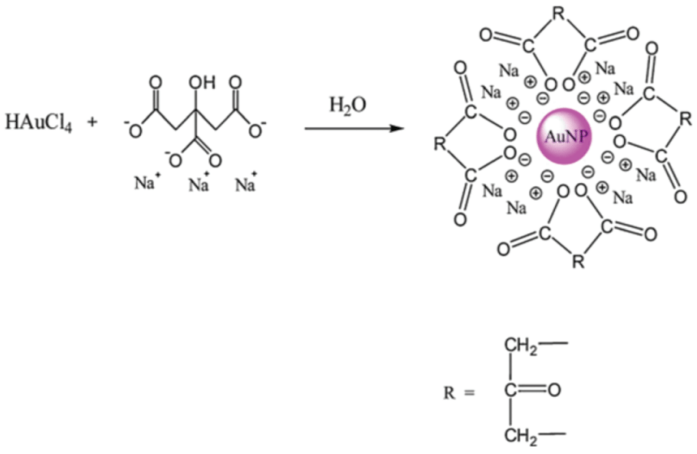

Figure 23. Turkevich's method for AuNPs fabrication.[135]

2.2.2. Fluorescence Quenching of Gold Nanoparticle in Different Buffer Solutions

The fluorescence quenching mechanism between PT–Pip and AuNP was investigated in TE buffer, PBS buffer, and MQ water, seperately. PT–Pip (1.4 mM monomer–based) 1:2 diluted with 1X TE buffer, 1X PBS buffer, and MQ water were used. PT–Pip solutions were titrated with AuNPs. The fluorescence spectra were recorded at all steps using Varioskan™ flash multimode reader (Thermo Scientific). The excitation wavelength was fixed at 405 nm. Fluorescence spectra were obtained between 450–700 nm.

2.2.3. Effect of PH on Gold Nanoparticle Stability

The pH–dependent stability of AuNP was investigated via UV–visible spectroscopy. 100 µL AuNP solution was titrated by water (pH = 2.05, pH = 7.0, and pH = 11.75) and 1X TE buffer (pH = 1.32, pH = 7.38, and pH = 12.05), seperately. The absorbance spectra were recorded after all titration steps. The absorbance spectra were obtained between 300–800 nm by using Varioskan™ flash multimode reader (Thermo Scientific)

2.2.4. Investigation of Fluorescence Quenching Mechanism of AuNPs

The fluorescence quenching mechanism of AuNP was investigated by fluorescence and UV–visible spectroscopy. PT–Pip (0,5 mg/ml) solution 1:2 diluted with MQ water (pH =7) was used. Initial fluorescence and absorbance spectra were recorded. PT–Pip solutions were titrated with 50 µl AuNP solution at 25 °C, 35 °C, and 45 °C, seperately. After all titration step, fluorescence and absorbance spectra of PT–Pip were recorded again. Fluorescence and absorbance measurement were performed following the previously–mentioned protocols. The K_{SV} values of AuNP was calculated by Stern–Volmer (S–V) equation[136] (Equation 1). The conformational alteration of PT–Pip upon complexation with AuNP at 25 °C, 35 °C, and 45 °C was examined by UV–visible spectoscopy.

Afterwards, PT–Pip (0,5 mg/ml) solution 1:2 diluted with TE buffer (pH = 7.08, pH = 9.64) and MQ water (pH = 7.00, pH = 9.70) were used. The initial fluorescence spectra of PT–Pip were recorded. PT–Pip solutions were titrated with 50 µl AuNP solution at 25 °C. The fluorescence spectra were recorded after all titration steps. Fluorescence measurement were performed following the previously–mentioned protocol. K_{SV} values of AuNP for four parameters were determined according to Equation 1.

$$I_0/I=1+ K_{SV} [quencher], \quad [1]$$

Where I_0 and I are the fluorescence intensity of PT–Pip in the absence and presence of AuNP, respectively. K_{SV} is the Stern–Volmer quenching constant determined by Linear Stern–Volmer plots.

2.2.5. Direct Sensing of Proteins

Bovine serum albumin (BSA), cytochrome C (CC) (from horse heart), acid phosphatase from potato (Phos A), alkaline phosphatase from bovine intestinal mucosa (Phos B), and protease (from *Bacillus licheniformis*) were purchased from Sigma–Aldrich Company. 1 mM stock solutions of proteins prepared with MQ water were stored at –20 ºC. Protein solutions 1:9 diluted with MQ water (pH =7.0, pH = 9.7) and TE buffer (pH = 7.08, pH =9.7) were used. Initially, the fluorescence spectrum of PT–Pip was recorded. The fluorescence of PT–Pip was then quenched with 50 µl AuNP solution. 110 µl (100 µM) protein solutions were added to the pre–quenched PT–Pip–AuNP complexes via titration. Following the previously–mentioned fluorescence measurement protocol, the fluorescence spectra were recorded after all titration steps.

2.3. Ratiometric Sensing of Mammalian Cells

BCE C/D–1b (an adult bovine corneal endothelial cell line, ATCC® CRL–2048™), NIH/3T3 (mouse fibroblast, ATCC® CRL–1658™), MDA–MB–231 (human epithelial breast adenocarcinoma, ATCC® HTB–26™), MCF–7 (human epithelial breast adenocarcinoma, ATCC® HTB–22™), SAOS–2 (human osteosarcoma, ATCC®

HTB–85™), SH–SY5Y (human bone–marrow neuroblastoma, ATCC® CRL–2266™), and HeLa (human epithelial cervix adenocarcinoma, ATCC® CCL–2™) cell lines were used as analytes for cell sensing studies.

Solvent optimization for cell sensing experiment was investigated by fluorescence spectroscopy. The pre–quenched PT–Pip–AuNP complexes were titrated with DMEM and MQ water solution (without cell) to observe DMEM and MQ water's effect on the sensing mechanism. After buffer optimization, cell concentration was optimized using SAOS–2 cell lines. These cell lines were dissolved in MQ water with two concentrations (200.000 cell/100 µl MQ water, and 2.000.000 cell/100 µl MQ water) prior to use. PT–Pip–AuNP complexes were titrated by the suspended cells. Fluorescence spectra between 450–700 nm were recorded after all titration steps.

A complete cell culture medium (DMEM media supplemented with 10% FBS and 1% penicillin–streptomycin) + alamar blue (without cell) was used as a blank. Initially, the viabilities of suspended and adherent cells were compared by using 50,000 SH–SY5Y cells. Cells were treated with 1% alamar–blue solution, then incubated for 4 hours. After incubation, the absorbance values of solutions were measured at 570 nm and 600 nm by Multiskan™ GO Microplate Spectrophotometer (Thermo Fischer Scientific). All experiments were repeated three times. Later, the viabilities of the suspended cells in water, 1X TE buffer, and 25 mM HEPES were investigated by using 50.000 MCF–7 cells. 1% alamar–blue solution was added to each well and incubated for 4 hours. After incubation, absorbance intensity was measured at 570 nm and 600 nm.

2.3.1. Ratiometric Sensing of Mammalian Cells and Zeta Potential Analysis for Seven Cell Lines

The cell pellets containing 200.000 cells were suspended in 100 µL 1X TE (pH = 7.4) buffer and 25 mM HEPES (pH = 7.4) buffer before use. Another 200.000 cells were also used as cell pellets without using any buffer solution (after centrifuging, the cell pellet was obtained and directly added to the PT–Pip–AuNP solution).

25 µL PT–Pip (0,5 mg/mL) and 50 µL MQ water were placed into the well. This solution was titrated by 70 µL AuNP solution to quench the fluorescence of PT–Pip. Next, 100 µL cell suspensions (200,000 cells in 1X TE buffer or 25 mM HEPES buffer) were added to each well for 1X TE buffer and 25 mM HEPES buffer sensor parameters.

In solvent–free parameters, 200.000 cells were added to PT–Pip–AuNP solution directly without using any buffer. The fluorescence spectra of each titration step were recorded. Scanning of the fluorescence intensity was carried out according to the measurement protocol explained previously.

Zeta potential measurement was performed to evaluate the electrostatic interaction between cell membranes and PT–Pip. Zeta potential (electro kinetic potential) displays the electrostatic double–layer potential that occurred at the slipping plane of the cells. The overall charge of the cell arises from lipid head groups, ions, and charged proteins of the cell membrane[137]. Zeta–potential analysis of the cell suspended in buffers was performed on a zeta potential and nano particle analyzer (Micromeritics Nanoplus4) device. 200.000 cells were dissolved in 1.5 ml buffers and analyzed for zeta–potential. Each measurement was performed three times.

2.3.2. Fluorescence Imaging of Cells

HeLa cells were used to observe the interaction between the PT–Pip–AuNP complex and PT–Pip localization in the cell suspension. After the PT–Pip–AuNP complex was treated with HeLa cells (200,000 cells/100 µL 20 mM HEPES buffer), this solution was examined under a fluorescence microscope.

The following protocol was used to obtain fluorescence images of fixed cells obtained after cell sensing experiments. The solution consisting of PT–Pip–AuNP and mammalian cells was incubated for 1 hour to increase PT–Pip–cell interaction. After 1 hour, this solution was centrifuged at 200 × g for 15 minutes. The pellet parts of the solutions were placed into wells and incubated with 100 µL of paraformaldehyde (4% in 1X PBS) for 15 minutes. At the end of the incubation, the paraformaldehyde was removed from the medium, and the fixed cells were washed twice with 1X PBS buffer. Then, 50 µL of nucleic acid probe DAPI (1:1000 in PBS) was added to each well and incubated for 5 minutes to target the nuclei. After incubation, DAPI was removed from the medium. Finally, these cells were washed three times with 1X PBS.

The excitation and emission wavelengths of the DAPI dye were 358 nm and 461 nm, respectively. A DAPI filter was used to visualize the DAPI dye in fluorescence microscopy. The excitation and emission center wavelengths of the DAPI filter were 377 nm and 447 nm. The passband wavelengths of the DAPI filter were 352 nm to 402

nm for excitation and 417 nm to 477 nm for emission. The excitation and emission wavelengths of PT–Pip observed in the experiments were 405 nm and 538 nm, respectively. A Texas Red filter was used to visualize PT–Pip in fluorescence microscopy. The excitation and emission center wavelengths of the Texas Red filter were 559 nm and 630 nm. The passband wavelengths of the Texas Red filter were 542 nm to 576 nm for excitation and 696 nm to 736 nm for emission. Fluorescence images were taken under a fluorescence microscope (Zeiss– Observer Z1).

2.4. Indirect Sensing of Amino Acids

The twenty amino acids used in amino acid sensing experiments are; L–alanine (CAS No: 56–41–7), L–arginine (CAS No: 74–79–3), L–asparagine (CAS NO:70–47–3), L–aspartic acid (CAS NO:56–84–8), L–cysteine (CAS No: 52–90–4), L–glutamine (CAS No: 56–85–9), L–glutamic acid (CAS NO:56–86–0), Glycine (CAS NO:56–40–6), L–histidine (CAS No: 71–00–1), L–isoleucine (CAS No: 73–32–5), L–leucine (CAS No: 61–90–5), L–lysine (CAS No: 56–87–1), L–methionine (CAS No: 63–68–3), L–phenylalanine (CAS NO:63–91–2), L–proline (CAS No: 147–85–3), L–serine (CAS No: 56–45–1), L–threonine (CAS No: 72–19–5), L–tryptophan, (CAS No: 73–22–3) L–tyrosine (CAS No: 60–18–4), and L–valine (CAS No: 72–18–4). All amino acids were analytical grade and purchased from Chem–Impex Company.

2.4.1. Optimization of Amino Acid Concentration

Firstly, PT–Pip (0.5 mg/ml MQ water) solutions 2:5 diluted with MQ water were used. The initial fluorescence spectra of PT–Pip were recorded. Later, the fluorescence of PT–Pip was quenched with 70 µl AuNP solution at room temperature. The fluorescence spectra of PT–Pip–AuNP solution were recorded again.

Secondly, 20 amino acids were dissolved in MQ water (pH = 7) at their maximum solubility for the initial optimization step. The pre–quenched PT–Pip–AuNP complexes were then titrated by 20 amino acid solutions, individually. Fluorescence spectra were obtained after all titration steps.

In order to optimize the amino acids concentration, 100 mM and 50 mM amino acid solutions were prepared at pH = 7 and pH = 9.8 by using MQ water. The initial

fluorescence spectra of PT–Pip solutions were recorded. The fluorescence of PT–Pip was quenched as explained previously. After fluorescence quenching, the amino acid solutions were introduced to the pre–quenched PT–Pip–AuNP complex. The fluorescence spectra of PT–Pip were recorded at each titration step.

After concentration optimization, the PT–Pip–AuNP complex was titrated by 50 mM 20 amino acid solutions (dissolved in TE buffer and water at pH = 6, pH = 7 pH = 8.2, and pH = 9.8). The fluorescence spectra of PT–Pip were recorded at each step. Amino acid sensing experiments were carried out three times. The percentages of Δ fluorescence intensities for each sample were calculated according to the Equation 2.

2.4.2. Investigation of the Interaction between PT–Pip, AuNP and 20 Amino Acid via Fluorescence and UV–visible Spectroscopy

The interactions between PT–Pip, AuNP, and amino acids were investigated by the fluorescence and the UV–visible spectroscopy.

The initial step was investigation of the interaction between PT–Pip and amino acids by the fluorescence spectroscopy. PT–Pip solutions 2:5 diluted with MQ water (pH = 7) were used. PT–Pip solutions were then titrated with 20 amino acids (100 µl 50 mM). The fluorescence spectra were recorded and evaluated.

The next step was examining the interaction between AuNP and 20 amino acids by UV–visible spectroscopy. 70 µl AuNP solutions were placed in the well and titrated by 20 amino acids (100 µl 50 mM) individually. The absorbance spectra were recorded at each step.

The third step was to investigate the interaction between PT–Pip–AuNP and amino acids by both UV–visible and the fluorescence spectroscopy, simultaneously. PT–Pip (0.5 mg /ml) 2:5 diluted with MQ water (pH = 7) was used. The fluorescence and absorbance spectra were recorded. The fluorescence of PT–Pip was quenched by 70 µl AuNP solution. 100 µl 50 mM amino acid solutions (in MQ water at pH = 7) were then introduced to the pre–quenched PT–Pip–AuNP complex. The fluorescence and absorbance spectra were recorded at each step.

2.4.3. Statistical Analysis

The statistical analysis of protein sensing study was performed as explained: Two different methods were utilized to calculate the fluorescence difference before and after protein addition. In the first method, the fluorescence intensity corresponding to the I_{max} was measured to calculate the maximum fluorescence intensity. In the second method, areas under the fluorescence curve were measured to calculate integrated fluorescence intensity. Percentages of Δ fluorescence intensity/integrated intensity were obtained according to Equation 2.

$$\Delta \text{ I. } \% = ([\text{Final I.} - \text{Quenched I.}] / \text{Initial I.}) \times 100 \quad [2]$$

Final I: Fluorescence intensity/integrated intensity of PT–Pip in the presence of analyte.
Quenched I: Fluorescence intensity/integrated intensity of PT–Pip in the absence of analyte.
Initial I: Fluorescence intensity/integrated intensity of PT–Pip in the absence of analyte and quencher molecule.

The fluorescence response for each protein was analyzed by PCA[138] by Minitab 17.3.1. PCA, which is the oldest and most popular multivariate technique has been widely used by many scientific disciplines. PCA analyzes positively correlated data of variables. This method transforms data of variables (by extracting important data) into a linear combination of orthogonal variables which is called principal components (PCs). PCA has an essential advantage over other statistical analysis methods. Most of the variations are retained while the dimensionality of data is reduced by PCA.[139]

LoD for each sensor element was calculated based on the fluorescence responses of five proteins. The detection limits were measured according to Equation 3.

$$LoD = 3\sigma bi/m \quad [3]$$

Where σbi was the standard deviation of blank and m is the slope of Δ I. – [protein] graphs.

The statistical analysis of cell sensing study was performed as explained: The mammalian cell sensing experiments were performed at three (1X TE buffer, HEPES buffer, and solvent–free) sensor parameters for seven cell lines. The fluorescence intensities obtained from the fluorescence spectra were recorded at each step. PT–Pip–AuNP complex emitted light at 542 nm (I_1). A novel peak appeared at 586 nm (I_2) with a shoulder at 632 nm (I_3) upon the addition of cells. Cell sensing experiments were repeated three times for seven cell lines. I_2/ I_1 and I_3/ I_1 ratios were calculated. The fluorogenic response of each cell against the sensor array was obtained as a ratio of intensities at three distinct wavelengths. The fluorescence responses within the 95% confidence interval were analyzed by PCA.

The statistical analysis of amino acid sensing study was performed as explained: Fluorescence intensities of PT–Pip corresponding to the I_{max} were measured to calculate maximum fluorescence intensity in the absence and presence of amino acids. Percentages of Δ I. were obtained according to Equation 2. The fluorescence responses for each amino acid were analyzed by PCA by Minitab 17.3.1.

CHAPTER 3

RESULTS & DISCUSSION

3.1. PH–dependent Spectroscopic Characterization of PT–Pip

In this thesis, water–soluble cationic PT derivative, poly–(1,4–dimethyl–1–(3–((4–methylythiophene–3–yl)oxy)propyl)piperazine–1–ium bromide), was used as a cross–reactive signal transduction element. The side chain of PT–Pip contains piperazine group, which is a six membered–ring having two opposing nitrogen atoms. 1,4–dimethylpiperazine is a weak base with pKa(1) = 3.81 and pKa(2) = 8.38 at 25° C in water.[140] The addition of a ethyl or propyl group on other nitrogen of the ring slightly changes the pKa. The two nitrogen atoms in the piperazine ring act as charge carriers; at pHs higher than the pKa(2), free amines of piperazine is deprotonated, and below the pKa(1), the two nitrogen atoms are protonated. The piperazine in conjugation with various fluorophores are widely utilized in pH–sensing applications[141], such as monitoring intracellular pH[142] etc. due to the protonation and deprotonation of nitrogen atoms. In this thesis, the piperazine group of side chain was utilized mainly for two purposes; i) to achive efficient fluorescence quenching of cationic PT–Pip via anionic AuNP due to the electrostatic interaction, ii) to target the anionic biomolecules or anionic cell membrane surfaces by the cationic centers of the piperazine groups.

This thesis aimed to developed multiple sensor elements by tuning the pH and buffer types of sensor environment. The effects of pH and buffer types on the sensor elements and sensory events were investigated. To investigate the optical response of PT–Pip against the pH, initially, the pH–dependent characterization of PT–Pip was carried out in detail by the UV–visible and fluorescence spectroscopy. The polymer structure were given in Figure 24.

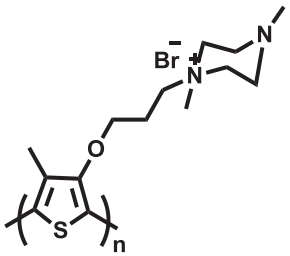

Figure 24. Structure of poly–(1,4–dimethyl–1–(3–((4–methylythiophene–3–yl)oxy) propyl)piperazine–1–ium bromide) (PT–Pip).[133]

3.1.1. UV–visible and Fluorescence Spectroscopy Analysis of PT-Pip

Figure 25. illustrates the fluorescence and absorbance spectra of PT–Pip titrated by HCl and NaOH, sequentially.

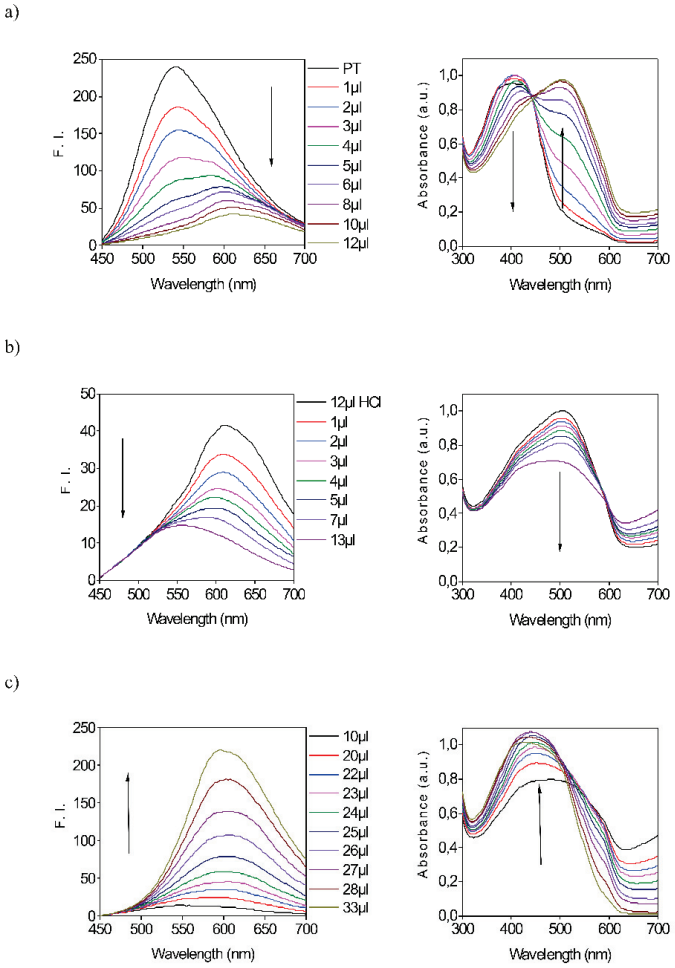

Figure 25. Fluorescence and absorbance spectra of PT–Pip (0.5mg/ml) in DI titrated with HCl and NaOH. (a) Titration of PT–Pip with 1M HCl; (b) titration of PT–Pip–HCl solution with 1M NaOH; (c) titration of PT–Pip–HCl–NaOH solution with 0.02M NaOH. The excitation wavelength is fixed at 405 nm

There was a significant change in the UV–visible absorption spectrum upon addition of HCl (1M). In the absence of HCl, PT–Pip exhibits an absorbance maximum at 402 nm. The absorbance intensity at 402 nm decreased with HCl addition, and a novel peak appeared at 504 nm. Moreover, the fluorescence intensity significantly decreases with HCl. A distinct red shift of the fluorescence maximum was observed (from 538 nm to 614 nm) as shown in Figures 25. (a) and Figure 26. (b).

The positively charged PT–Pip absorbed light at 402 nm at a neutral pH, indicating that PT–Pip was in the random coil or less conjugated (nonplanar) conformation.[143] The pH value of the solution decreased from 7 to 1.25 with HCl. As the two nitrogen atom of piperazine group became protonated, coulombic repulsion between the cationic centers of the pendant group induced streching and planarization of the PT–Pip backbone. The isosbestic point of the absorbance spectrum in Figure 25. (a) proves the transition from non–planar to planar conformation. Due to the planarization of PT–Pip backbone, interchain interaction (π– π stacking) and aggregation occurred. Non–radiative energy transfer of PT–Pip excitons between different PT–Pip chains was observed. The weak emissive PT–Pip chains were formed[111], as shown in Figure 25. (a).

Absorbance and fluorescence intensities decreased during titration of PT–Pip–HCl solution by 1M NaOH. Blue shifts in the fluorescence (from 614 nm to 556 nm) and absorbance maxima (from 504 nm to 486 nm) were observed, as shown in Figure 25. (b).

The solution's pH was gradually increased from 1.25 to 11.65 with 1M NaOH. As pH increased, the degree of protonation of PT–Pip decreased. PT–Pip chains began to collapse due to lower repulsive forces between side chains. Up to pH = 11.65, aggregation of the planar region of PT–Pip chains still existed, and the fluorescence intensity of PT–Pip decreased further.

Upon addition of 0.02 M NaOH, the pH of the solution increased from 11.65 to 11.80. At this pH, the two nitrogen atoms of the all piperazine groups were most likely deprotonated. As the protonation of PT–Pip chains disappeared, the region with the random coil conformation started to fold over the planar region of the PT–Pip chain. The absorbance intensity was gradually recovered at a shorter wavelength (426 nm). The planar regions of different PT–Pip chains did not interact with each other, which prevents aggregation and non–radiative energy transition. Therefore, fluorescence

intensity sharply increased. PT–Pip excitons recovered their fluorescence at a higher wavelength (594 nm)), as shown in Figure 25. (c) and Figure 26. (b).

The reversibility of pH–dependent conformational changes of PT–Pip was investigated. As shown in Figure 26. (a), PT–Pip exhibited a progressive fluorescence recovery that was pH–dependent. These reversible cycles could be retained at least 10 times.

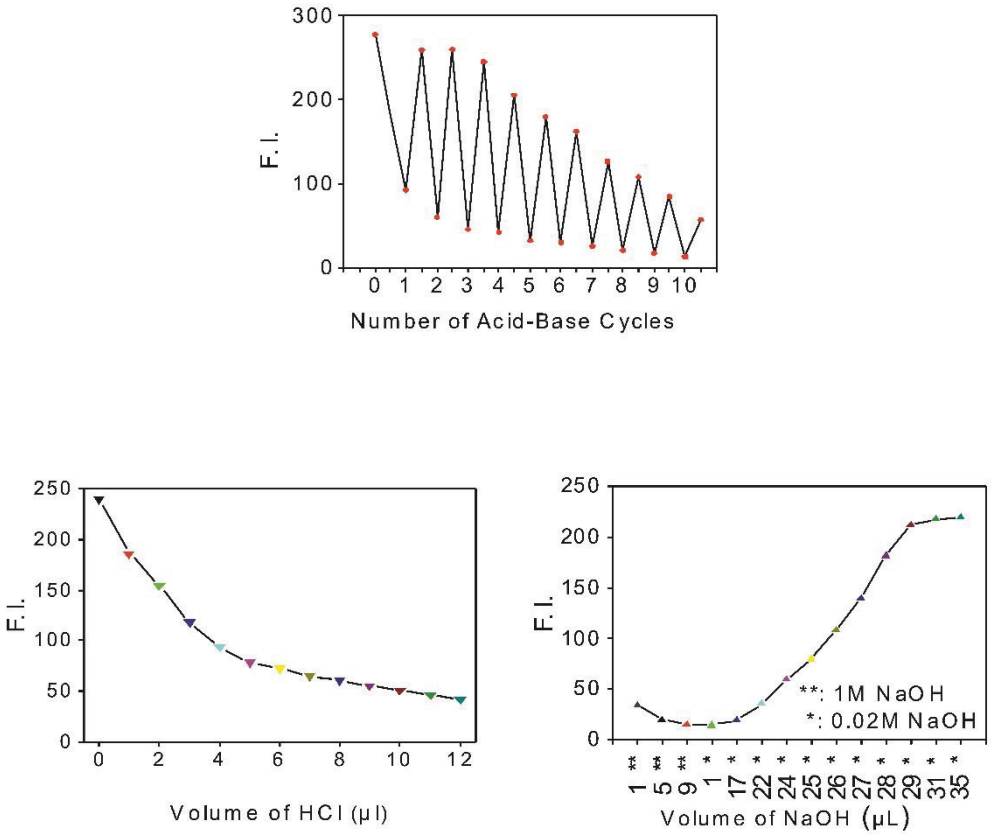

Figure 26. Acid–base titration of PT–Pip with HCl and NaOH. (a) pH–dependent reversible fluorescence intensity changes of PT–Pip. Acid–base addition cycles were repeated 10 times (b) Plots of fluorescent intensity at 530 nm vs. volume of HCl and NaOH; data were extracted from Figure 25.

The pH–dependent optical and structural changes of PT–Pip resulted from protonation/deprotonation of the chromophores, as no further chemical reaction occurred. These fluorescence turn on/off behaviors caused by protonation and deprotonation of side chains were visible to the naked eye, as shown in Figure 27.

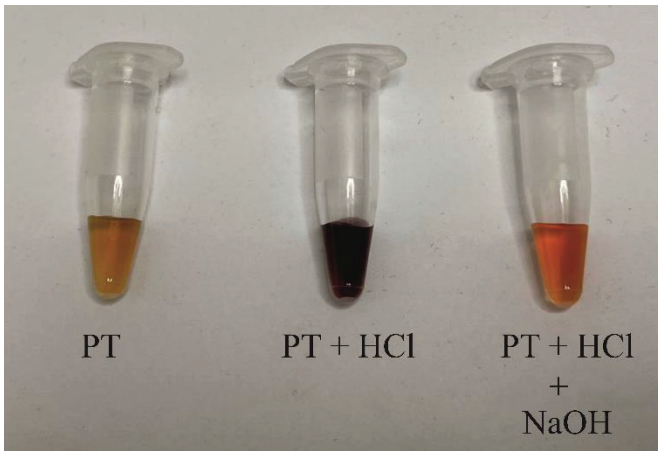

Figure 27. Color of PT–Pip after HCl titration and after NaOH titration

Initially, the color of PT–Pip was dark yellow which is a characteristic to the random coil conformation of PT–Pip. After HCl titration, the yellow to red color transition of PT–Pip was observed due to planarization and aggregation of PT–Pip chains. Upon addition of NaOH, PT–Pip turned bright orange arising from the partial planarization of non–aggregated PT–Pip chains.

This study investigated the highly sensitive and reversible pH–dependent protonation/deprotonation processes of PT–Pip by fluorescence and UV–visible spectroscopy. The pH of the surrounding environment controls the structural and optical properties of PT–Pip. Reduction of pH with HCl induced planarization and aggregation of PT–Pip, which decreased absorption and emission intensity. Enhancement of pH with NaOH increased the fluorescence intensity of PT–Pip. The chromophoric absorption maximum was blue–shifted by NaOH addition resulting from the partially random coil and partially planar structure of the polymeric backbone.

The interaction between sensor elements and analytes mainly depended on electrostatic interaction. The pH of the environment influenced the optical properties of PT–Pip, which then affected the interaction of the PT–Pip with the target analytes. These pH–induced conformational changes of PT–Pip could be utilized to develop multiple sensor elements by changing the pH of the environment.

3.2. Direct Sensing of Proteins

In this thesis, at first fluorescence ‘turn–on/off’ biosensor was developed for protein discrimination. This sensing approach included two sensory events; in the first

step, the fluorescence of PT–Pip was quenched by the AuNP, called the fluorescence 'tun–off' mode, and in the second step the fluorescence of PT–Pip–AuNP was modulated by the target analytes, called the fluorescence 'turn–on' mode. The aim of the study was to distinguish 5 different proteins according to their isoelectric point (pI), molecular weight (MW), and other physicochemical properties. The optimization steps of the sensor array were explained in the following sections.

3.2.1. Spectroscopic Analysis of Gold Nanoparticle

AuNPs were efficient fluorescence quenchers. In order to quench the fluorescence of cationic PT–Pip, negatively charged AuNPs were used. AuNPs synthesis was performed according to the citrate reduction Turkevich's method. The color transition of the $AuHCl_4$ solution and the localized surface plasmon resonance peak of the AuNPs are illustrated in Figure 28.

a) b)

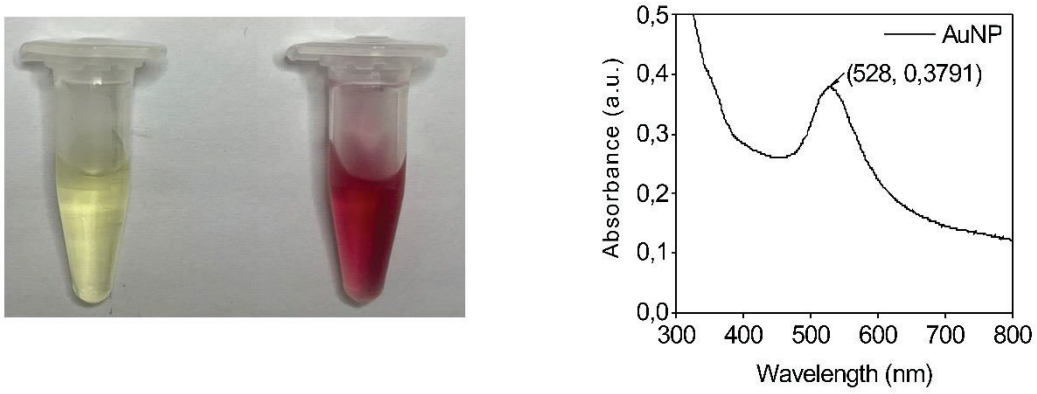

Figure 28. (a) $AuHCl_4$ solution (left) and citrate–capped AuNP solution (right); (b) UV–visible absorbance spectrum of AuNPs

The yellow color of $AuHCl_4$ solution turned to wine red, and the localized surface plasmon resonance peak appeared at 528nm, with an intensity of 0.3791 a.u. indicating the formation of colloidal gold nanoparticles[144], as shown in Figure 28. The zeta potential was measured as –44.76 mV. The zeta size of the AuNP was approximately 40.3 nm, which correlated with the literature, indicating that the AuNP with a mean diameter of 39.9 had its SPR position at 528.5 nm.[145]

3.2.2. Fluorescence Quenching of Gold Nanoparticle in Different Buffer Solutions

The fluorescence quenching between PT–Pip and AuNP was investigated in detail. The emission maximum of cationic PT–Pip (at 538 nm) and the absorption maximum of anionic AuNPs (at 528 nm) perfectly overlapped, as shown in Figure 29. As a result of electrostatic interaction and spectral overlap, the fluorescence of PT–Pip was successfully quenched by AuNPs via RET based[146] energy transfer.[147]

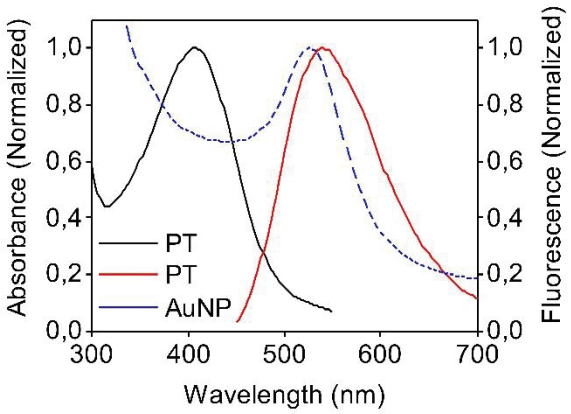

Figure 29. Absorbance and fluorescence spectra of PT–Pip (467 µM (monomer based)) in MQ water at pH = 7 and localized surface plasmon resonance peak of AuNPs (0.15 µM) in MQ water at pH = 7

In order to sense the biomolecule, biomolecules were supposed to preserve their integrity in sensor environment. Besides, the sensor environment should not effect the sensing mechanism. Therefore, MQ water, 1X PBS, and 1X TE buffer were investigated in terms of their suitability for sensing applications. The effects of buffer on the fluorescence quenching mechanism were investigated by fluorescence spectroscopy. PT–Pip (0.5 mg/ml), 1:2 diluted with MQ water, 1X PBS, and 1X TE buffer were titrated with AuNPs. The fluorescence spectra are given in Figure 30**.**

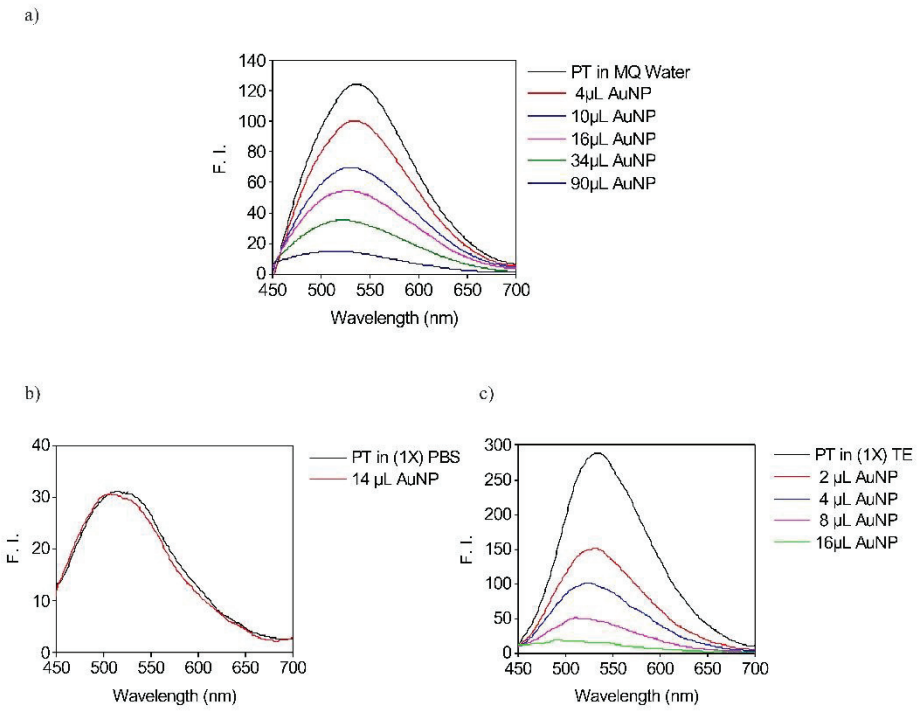

Figure 30. Fluorescence spectra of PT–Pip titrated by AuNPs in different solvents: (a) MQ water, (b) (1X) PBS buffer, (c) (1X) TE buffer. The black line represents the fluorescence spectrum of PT–Pip. The other lines represents the fluorescence spectra of PT–Pip titrated by AuNPs. Excitation wavelength is fixed at 405 nm

PT–Pip solution, 1:2 diluted with MQ water, 1X TE buffer, and 1X PBS were used. The initial fluorescence intensities of PT–Pip diluted with 1X TE buffer and MQ water were higher than 1X PBS. The phosphate groups ($PO4^{3-}$) are known to induce planarization of the PT-Pip backbone by interacting with cationic pendant groups of PT-Pip[102], which result in a drastic reduction in the initial fluorescence of PT–Pip. An efficient fluorescence quenching was observed in 1X TE buffer and MQ water but not in 1X PBS, as shown in Figure 30. Unlike TE buffer and MQ water, PBS was not a suitable solvent for AuNPs, as PBS are known to affect the distribution of AuNPs in the solvent while disrupting its stable structure.[148] As a result of the destabilization of AuNPs in PBS, AuNPs had not been able to quench the fluorescence of PT–Pip. Therefore, following experiments were carried out using MQ water and TE buffer as appropriate solvents.

3.2.3. Effect of pH on Gold Nanoparticle Stability

The stability of AuNPs was investigated at various pHs to determine the optimum pH range for sensing applications. AuNPs were titrated by MQ water (pH = 2.05, 7.0, and 11.75) and 1X TE buffer (pH = 1.32, 7.38, and 12.05) individually. The optical properties of AuNPs in acidic, neutral, and basic solutions were investigated by UV–visible spectroscopy.

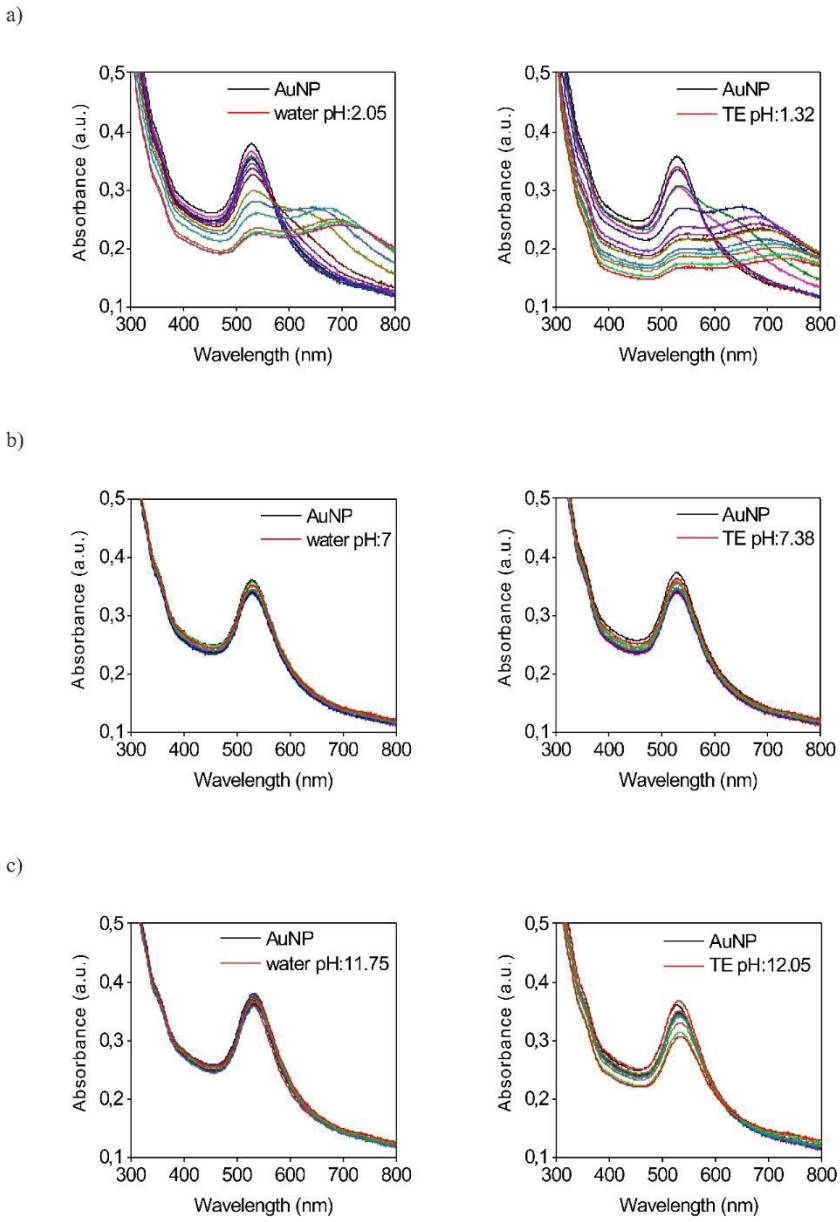

Figure 31. Variation in LSPR band of AuNPs titrated with MQ water and TE buffer at (a) acidic pH, (b) neutral pH, and (c) basic pH

The AuNPs remained stable during titration by MQ water and 1X TE buffer at pH = 7 and 12. Titration with 1X TE buffer at pH = 12.05 absorbance maximum slightly decreased, as seen in Figure 31. (b) and (c). Nevertheless, the AuNPs maintained their optical properties at neutral and basic pH values. As shown in Figure 31. (a), during titration of AuNPs with 1X TE buffer and MQ water at pH ~ 2, the absorbance maximum was significantly red–shifted, and the absorbance intensity decreased, implying that the monodispersed AuNPs aggregated to larger clusters.

The carboxyl (–COOH) group of citrate on the AuNP surface was protonated by the H^+ ions in the acidic environment. The H^+ ions formed a compact layer called the "Stern layer" on the nanoparticle surface.[149] The second layer named the ''Diffuse layer'' was attracted by coulomb forces. Therefore, titration of AuNPs with acidic solutions reduced the negative charges of the AuNP surfaces and decreased the repulsive forces between two adjacent nanoparticles. The delocalized conduction electrons of the nanoparticle were shared with the neighboring nanoparticle. Thus, acidic solutions caused the aggregation of nanoparticles which resulted in the red shift of the surface plasmon resonance to a higher wavelength. Since the number of stable nanoparticles decreased in an acidic environment, the absorbance intensity of the extinction peak decreased, as shown in Figure 31.

3.2.4. Investigation of Fluorescence Quenching Mechanism of AuNPs

In order to investigate the fluorescence quenching mechanism between PT–Pip and AuNP, the temperature–dependent behavior of the fluorescence quenching mechanism was investigated by UV–visible and fluorescence spectroscopy. The fluorescence quenching study was performed at three temperatures (25, 35, and 45 ^oC). Table 1 shows the Stern–Volmer constants (K_{SV}) for the AuNP and PT–Pip complexes at the three temperature values.

Table 1. Stern–Volmer constants (K_{SV}) for the AuNP and PT–Pip coordination at three temperature values in MQ water (pH = 7) based on fluorescence titration studies

T (^oC)	**K_{SV} / 10^3 M^{-1}**	**R^2 (COD)**
25	152.16608	0.98043
35	116.50695	0.98677
45	106.80267	0.98177

Fluorescence intensities were reduced by about 82%, 80%, and 77% at 25 °C, 35 °C, and 45 °C, respectively. K_{SV} values of AuNP at three temperatures were obtained via Equation 1. I_0/I vs. [AuNP] plots were linear in the concentration range between 0 to 0.033 μM. The slopes were equal to the Stern–Volmer constants (K_{SV}), as shown in Table 1. The results indicated that the K_{SV} values decreased as temperature increased.

UV–visible spectroscopy was used to examine the conformational alteration of PT–Pip upon complexation with AuNP at the three temperature values. Changes in the absorbance spectra of PT–Pip were used an indicators of the quenching mechanism. Figure 32. represents the temperature–dependent alteration in the UV–visible spectra of PT–Pip–AuNP complexes.

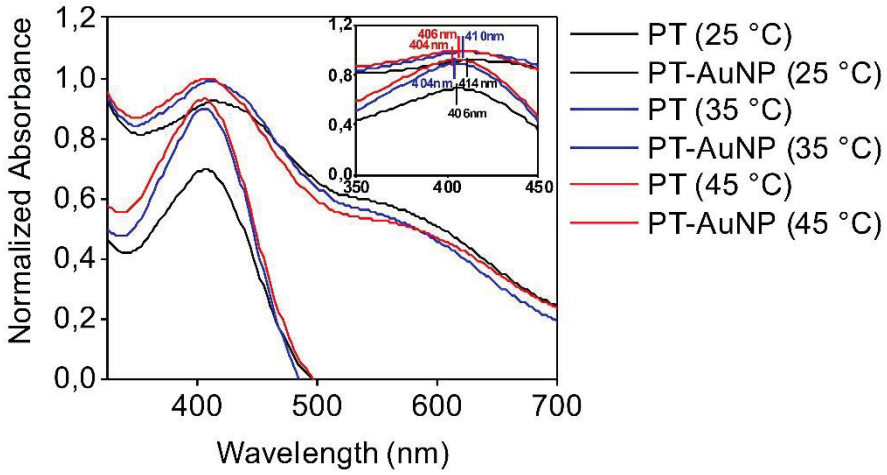

Figure 32. Normalized UV–visible spectra of PT–Pip in the absence and presence of AuNPs at 25 °C, 35 °C and 45 °C

Investigation of the UV–visible absorption spectra of PT–Pip in the absence and presence of AuNPs at three different temperatures confirmed that the absorbance of PT–Pip changed as a result of PT–Pip–AuNP complexation, as seen in Figure 32. Moreover, higher temperatures reduced these alterations, which indicates that the stability of the PT–Pip–AuNP complex was decreased at higher temperatures.

Fluorescence quenching approaches can be divided into three mechanisms: (I) static quenching, (II) dynamic (collisional) quenching, or (III) a combination of the two mechanisms.[150] In dynamic quenching, a collision between quencher molecules and fluorophores in the excited state leads to fluorescence quenching without quencher–fluorophore complexation.[151] Contrary to dynamic quenching, static quenching is

observed when the quencher and fluorophore form a non–fluorescent dark complex in the ground state.[151] The mixed fluorescence quenching process combines both static and collisional quenching by the same quencher.[152]

In the dynamic quenching process, the absorption spectrum of the fluorophore is not supposed to differ, as this quenching only affects the excited state of fluorophores. In the static quenching, fluorophore–quencher dark complex formation results in changes in the UV–visible spectrum of fluorophores.[153] The temperature–dependent alterations in fluorescence quenching behavior vary between static and dynamic fluorescent quenching. In dynamic quenching, the rate of collisional quenching increases via rapid diffusion of the quenchers at a higher temperature, which also increases the K_{SV} values of the quenchers. In static quenching, the stability of the quencher–fluorophore complex is reduced at higher temperatures, which decreases the K_{SV} values of the quenchers.[154] Fluorescence and UV–visible spectroscopy confirmed that the possible fluorescence quenching mechanism of PT–Pip via AuNP involved mainly ‘‘static quenching’’.[153]

Fluorescence quenching optimization experiments for sensor development were carried out with various buffers and pH parameters, such as 1X TE buffer and MQ water at pH = 2, pH = 4, pH = 6, pH = 7, pH = 9, and pH = 12, to tune the interaction between PT–Pip and AuNP. At acidic pH values, such as pH = 2, pH = 4, and pH = 6, the PT–Pip backbone became planar. Aggregation of PT–Pip chains occurred. The formation of aggregates reduced the initial fluorescence intensity of polymers due to the π–π stacking of polymer chains and self–quenching.[111] AuNPs also became destabilized at acidic pH values. Efficient fluorescence quenching was not observed between planar and aggregated PT–Pip and AuNPs at acidic pH values.

On the other hand, at very high pH values, such as pH = 12, although the initial fluorescence intensity of PT–Pip increased, the (–OH) hydroxyl ions in the medium prevented the interaction of PT–Pip with the AuNP. Optimization experiments were carried out in a broad spectrum pH range (data not shown here), and two pH values were determined as the optimum pH values: pH = 7.08 and pH = 9.64 for TE buffer and pH = 7 and pH = 9.7 for MQ water.

The fluorescence quenching efficiency of AuNPs in four sensor elements was investigated by fluorescence spectroscopy. A plot of normalized fluorescence intensity alterations by AuNP titrations in four different solvents displays efficient and

measurable fluorescence quenching. The fluorescence quenching arose from the PT–Pip–AuNP pairing at the submicromolar level of AuNPs, as seen in Figure 33.

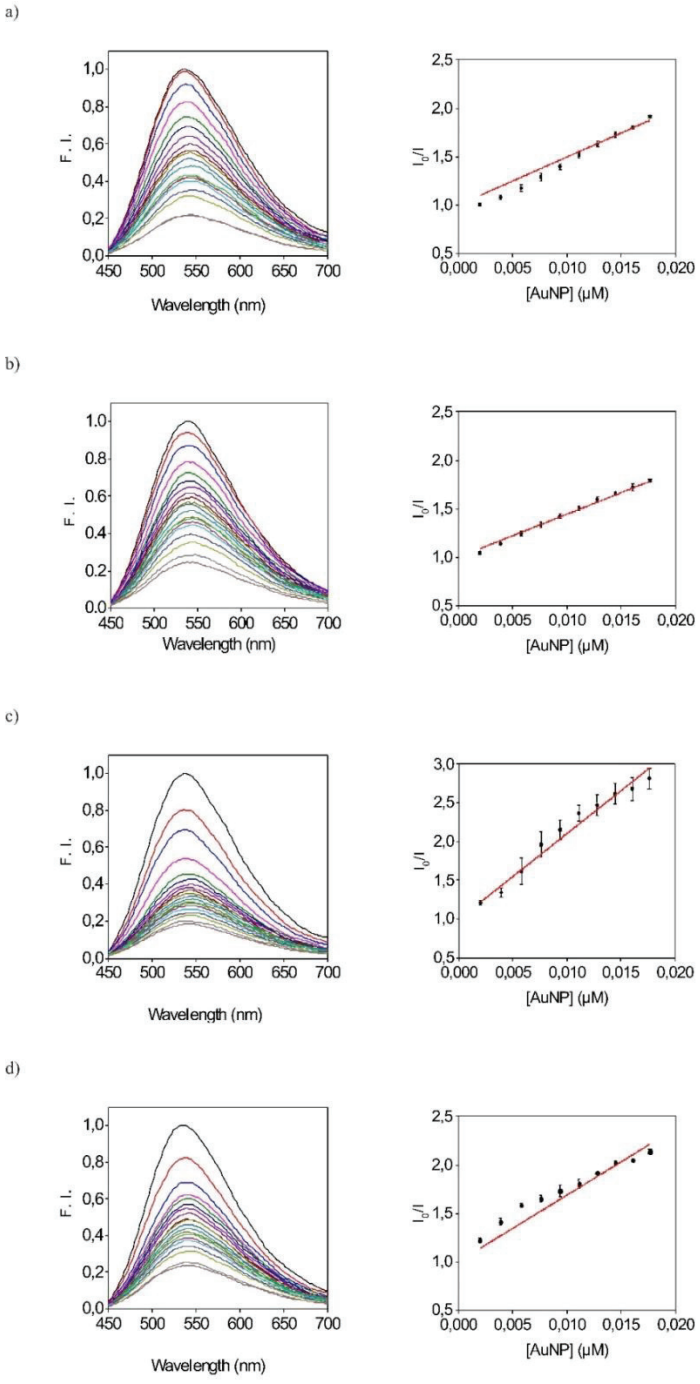

Figure 33. Normalized fluorescence intensity of PT–Pip (467 μM (monomer–based)) titrated by AuNPs (with increasing AuNP concentration from top to bottom of the graph) and the Stern–Volmer plots of PT–Pip (467 μM (monomer–based)) quenching by AuNPs in a linear range for low AuNPs concentration regime. AuNPs concentrations ranged from 0 to 0.06 μM (from top to bottom) in (a) TE buffer (pH = 7.08), (b) TE buffer (pH = 9.64), (c) Water (pH = 7.00), (d) Water (pH = 9.70). Excitation wavelength is fixed at 405 nm

K_{SV} values were calculated by the Stern–Volmer formula in Equation 1. The plots of I_0/I vs. [AuNP] were linear in the concentration range of 0 to 0.02 μM. The slopes are equal to the Stern–Volmer constants (K_{SV}) given in Table 2. The results show that the pH and solvent types significantly influenced PT–Pip–AuNP complexation. The interactions between AuNPs and PT–Pip were reduced in a solution with high ionic strength as expected, which was correlated by the literature[155] Higher binding efficiency between AuNPs and PT–Pip was obtained in MQ water compared to TE buffer. The binding efficiency between AuNP and PT–Pip was stronger at neutral pH than at basic pH. The appropriate stoichiometry of AuNP was utilized to quench the fluorescence of PT–Pip in the four different solutions. The final concentrations of PT–Pip was fixed at 280.2 μM, and the final concentration of AuNPs was fixed at 0.06–0.08 μM for the protein sensing study.

Table 2. Stern–Volmer constant (K_{SV}) for the AuNP and PT–Pip complexation in various buffer systems calculated from fluorescence titration experiments

Solvent types and pH values	**K_{SV} / 10^3 M^{-1}**	**R^2 (COD)**
MQ water pH = 7.00	110.4154	0.99871
MQ water pH = 9.70	68.72296	0.99817
TE buffer pH = 7.08	49.55485	0.99831
TE buffer pH = 9.64	44.44079	0.99959

3.2.5. Direct Sensing of Proteins

The non–covalent pre–quenched PT–Pip–AuNP supramolecular complexes were used to discriminate proteins. Five different protein solutions including metalloproteins and nonmetalloproteins were used as target analytes. The physicochemical features of the five proteins were comparable such as MW (ranging from 12.38 to 160 kDa) and pI (ranging from 4.7 to 10.5), as shown in Table 3.

Table 3. Physicochemical features of proteins

Proteins	**MW (kDa)**	**pI**	**Charge at pH = 7.00**	**Charge at pH = 9.70**
Bovine serum albumin (BSA)	66.43	4.7	negative	negative
Cytochrome C (CC)	12.38	10.0–10.5	positive	positive
Acid phosphatase (Phos A)	69	5.2	negative	negative
Alkaline phosphatase (Phos B)	160	5.7	negative	negative
Protease	27.29	9.4	positive	negative

The fluorescence responses of each protein were investigated. All experiments were repeated five times. Figure 34. illustrates the fluorescence response of bovine serum albumin against sensor array.

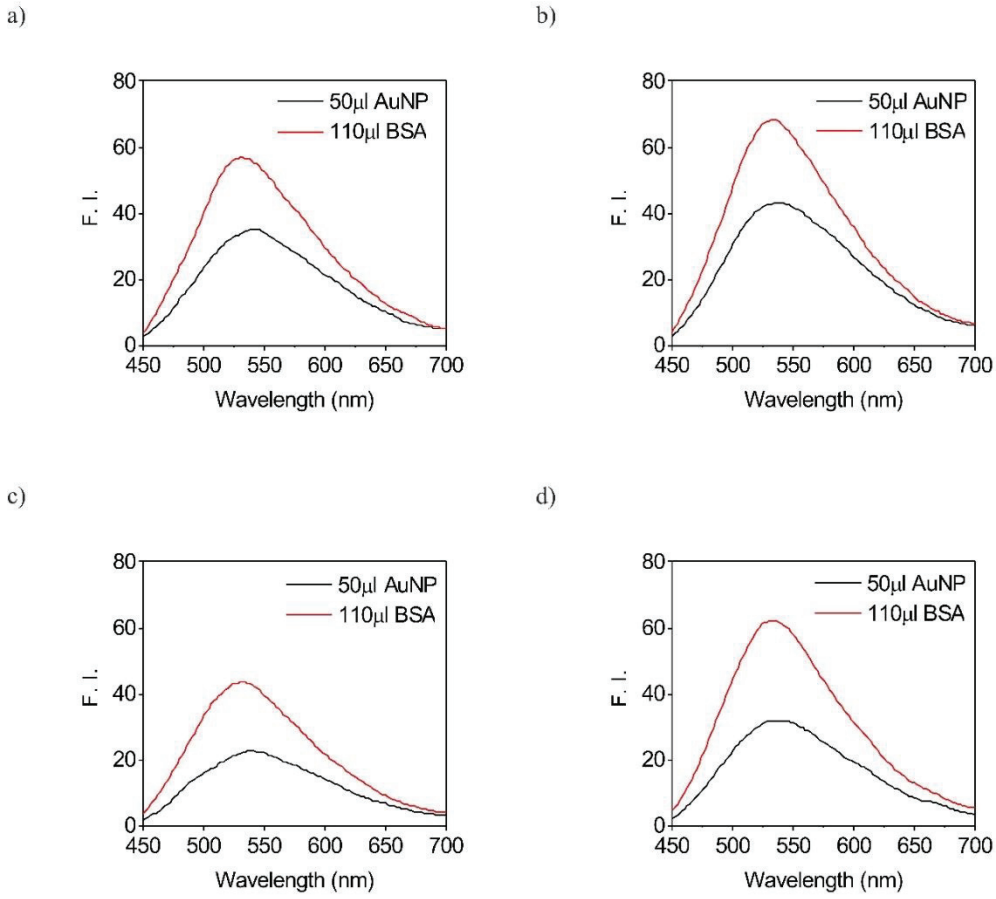

Figure 34. Fluorescence spectra of PT–Pip–AuNP complex prior and post addition of BSA (100 µM): (a) in TE buffer (pH = 7.08), (b) in TE buffer (pH = 9.64), (c) in water (pH = 7.0), and (d) in water (pH = 9.7). Excitation wavelength is fixed at 405nm

The pI of BSA (non–metalloprotein) is 4.7. The MW is 66.43 kDa[156] BSA is negatively charged at pH ~ 7.0 and pH ~ 9.7. Therefore, BSA competed with the negatively charged AuNPs to interact with the positively charged PT–Pip. As a result of the competitive binding of BSA and AuNP to PT–Pip, the PT–Pip–AuNP complex was dissociated. Thus, the selective displacement of PT–Pip resulted in fluorescence recovery. At pH ~ 9.7, the fluorescence recovery was higher than at pH ~ 7.0, as shown in Figure 34. This result reveals that the negative charge of BSA and the interaction between BSA and PT–Pip are directly proportional. Besides, due to the surfactant–like character of BSA[157], the hydrophobic regions of BSA can interact with the PT–Pip backbone. As a results of the interaction between PT–Pip and BSA, the interchain interaction of PT–Pip chains decreased and the fluorescence of PT–Pip increased.[158] Figure 35. illustrates the fluorescence response of acid phosphatase against sensor array.

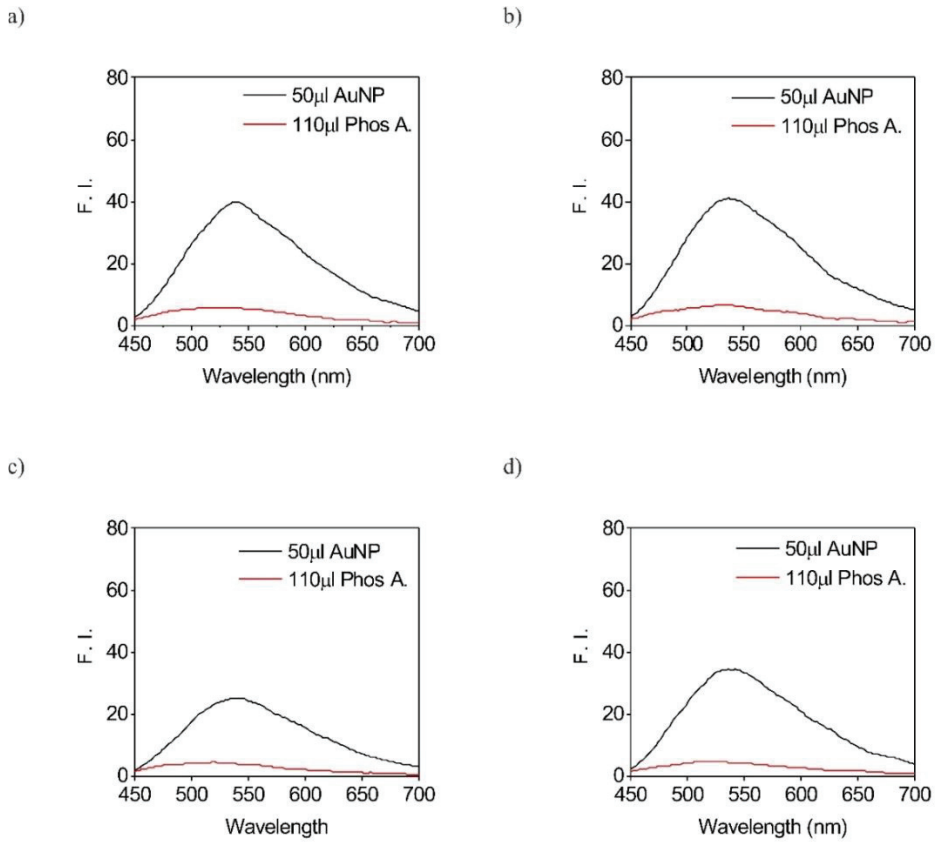

Figure 35. Fluorescence spectra of the PT–Pip–AuNP complex solution prior and post addition of Phos A (100 µM): (a) in TE buffer (pH = 7.08), (b) in TE buffer (pH = 9.64), (c) in water (pH = 7.0), and (d) in water (pH = 9.7)

The pI of Phos A (iron containing metalloenzyme) is 5.2. The MW is 69 kDa.[159] Phos A had a negative net charge at pH ~ 7.0 and pH ~ 9.7. Upon addition, Phos A

competed with the AuNPs to interact with PT–Pip. The competitive binding between Phos A and AuNPs to PT–Pip resulted in the selective displacement of PT–Pip. At pH ~ 7.0 and pH ~ 9.7, interaction between Phos A and PT–Pip decreased the fluorescence of PT–Pip. At pH ~ 9.7, the electrostatic interaction between Phos A and PT–Pip was greater, and the fluorescence intensity of PT–Pip further decreased, as shown in Figure 35. Iron–containing metalloproteins are efficient fluorescence quenchers.[158] Phos A from potato tubers is a member of a binuclear metalloenzymes family.[160] There are three isoforms of Phos A isolated from potato tubers which contain either Fe(III)–Zn(II), Fe(III)–Mn(II), or Fe(III)–Fe(II) heterovalent centers in their active site.[161] The iron at the Fe(III)–M(II) centers is in oxidation states.[162] Therefore, the Fe(III)–M(II) center of Phos A acting as a strong chromophore is responsible for the fluorescence quenching of PT–Pip by electron transfer between Fe(III) and PT–Pip. Figure 36. illustrates the fluorescence response of alkaline phosphatase against sensor array.

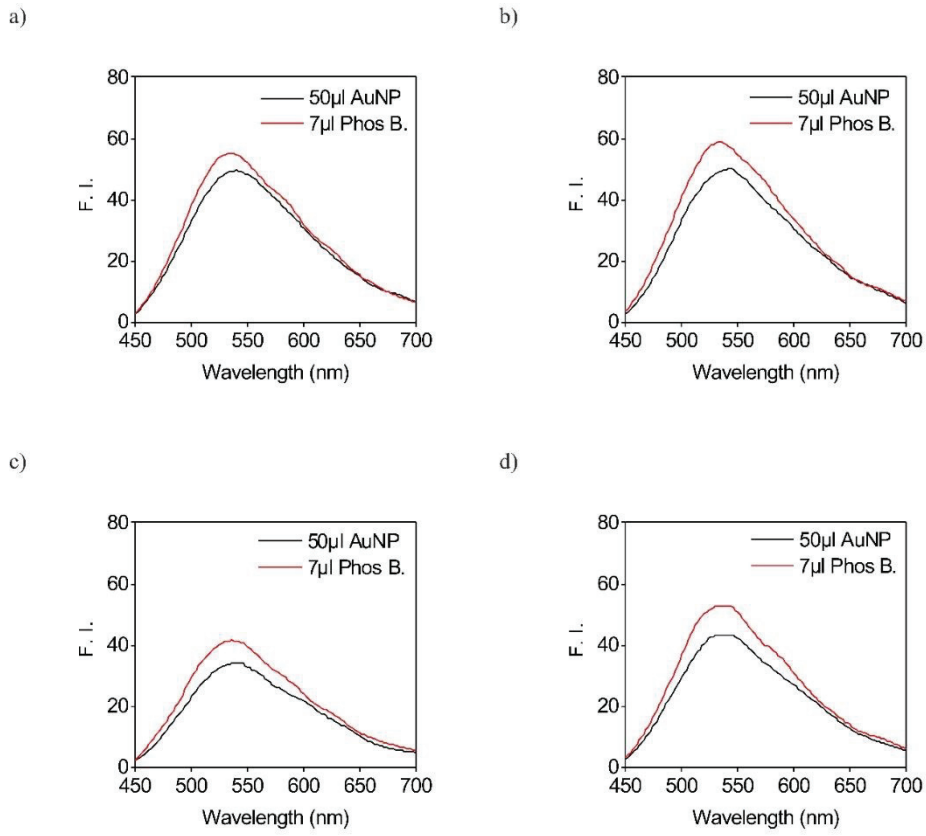

Figure 36. Fluorescence spectra of the PT–Pip–AuNP complex prior and post addition of Phos B (100 µM): (a) in TE buffer (pH = 7.08), (b) in TE buffer (pH = 9.64), (c) in water (pH = 7), and (d) in water (pH = 9.7)

Phos B (Mg^{2+}, and Zn^{2+} containing metalloenzyme[163]) is a dimeric, membrane–derived glycoprotein. The pI of Phos B is 5.7[164], and the MW is 160 kDa[165]. Phos B had a negative net charge at pH ~ 7 and pH ~ 9.7. The electrostatic interaction between Phos B and PT–Pip disrupted the PT–Pip–AuNP complexation. The selective displacement of PT–Pip resulted in fluorescence recovery. Electrostatic interaction between Phos B and PT–Pip increased at higher pH values, as shown in Figure 36. However, these interactions were not as pronounced as observed in BSA. Lower fluorescence enhancement was observed due to the higher pI of Phos B.

The MW of Phos B is higher compared to the other proteins. Therefore, while other proteins could interact with PT–Pip up to 46.8 µM, Phos B could interact up to 5.3 µM. Figure 37. illustrates the fluorescence response of protease against sensor array.

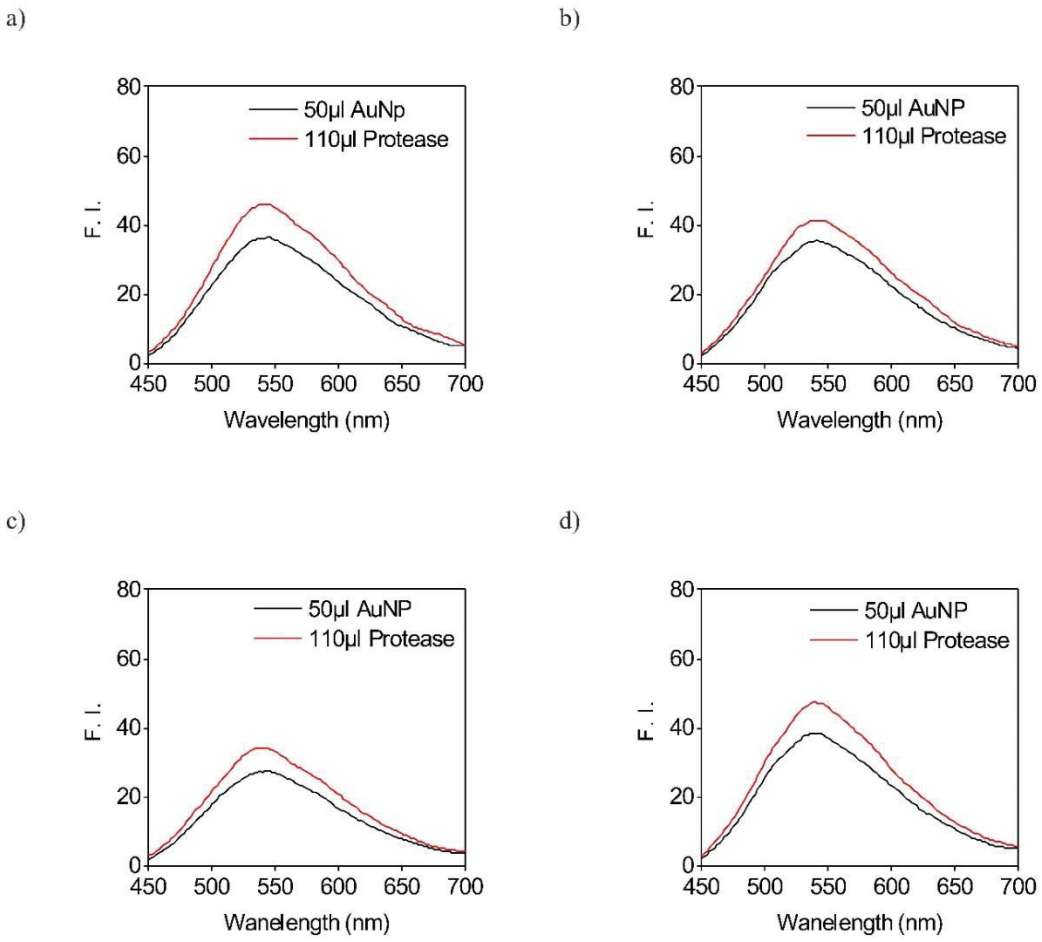

Figure 37. Fluorescence spectra of the PT–Pip–AuNP complex prior and post addition of protease (100 µM): (a) in TE buffer pH = (7.08), (b) in TE buffer pH = (9.64), (c) in water (pH = 7), and (d) in water (pH = 9.7)

Protease is a Zn^{2+} containing metalloenzyme.[166] This protein is made up of a non–glycosylated single polypeptide chain.[167] The pI of protease is 9.4. The MW is 27.287 kDa.[168]

Protease has a positive net charge at pH = 7 and a negative net charge at pH = 9.7. At pH ~ 7, as a result of the electrostatic interaction between positively charged protease and negatively charged AuNPs, the PT–Pip–AuNP complexation was dissociated and PT–Pip recovered its fluorescence, as seen in Figure 37. Moreover, at pH = 9.7, electrostatic interaction between negatively charged protease and positively charged PT–Pip resulted in disruption of the PT–Pip–AuNP complex. The selective displacement of PT–Pip gave rise to fluorescence recovery at pH = 9.7. Figure 38. illustrates the fluorescence response of cytochrome c against sensor array.

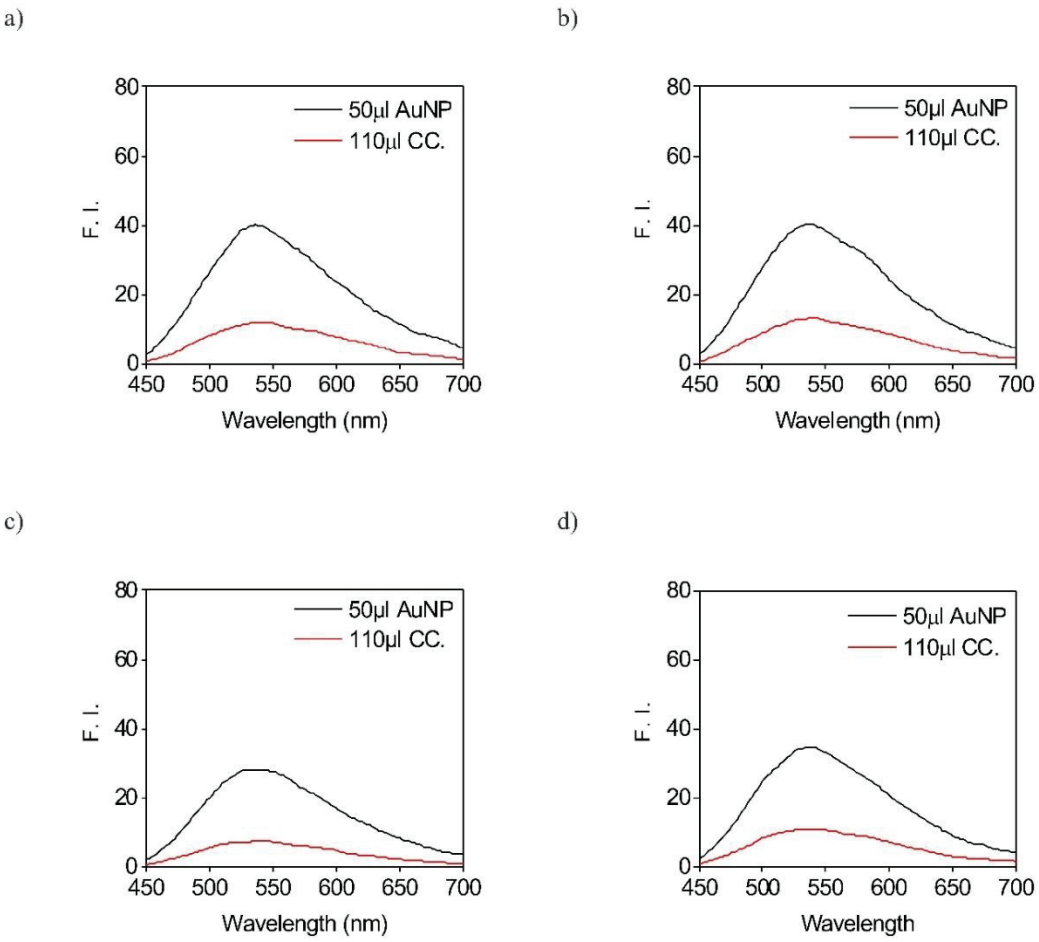

Figure 38. Fluorescence spectra of the PT–Pip–AuNP complex prior and post addition of CC (100 µM): (a) in TE buffer (pH = 7.08), (b) in TE buffer (pH = 9.64), (c) in water (pH = 7), and (d) in water (pH = 9.7)

The pI of CC is in a range of 10.0–10.5. The MW is 12.384 kDa. CC is a metalloprotein with a small globular structure containing an iron porphyrin cofactor (heme c).[169] This heme group containing an electron–deficient Fe (III) is a strong chromophore and quenches the excited state of the fluorescent polymer via an energy and electron process[170,171], as seen in Figure 38. The energy and electron transfer between fluorescent polymer and CC led to the fluorescence quenching. The fluorescence quenching occurred as shown below:

$$\text{PT–Pip} + h\nu \longrightarrow \text{PT–Pip}^*$$

$$\text{PT–Pip}^* + \text{CC} \longrightarrow \text{PT–Pip} + \text{CC}^*$$

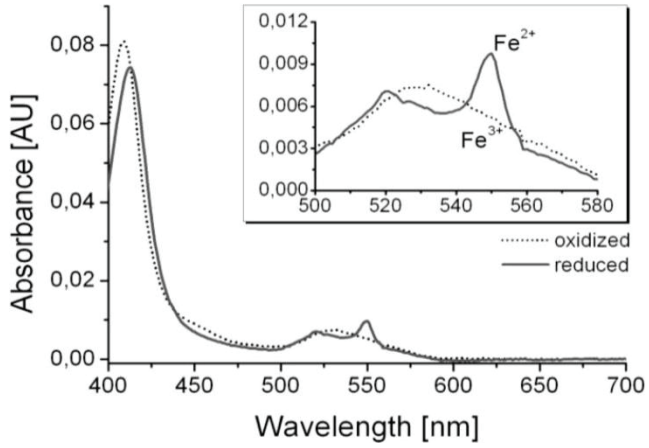

Figure 39. UV–visible spectra of reduced and oxidized form of CC protein.[172]

Figure 39. shows that the oxidized form of CC has two peaks at 530 nm (Q band) and 408 nm (Söret band) in the UV–visible region, while the reduced form of CC has three peaks at 550 nm and 521 nm (Q bands) and 414 nm (Söret band). The emission of PT–Pip and the Q band of oxidized CC overlapped which proves that the CC decreased the fluorescence of PT–Pip via an efficient resonance energy transfer (RET). It is known from the literature that Fe^{3+} can also quench the fluorescence by electron transfer.[173,174] As a results, the fluorescence quenching of PT–Pip by CC occurred possibly by energy and electron transfer mechanism.

The CC protein had a positive net charge at pH ~ 7 and pH ~ 9.7. Higher pH resulted in a lower positive charge on the CC. Therefore, at pH = 9.7, the charge state of CC became less positive than at pH = 7. As a result of the weaker repulsive forces

between CC and PT–Pip, the fluorescence quenching capacity of CC increased at pH ~ 9.7, as shown in Figure 38.

This result indicates that the electrostatic attraction/repulsion between CC and PT–Pip was still significant for efficient energy and electron transfer. Although positively charged CC was not expected to interact with the cationic polymer due to the repulsive forces, CC could still significantly quench the fluorescence of PT–Pip.[175] These results imply that electrostatic attractive forces are not indispensable for the fluorescence quenching mechanism between CC and PT–Pip.

3.2.6. Statistical Analysis of Protein Sensing Assay

Two different methods were used to obtain the multi–dimensional fluorescence responses for protein sensing studies. In the first method, the percentages of the fluorescent intensity changes between the absence and presence of proteins were calculated. In the second method, the percentages of the integrated fluorescent intensity changes between the absence and presence of proteins were calculated.

The fluorescence intensity response patterns (Δ I. %) of the PT–Pip–AuNP sensor array against five proteins were calculated according to Equation 2 and are shown in Figure 40.

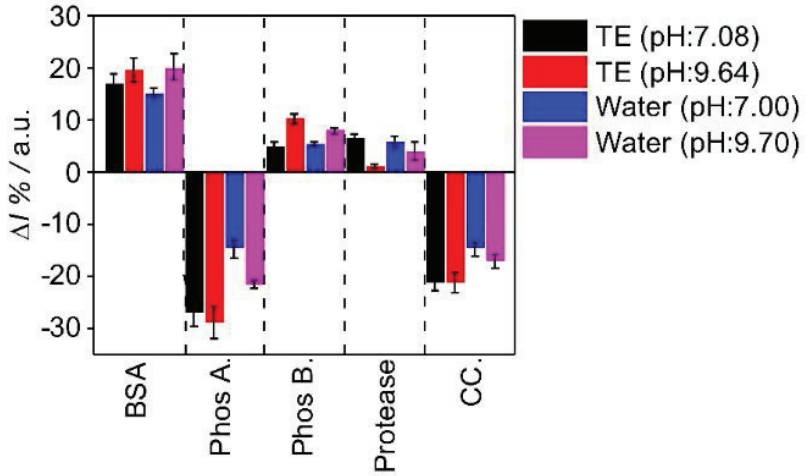

Figure 40. Fluorescence response (Δ I. %) patterns of the PT–Pip–AuNP sensor array with different parameters (TE pH = 7.08; TE pH = 9.64; Water pH = 7; Water pH = 9.7) against various proteins: BSA, bovine serum albumin; Phos A, acid phosphatase; Phos B, alkaline phosphatase; protease; CC, cytochrome c. Each value was an average of five parallel measurements

Two different solvents and two different pH parameters were utilized to tune the electrostatic interaction between the PT–Pip–AuNP complex and proteins. BSA and Phos B induced fluorescence increment as a result of selective displacement of PT–Pip due to the electrostatic interaction between PT–Pip and proteins. BSA was more negatively charged than Phos B at similar pH values, as BSA had a lower pI. Therefore, BSA induced more fluorescence increment compared to Phos B. Moreover, the amphiphilic surfactant–like character of BSA contributed to the protein–induced PT–Pip disagregation, thus increasing the fluorescence intensity of PT–Pip more effectively than the other proteins.

Protease (Zn^{2+} containing metalloenzyme) was positively charged at pH = 7 and negatively charged at pH = 9.7. Protease displayed distinct electrostatic interaction behavior. It interacted with AuNPs at pH = 7 and with PT–Pip at pH = 9.7. Both interactions resulted in fluorescence enhancements. Besides, the interaction between protease and AuNP at neutral pH result in a higher fluorescence recovery compared to interaction between protease and PT–Pip at basic pH.

The fluorescence quenching ability of iron–containing metalloproteins, i.e. CC and PhosA, resulted in further fluorescence reduction of pre–quenched PT–Pip–AuNP complexes, as seen in Figure 40.

The fluorescence response patterns of proteins obtained with the PT–Pip–AuNP sensor array are displayed via scatter plot graphs in Figures 41. and Figure 42. to investigate the disccrimination power of each sensor element. Each point has the value of one variable determining the position on the horizontal axis and the value of the other variable determining the position on the vertical axis.

a) b)

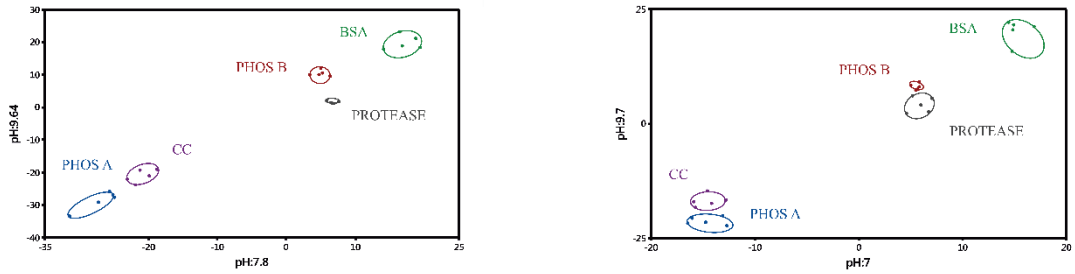

Figure 41. Scatter graph of simplified fluorescence response patterns obtained with the PT–Pip–AuNP sensor array with different parameters against various proteins (BSA; bovine serum albumin, Phos A; acid phosphatase, Phos B; alkaline phosphatase, protease, CC, cytochrome c). (a) Scatter graph with responses in TE buffer at two different pH values; (b) scatter graph with responses in water at two different pH values

a) b)

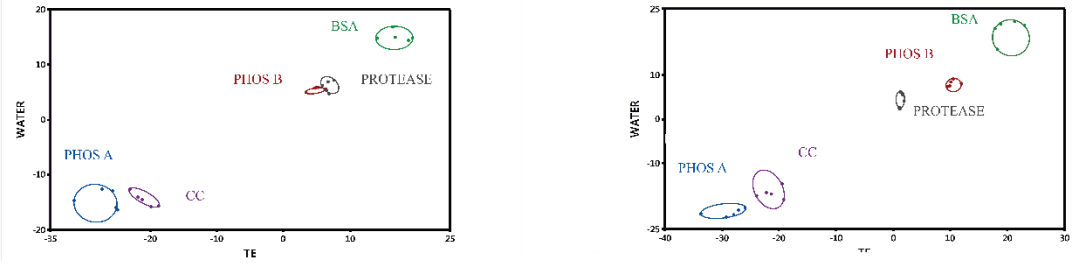

Figure 42. Scatter graph of simplified fluorescence response patterns obtained with the PT–Pip–AuNP sensor array with different parameters against various proteins (BSA; bovine serum albumin, Phos A; acid phosphatase, Phos B; alkaline phosphatase, protease, CC, cytochrome c). (a) Scatter graph with responses in two different buffers at pH = 7; (b) scatter graph with responses in two different buffers at pH = 9.7

The scatter plot graphs in Figure 41. (a) and (b) display the differentiation of proteins by using a single buffer at two different pH values. It was observed that the proteins were distinguished from each other better with TE buffer compared to MQ water. The scatter plot graph in Figure 42. (a) and (b) represents the differentiation of proteins by using two different solvents at constant pH. These graphs represents that the proteins were distinguished successfully from each other at pH = 9.7 but not at pH = 7.

Later, the fluorescence response patterns obtained by the four sensor elements were used for protein identification and discrimination. The training set consisted of 100 data points (four factors × five proteins × five replicates) that were statistically analyzed by the PCA method, as shown in Figure 43.

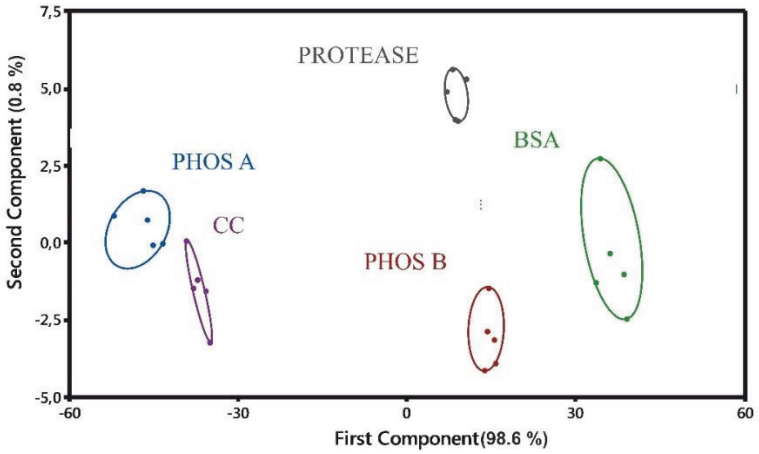

Figure 43. PCA graph of simplified fluorescence response patterns obtained with the PT–Pip–AuNP sensor array with four different parameters against various proteins (BSA; bovine serum albumin, Phos A; acid phosphatase, Phos B; alkaline phosphatase, protease, CC; cytochrome c)

PCA was used as a dimensional reduction method. This method enhanced the analysis efficiency while reducing data loss.[88] In this study, two–component PCA explained 99.4% of the total variance, as shown in Figure 43.

Fluorescence response patterns against multidimensional sensor arrays were clustered into five non–overlapping groups. These results indicated that PCA was an appropriate method for clustering the fluorescence response patterns of five proteins with comparable structures. For instance, although Phos B and Protease showed similar fluorescence patterns against the sensor array, PCA clustered them into two distinct groups. Similarly, both iron containing metalloenzymes Phos A and CC, which quenched the fluorescence of PT–Pip, could be clustered into two non–overlapping groups.

The integrated fluorescence response (area) patterns (Δ I. %) of the PT–Pip–AuNP sensor array against the five proteins were calculated according to Equation 2 and are shown in Figure 44.

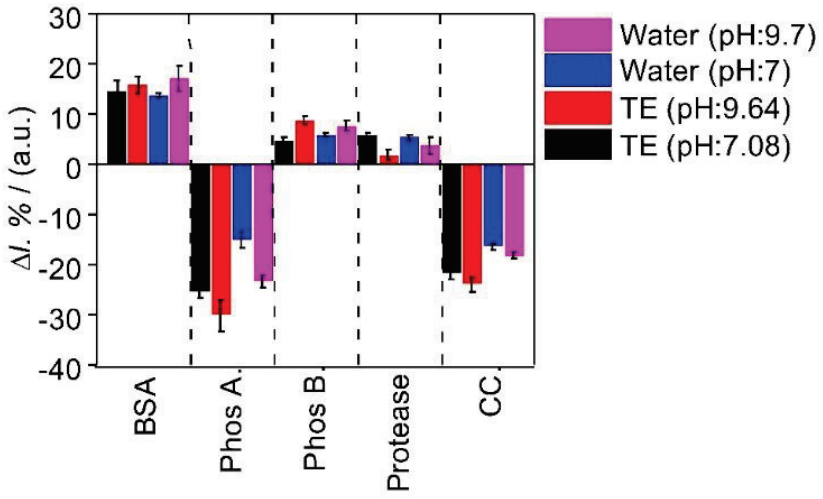

Figure 44. Fluorescence response (Δ I. %) patterns of the PT–Pip–AuNP sensor array with different parameters (TE pH = 7.08; TE pH = 9.64; Water pH = 7; Water pH = 9.7) against various proteins (BSA; bovine serum albumin, Phos A; acid phosphatase, Phos B; alkaline phosphatase, protease, CC, cytochrome c). Each value was an average of five parallel measurements

The proteins' fluorescence response patterns were calculated by measuring integrated fluorescence intensity (area). These response patterns displayed similar results to the fluorescence response calculated by fluorescence intensity differences. In Figures 45. and 46. , the scatter plot graphs are generated by using the fluorescence response patterns given in Figure 44.

a)

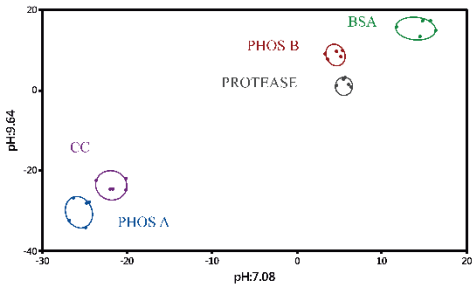

b)

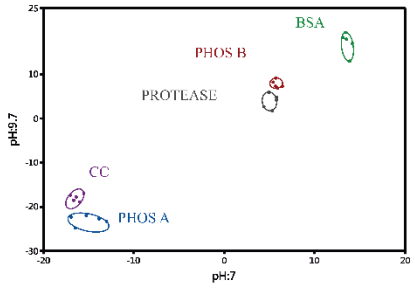

Figure 45. Scatter graph of simplified fluorescence response patterns obtained with the PT–Pip–AuNP sensor array with different parameters against various proteins (BSA; bovine serum albumin, Phos A; acid phosphatase, Phos B; alkaline phosphatase, protease, CC, cytochrome c). (a) Scatter graph including responses in TE buffer with two different pH parameters; (b) scatter graph including responses in MQ water with two different pH parameters

a) b)

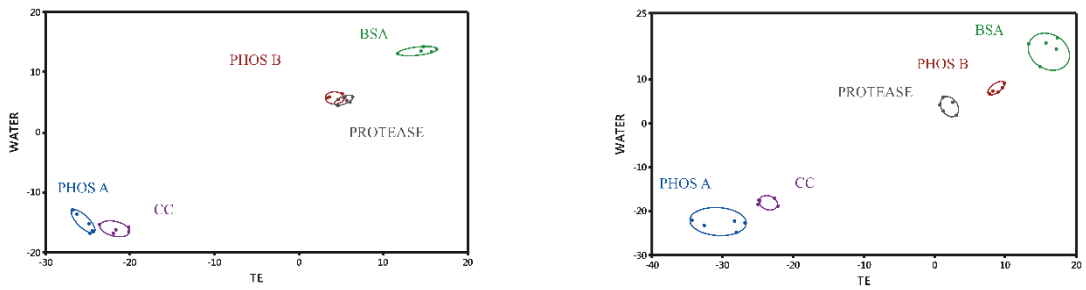

Figure 46. Scatter graph of simplified fluorescence response patterns obtained with the PT–Pip–AuNP sensor array with different parameters against various proteins (BSA; bovine serum albumin, Phos A; acid phosphatase, Phos B; alkaline phosphatase, protease, CC, cytochrome c). (a) Scatter graph including responses in two different buffer parameters at pH = 7; (b) scatter graph including responses in two different buffer parameters at pH = 9.7

This sensor enabled discrimination of five proteins by using a single solvent at two different pH values. As seen in Figure 45. (a) and (b), there was no overlap between the clusters of proteins. The scatter graphs in Figure 46. (a) and (b) illustrates the experimental results using two different buffers at constant pH. It was observed that the proteins' fluorescence response were clustered without overlapping at pH = 9.7, but not at pH = 7. For the statistical analysis, 100 data points (four factors × five proteins × five replicates) were used as a training set. The proteins' integrated fluorescence responses were analyzed by PCA, as shown in Figure 47.

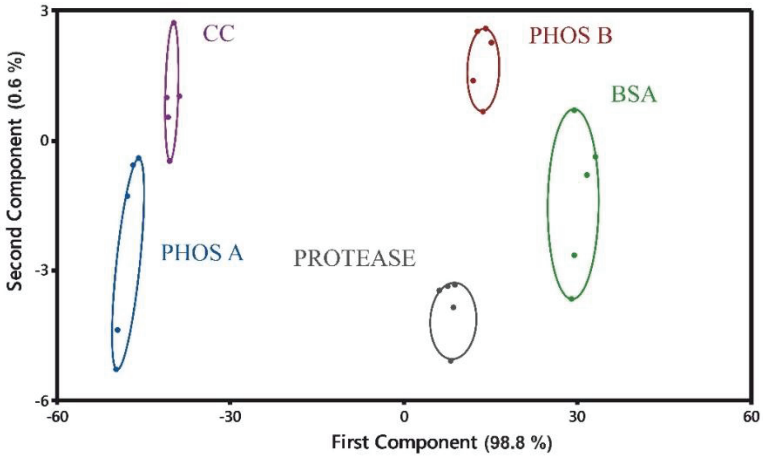

Figure 47. PCA graph of simplified fluorescence response patterns obtained with the PT–Pip–AuNP sensor array with four parameters against various proteins (BSA; bovine serum albumin, Phos A; acid phosphatase, Phos B; alkaline phosphatase, protease, CC; cytochrome c)

It was observed that both the fluorescence intensity and integrated fluorescence intensity (area) calculation methods yielded similar discrimination results. When these two statistical analysis methods were compared, it was obvious that using the fluorescent intensities more efficiently discriminated the five proteins. Therefore this calculation method could be used to develop a robust biosensor for biomolecule detection and identification for further experiments. LoD of each sensor element for each protein was calculated according to Equation 3.

Table 4. LoD values of sensor elements for proteins

	TE PH = 7	**TE PH = 9.64**	**WATER PH = 7**	**WATER PH = 9.7**
BSA	17.73μM	12.10 μM	19.81 μM	6.68 μM
PhosA	14.41 μM	11.07 μM	14.70 μM	12.87 μM
Phos B	45.48 μM	6.07 μM	11.05 μM	7.65 μM
Protease	133.63 μM	397.07 μM	118.84 μM	47.19 μM
CC	18.39 μM	19.18 μM	27.87 μM	27.12 μM

The LoD value is the minimum concentration that is measurable or detectable with statistical significance by a given procedure. The LoD values of the four different sensor elements for five different proteins are presented in Table 4. The detection limit of each sensor element is shown in Table 4. The LoD values of the protein sensor array were 46.8 μM for Phos A, BSA, CC, and protease and 5.3 μM for Phos B. In summary, the combination of the fluorescence turn on/off sensor array with PCA methods could succesfully distinguish five protein. Moreover, these sensor array showed high selectivity to iron containing metalloenzyme.

PT derivatives were used as a fluorescence transducing element in many sensor application for protein detection and discrimination. Abérem et al. developed a sensor array using the combination of water soluble cationic PT derivative and DNA aptamer to detect human thrombin.[176] Initially, introducing DNA aptamer to the fluorescent PT derivative induced aggregation and fluorescence quenching. Upon addition of human thrombin, the conformation of DNA aptamer changed from unfolded to a folded structure, which then recovered the fluorescence of PT derivative. The limit of detection (LOD) of this sensor for human thrombin was 6.2×10^{-11} M.

Wu et al. reported a colorimetric and fluorescence sensor using an anionic PT derivative to detect protamine, which is arginine–rich and strongly basic protein.[177] Upon addition of cationic protamine to the anionic PT derivative, the complexation

between protamine and PT derivative through multiple electrostatic interactions was observed. These interactions induced the conformational transition and aggregation of PT derivative, which quenched the fluorescence and changed the color of polymer. This color change enabled the detection of protamine by PT derivative with the detection limit of 0.1 μg mL^{-1}. Although these sensors show high sensitivity and selectivity to target protein, they can not be useful for simultaneous detection of multiple proteins, and moreover former sensor array was very labor intensive and time consuming.

You et al. also proposed a chemical ‘‘nose/tongue’’sensor array containing six cationic gold nanoparticles as an efficient fluorescence quenchers and a poly(p–phenyleneethynylene) as a fluorescence indicator to detect and discriminate seven proteins.[126] Initially, the fluorescence of polymer was quenched by nanoparticles, the protein addition created fluorescence alteration by interacting with AuNP. The fluorogenic responses of proteins were evaluated by LDA, and seven proteins discriminated for 5 μM protein concentration.

In this thesis, we reported a novel fluorescence turn on–off sensor array for the first time to detect and discriminate five different proteins by using cationic PT–Pip, in combination with anionic AuNP. After fluorescence quenching of cationic PT–Pip by anionic AuNPs, the protein sensing event occured, which relied on the competitive interaction between proteins and AuNP against PT–Pip. As a result of this interactions, distinct multidimentional fluorogenic responses were obtained for each protein. The LoD values of the protein sensor array were 46.8 μM for Phos A, BSA, CC, and protease, and 5.3 μM for Phos B. Moreover, compared to the similar sensor arrays in literature, this sensor array containing 4 sensor elements showed a high selectivity to iron containing metalloproteins; such as Phos A, and CC. The ferric ion is known to be among the most effective fluorescence quenchers due to its paramagnetic nature.[178] Tu et al reported a sensor containing pre–quenched copolymer–ATP complex, which displayed sensitive and selective fluorometric and colorimetric recovery in response to Al^{3+} among various metal ions.[114] This study also revealed that the Fe^{3+} could significantly quench the fluorescence of PT random copolymer. CC is an iron–containing metalloprotein, which favors electron transfer through the Fe^{3+} and energy transfer through the porphyrin ring. Although the sensors developed for CC detection to date are based on the fluorescence quenching of anionic polymers by the electrostatic interaction between cationic CC and anionic fluorescent polymers. It has been observed

that even at high pH, at which CC was slightly negative, CC could still quench the fluorescence of anionic polymers with low quenching efficiency.

Therefore, the protein sensor developed in this thesis reveals that the fluorescence of the cationic PT–Pip is quenched by the positively charged CC by energy and electron transfer.[179] Besides, the fluorescence quenching efficiency was further increased at high pH with the decrease of positive charge of CC. These results are compatible with the literature. Similar fluorescence quenching was observed for Phos A, due to the electron transfer between Fe^{3+} on the heterovalent active site of Phos A and PT–Pip.[179]

3.3. Ratiometric Sensing of Mammalian Cells

This study aimed to develop a robust biosensor for the discrimination of different mammalian cell lines, including healthy, cancerous, and metastatic cells according to their cell membrane surface properties. Initially, the buffers and mammalian cell concentration were optimized for mammalian cell sensing applications.

3.3.1. Optimization of Buffer Types and Cell Concentration

The pre–quenched PT–Pip–AuNP complexes were titrated by DMEM media, in which the mammalian cells were grown, and MQ water to observe the effects of DMEM on sensing mechanism

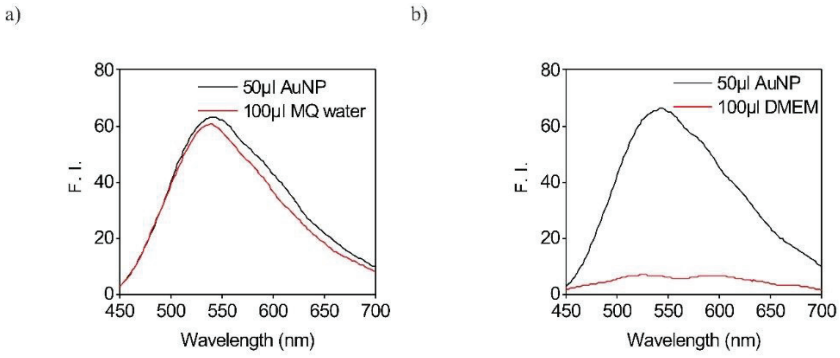

Figure 48. Fluorescence spectra of PT–Pip–AuNP complex titrated by (a) MQ water and (b) DMEM

The fluorescence of PT–Pip slightly decreased upon addition of MQ water due to the dilution effect. On the other hand, DMEM addition caused a significant decrease in fluorescence intensity, as shown in Figure 48. This decrease resulted from the phenol red dye (phenolsulfonphthalein) in DMEM media. The phenol red dye absorbed light at 560 nm[180] which is close to the emission maximum of PT–Pip (538 nm). As a result of spectral overlap, the fluorescence of PT–Pip was almost completely quenched by phenol red dye via energy transfer. In the ligth of these results, following experiments were performed using MQ water as an optimum solvent.

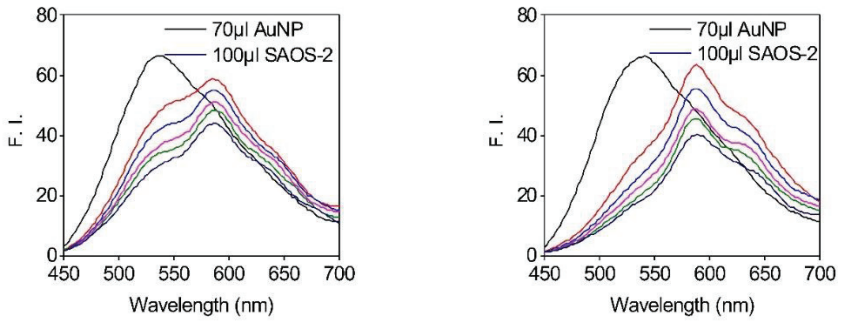

Figure 49. Fluorescence spectra of PT–Pip–AuNP complex titrated by low concentration (left) and high concentration (right) of SAOS–2 cells

Strong interaction between cells and PT–Pip was observed at concentration of 200,000 (left graph) and 2,000,000 (right graph) cells, as shown in Figure 49. No significant difference was observed between the responses of 200,000 cells and 2,000,000 cells. Therefore, the cell concentration was fixed at 200,000 cells/µL. Table 5 shows the seven mammalian cell lines incluiding metastatic, cancerous, and healthy cells which were used as analytes.

Tablo 5. Mammalian cell lines used for the study

Origin	**Tissue**	**Cell line**		**Disease**
Human	Breast; mammary gland	MDA–MB–231	Metastatic	Adenocarcinoma
Human	Breast; mammary gland	MCF–7	Cancerous	Adenocarcinoma
Human	Bone	SAOS–2	Metastatic	Osteosarcoma
Human	Bone; marrow	SH–SY5Y	Cancerous	Neuroblastoma
Human	Uterus; cervix	HeLa	Cancerous	Adenocarcinoma
Mouse	Embryo	NIH/3T3	Normal	Healthy
Cow	Eye; cornea	BCE C/D–1b	Normal	Healthy

The mammalian cell–sensing assay was carried out three times for seven cell lines using 200,000 cells/100 µl in MQ water. The results are shown in Figure 50.

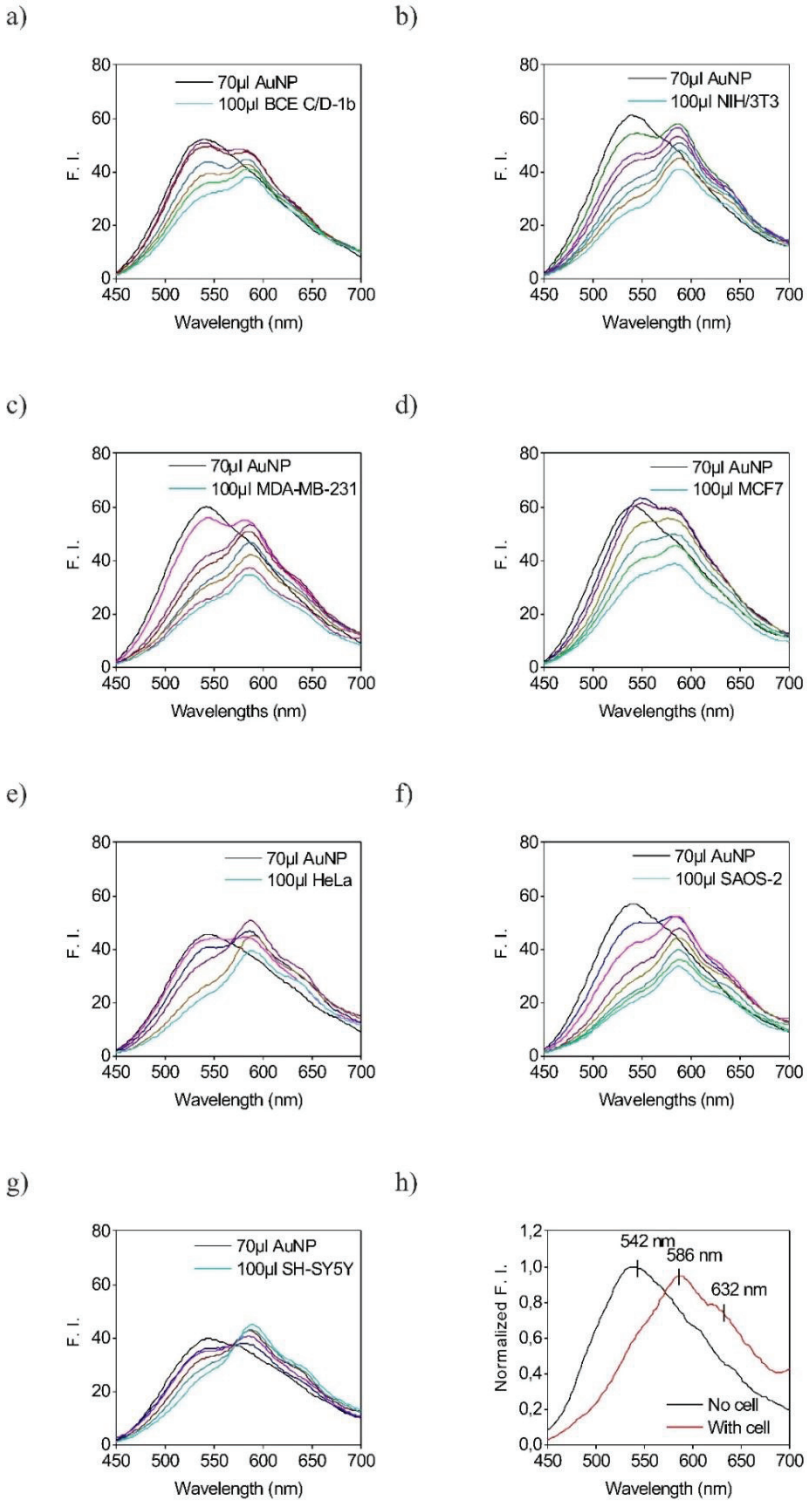

Figure 50. Fluorescence spectra of PT–Pip–AuNP complexes titrated by (a) BCE C/D–1b, (b) NIH/3T3, (c) MDA–MB–231, (d) MCF–7, (e) HeLa, (f) SAOS–2, and (g) SH–SY5Y, and (h) fluorescence alteration created by cell addition

Figure 50. illustrates the fluorescence spectra of PT–Pip–AuNP complexes titrated by different mammalian cell lines. Unique interactions between PT–Pip and seven different cell lines were observed.

PT–Pip emitted light between 535 nm and 538 nm which was related to intrachain interactions and indicated that the polymer was non–planar and had random–coil conformation.[143] After fluorescence quenching of PT–Pip with AuNP, the fluorescence maximum of the PT–Pip shifted to longer wavelengths (ranging from 538 nm to 544 nm) indicating the formation of the PT–Pip–AuNP complex. As seen from Figure 50. (h), cell addition resulted in non–planar to planar conformational transition of the PT–Pip backbone due to the hydrogen bonding or hydrophobic interaction established between PT–Pip and cell surfaces.[143] The interaction between PT–Pip and cells did not induce fluorescence recovery, indicating that the PT–Pip–AuNP complexation still existed.

Novel peaks appeared at 586 nm and 632 nm (as a shoulder) due to the planarization of the polymeric backbone. Therefore, the PT–Pip backbone adopted a more rod–shaped conformation as a result of PT–Pip–AuNP–cell interactions. The intensity of the emitted light at longer wavelengths was also decreased upon addition of cells. This fluorescence decrement indicated aggregation of PT–Pip chains arising from interchain interactions.[143]

The ratio of fluorescence intensities corresponding to 542 nm, 586 nm, and 632 nm varied from cell to cell. These distinct ratios proved the existence of unique electrostatic, hyrophobic, or hydrophobic interactions between the PT–Pip–AuNP complex and each cell. The λ_{max} of the PT–Pip–AuNP complex, 542 nm, was called I_1. The novel peak at 586 nm was called I_2. The shoulder at 632 nm was called I_3. The ratios of I_2 / I_1 and I_3 / I_1 were calculated to obtain the fluorescence response of each cell line.

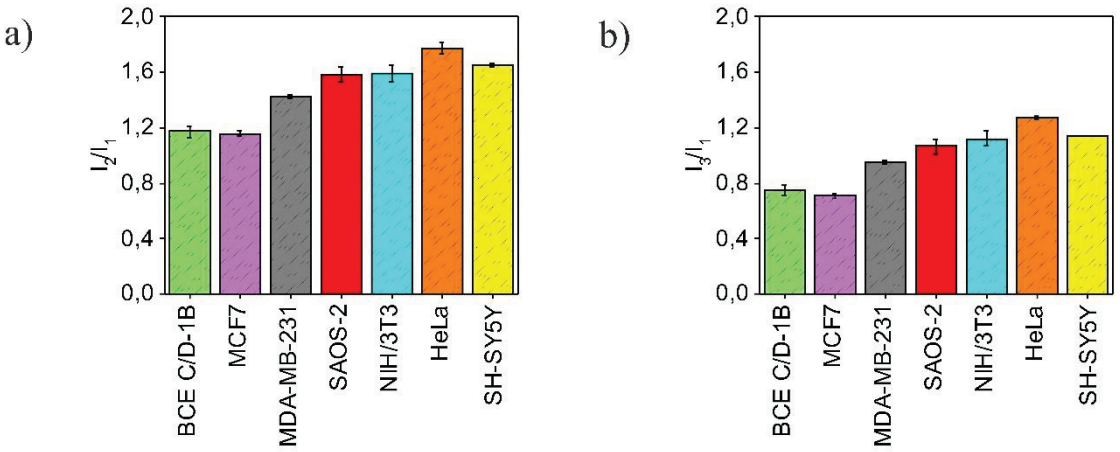

Figure 51. Fluorescence intensity ratio of the emitted light of PT–Pip at (a) 586 nm/ 542 nm and (b) 632 nm/542 nm for seven cell lines

This preliminary results showed that the fluorescence ratios of I_2/I_1 and I_3/I_1 varied between different cell types, as seen in Figure 51. The differences between the fluorescence intensity ratios for different cell lines were used to reveal the unique but subtle differences between normal, cancerous, and healthy cells. The ratios of fixed wavelengths were used for the ratiometric sensing of mammalian cells.

3.3.2. Alamarblue Assay

Cells were submitted to alamarBlue assay to investigate cell viability in different buffer systems. Initially, the cell viabilites of adherent cells and suspended cells (in DMEM) were compared. The viability of adherent cells was 45.51%, while the viability of suspended cells was 35.22%. The viability of the suspended cells relative to the adherent cell was 77.39%.

The viability of cells suspended in water, 1X TE buffer, and 25 mM HEPES buffer was compared. 25 mM HEPES buffer was selected, as HEPES buffer is widely used in biosensor applications containing PT derivatives and biological analytes.[102,181] The viability of cells suspended in water was 45%. The viability of cells suspended in 1X TE buffer was 52.7%. The viability of cells suspended in 25 mM HEPES buffer was 82.5%. The viabilities of cells were higher in TE buffer and HEPES buffer than in MQ water. The highest viability was obtained in the 25 mM HEPES buffer.

To investigate the effects of 25 mM HEPES and 1X TE buffer on the sensing mechanism, PT–Pip was diluted by MQ water, HEPES, and TE buffer, individually.

The PT–Pip–AuNP complex was then titrated with HEPES and TE buffer (without cells). The results are shown in Figure 52.

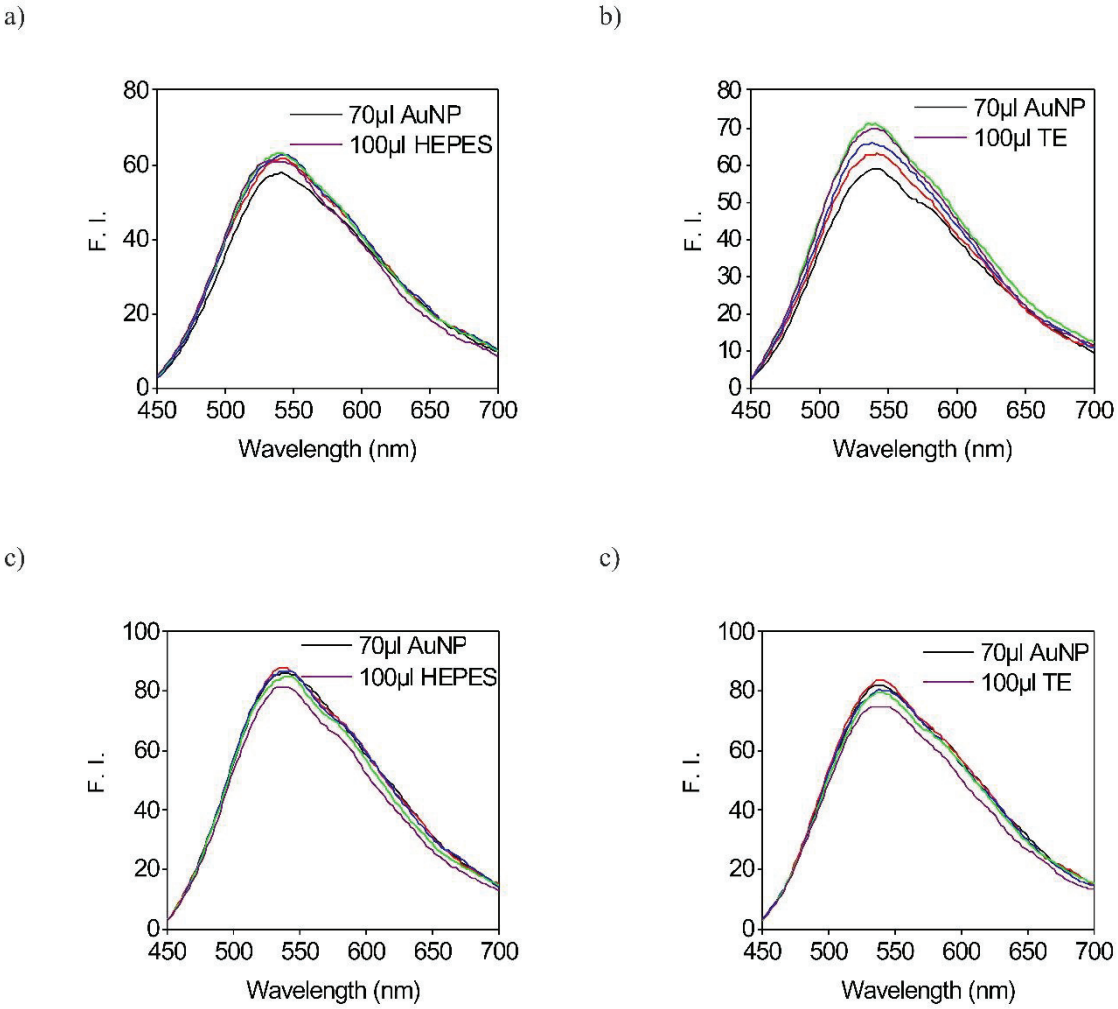

Figure 52. Fluorescence spectra of PT–Pip–AuNP complex (black curve) titrated by HEPES and TE buffer: (a) PT–Pip (in water)–AuNP complex titrated by 25 mM HEPES buffer, (b) PT–Pip (in water)–AuNP complex titrated by 1X TE buffer, (c) PT–Pip (in 25 mM HEPES)–AuNP complex titrated by 25 mM HEPES buffer, and (d) PT–Pip (in 1X TE)–AuNP complex titrated by 1X TE buffer

PT–Pip diluted with MQ water was quenched by AuNPs. Addition of HEPES buffer slightly increased the fluorescence of the PT–Pip, as seen in Figure 52. (a). Under the same parameters, the TE buffer caused a more significant fluorescence increase than the HEPES buffer, as seen in Figure 52. (b).

Dilution of PT–Pip with HEPES and TE buffer increased the initial fluorescence intensity of the polymer and reduced the fluorescence quenching efficiency of AuNPs.

After fluorescence quenching, the addition of HEPES and TE buffer to the PT–Pip–AuNP complex did not cause significant changes, as shown in Figure 52. (c) and (d).

To investigate the interaction between the PT–Pip–AuNP complex and mammalian cells in the presence of TE and HEPES buffers, PT–Pip was diluted with different solvents (water, TE, and HEPES buffer). Initially, AuNPs quenched the fluorescence of PT–Pip. Then, the pre–quenched PT–Pip–AuNP complexes were titrated with SAOS–2 cells (200,000 cells in 100 µl MQ water, in 1X TE buffer, and in 25 mM HEPES buffer). The fluorescence spectra of the experiments are given in Figure 53.

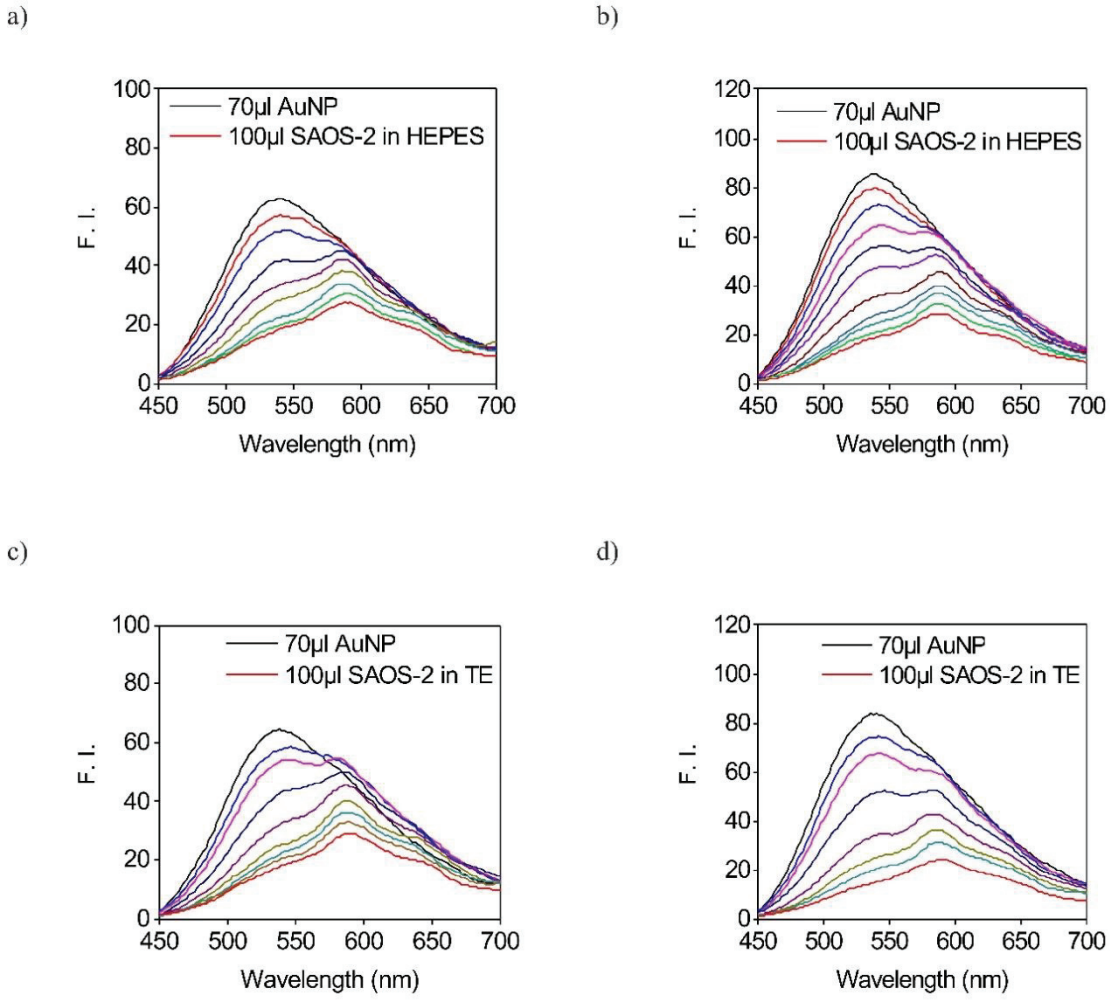

Figure 53. PT–Pip–AuNP complex titrated by SAOS–2 cells: (a) PT–Pip was diluted by MQ water, SAOS–2 cells were suspended in HEPES buffer; (b) PT–Pip was diluted by HEPES buffer, SAOS–2 cells were suspended in HEPES buffer; (c) PT–Pip was diluted with MQ water, SAOS–2 cells were suspended in TE buffer; (d) PT–Pip was diluted with TE buffer, SAOS–2 cells were suspended in TE buffer

The interaction between the PT–Pip–AuNP complex and cells was stronger when PT–Pip was diluted with MQ water. Dilution of PT–Pip with TE or HEPES buffer (at the beginning of the experiment) weakened the interaction between PT–Pip–AuNP complex and cells, as shown in Figure 53. In light of these results, the cell sensing assay studies were continued by diluting PT–Pip with water and by diluting cells with 25 mM HEPES buffer and 1X TE buffer, individually. To exclude the high ionic strength of the buffer, cell pellets were also added to the PT–Pip–AuNP complex directly without using any solvents.

3.3.3. Ratiometric Sensing of Mammalian Cells and Zeta Potential Analysis for Seven Cell Lines

This study aimed to develop a sensor array to discriminate seven cell line according to their cell surface properties by using three sensor elements containing PT–Pip–AuNP complexes. In the first sensor element; 200,000 cells were suspended in 100 µl 25 mM HEPES buffer and used as an analyte. In the second sensor element, cells were suspended in 100 µl 1X TE buffer. In the third sensor element, cell pellets were added directly into the PT–Pip–AuNP complex without using any buffer. The third sensor element will be addressed as a ‘‘solvent free’’ parameter. Experiments were conducted three times for each cell line with optimized sensor parameters.

a)

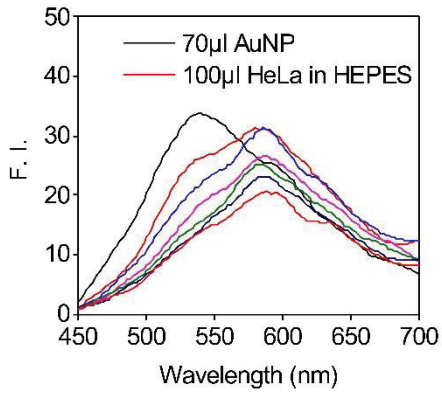

b)

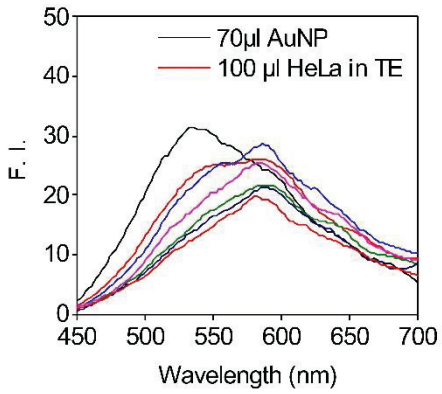

c)

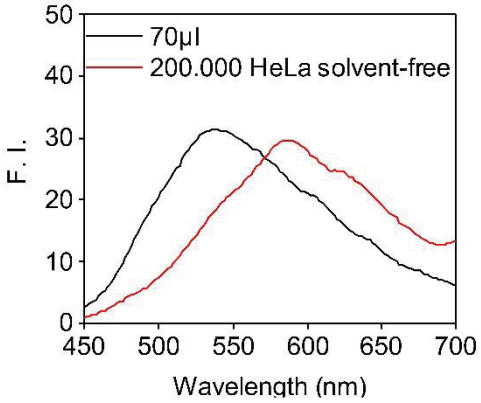

Figure 54. Fluorescence spectra of PT–Pip titrated by HeLa cells suspended in (a) HEPES buffer, (b) TE buffer, and (c) solvent–free addition of cells

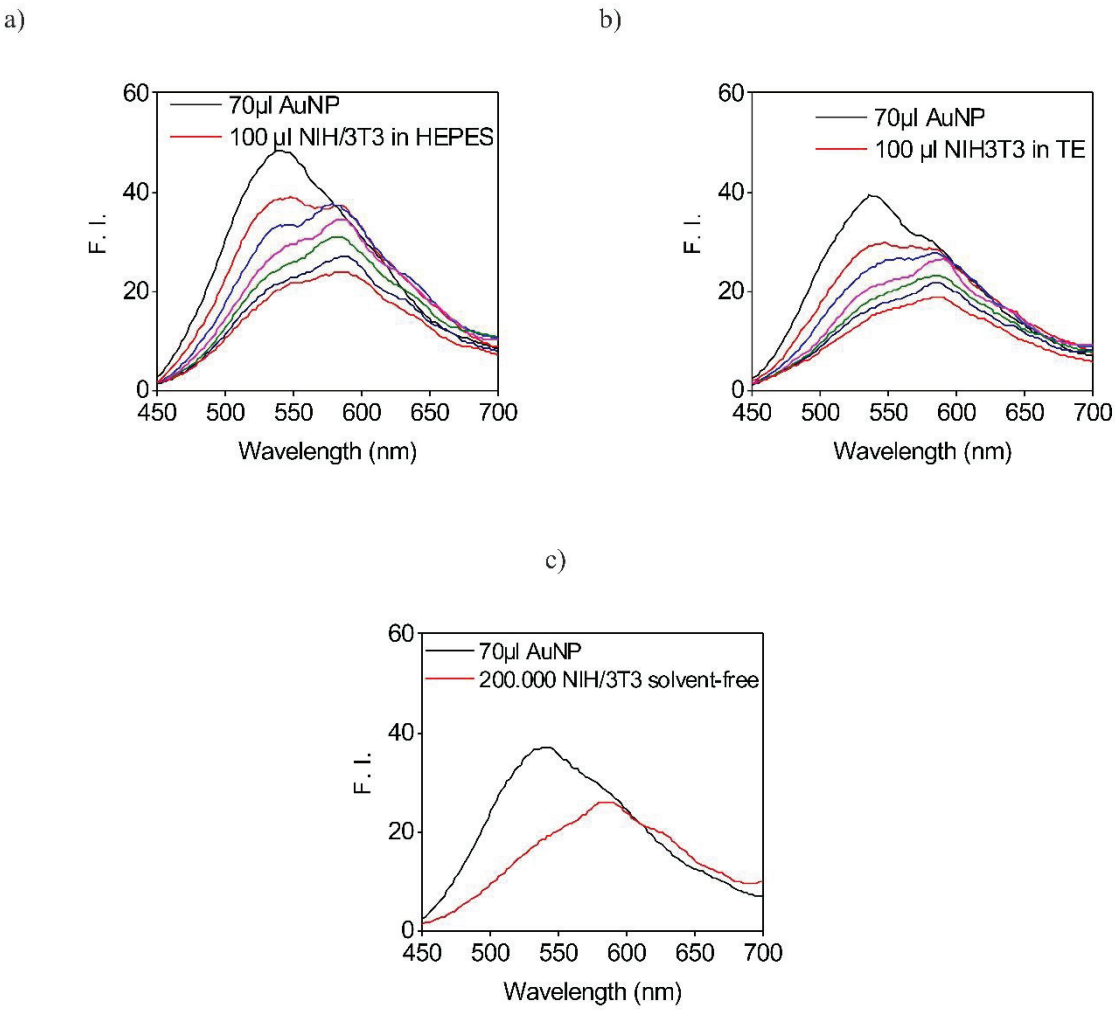

Figure 55. Fluorescence spectra of PT–Pip titrated by NIH/3T3 cells suspended in (a) HEPES buffer (b) TE buffer, and (c) solvent–free addition of cells

a)

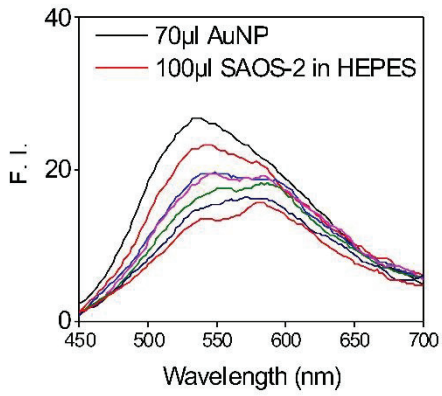

b)

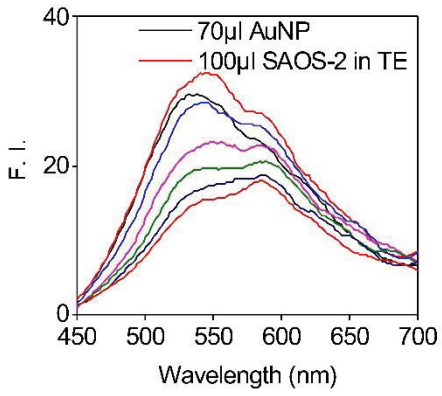

c)

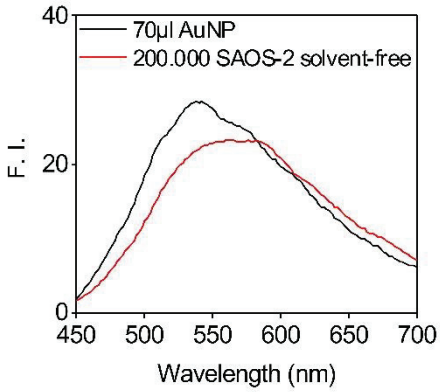

Figure 56. Fluorescence spectra of PT–Pip titrated by SAOS–2 cells suspended in (a) HEPES buffer, (b) TE buffer, and (c) solvent–free addition of cells

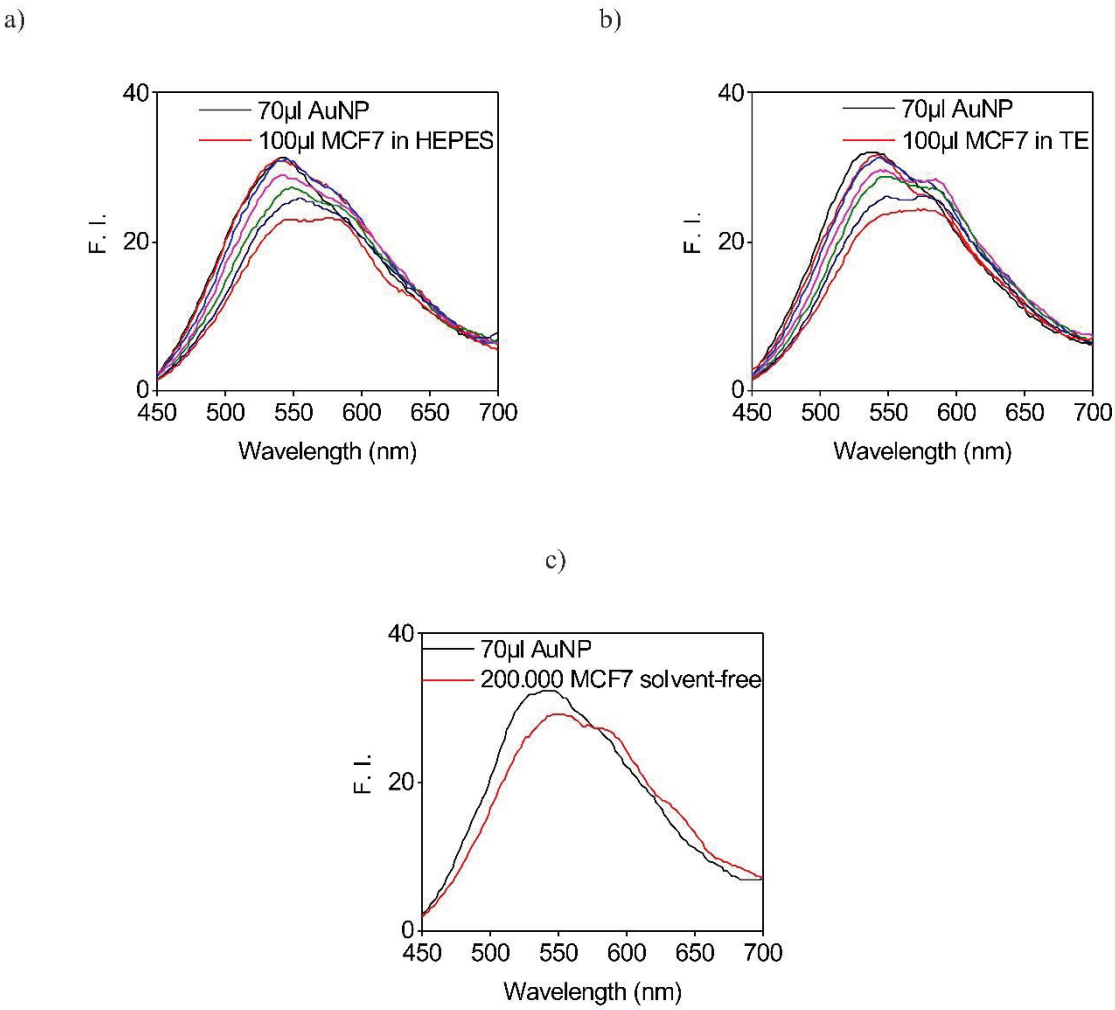

Figure 57. Fluorescence spectra of PT–Pip titrated by MCF–7 cells suspended in (a) HEPES buffer, (b) TE buffer, and (c) solvent–free addition of cells

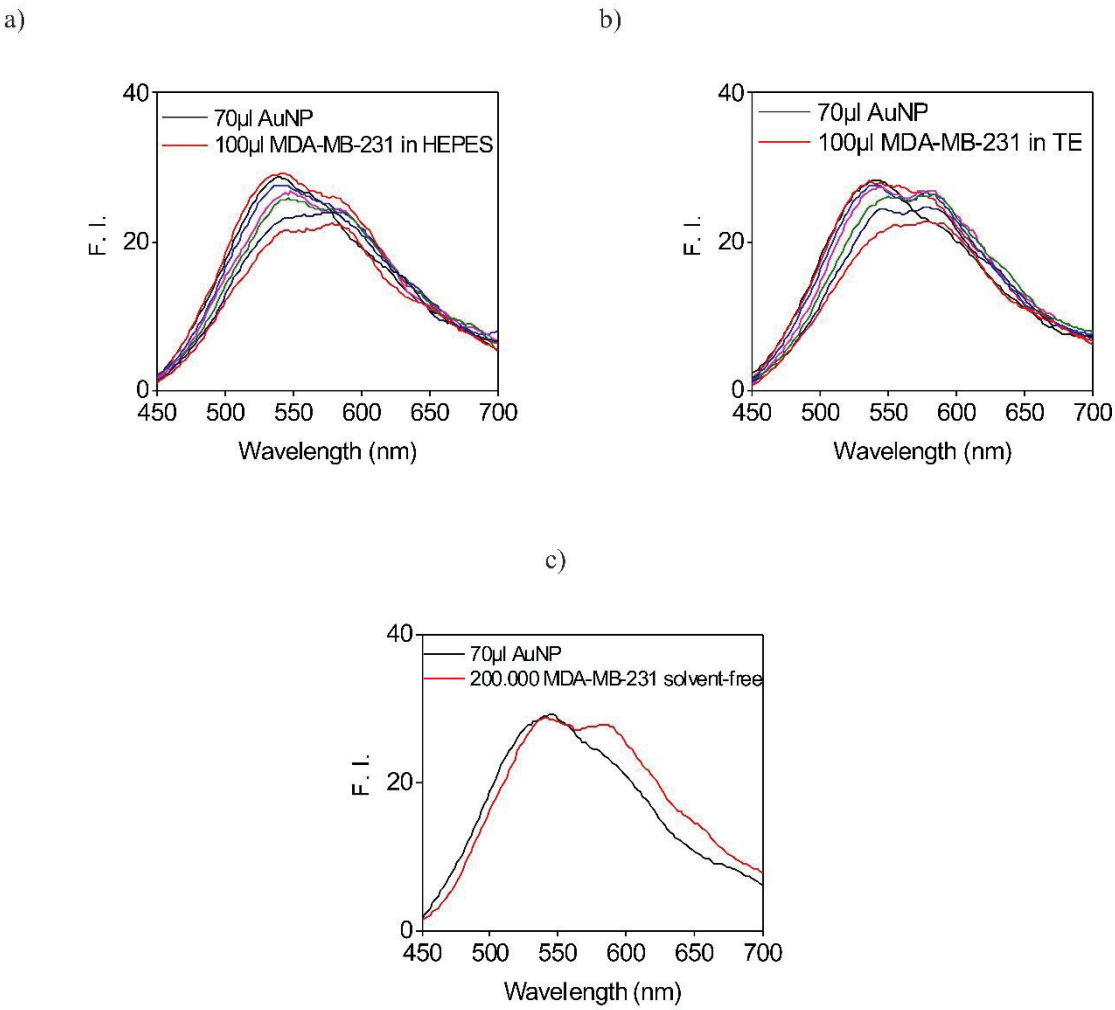

Figure 58. Fluorescence spectra of PT–Pip titrated by MDA–MB–231 cells suspended in (a) HEPES buffer, (b) TE buffer, and (c) solvent–free addition of cells

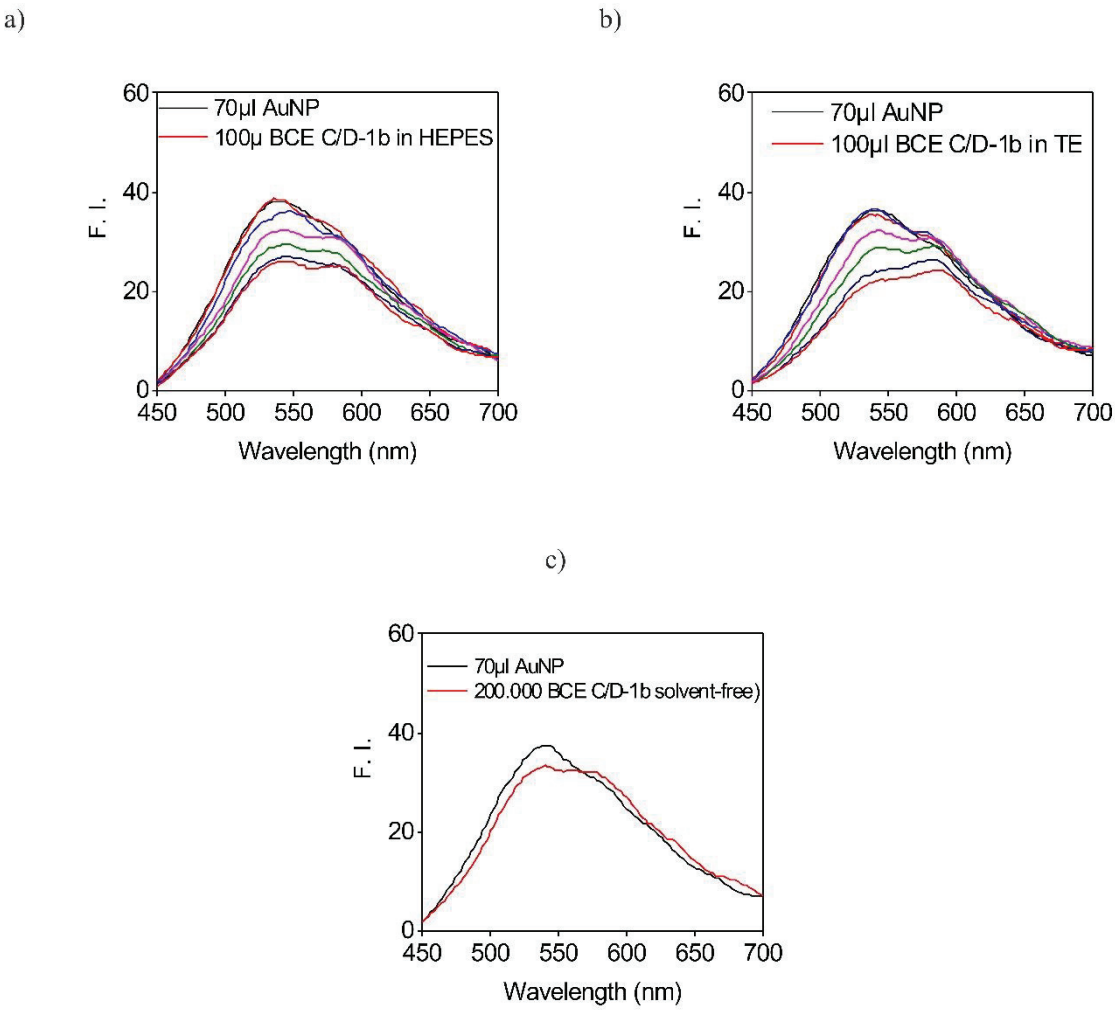

Figure 59. Fluorescence spectra of PT–Pip titrated by BCE C/D–1b cells suspended in (a) HEPES buffer, (b) TE buffer, and (c) solvent–free addition of cells

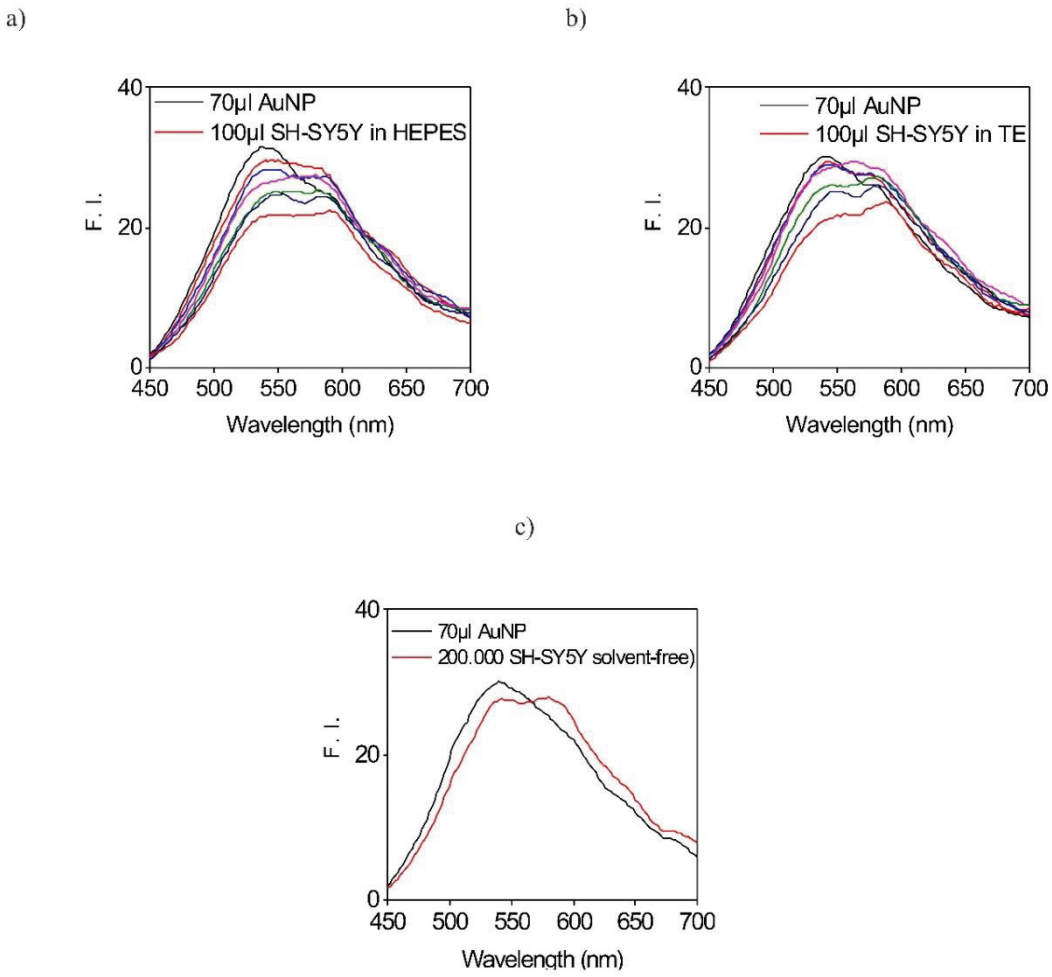

Figure 60. Fluorescence spectra of PT–Pip titrated by SH–SY5Y cells suspended in (a) HEPES buffer, (b) TE buffer, and (c) solvent–free addition of cells

The fluorescence spectra of the cell sensing assay with seven cell lines are given in Figures 54–60. The seven cell lines interacted with the PT–Pip–AuNP complex with various affinities. These affinity differences arose from cell surface physicochemical properties. This diversity in the cells' membrane compositions resulted in charge differences of the cell membrane surfaces. Charge differences in the cell membrane surfaces of the seven cell lines altered mainly the electrostatic interactions between cells and the PT–Pip–AuNP complex. The ratios of the three I_{max} values vary from cell to cell, as shown in Figure 61. Zeta potential analysis was carried out for each cell line to compare the fluorogenic responses and zeta potentials, as seen in Figure 61. (c).

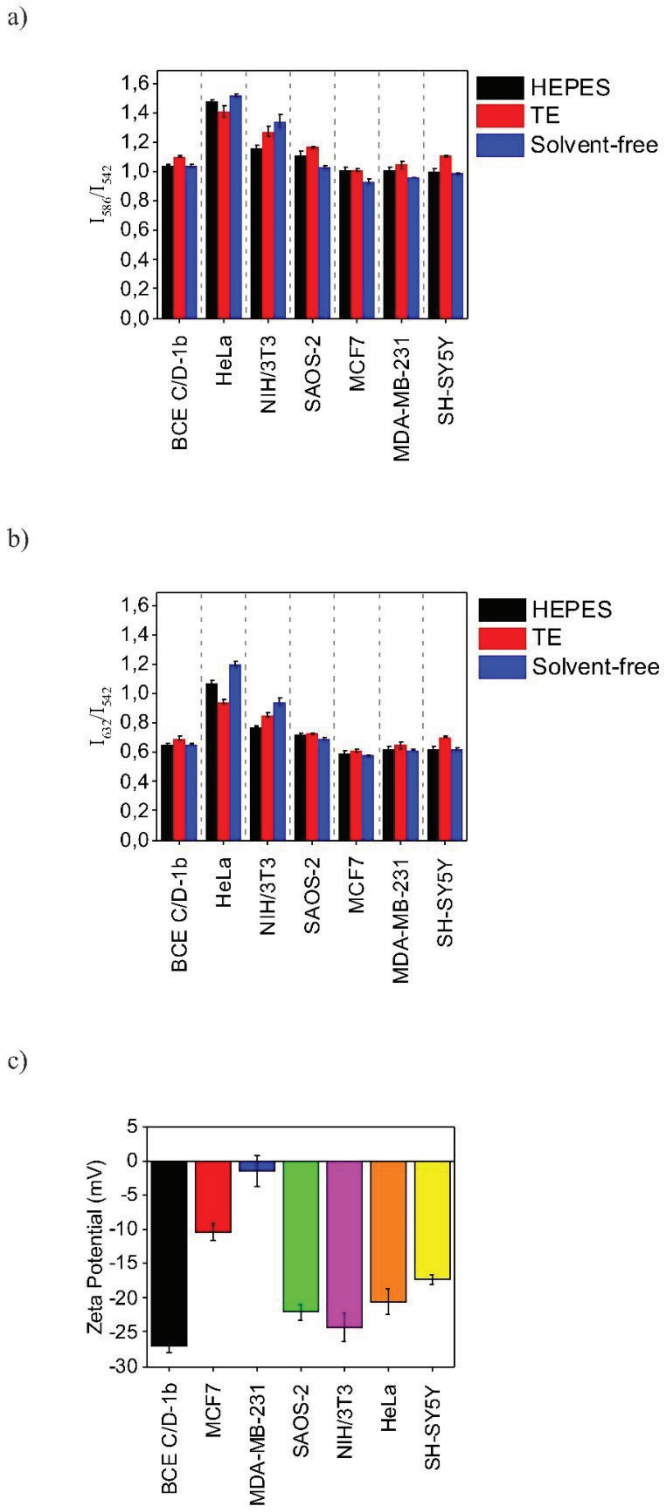

Figure 61. Ratiometric fluorescence response of PT–Pip–AuNP complex to seven cell lines and zeta potential measurement of cells in buffer. (a) I_2/I_1 ratios of seven cell lines in HEPES (25 mM), in TE (1X), and solvent free; (b) I_3/I_1 ratios of seven cell lines in HEPES (25 mM), in TE (1X) ,and solvent free; (c) zeta–potential of seven cell lines in HEPES (25 mM)

The five types of human cancer and metastatic cells originated from the breast, bone, and uterus. The two types of normal cells originated from mouse embryo and cow cornea, as shown in Table 5. The multidimensional fluorescence responses of cells were quantified by the ratio of I_1 to I_2 and I_3 to I_1, as shown in Figure 61. (a) and (b). Distinct fluorogenic responses were obtained especially for three cells: HeLa, SAOS–2, and NIH/3T3, which indicated that these three cell lines strongly interacted with PT–Pip–AuNP complexes. On the other hand, BCE C/D–1b, MCF–7, MDA–MB–231, and SH–SY5Y showed similar fluorogenic responses to the sensor array.

To investigate the relation between cell surface charge and fluorogenic responses, the zeta potential measurement was performed. BCE C/D 1b cells had the lowest zeta potential among the seven cell lines. The advanced glycation end products AGE receptors (pI = 5.83)[182] found in the BCE C/D–1b cell membrane might contribute to the very low zeta potential of BCE C/D 1b cells. The second–lowest zeta potential, belonging to the NIH/3T3 cell membrane, might arise from tyrosine kinase ARK receptors, which were highly expressed in NIH/3T3 cell membrane (pI = 5.27)[183]. HeLa cells' negative cell membrane resulted from phosphatidylethanolamine (PE) and phosphatidylserine (PS) found on the membrane surface.[184] SAOS–2 cells, which had the third–lowest membrane zeta potential, also had the characteristic membrane phospholipid composition of cancer cells, as well as membrane receptors such as EGF (pI = 6.26), and CaSR (pI = 5.62), which contributed to the negative charge of the SAOS–2 cell membrane.

SH–SY5Y, MCF–7, and MDA–MB–231 had less negative zeta potential on their membrane surfaces. Although SH–SY5Y had the characteristic membrane phospholipid composition of cancer cells, this cell line expressed some positively charged receptors at pH = 7, such as dopamine receptor subtypes (pI = 9.55, pI = 9.2)[185] and G–protein coupled muscarinic receptors (pI = 9:33)[186], which reduced the negative charge on the cell membrane. The zeta potential value of MCF–7 cells was higher than that of the other cell lines but MDA–MB–231 due to estrogen receptors (pI = 10.1), which were abundant in the MCF–7 cell membrane and had positive net charge at neutral pH.[187,188] Since anionic DAG glycerides were abundant in the MDA–MB–231 cell membrane (51.7%)[65], the cell membrane zeta potential was expected to be quite negative. However, the zeta potential value measured higher than expected. This charge difference may arise from the A2b adenosine receptors of the MDA–MB–231 cell

membrane. These receptors control the growth and proliferation of tumor cells and have a positive net charge at neutral pH.[189]

Generally, cancer cells' membrane surface had more negative charges compared to healthy cells. In healthy cells, charged lipids were asymmetrically distributed between the two leaflets, but cancer cells could not maintain this asymmetric distribution.[69] Besides phospholipid distribution, the high concentration of negatively charged sialic acid in the cancer membranes and increased lactic acid secretion due to high–speed glycolysis reduced the cell membrane surface charges of cancerous cells.[73–75] However, there are studies in the literature that conflict with this generalization. For example, Selvi et al. measured the zeta–potentials of HeLa and NIH/3T3 cells as –7 mV and –14 mV, respectively, in a 40 mM HEPES buffer.[190] Zhang et al. measured the zeta–potentials of MCF10A and MCF7 cells as −31.16 mV and −20.32 mV.[191]

Metastatic properties of cells have been characterized by altered lipid compositions and cell surface membrane fluidity, which is affected by the amount of cholesterol, cholesterol/phospholipid ratio, fatty acid composition, and phosphatidylcholine/ phosphatidylethanolamine ratio.[192] For instance, increase in high-MW sialylated glycoproteins (negatively charged) at the surface of cells, and decrease in membrane cholesterol content cause an increase on membrane fluidity and plasticity, which is associated with metastatic ability.[193,65] The alterations in cell membrane composition changes the surface charge of the cells. While overexpressed sialic acid significantly reduces the surface charge of metastatic cells, the low level of cholesterol on the surface of cell membrane cause an increase on the surface charge by enhanced Na^+ ion binding with the lipid headgroups.[194] Many studies investigating the membrane surface differences of cancer and metastatic cells have shown a direct relationship between cell surface negativity and metastatic potential.[193,195] For instance, Riedl et al. measured the zeta potential of noncancer cells NHDF, low tumorigenic melanoma cells from primary lesions SBcl–2 and melanoma cells from metastases WM164. Results showed that NHDF cell has the highest zeta potential, and the WM164 cell has the lowest zeta potential.[196]

In our study, the interaction between cells and the PT–Pip–AuNP complex did not correlate with the zeta potentials of the cell membrane surfaces, suggesting that there may be hydrophobic interactions as well as electrostatic interactions between the PT-Pip-AuNP complex and the phospholipids, membrane proteins and carbohydrates of the cell surface.

3.3.4. Statistical Analysis of Cell Sensing Assay

The multidimentional fluorescence response patterns of seven cell lines obtained by the ratios of I_{max} values of cell–sensing experiments were statistically evaluated by PCA. The PCA graphs are shown in Figure 62.

a)

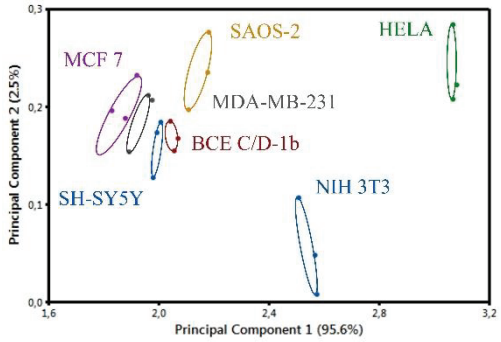

b)

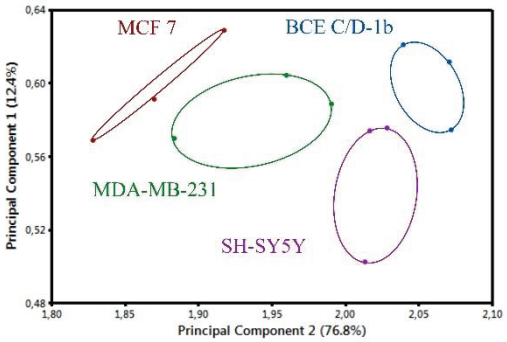

Figure 62. Detection and differentiation of different mammalian cells. A PCA plots for the first two factors of simplified fluorescence response patterns obtained with sensor arrays against seven mammalian cells. (a) PCA plot for the fluorescence responses of BCE C/D–1b, NIH/3T3, MDA–MB–231, MCF–7, SAOS–2, SH–SY5Y, and HeLa cell lines; (b) PCA plot for the fluorescence responses of BCE C/D–1b, MDA–MB–231, MCF–7, and SH–SY5Y. Each value is an average of three parallel measurements

Statistical analysis of the training matrix containing 126 data points which consisted of (six factors × seven cells × three replicates) was carried out via PCA. Each point showed a response pattern for different cell types against the fluorescence sensor array. HeLa, NIH/3T3, and SAOS–2 cell lines were clustered into three non–overlapping groups, as shown in Figure 62. (a) (p–value ≤ 0.05) due to the strong

interaction between cells and the PT–Pip–AuNP complex. The fluorescence responses of MDA–MB 231, MCF–7, SH–SY5Y, and BCE C/D 1b cell lines were compressed but not overlapped in the PCA plot. None of our test results were outliers.

The fluorescence response patterns of the MCF–7, MDA–MB–231, SH–SY5Y, and BCE C/D 1b cells were analyzed by the second PCA, as shown in Figure 62. (b). Although the results for a single cell were spread over a wide area in the second PCA plot, MCF–7, MDA–MB 231, SH–SY5Y, and BCE C/D 1b did not overlap with each other, as seen in Figure 62. (b). Outlier analysis shows that none of our test results were outliers.

Bajaj et al. decribed an array based system using the conjugates between 3 cationic nanoparticle (NP) an a fluorescent poly(para–phenyleneethynylene) (PPE). The fluorescence of PPE was quenched with the NP via a non–covalent, electrostatic interactions. Upon addition of mammalian cells to the pre–quenched NP–PPE complexes, the competitive binding between NP–PPE complexes and cells was observed. The cationic NPs exhibited different affinities to dissimilar cell surfaces, which resulted in the selective displacement of PPE regenerating fluorescence alterations. This sensor array was able to distinguish between 4 different cancer types; MCF7, HeLa, NT2,and HepG, 3 different mammalian cell types; MCF10A,MCF7 and MDA–MB–231, and 3 different isogenic cell types; TD,V14, and CDBgeo. However, the discriminative power of the sensor decreased in complex training matrix containing 2 cancer; TD, MCF7, 2 normal; MF10A, CDBgeo and 2 metastatic; MDA–MB–231, V14 cell types with the same sensor. Same group was also developed an array based sensing system to discriminate four different human cancer cell lines; Hela, MCF7, HepG2, and NT2 and three isogenic cell lines; CDBgeo, TD, and V14 by using a combination of PPE derivatives. Although this sensor can clearly discriminate isogenic cell lines, the three of the four cancer cell lines were compressed in LDA plot.

In our study, we aimed to differentiate metastatic, cancer, and normal cells depending on the membrane surface features, by using differential affinity based approach as opposed to specific biomarker recognition. The PT–Pip–AuNP complexes showed different aggregation behaviors on the cell surfaces through both electrostatic, and hyrophobic interactions etc. between lipids, proteins, and polysaccharides on the cell surfaces, which enabled the ratiometric sensing of mammalian cells. Although the cell lines were not clustered as metastatic, cancerous, and normal cell lines by PCA, these cell lines were successfully clustered into seven non–overlapping groups in the

PCA plot. The combination of PT–Pip–AuNP sensor elements and the PCA method became a powerful non–targeted approach to provide a model for detection of cancer in clinical settings. This sensor, developed with a single PT and a single AuNP derivative, is comparable to its counterparts in the literature in terms of its power to discriminate different cell types.

3.3.5. Fluorescence Imaging of Cells

The interaction between PT–Pip–AuNP and cells, and PT–Pip localization in solution obtained after cell sensing experiments were investigated by fluorescence microscopy.

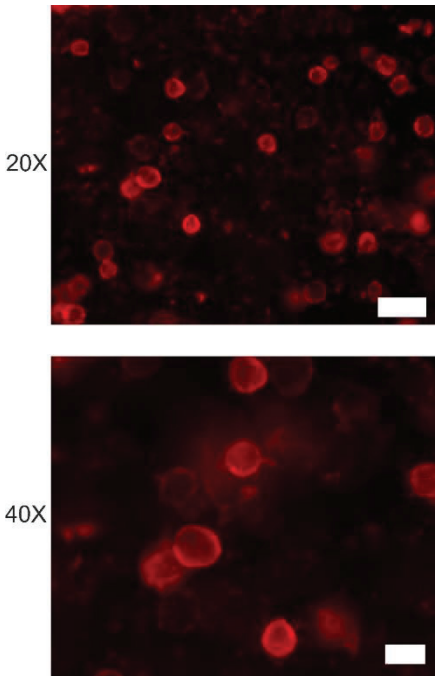

Figure 63. Cellular fluorescence imaging of PT–Pip–AuNP complex in HeLa cells suspended in 25 mM HEPES buffer. Scale bars of 20X and 40X magnifications are 50 μm and 20 μm, respectively

The distribution of PT–Pip–AuNP complex in 25 mM HEPES buffer was not homogeneous. Rather, the PT–Pip–AuNP complexes accumulated close to the HeLa cells in 25 mM HEPES buffer, as shown in Figure 63.

The fluorescence images of solution consisting of PT–Pip–AuNP complexes and cervical cancer cells (HeLa cells) and healthy mouse embryonic fibroblast cells (NIH/3T3 cells) (obtained from the cell–sensing assay) were compared to observe the

accumulation and localization of PT–Pip, as shown in Figure 64. and 65. These solution were examined after PFA fixation of cells and DAPI staining of nuclei of cells.

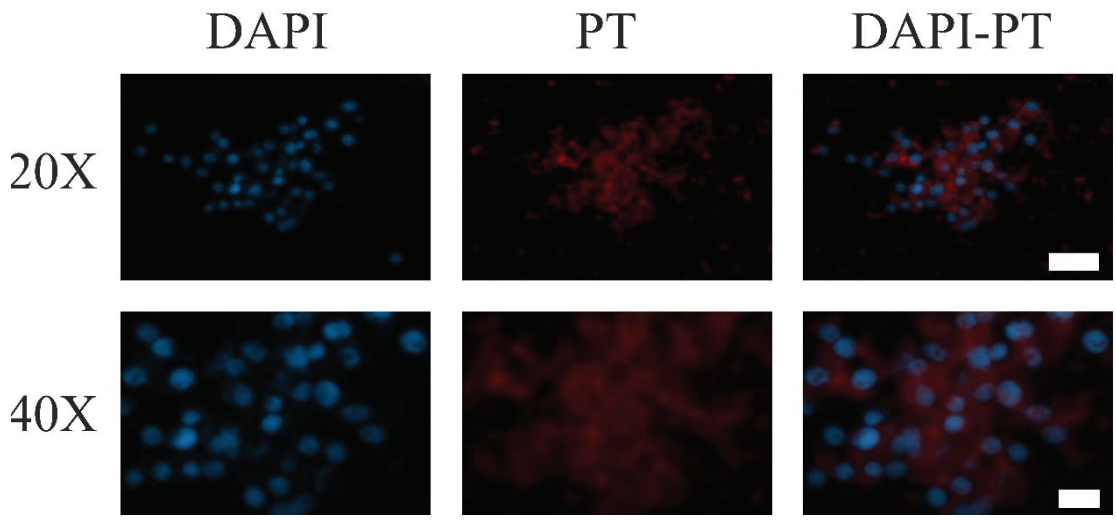

Figure 64. Fluorescence and merged images of NIH/3T3 cells using DAPI (1:1000 in 1X PBS) and PT–Pip as the cell fluorescence staining agents. Scale bars of 20X and 40X magnifications are 50 μm and 20 μm, respectively

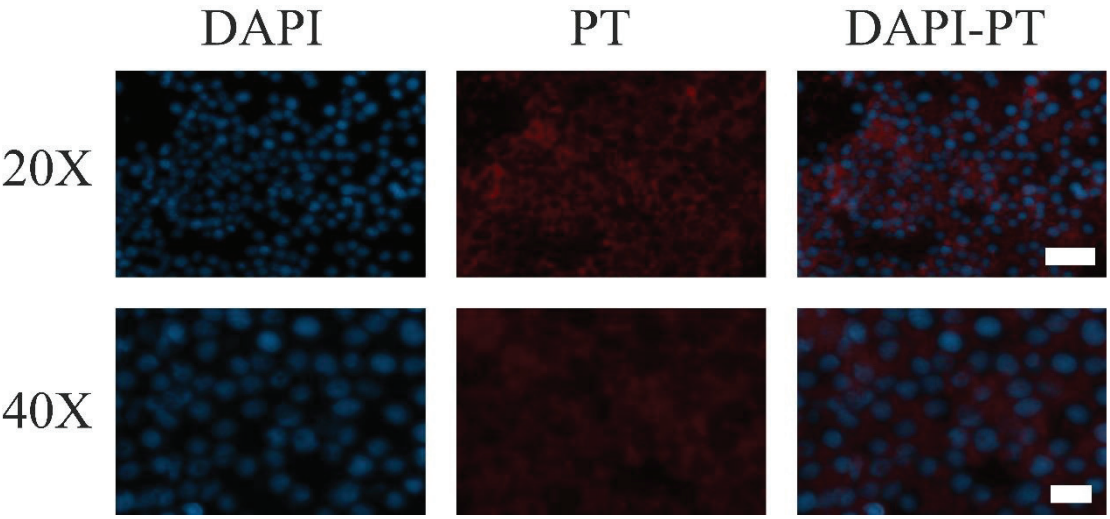

Figure 65. Fluorescence and merged images of HeLa cells using DAPI (1:1000 in 1X PBS) and PT–Pip as the cell fluorescence staining agents. Scale bars of 20X and 40X magnifications are 50 μm and 20 μm, respectively

In Figure 64. and 65, the left columns represent the nuclei of cells stained with DAPI dye. The middle columns display PT–Pip distribution in the sample, and the right columns are merged images of the previous two columns. As seen in the merged images of Figures 64. and 65, PT–Pip showed no diffuse signal in the nuclei of the treated cells. In contrast, signals for the polymer were located in the cytoplasm or perinuclear areas.

Similar patterns of signal distribution were observed for healthy cells and cancerous cells. Transportation of macromolecules between the cytoplasm and the nucleus was mediated by the nuclear pore complex (NPC), the size of which was between 5 nm and 10 nm.[133] The hydrodynamic radius of PT–Pip was reported to be approximately 13 nm in water solution (random coil conformation).[197] The nuclear pores of cancer cells were larger, and their nuclear membrane structures were different from those of healthy cells.[133] It is known from our group's study that PT–Pip can diffuse into the cancerous cell nucleus after 4–5 hours of incubation. As our experimental procedure did not include an incubation step, PT–Pip could not diffuse into the cell nucleus, and no significant difference was observed in the accumulation and localization of PT–Pip between cancer cells and healthy cells by fluorescence microscopy.

3.4. Indirect Sensing of Amino Acids

The objective of the study is to develop an efficient biosensor for amino acid detection and discrimination. Discrimination of amino acids by the non–covalent PT–Pip–AuNP complexes were aimed to achieved by the selective interaction between amino acid's distinct radical group and sensor elements. Initial optimization step was performed for the amino acid concentration.

3.4.1. Optimization of Amino Acid Concentrations

The solubility values of each amino acid in water at pH = 7 were found on the Sigma–Aldrich Company website. Amino acid solutions were prepared at their maximum solubility to observe the maximum fluorescence response for each amino acid. The fluorescence of PT–Pip was quenched by AuNPs; then, the pre–quenched PT–Pip–AuNP complex was treated with 20 amino acids individually. Fluorescence spectra are given in Figures 66–70.

Figure 66. illustrates the fluorescence responses of non-polar aliphatic amino acids against the sensor.

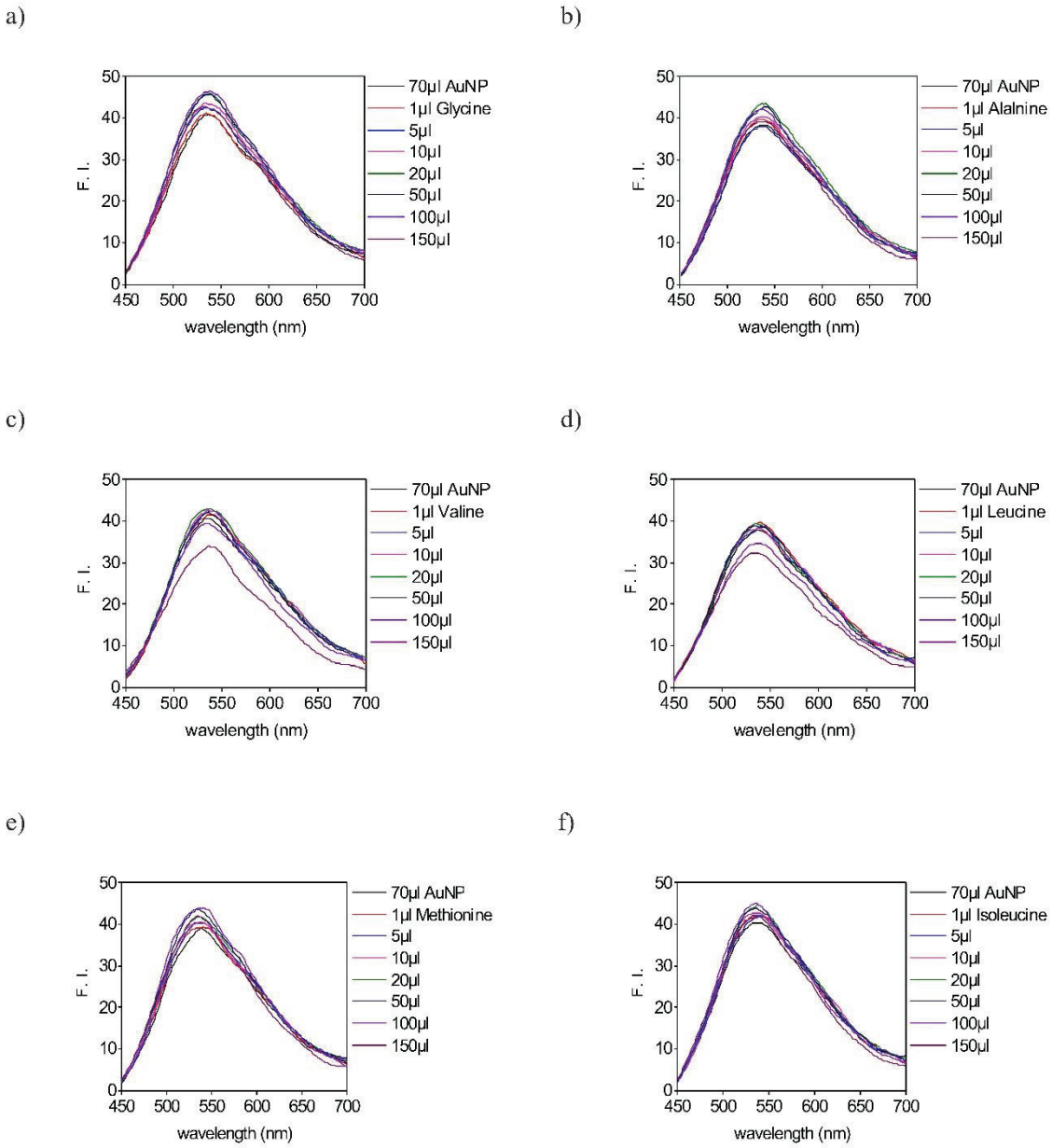

Figure 66. Fluorogenic response of nonpolar aliphatic amino acids: (a) glycine 3330 mM in MQ water, (b) L–alanine 1000.1 mM in MQ water, (c) L–valine 756 mM in MQ water, (d) L–leucine 175 mM in MQ water, (e) L–methionine 322 mM in MQ water, and (f) L–isoleucine 314 mM in MQ water

Figure 67. illustrates the fluorescence responses of polar uncharged amino acids against the sensor.

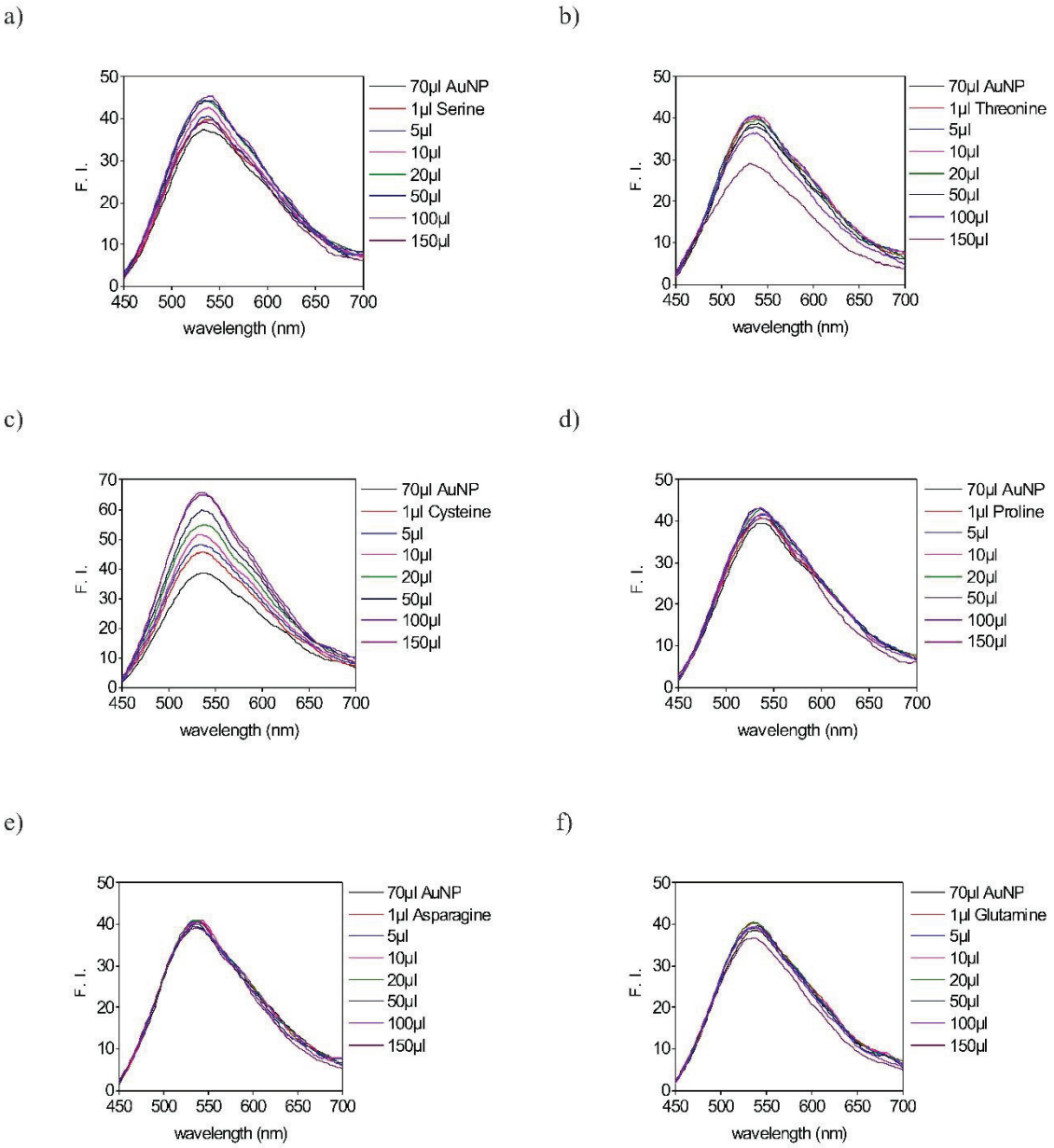

Figure 67. Fluorogenic response of polar uncharged amino acids: (a) L–serine 3.422 M in MQ water, (b) L–threonine 719 mM in MQ water, (c) L–cysteine 825 mM in MQ water, (d) L–proline 998 mM in MQ water, (e) L–asparagine 189 mM in MQ water, and (f) L–glutamine 102 mM in MQ water

Figure 68. illustrates the fluorescence responses of aromatic amino acids against the sensor.

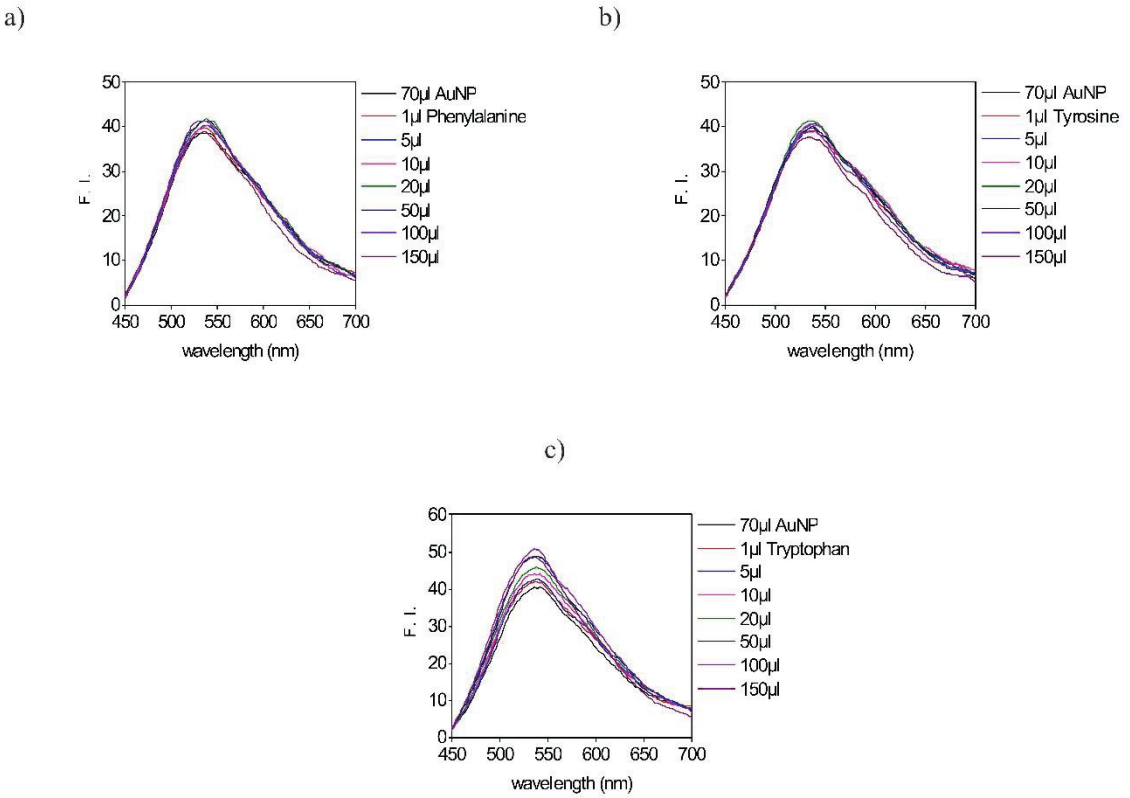

Figure 68. Fluorogenic response of aromatic amino acids: (a) L–phenylalanine 99.8 mM in MQ water, (b) L–tyrosine 2.6 mM in MQ water, and (c) L–tryptophan 56 mM in MQ water

Figure 69. illustrates the fluorescence responses of positively charged amino acids against the sensor.

a)

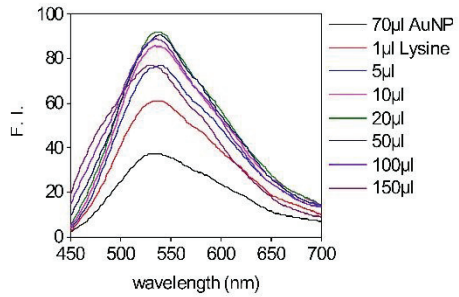

b)

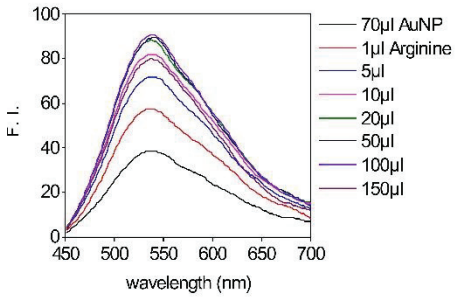

c)

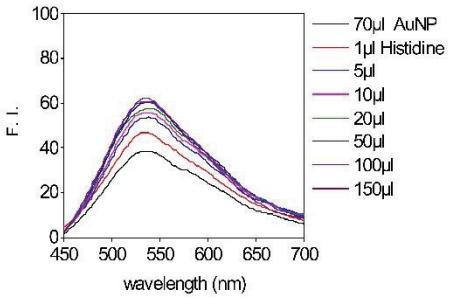

Figure 69. Fluorogenic response of basic amino acids: (a) L–lysine 2051 mM in MQ water, (b) L–arginine 1.045 M in MQ water, and (c) L–histidine 277 mM in MQ water

Figure 70. illustrates the fluorescence responses of negatively charged amino acids against the sensor.

a)

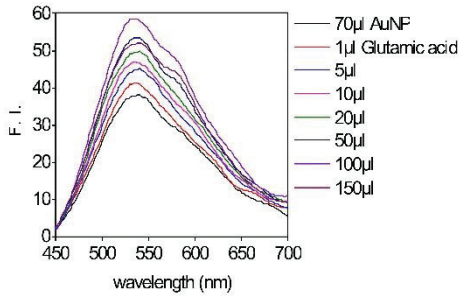

b)

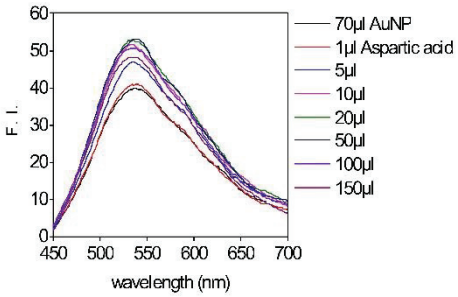

Figure 70. Fluorogenic responses of acidic amino acids: (a) L–glutamic acid 59 mM in MQ water, and (b) L–aspartic acid 32 mM in MQ water

The fluorescence response of each amino acid is given in Figure 71.

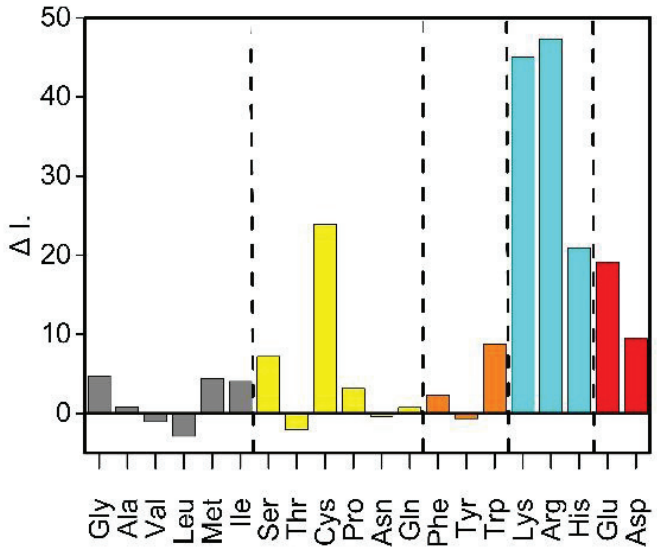

Figure 71. Fluorescence response pattern of 20 amino acids. 20 amino acid solutions were prepared at their maximum solubility in MQ water (pH = 7)

The fluorescence response patterns in Figure 71. were obtained by a fluorescence titration study of 20 amino acids. The Δ I. values were calculated by Equation 2. This preliminary study showed that especially basic and acidic amino acids interacted strongly with one of the sensor components and caused dissociation of the non–covalent PT–Pip-AuNP complex. This selective displacement of PT–Pip created a unique fluorogenic response for particular amino acids. Non–polar aliphatic amino acids did not significantly alter the fluorescence of PT–Pip. In polar uncharged amino acids, only L–cysteine enhanced the pre–quenched fluorescence of PT–Pip. Among aromatic amino acids, only L–tryptophan created an increment in the fluorescence intensity.

To sense the differences arising only from the chemical structure of amino acids, all amino acid solutions were prepared using water as the solvent at pH = 7 and pH = 9.8 with a concentration of 100 mM. The solubility of L–aspartic acid, L–glutamic acid, L–tyrosine, and L–tryptophan was below 100 mM in MQ water. Therefore, L–aspartic acid and L–glutamic acid could be prepared at 50 mM, L–tyrosine at 2.6 mM, and L–tryptophan at 76 mM. The PT–Pip–AuNP complex was then treated with these amino acids. Amino acid sensing experiments were repeated twice under identical conditions. The fluorescence responses of 20 amino acids under two pH parameters are given in Figure 72.

a)

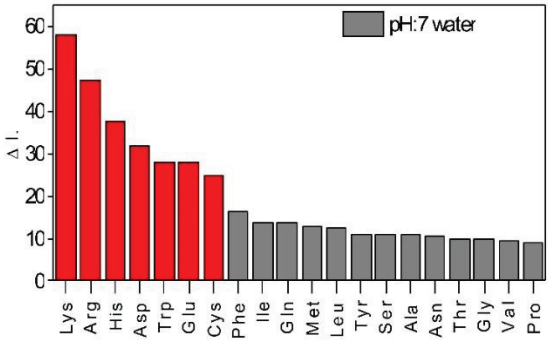

b)

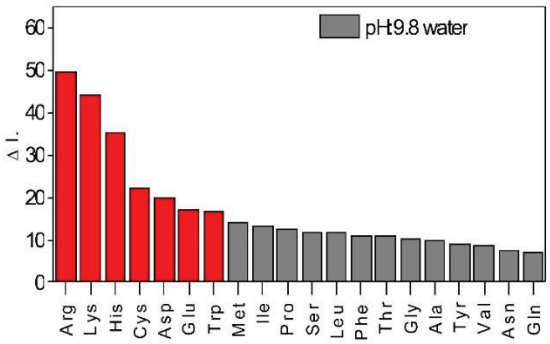

Figure 72. Fluorescence response patterns of 20 amino acids. (a) Fluorescence response patterns obtained in water (pH = 7); (b) fluorescence response patterns obtained in water (pH = 9.8)

The addition of 20 amino acids to the pre–quenched PT–Pip–AuNP complex created characteristic fluorescence alterations. Among the 20 proteinogenic amino acids, L–lysine, L–arginine, L–histidine, L–aspartic acid, L–glutamic acid, L–cysteine, and L–tryptophan significantly recovered the fluorescence of PT–Pip, as shown in Figure 72.

3.4.2. Indirect Sensing of Amino Acids

Amino acid (50mM) sensing experiments using MQ water at pH = 7 and pH = 9.8 as the solvent were performed three times. Results are illustrated in Figure 73.

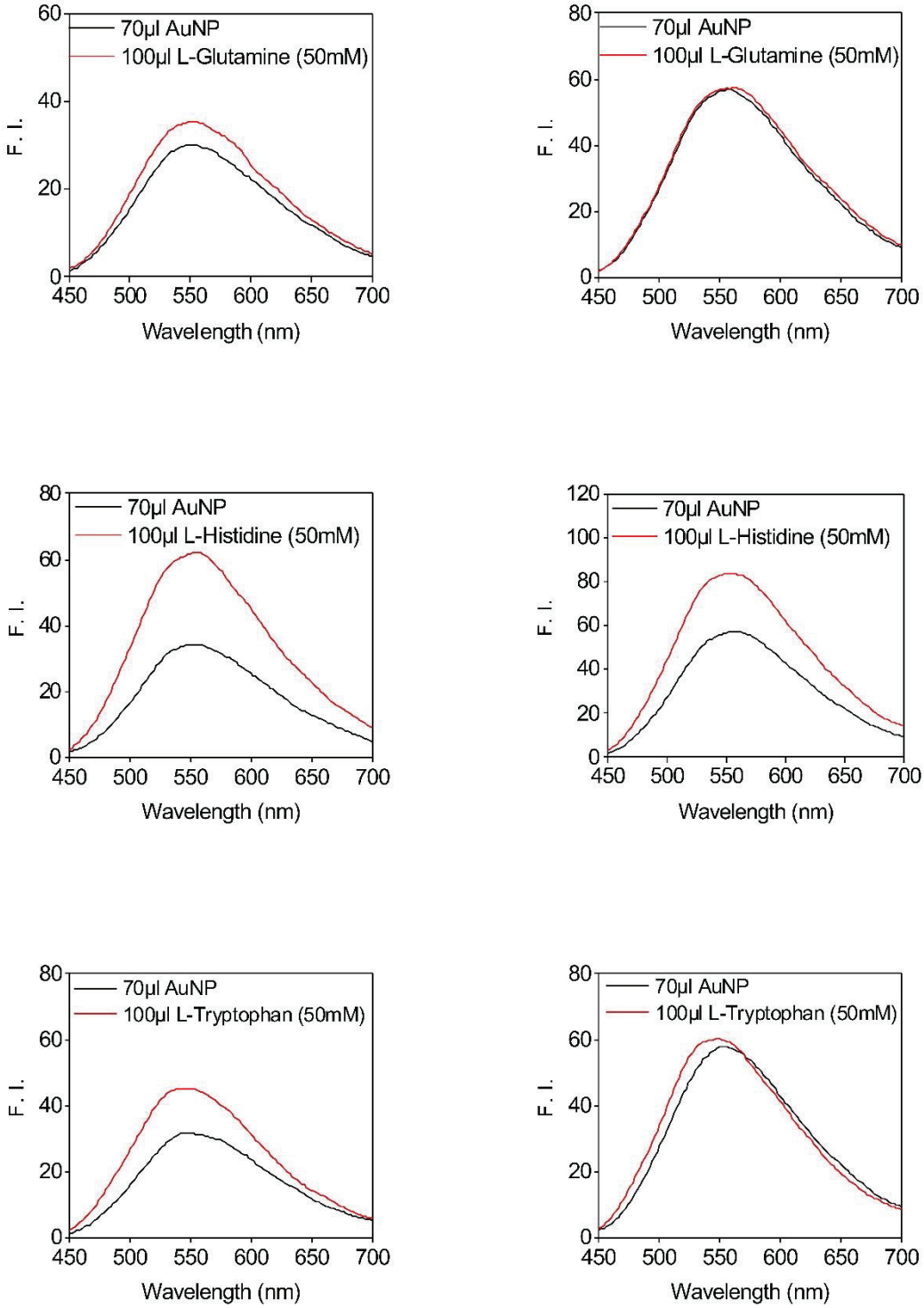

Figure 73. Fluorescence spectra of PT–Pip–AuNP complex titrated by 20 proteinogenic amino acids at 50 mM concentration except L–tyrosine (2.6 mM). The right– and left–side graphs represent the fluorescence spectra of PT–Pip at pH = 9.8 and pH = 7.0, respectively. (Cont. on the next pages.)

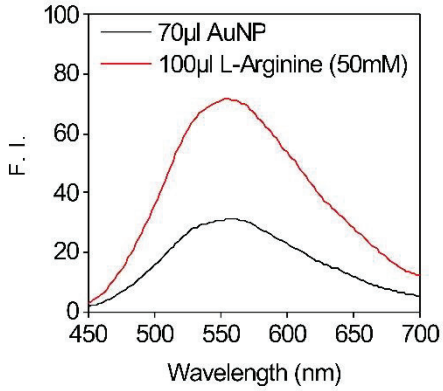

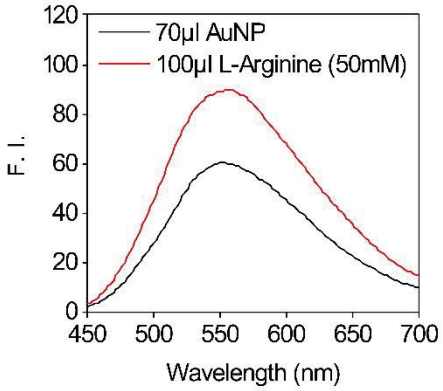

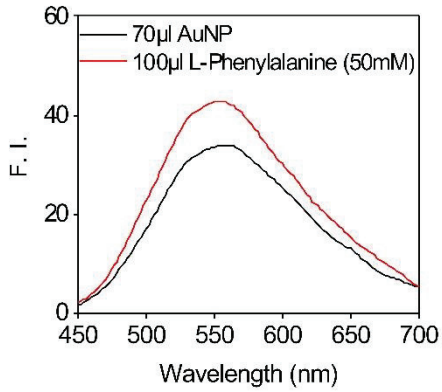

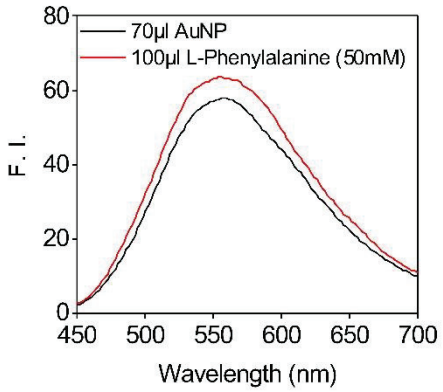

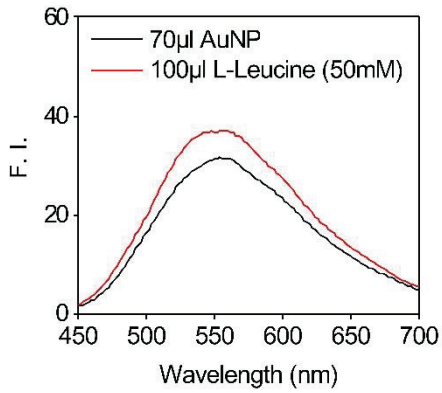

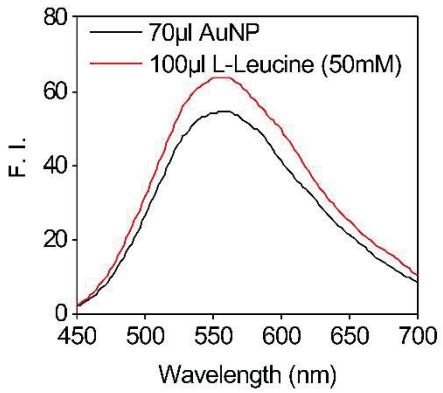

Figure 73. (Cont.)

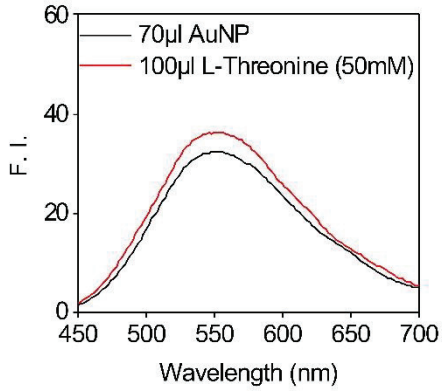

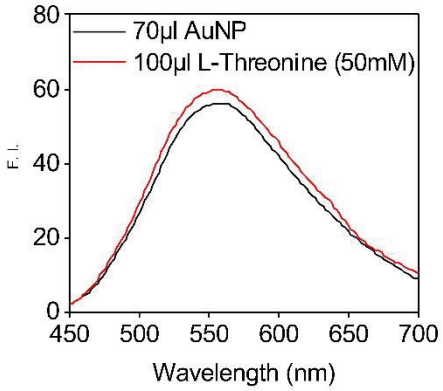

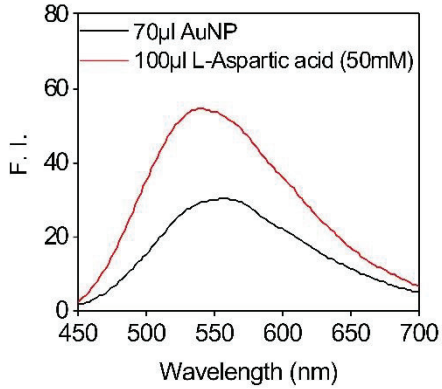

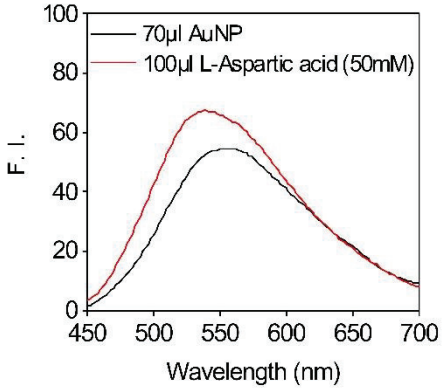

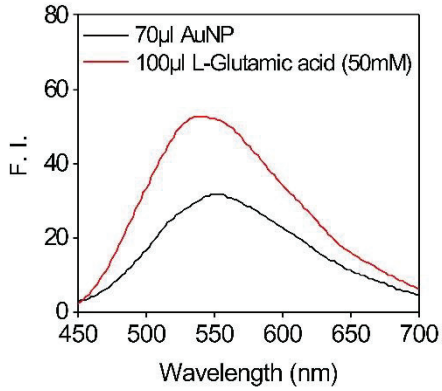

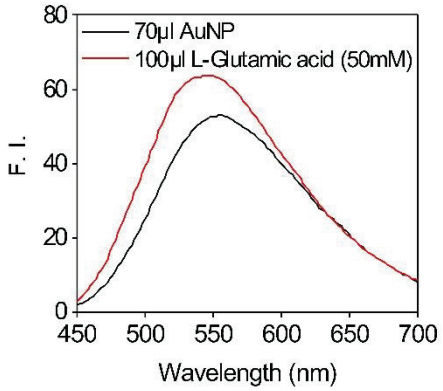

Figure 73. (Cont.)

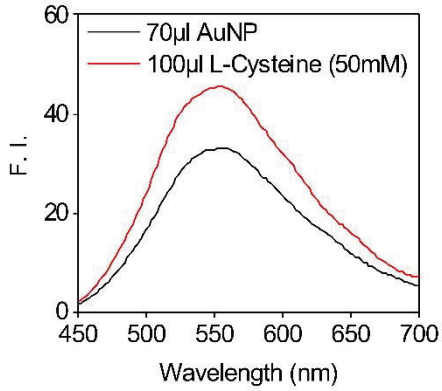

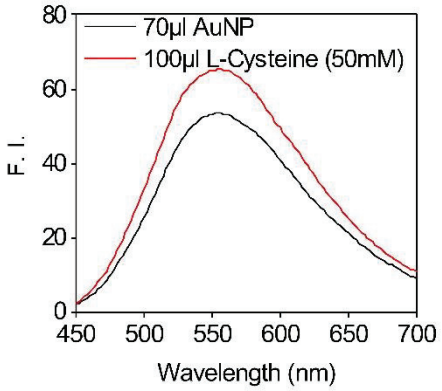

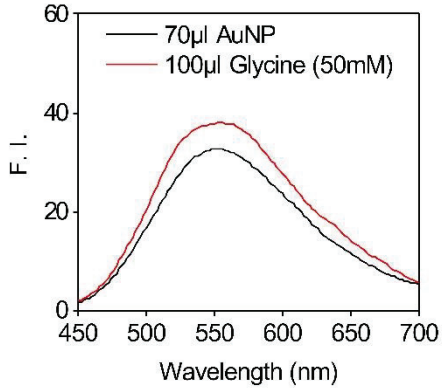

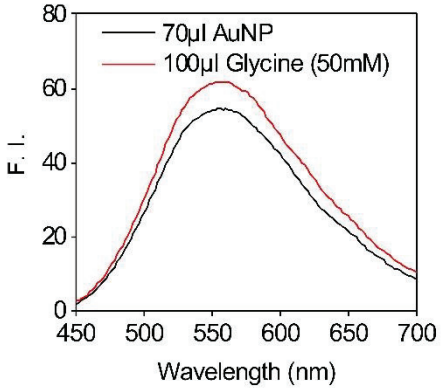

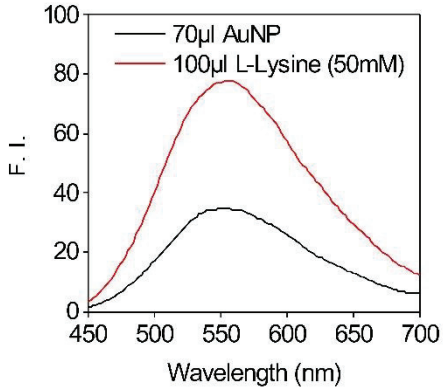

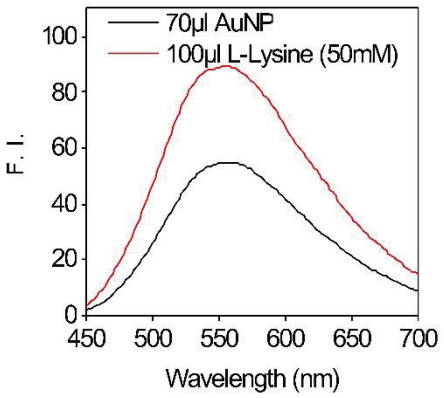

Figure 73. (Cont.)

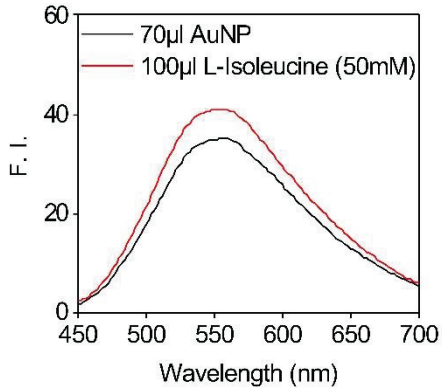

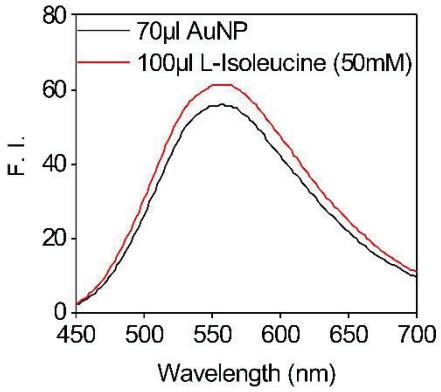

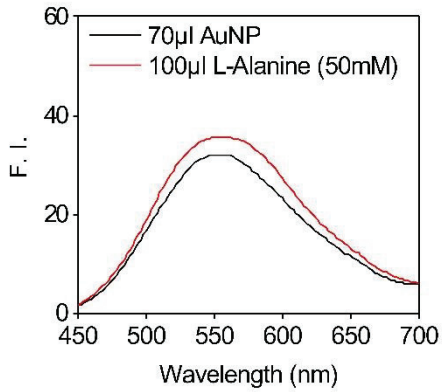

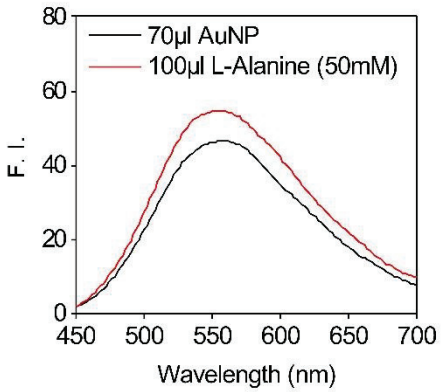

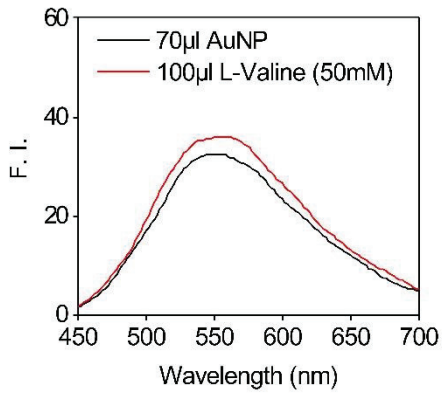

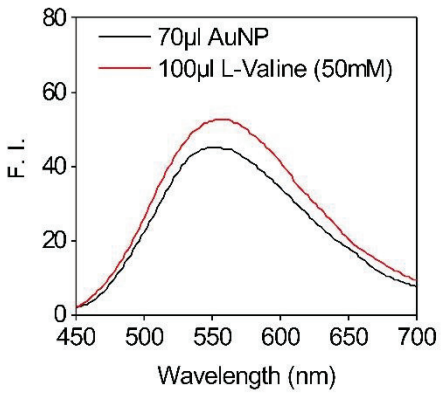

Figure 73. (Cont.)

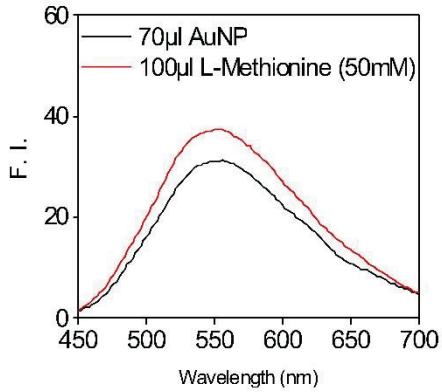

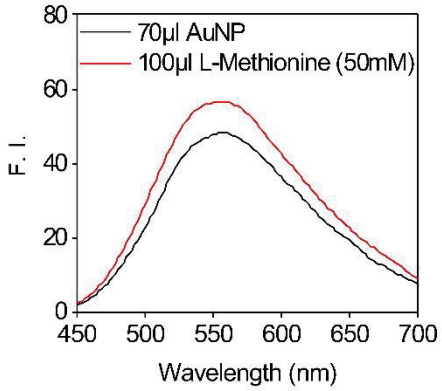

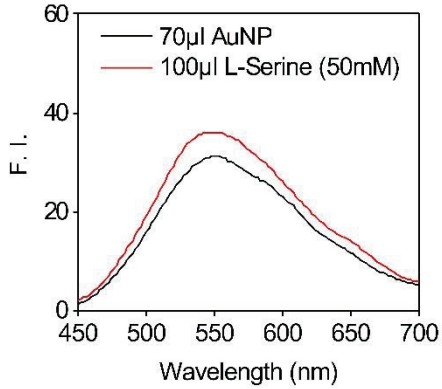

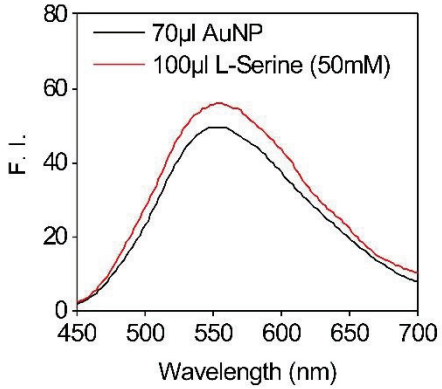

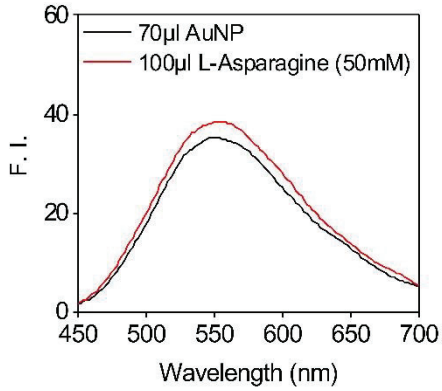

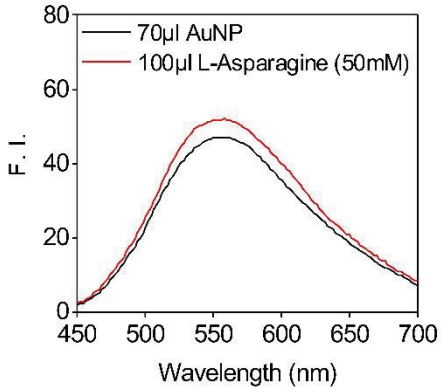

Figure 73. (Cont.)

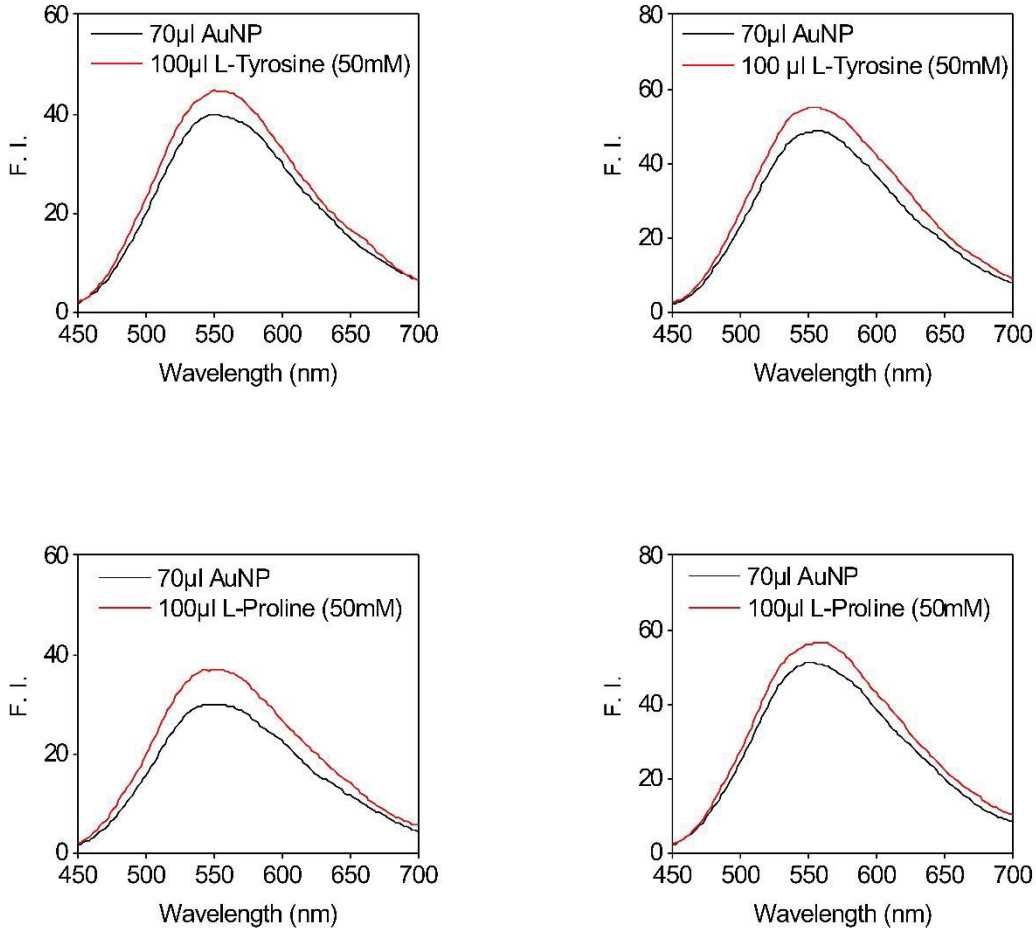

Figure 73. (Cont.)

Identical experiments were carried out using MQ water at pH = 6 and pH = 8.2 as well as TE buffer at pH = 6, pH = 7, pH = 8.2, and pH = 9.8. the fluorescence responses of 20 proteinogenic amino acids to a sensor array containing eight sensor elements are given in Figures 74. and 75.

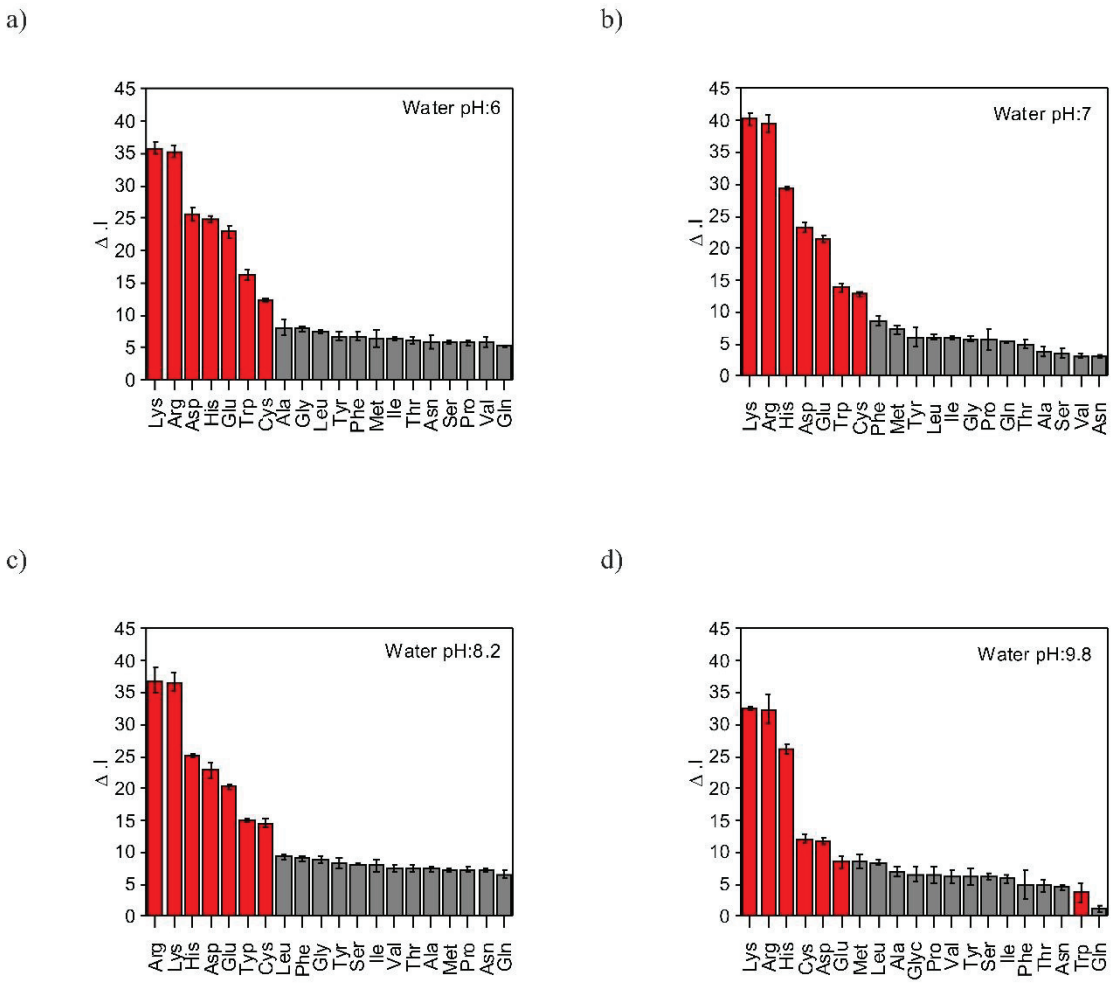

Figure 74. Fluorescence response patterns of 20 amino acids at 50 mM concentration in MQ water except L–tyrosine (2.6 mM). Each value is an average of three parallel measurements

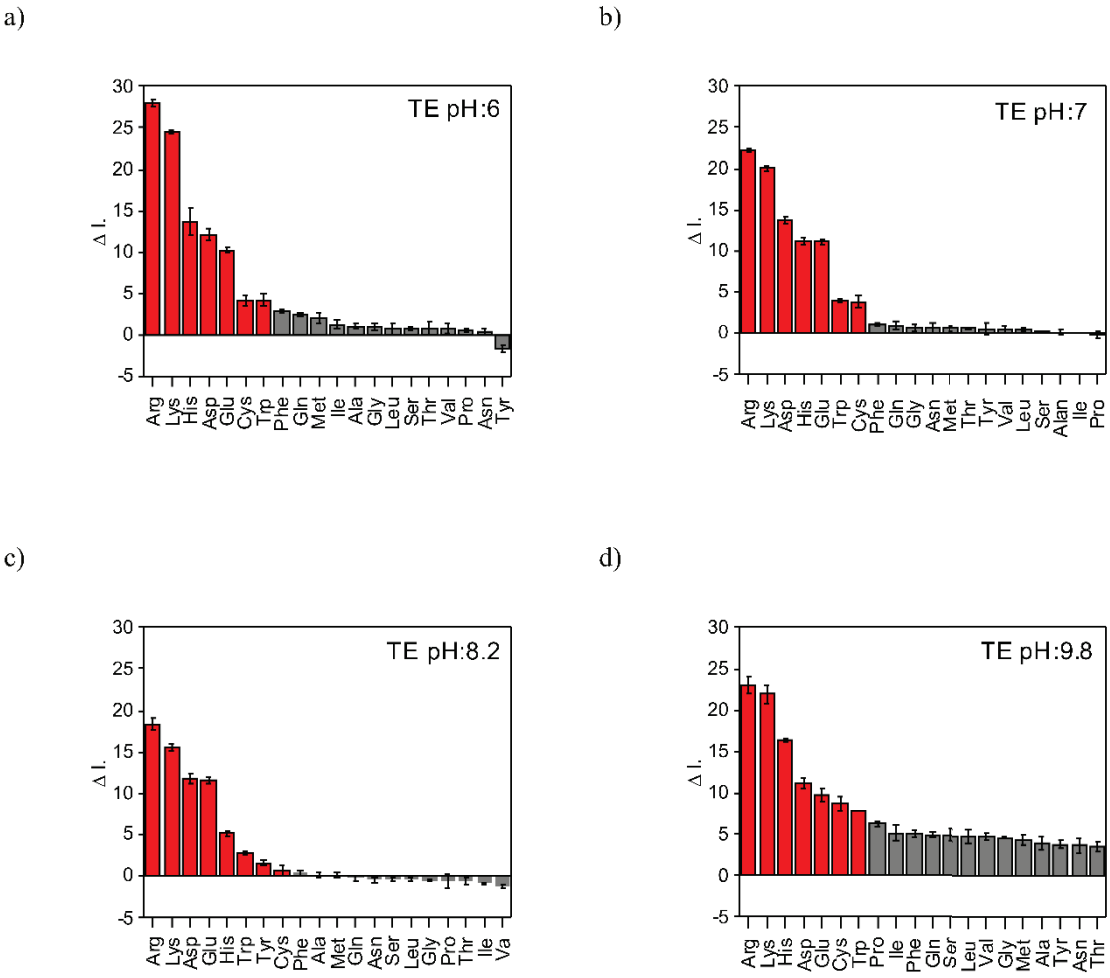

Figure 75. Fluorescence response patterns of 20 amino acids at 50 mM concentration in TE buffer except L–tyrosine (2.6 mM). Each value is an average of three parallel measurements

Amino acid sensing experiments were performed three times, each with water and TE buffer at pH = 6, pH = 7, pH = 8,2, and pH = 9.8. It was observed that particular amino acids such as L–lysine, L–arginine, L–histidine, L–aspartic acid, L–glutamic acid, L–tryptophan, and L–cysteine disrupted the coordination of the PT–Pip–AuNP complex and recovered the fluorescence of PT–Pip effectively.

3.4.3. Investigation of the Interaction between PT-Pip, AuNPs and 20 Amino Acids via Fluorescence and UV–visible Spectroscopy

This study aimed to evaluate the role of AuNPs in the amino acid sensing mechanism. The controlled experiments were carried out by introducing 20 amino acids to PT–Pip solutions (without AuNPs) in MQ water at pH = 7. The fluorescence spectra are given in Figure 76.

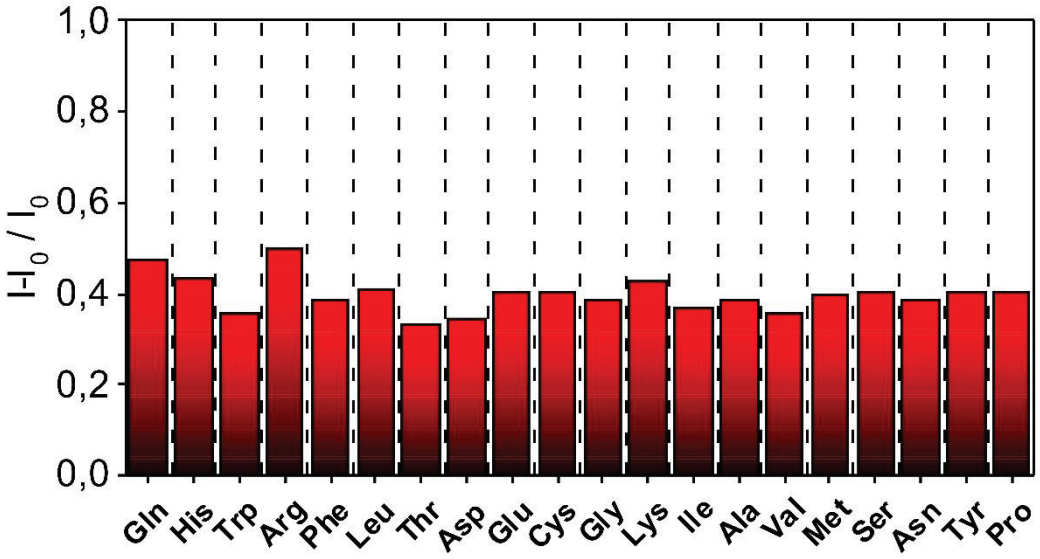

Figure 76. Fluorogenic response pattern of PT–Pip (467 μM (monomer–based)) at pH = 7, after treating with 20 proteinogenic amino acids

Fluorescence spectra displayed increasing fluorescence intensity upon addition of amino acids without showing selectivity to particular amino acids. The carboxyl groups of amino acids which interacted with the positively charged polymer side–chains reduced the interchain interaction of the polymer, thus increasing the solubility of PT–Pip in water and enhancing the fluorescence. The 20 amino acids increased the fluorescence intensity of PT–Pip at a similar rate, as shown in Figure 76. The results show that there were no selective interactions between the amino acids and PT–Pip. Functional groups of amino acids did not play a vital role on the interaction between PT–Pip and the amino acids.

Therefore, the selective fluorescence alteration observed in this sensor array originated from competitive binding between PT–Pip and amino acids to AuNPs. Thus,

the unique fluorescence alterations were caused by the interactions between amino acids and AuNPs.

Interactions between metals and amino acids are also known from biological systems. Amino acids are known to have special affinities for some metal ions, which play an essential role in metalloenzymes activities. For instance, Mn^{2+} in metalloenzymes has a significant affinity to L–aspartic and L–glutamic acids. Co^{2+} metal ions preferably bind to L–histidine, L–cysteine, L–aspartic acid, etc.[198]
The possible mechanism of interaction between amino acids and metal ions via chelation[199] (without taking side chains into account) is explained in Figure 77.

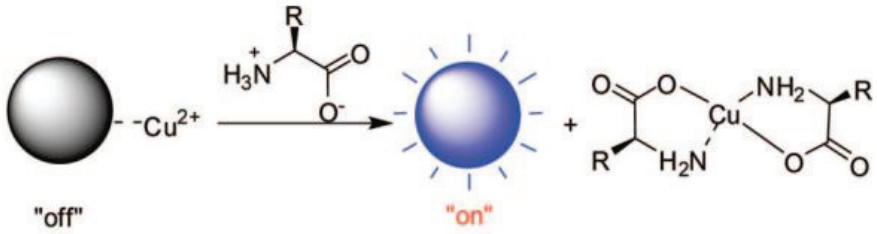

Figure 77. Complexation of amino acids and metal ions in fluorescence "turn–on" amino acid sensor.[200]

Guo et al. developed a fluorescence sensor for heavy metal ions, homocysteine (HCy), and glutathione (GSH) detection.[201] The fluorescence–based sensor was created by fluorescence quenching of PT derivative by Cu^{2+} metal ions. Subsequent addition of homocysteine and glutathione disrupted the PT–Cu^{2+} complex coordination by interacting with Cu^{2+}. The indirect sensing mechanism here, depending on the mediation of the metal ion, resulted in the formation of the Cu^{2+}–GSH and Cu^{2+}–HCy complexes. Therefore, this mechanism was demonstrated as an indirect "turn–on/off" sensor to probe for these two amino acids. Similarly, Liu et al. also utilized a similar sensing mechanism depending on indirect sensing of L–cysteine.[202] Negatively charged AuNPs quenched the fluorescence of cationic polymer (PDPMT–Cl). The addition of L–cysteine to the polymer–AuNP complex disrupted this coordination via L–cysteine–AuNP interaction. Therefore, selective displacement of PDPMT–Cl resulted in fluorescence recovery. L–cysteine detection was achieved with an LoD of 1.39×10^{-10} M.

In our study, some amino acids might snatch the AuNPs from the PT–Pip and give rise to an indirect sensing approach by releasing PT–Pip into the solution phase. To

investigate the interaction between AuNP and the 20 amino acids in detail, AuNP solution (pH = 7) was titrated by the 20 amino acids individually. Figure 78. represents the absorbance spectra of AuNPs titrated by the 20 amino acids.

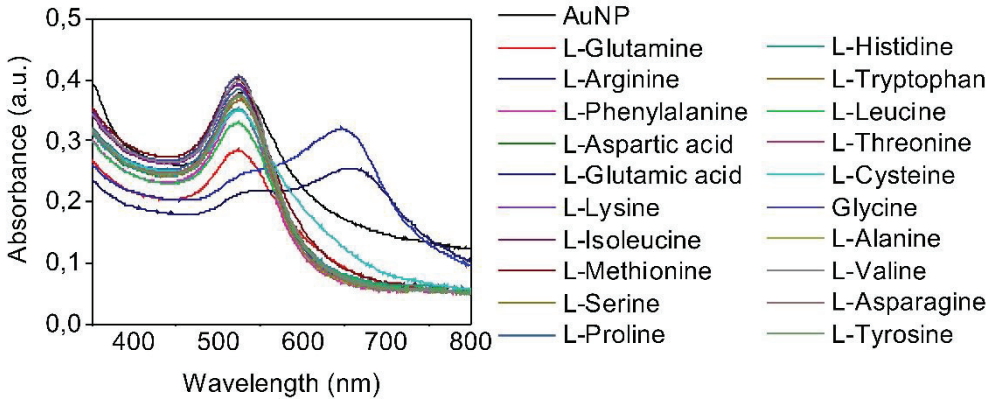

Figure 78. UV–visible spectra of AuNPs (0.15 µl) titrated by 20 amino acids (50 mM)

Among the 20 amino acids, the absorbance spectra of two different amino acids (L–glutamic acid and L–arginine) indicated strong interaction with AuNPs. Moreover, the color of the AuNP solution changed from reddish to blue upon the addition of L–glutamic acid and L–arginine, as shown in Figure 79. The absorbance spectra of these two amino acids indicated that AuNP aggregation occurred due to AuNP–amino acid complexation. Moreover, the addition of L–cysteine increased the absorbance intensity without shifting the absorbance maximum of AuNP. It increased the color density of the AuNP–L–cysteine solution as well, which indicated that L–cysteine interacted with AuNPs without inducing aggregation.

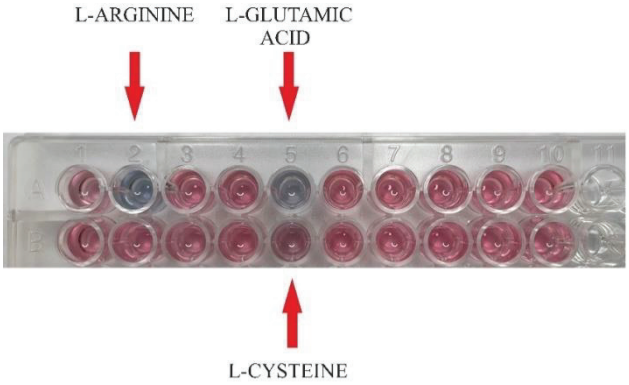

Figure 79. Photograph of L–arginine, L–glutamic acid, and L–cysteine induced color changes of AuNPs

Two approaches have been proposed to understand the interaction between AuNPs and amino acids. The first approach indicates that amino acids partially replace the citrate capping on AuNPs, and the zwitterionic heads of neighboring amino acids interact and generate amino acid clusters on the AuNP surface. Inducing electronic dipoles through AuNPs gives rise to the formation of AuNP aggregates. The second approach indicates that some amino acids interact explicitly with the surface of AuNPs by radical chains. Hydrogen bonds between these amino acids on the adjacent AuNPs resulted in the aggregation of AuNPs.[203]

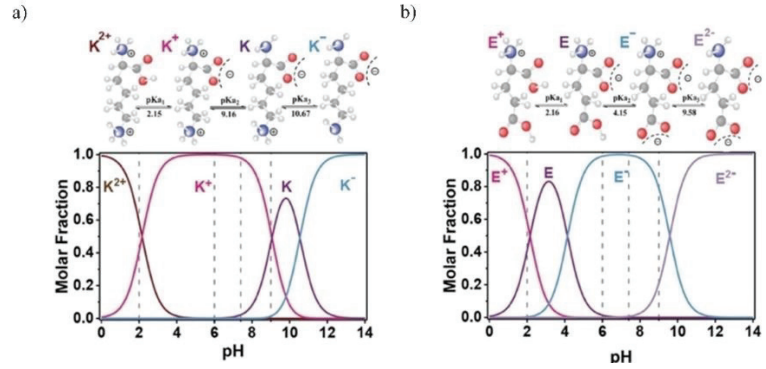

Figure 80. Ionization steps of some amino acids, such as (a) L–glutamic acid, and (b) L–lysine, as a function of pH.[204]

Based on the amino acid dissociation graphs given in Figure 80, the pKa values of the carboxyl, amino, and radical groups and the net charge of amino acids at different pH values could be predicted.

The pKa of the α–carboxyl group of L–arginine was 2.17, the pKa of the α–amino group was 9.04, and the pKa of the side chain was 12.48. At pH = 7, the +1 charged form of the amino acid was concentrated.[205] The addition of L–arginine to the AuNP solution led to the formation of a new shoulder at 647 nm. This broad peak at a longer wavelength indicated increased particle size and anisotropic optical properties induced by L–arginine adsorption. Moreover, this broad new peak was consistent with the nanoparticle aggregation. The interparticle distance AuNPs became lower than the average particle size, and coupling of the SPR of two neighboring AuNPs occurred.[205]

The interaction between L–arginine and AuNPs occurred as a result of anchoring the positively charged guanidinium group of L–arginine on the negatively charged AuNPs. The amino and carboxyl groups of L–arginine, which were left free, induced

electrostatic interaction between neighboring amino acids on AuNPs, making stable aggregates.[205] The red–to–blue color change of the AuNP solution resulted from the bathochromic shift of the absorption peak. Figure 81. illustrates the interactions between L–arginine and AuNP.

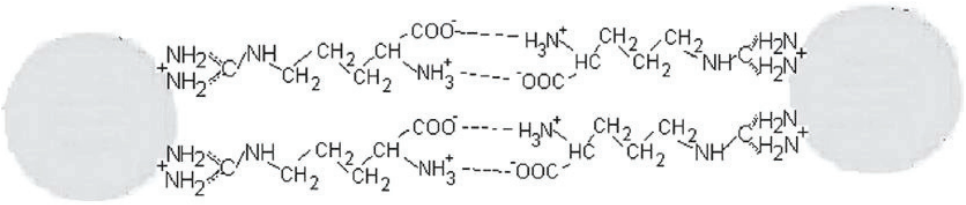

Figure 81. Possible interactions of L–arginine and AuNPs.[205]

The pKa of the side chain of L–glutamic acid was 4.25, the pKa of the α–amino group was 9.67, and the pKa of the α–carboxyl group was 2.19. The L–glutamic acid was mainly –1 charged at pH = 7.[204] L–glutamic acid caused aggregation of AuNPs, as shown in Figure 78. The concentration of L–glutamic acid was crucial for AuNP aggregation. While 1 mM L–glutamic acid was utilized to functionalize and stabilize the AuNPs by interacting with AuNPs via the NH^{3+} group[206], higher concentrations of L–glutamic acid (10 mM to 20 mM) caused aggregation of AuNPs.[203] In our study, the final concentration of L–glutamic acid was 29.4 mM. It was an expected result that such a high concentration led to AuNP aggregation.

L–aspartic acid, which is structurally very similar to L–glutamic acid, is known to utilize AuNP synthesis. L–aspartic acid bonds with nanoparticle surfaces and stabilizes by reducing chloroaurate ions. L–aspartic acid creates no difference in the SPR peak of AuNPs. Nevertheless, in our study, L–aspartic and L–glutamic acid interacted with AuNPs and disrupted the PT–Pip–AuNP complexation in amino acid sensing experiments.

Guan et al. developed a sensor explaining the interaction between acidic amino acids and AuNP.[147] After fluorescence quenching of cationic PT derivative by AuNPs, 20 amino acids were introduced to polymer–nanoparticle complexes. L–aspartic acid and L–glutamic acid gave out one more H^+ in an aqueous solution compared to other amino acids. Competitive electrostatic interaction between the cationic PT derivative and H^+ ions occurred. H^+ ions were more prone to combining with AuNPs compared to

PT. PT derivative was released into the solution phase and emitted light.[147] These groups explained a possible fluorescence recovery mechanism schematically represented in Figure 82.

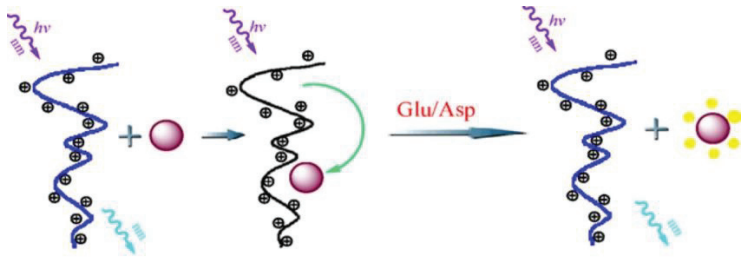

Figure 82. Schematic representation of fluorescence ‘‘turn–on’’ mechanism induced by L–aspartic and L–glutamic acids.[147]

In contrast to L–arginine and L–glutamic acid, L–lysine, L–histidine, L–aspartic acid, L–tryptophan, and L–cysteine, which disrupted the PT–Pip–AuNP complex and increased fluorescence intensity, did not change the absorbance of AuNPs. In the literature, studies indicate that besides L–arginine and L–glutamic acid, other amino acids could induce AuNP aggregation as well. Still, some amino acids require higher concentrations than others to induce aggregation of AuNPs.

The absence of any change in the absorbance spectra of AuNPs with the addition of amino acids did not in itself prove that there was no interaction between AuNPs and amino acids. Amino acids that did not alter the SPR peak of AuNPs might be adsorbed on the AuNP surface and make AuNP more stable. However, Doyen et al. indicated that amino acids that did not cause any change in the absorbance of AuNPs and did not cause any difference in the zeta potential of AuNPs were indeed not interacting with AuNPs.[203]

The 13 amino acids that were zwitterionic molecules in physiological pH were settled by the $–NH_3^+$ group on the AuNP surface, while their –COO group made a negative surface charge of the AuNPs. These relatively weaker interactions also led to fluorescence enhancement, but not as much as the others.

Three amine–containing amino acids created significant fluorescence enhancement in this sensor array. These strong interactions could be explained electrostatically. When the amino groups in L–lysine (ε–amine group) and L–arginine were converted to ammonium, it was adsorbed on the AuNP surface by electrostatic

interaction.[207] The possible binding mechanisms of L–arginine and L–lysine to citrate–capped AuNPs are given in Figure 81. and 83, respectively.

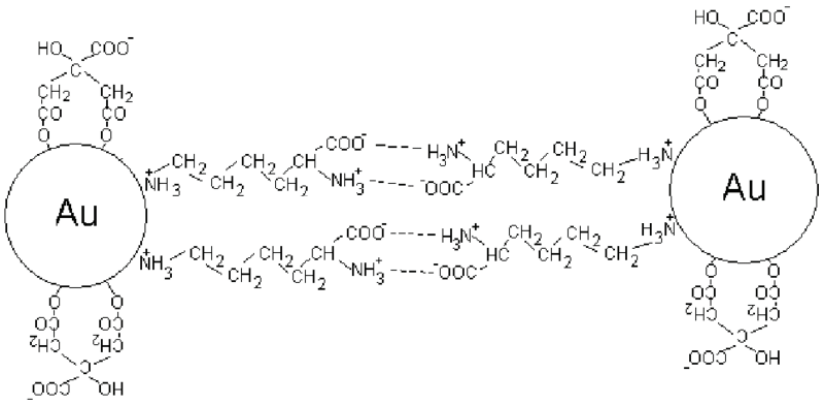

Figure 83. Schematic representation of interaction between L–lysine and citrate–capped AuNPs.[208]

At the pH values used in this sensor, the amino group in the side chains of L–lysine and L–arginine were mainly positively charged. Also, at pH = 9.74, which was very close to the pI of the amino acid L–lysine, the amino group in the side chain was still in the form of ammonium. As a result, the L–lysine and L–arginine side chains had a strong affinity to negatively charged AuNP via their positively charged ammonium groups. They disrupted the PT–Pip-AuNP complexation and enhanced fluorescence of PT–Pip.

L–histidine, the third basic amino acid, has two nitrogen atoms in its side chain, which have a weaker affinity (compared to L–arginine and L–lysine) for an H^+ ion because L–histidine has a lower charge density. Some of the L–histidine in the solutions was positive at a neutral pH. Therefore, the weaker basic character of L–histidine reduced the affinity of L–histidine to AuNPs. It resulted in a weaker interaction between AuNPs and L–histidine. However, L–histidine still significantly increased the fluorescence of PT–Pip compared to other amino acids due to its basic character. This fluorescence enhancement was less than that of L–arginine and L–lysine but more than that of many other amino acids. The addition of L–tryptophan, a fluorescence amino acid[209], also increased the fluorescence of PT–Pip in water at pH = 6, pH = 7, and pH = 8.2. The indole group of L–tryptophan contains secondary amine, which interacted with the gold surface besides the primary amine group. Still, it is known from the literature that the primary interaction occurred via an α–amino group.[210] L–tryptophan required a positively charged α–amino group to interact with negatively charged AuNPs. At pH =

9.8, the fluorescence enhancement could not be observed, as the α–amino group of all L–tryptophan is not completely positively charged in water at pH = 9.8. Although PT–Pip–AuNP coordination was disrupted and PT–Pip was released into the solution phase at pH = 6, pH = 7, and pH = 8.2, this interaction was weaker than the interaction created by the amine group in the side chain of basic amino acids. The fluorescence thus increased with the addition of L–tryptophan, albeit less than with the basic amino acids.

Investigation of the fluorescence and UV–visible spectra during titration of PT–Pip–AuNP complex by 20 amino acids at pH = 7 was carried out simultaneously. Initially, the fluorescence of PT–Pip was quenched by AuNPs. Afterward, amino acid solutions were added to the PT–Pip–AuNP complex. The fluorescence and UV–visible spectra are given in Figure 84.

a)

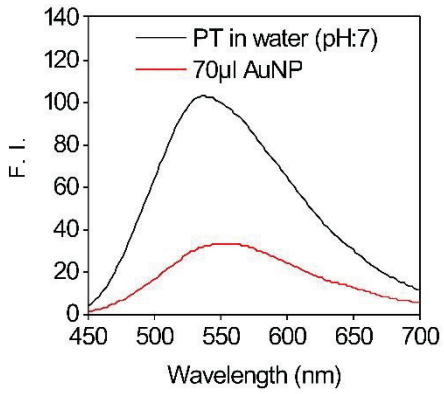

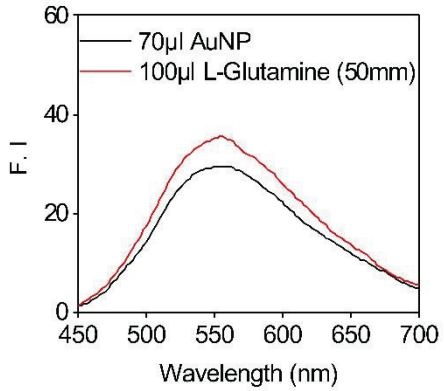

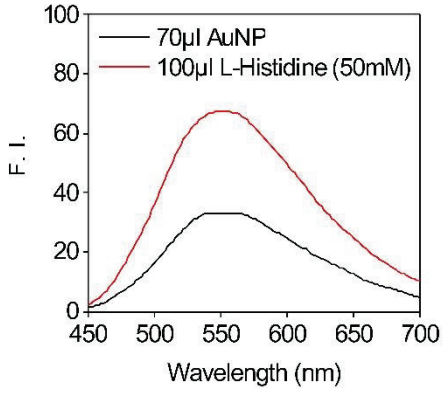

b)

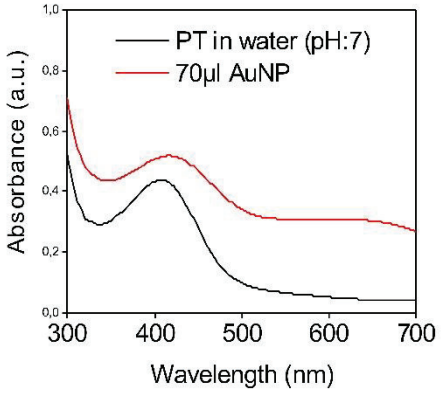

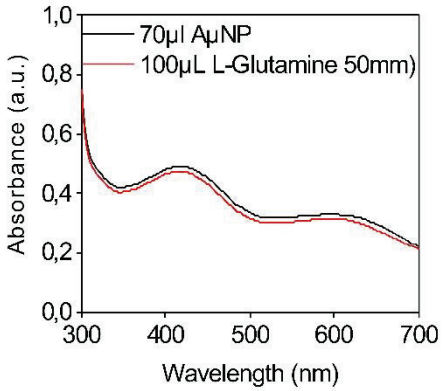

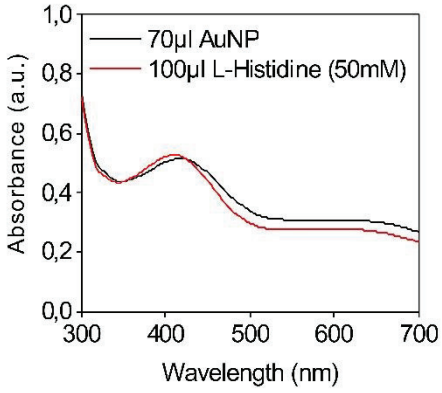

Figure 84. Investigation of simultaneous changes of fluorescence and UV–visible spectra of PT–Pip–AuNP complex upon addition of 20 proteinogenic amino acids: (a) fluorescence and (b) UV–visible spectra of amino acid sensing experiments at pH = 7 (water). (Cont. on the next pages.)

a)

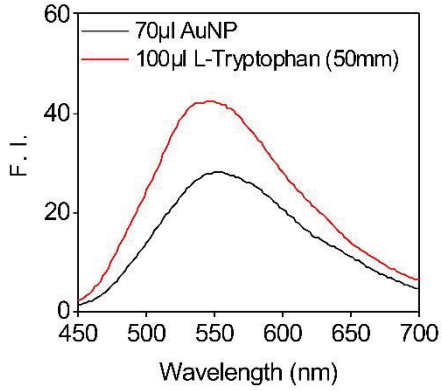

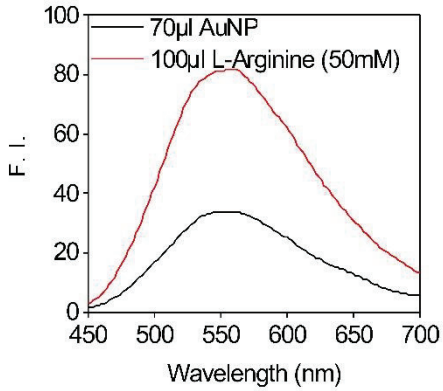

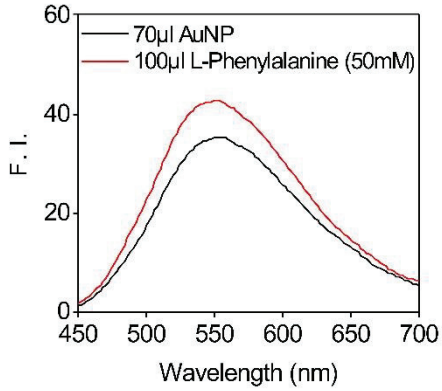

b)

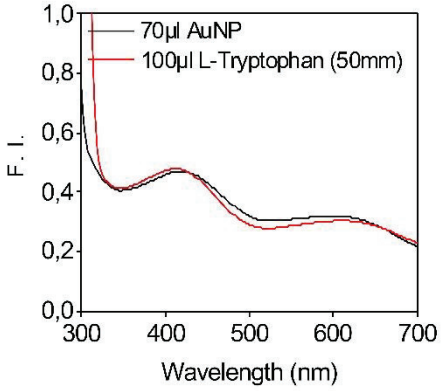

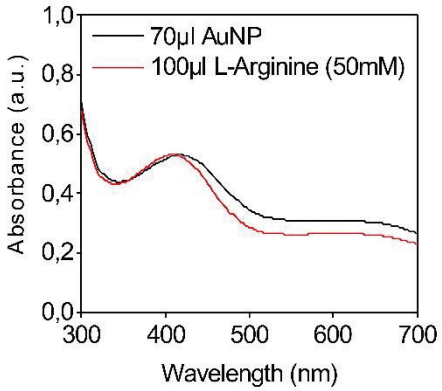

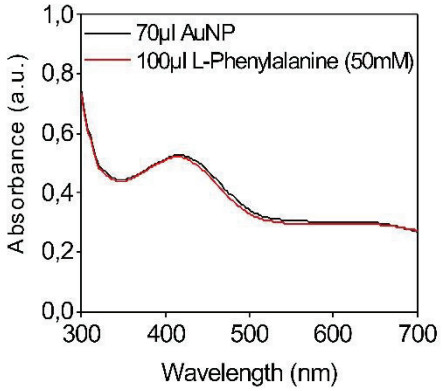

Figure 84. (Cont.)

a)

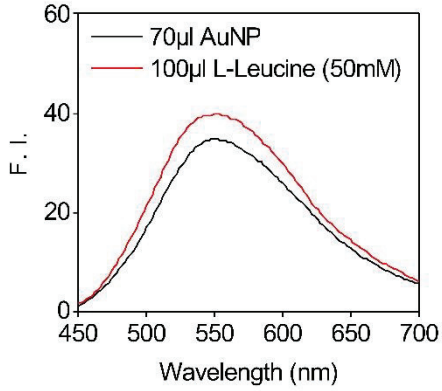

b)

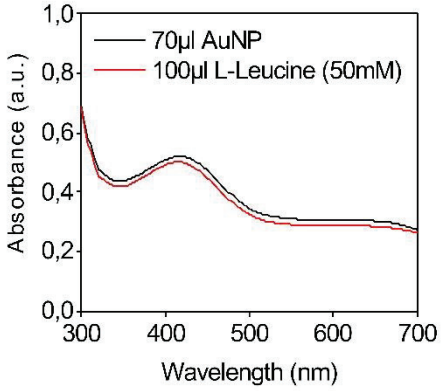

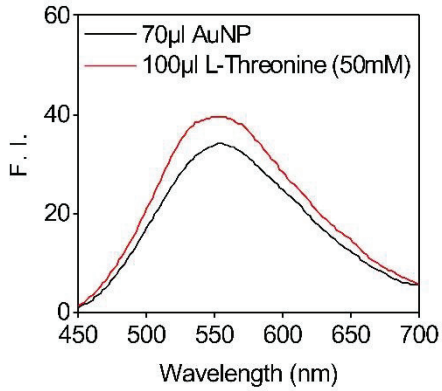

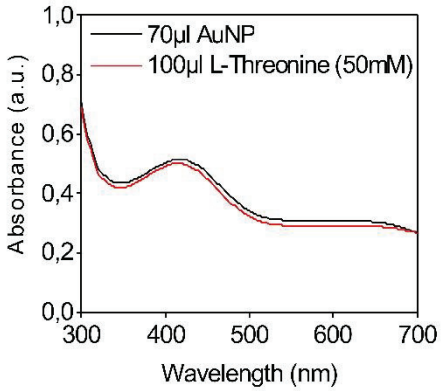

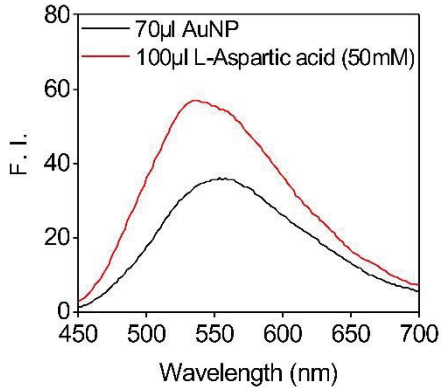

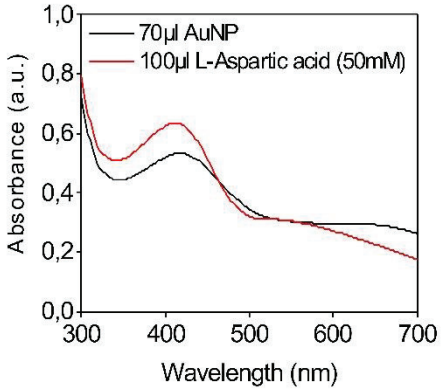

Figure 84. (Cont.)

a)

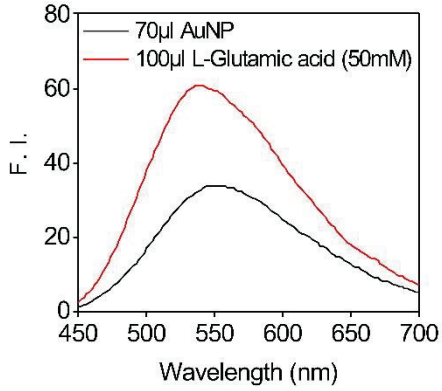

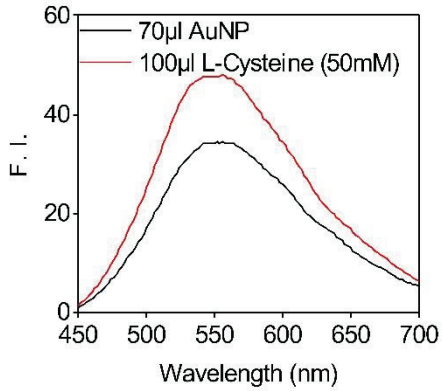

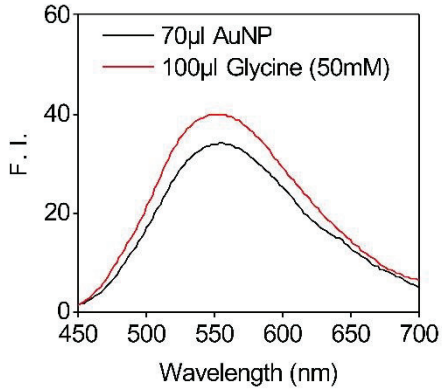

b)

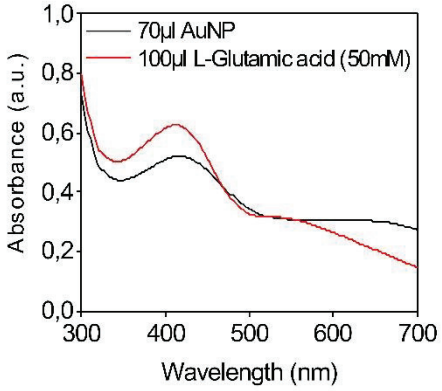

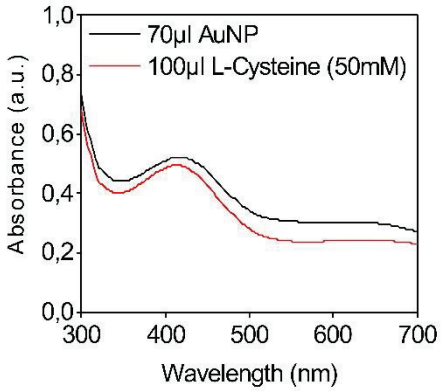

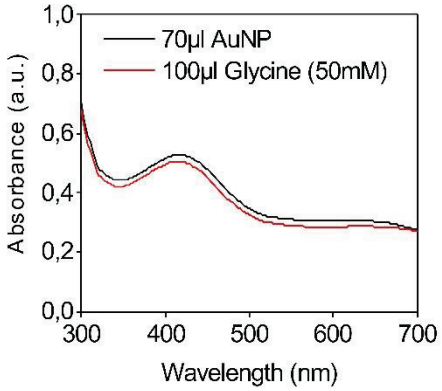

Figure 84. (Cont.)

a)

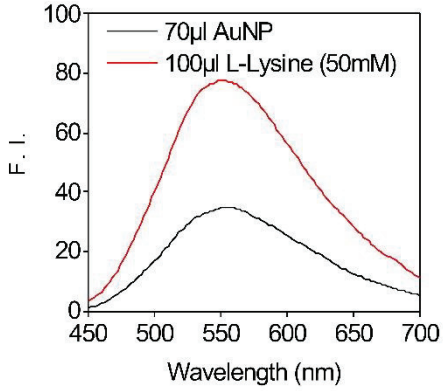

b)

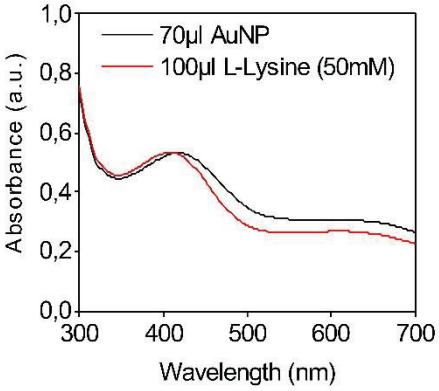

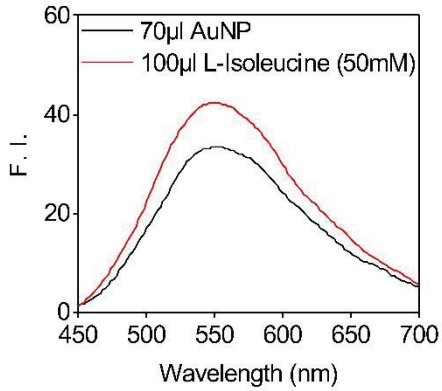

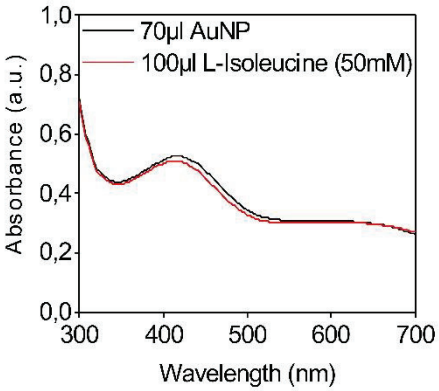

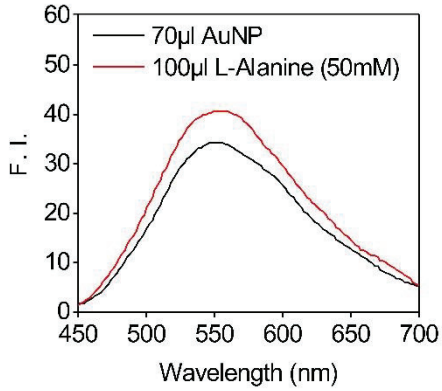

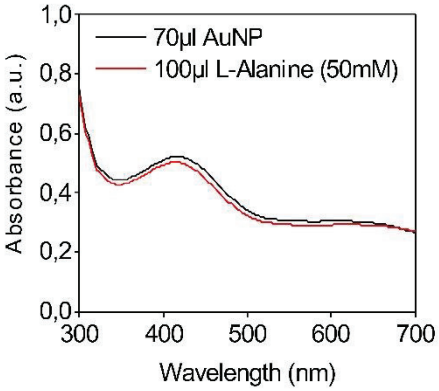

Figure 84. (Cont.)

a)

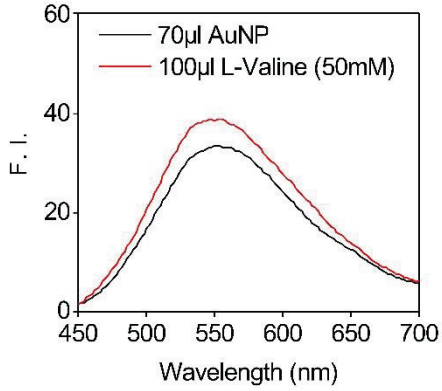

b)

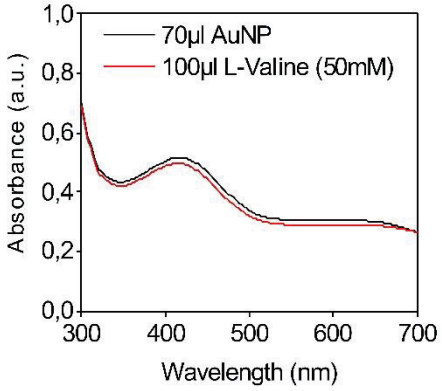

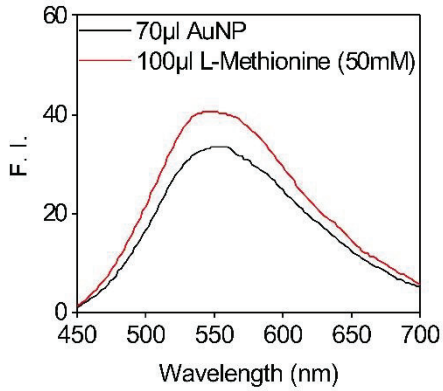

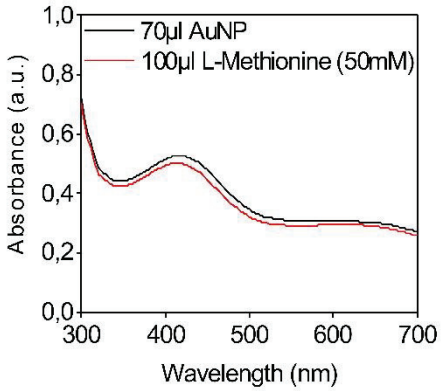

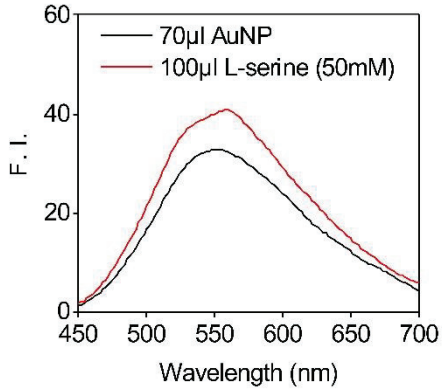

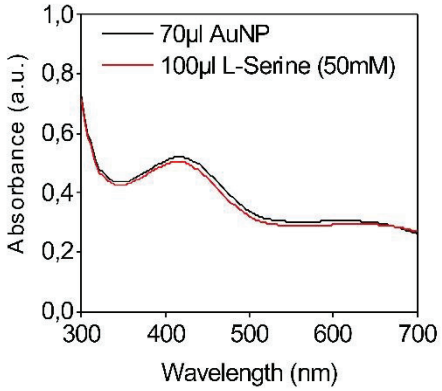

Figure 84. (Cont.)

a)

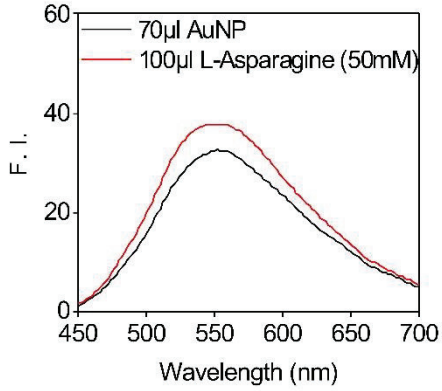

b)

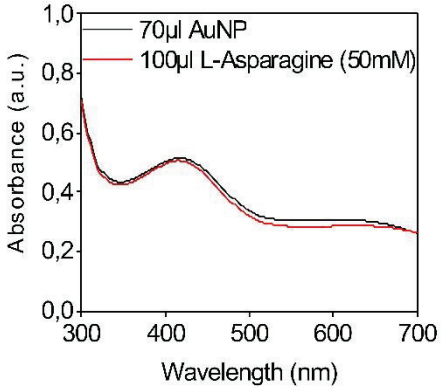

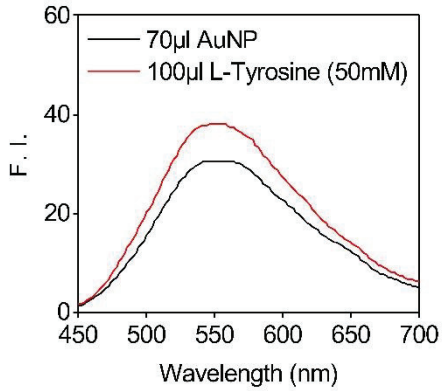

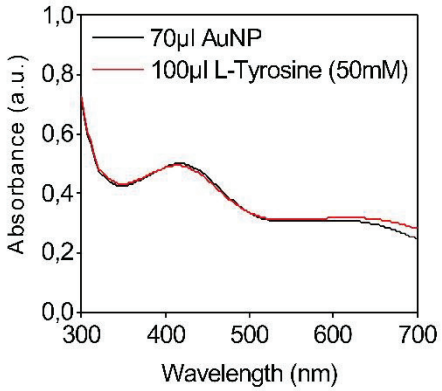

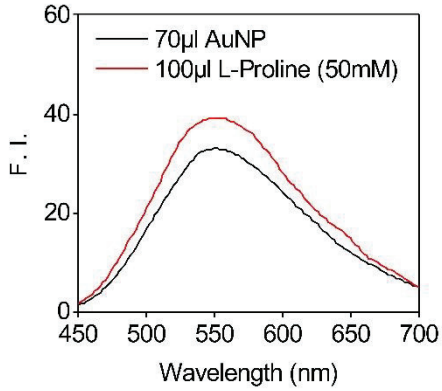

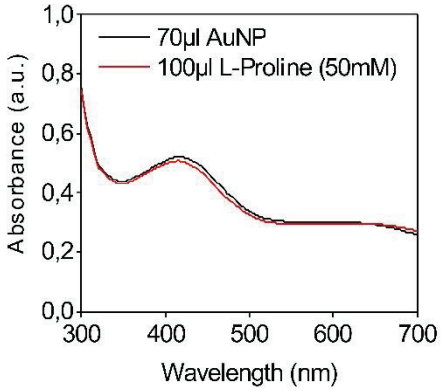

Figure 84. (Cont.)

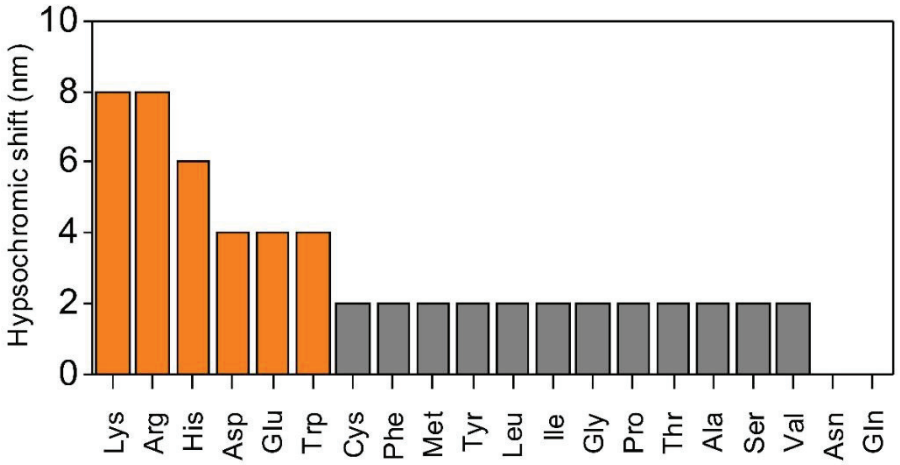

Figure 85. Hypsochromic shifts in UV–visible maximum of PT–Pip–AuNP complex induced by 20 proteinogenic amino acids

Upon addition of AuNPs, the fluorescence maximum of PT–Pip was red–shifted from 538 nm to a longer wavelength, and the UV–visible maximum was red–shifted (bathochromic shifts) from 408 nm to 416 nm. Blue shifts (hypsochromic shifts) of the UV–visible maximum, as shown in Figure 85. and increasing fluorescence intensity with the addition of amino acids were observed from the fluorescence spectra, indicating that PT–Pip was released into the solution phase by disruption of the PT–Pip–AuNP complex.

Except for L–cysteine, changes in the UV–visible maximum of PT–Pip induced by amino acids were consistent with the amino acid–induced fluorescence increment results of PT–Pip. It is known from the literature that AuNPs have high affinities to some functional groups, such as cyano (–CN), mercapto (–SH), and amino (–NH2) groups.[211] The interaction between L–cysteine and AuNPs was explained by thiolate linkage between L–cysteine and AuNPs via the thiol group of L–cysteine due to the peculiar affinity of S–atoms for gold.[212] Although L–cysteine did not induce AuNP aggregation and did not create more hypsochromic shifts in the UV–visible maximum of PT–Pip, it was known from the literature that L–cysteine addition alters the zeta potential of AuNPs.[203] In light of this information, L–cysteine was thought to interact with AuNPs due to the strong binding ability between L–cysteine and AuNPs and enhanced the fluorescence of PT–Pip. A possible interaction between L–cysteine and citrate–capped AuNPs is illustrated in Figure 86.

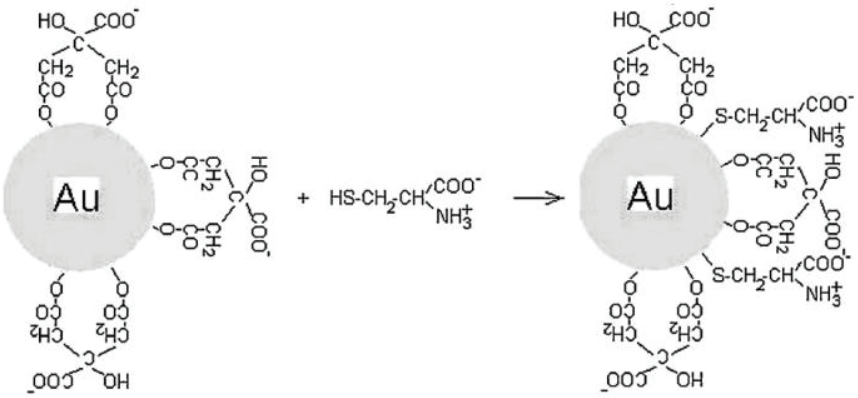

Figure 86. Schematic representation of binding of L–cysteine to citrate–capped AuNPs.[213]

3.4.4. Statistical Analysis of Amino Acid sensing assay

Fluorescence response patterns were analyzed by PCA, and results are illustrated in 2D PCA plot, as seen in Figure 87.

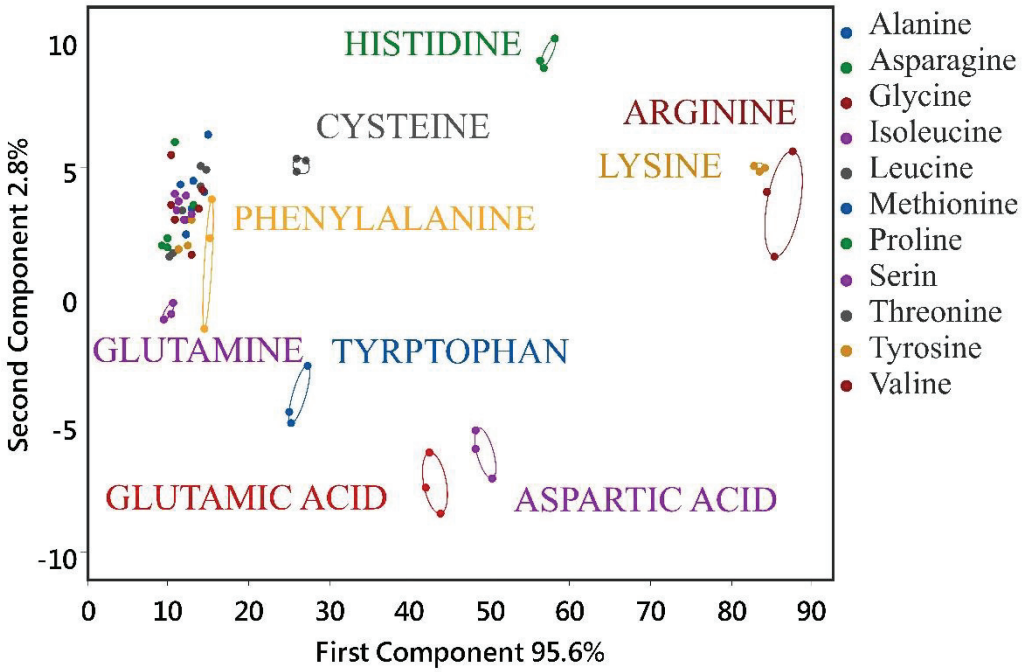

Figure 87. PCA graph of simplified fluorescence response patterns obtained with the PT–Pip–AuNP sensor array with six parameters against 20 proteinogenic amino acids

The basic amino acids (L–lysine, L–arginine, and L–histidine), which significantly increased the fluorescence, are located in the upper right corner of the graph. L–aspartic acid and L–glutamic acid are located very close to each other. They could also be clustered into two non–overlapping groups by this sensor array. In addition to acidic and basic amino acids, L–tryptophan and L–cysteine, which increased fluorescence, clustered into two groups, successfully. Although 13 amino acids that did not cause a significant increase in fluorescence were closely localized, L–glutamine and L–phenylalanine could be differentiated among these 13 amino acids.

Detection and differentiation of L–lysine and L–arginine based on their positive charge were essential. They play a vital role in biological events: the trypsin enzyme recognizes both amino acids, and both amino acids take part in protein–protein interactions. It is known that L–arginine plays an essential role in penetrating antimicrobial peptides through the cell membrane.[82] L–histidine, which has a lower charge density than the other two basic amino acids, was a difficult target. L–histidine detection was crucial, as the imidazolium group of the side chain had unique functions that could not be replaced by other amino acids, such as the base catalysis function in the serine protease's catalytic triad.[214] This chemical tongue sensor array could successfully discriminate these three basic amino acids. Moreover, as the fluorescence responses of L–arginine and L–lysine were similar, they are located close to each otherin the PCA graph. Because the fluorescence response of L–histidine was lower than that of L–arginine and L–lysine, it is localized a little further away from these two amino acids.

Two acidic amino acids (L–glutamic acid and L–aspartic acid) have various functions beyond being protein monomers. L–glutamic acids are precursors to several biomolecules, such as gamma–aminobutyric acid (GABA). These amino acids play a vital role in the urea cycle, especially in the elimination of ammonium. L–aspartic acids also have a function in the urea cycle. These amino acids are also essential for the malate aspartate shuttle and gluconeogenesis.[82] L–glutamic acid and L–aspartic acid represented unique fluorogenic responses and clustered into two non–overlapping groups in the PCA graph. The results show that this fluorescence turn–on/off biosensor could successfully discriminate these two amino acids.

Among the aromatic amino acids, only L–tryptophan and L–phenylalanine could be clustered into non–overlapping groups in the PCA plot. They have important roles in protein–protein interaction and electron transport. These amino acids act as precursors

to some neurotransmitters. Besides these functions, they absorb light near 280 nm and emit light at a longer wavelength. The light absorption properties of the aromatic amino acids allow qualitative and quantitative analysis of proteins.

The detection of L–cysteine mainly depends on the supramolecular recognition of these amino acid by metal ions. In our study, L–cysteine detection was achieved successfully. Although L–cysteine did not enhance the fluorescence of PT–Pip as much as basic amino acids, these amino acids represented distinct fluorescence behavior against the sensor array.

Among non–polar aliphatic amino acids, L–glutamine was located separately in the PCA plot, as this amino acid had the lowest interaction with AuNPs.

The fluorescent conjugated polymer–gold nanoparticle complexes have been widely used as a sensing element for amino acids. Shang et al. proposed a sensor for cysteine detection.[128] Poly(9,9–bis(4¢–sulfnoatobutyl)fluorene–co–alt–1,4–phenylene) sodium salt (PFS) was used as a fluorescence source, and AuNPs were used as fluorescence quenchers. The fluorescence of pre–quenched polymer–nanoparticle complex was recovered upon addition of cysteine. This sensor enabled the detection of cysteine among 20 amino acids with (LOD) of 25 nM.

Guan et al. developed a sensor for amino acid sensing that was very comparable with our study.[147] In this study, the cationic PT derivative Poly(1H–imidazolium–1–methyl–3–[2–[(4–methyl–3–thienyl)– oxy]ethyl]) chloride was used as the fluorescence element. The fluorescence of PT was quenched by charged complementary citrate–capped AuNPs. The K_{SV} of AuNP was 1.29×10^{10} M^{-1}, which was significantly greater than our finding (110.42×10^{3} M^{-1}). Due to the strong interaction between PT derivative and AuNPs, only two of the 20 amino acids could disrupt the PT–AuNP complex and enhance the fluorescence of PT. Therefore, only 2 of 20 amino acids were detected by Guan et al. In our study, the interaction between PT–Pip and AuNPs was relatively weak. This mild interaction allowed the detection of basic amino acids, acidic amino acids, and amino acids with functional side groups such as L–cysteine and L–tryptophan. In addition to these, L–phenylalanine and L–glutamine were also discriminated by the PCA analysis.

Wang et al. developed an optoelectronic tongue that combined a poly(para–phenyleneethynylene) (PPE) (fluorescence sources) with three metal ions((Fe^{2+}, Co^{2+}, and Cu^{2+}) (fluorescence quenchers) at three pH values (7, 10, and 13) to discriminate 20 natural amino acids.[31] This sensor array containing nine sensing elements could not

dicriminate 20 natural amino acids, individually, only grouped them as aromatic, polar, hydrophobic, positive, and negative. Besides, histidine, and glutamine were not grouped with the positive, and polar amino acids, respectively. Moreover, glycine, methionine, and cysteine could not be classified at al. The second sensor array was developed by combining green fluorescent protein (GFP) with three metal ions at pH=7. The discriminative power of sensor array was higher than the first one, but still some amino acids could not be clustered into non–overlapping groups. The combination of these two sensor arrays enhanced the sensitivity and discriminative power. However, it could only clustered 20 amino acids into five groups; such as positive, negative, polar, hydrophobic, and aromatic, some amino acids still were not grouped; such as cysteine, and histidine.

In this thesis, among 20 proteinogenic amino acids, 9 of them were clearly discriminated by using indirect amino acid sensing appoach. Besides, the amino acid discrimination was achieved with a single water soluble cationic PT derivative and single anionic AuNP. Our amino acid sensing strategy offers some advantages such as high discriminative power, basic procedure, less reagent usage, and cost–effectiveness.

CHAPTER 4

CONCLUSION

This thesis aimed to develop a novel fluorescence turn–on/off biosensor for biomolecule and cell analysis. Water–soluble cationic PT derivative poly(1,4–dimethyl–1–(3–((4–methylthiophen–3–yl)oxy)propyl)piperazine–1–ium bromide) was used as a fluorescence transducing element due to its excellent light–harvesting and molecular wire properties, as well as its optical sensitivity to external stimuli. Charge–complementary AuNPs were utilized as a fluorescence quencher.

In this biosensor, the interaction between the recognition element (PT–Pip–AuNP construct) and analyte mainly occurred electrostatically. The buffer type and pH value of the environment significantly influenced the electrostatic interaction between recognition elements and target analytes, as well as the optical characteristics of PT–Pip. For the first time, the pH–dependent spectroscopic characterization of the PT–Pip was performed. The investigation of the pH–responsiveness of PT–Pip indicated that the aggregation and disaggregation processes in the PT–Pip backbone were controlled by the addition of acids and bases sequentially. Acid and base treatments affected interchain and intrachain interactions. These interactions influenced the conformational and optical properties of PT–Pip. Three distinct PT–Pip conformations were obtained reversibly by acids and base additions:

i) Random–coil and disaggregated
ii) Planar and aggregated
iii) Planar and disaggregated conformations

Three conformations of PT–Pip chains were observed spectroscopically and colorimetrically.

Fluorescence quenching of PT–Pip with AuNP was investigated for biosensor development studies. Citrate–capped AuNPs were synthesized by the modified Turkevich's method and utilized as an efficient fluorescence quencher. PT–Pip emitted light at 540 nm, and AuNPs absorbed light at 528 nm. The spectral overlap between emission by PT–Pip and absorption by AuNPs resulted in fluorescence quenching due to RET–based energy transfer from PT–Pip to AuNPs. The fluorescence quenching

mechanism was investigated in detail in MQ water, 1X TE buffer, and 1X PBS buffer. Fluorescence quenching of PT–Pip via AuNPs was observed in MQ water and 1X TE buffer but not in 1X PBS. The temperature–dependent alterations of the fluorescence quenching process were investigated to determine whether the fluorescence quenching mechanism occurred by static or dynamic (collisional) quenching. The temperature–dependent decrease in the AuNPs' K_{SV} values (K_{SV}@25 ºC:152.16608, K_{SV}@35 ºC: 116.50695, K_{SV}@45 ºC: 106.80267) and the temperature–dependent changes of the absorbance spectra confirmed that the fluorescence quenching mechanism mainly occurred by static quenching.

Five protein samples, including metalloproteins and non–metalloproteins (BSA, Phos A, Phos B, protease, and CC), were used as analytes in the protein sensing study. Comparable pI (ranging from 4.7 to 10.5) and MW values (12.38 to 160 kDa) of proteins created a challenging testbed for protein discrimination. Various pH values of MQ water and 1X TE buffer were tested to tune the interaction between proteins and the PT–Pip–AuNP complex. PH ~ 7 and pH ~ 9.7 were used as optimum pH parameters. Thus, five proteins were tested by four cross–reactive sensor elements (TE buffer at pH = 7.08 and 9.64, and water at pH = 7.00 and 9.70) five times to obtain 100 data points (four factors × five proteins × five replicates). Alterations of fluorescence intensity depend on the physicochemical properties of proteins, such as pI, MW, or whether they are iron–containing proteins. BSA, Phos B, and protease enhanced the fluorescence of PT–Pip, while the two iron–containing metalloproteins, Phos A and CC, significantly reduced it. Thus, the five proteins created distinct and multidimensional fluorescence response patterns against the sensor array. PCA, a non–targeted multivariate statistical technique, was utilized to visualize these fluorogenic response patterns by explaining 99.4% of the total variance. PCA enabled the clustering of five proteins into five non–overlapping groups. This novel protein sensing approach demonstrated that the combination of four cross–reactive sensor elements (PT–Pip–AuNP complexes) and an appropriate multivariate statistical technique (PCA) successfully discriminates five proteins. Moreover, this biosensor showed high selectivity toward the two iron–containing metalloproteins. As a result, a rapid, sensitive, and selective chemical ‘‘tongue’’ sensor array was developed for protein detection and discrimination fort he first time. The detection limits of the sensor for proteins were 46.8 μM for BSA, Phos A, protease, and CC and 5.3 μM for Phos B.

The biosensor development studies continued by using seven types of mammalian cells, including healthy, cancerous, and metastatic cells, as target analytes. Three cross–reactive sensor elements (1X TE buffer, 25 mM HEPES buffer, and without buffer) were developed to obtain differential interaction between the PT–Pip–AuNP construct and cells. The fluorescence microscopy studies performed to investigate PT–Pip–cell interaction and PT–Pip localization revealed that the PT–Pip–AuNP complex strongly interacted with cells via electrostatic and hydrophobic interactions. The fluorescence spectroscopy displayed that PT–Pip–cell interactions induced the aggregation and planarization of PT–Pip. The degree of aggregation and planarization of PT–Pip varied from cell to cell, depending on the cell surface's physicochemical features. Multidimensional fluorogenic response patterns were obtained by ratiometric sensing of the seven cell lines. These fluorogenic response patterns were then quantified by the relative changes in the fluorescence response (the ratio of I_{586} to I_{542} and I_{632} to I_{542}) for the three sensor elements. Thus, seven cell lines were tested by three cross–reactive sensor elements three times to obtain 126 data points (six factors × seven proteins × three replicates) as a training matrix. PCA explaining 98.1% of the total variance demonstrated that three cell lines (NIH/3T3, HeLa, and SAOS–2) were successfully clustered into three non–overlapping groups. In contrast, the other four cell lines (MDA–MB–231, MCF–7, SH–SY5Y, and BCE C/D–1b) were compressed without overlapping. Further PCA performed with these four cell lines explained 89.2% of the total variance and displayed that these cell lines were also clearly clustered into four groups without overlapping. As a result, this novel cell sensing assay allowed rapid, sensitive, and selective detection and differentiation of each cell possessing different physicochemical properties. The detection limit of the chemical ''tongue'' sensor array was ~ 2×10^5 cells.

Further studies continued by using 20 proteinogenic amino acids as target analytes. The goal of this study was to discriminate 20 proteinogenic amino acids by their dictinct –R groups. Amino acid sensing experiments were performed in MQ water and TE buffer with four pH values (pH = 6, pH = 7, pH = 8.2, pH = 9.8) as solvents. Thus, 20 amino acids were tested by eight cross–reactive sensor elements three times to obtain 480 data points (eight factors × 20 proteins × three replicates) as a training set. The results show that basic amino acids, acidic amino acids, L–cysteine, and L–tryptophan significantly enhanced the fluorescence of PT–Pip, while the other amino acids induced lower fluorescence enhancement similarly. 20 amino acids were

introduced to PT–Pip and AuNPs individually and the absorbance spectra of the PT–Pip–AuNP complex were examined before and after amino acid addition for a detailed investigation of the amino acid sensing mechanism. The findings show that amino acids interacted selectively with AuNPs instead of PT–Pip, which disrupted the non–covalent coordination between PT–Pip and AuNPs and resulted in the selective displacement of PT–Pip. PCA performed for statistical evaluation of the fluorogenic responses of the 20 amino acids explained 98.4% of the total variance. In the PCA plot, nine amino acids were clustered into non–overlapping groups, while the results of 11 amino acids were very compressed and overlapped. L–arginine, L–lysine, L–histidine, L–glutamic acid, L–aspartic acid, L–cysteine, L–tryptophan, and L–phenylalanine, which increased the fluorescence of PT–Pip at different rates, were clustered into eight non–overlapping groups. Moreover, L–glutamine, which induced almost no fluorescence enhancement, was clustered as an individual group close to the overlapping results of the other 11 amino acids. This indirect sensing mechanism enables the detection and identification of nine amino acids by using their specific interaction with AuNPs. The detection limit of this sensor was 20.8 mM for all amino acids except L–tyrosine (1.1 mM). As a result, this indirect amino acid sensing assay allowed rapid, sensitive, and selective detection and differentiation of amino acids possessing specific side chains.

We developed sensitive, selective, and cost–effective ‘‘add and read’’ type fluorescence turn–on/off chemical tongue sensor arrays. The protein, cell, and amino acid sensing approaches utilized novel PT–Pip–AuNP supramolecular constructs as recognition elements. The fluorescence was restored and the binding events were transduced by the selective displacement of PT–Pip which is induced by analyte additions. Various buffers and pH values were used to tune the interaction between analytes and PT–Pip–AuNP constructs and create multiple sensor elements. The sensor arrays generated multidimensional signal outputs. These signal outputs were analyzed via PCA, an unsupervised method that allows for obtaining a unique fingerprint for each analyte in an efficient fashion. This chemical ‘‘tongue’’ sensor array achieved rapid sensitive and selective detection and identification of biomolecules and cells despite the structural complexity, heterogeneity, and similarity of target analytes, making these sensors a challenging testbed. Further improvements of differential sensing methodology to develop a chemical tongue sensor array would increase the sensitivity and selectivity and provide a functional sensing approach for diagnostic, environmental, pharmaceutical, and food quality control applications. Thus,

these approaches become a powerful alternative to time–consuming, expensive, and complex routine methods due to their rapid, cost–effective, and effortless operation.

The major impact of this work is to demonstrate the benefit of using the PT–Pip–AuNP complex as a recognition element to discriminate proteins, mammalian cells, and amino acids. Combination of water–soluble cationic PT derivative poly(1,4–dimethyl–1–(3–((4–methylthiophen–3–yl)oxy)propyl)piperazine–1–ium bromide) and AuNPs was used for the first time utilizing fluorescence turn on/off sensing approach for biomolecule and mammalian cell discrimination. As a future perspectives, the discriminative power of the sensor array can be enhanced by using differentially functionalized AuNP derivatives, or different metal ions with a fluorescence quenching ability. This developed sensor array can also be used for the detection and identification of other biomolecules; such as nucleic acids or carbohydrates in following studies. Further from the biomedical point of view, the qualitative and quantitative determination of specific biomarkers in body fluids (serum or urine) can be achieved with this sensor array for the diagnosis, prognosis, and treatment of diaseases.

REFERENCES

(1) Fraden, J. Handbook of modern sensors physics, designs, and applications; Springer, 2016.

(2) Electrical transducer nomenclature and terminology; Instrument Society of America, 1982.

(3) Yoon, J.-Y. Introduction to biosensors. Springer 2013 https://doi.org/10.1007/978-1-4419-6022-1.

(4) Czarnik, A. W. Supramolecular chemistry, fluorescence, and sensing. ACS Symposium Series 1993, 1–9 https://doi.org/10.1021/bk-1993-0538.ch001.

(5) Fong, J. F. Y.; Ng, Y. H.; Ng, S. M. Carbon dots as a new class of light emitters for Biomedical Diagnostics and Therapeutic Applications. Fullerens, Graphenes and Nanotubes 2018, 227–295 https://doi.org/10.1016/b978-0-12-813691-1.00007-5.

(6) Prasad, P. N. Introduction to Biophotonics; Wiley: Hoboken, 2004.

(7) Bhalla, N.; Jolly, P.; Formisano, N.; Estrela, P. Introduction to biosensors. Essays in Biochemistry 2016, 60 (1), 1–8 https://doi.org/10.1042/ebc20150001.

(8) Preda, G.; Bizerea, O.; Vlad-Oros, B. Sol-gel technology in enzymatic electrochemical biosensors for clinical analysis. Biosensors for Health, Environment and Biosecurity 2011 https://doi.org/10.5772/19622.

(9) Zamora-Gálvez, A.; Morales-Narváez, E.; Mayorga-Martinez, C. C.; Merkoçi, A. Nanomaterials connected to antibodies and molecularly imprinted polymers as Bio/receptors for bio/sensor applications. Applied Materials Today 2017, 9, 387–401 https://doi.org/10.1016/j.apmt.2017.09.006.

(10) Graham, T. Biocompatible low-cost CMOS electrodes for neuronal interfaces, cell impedance and other biosensors. Ph.D. Dissertation, University of Bath, England, 2010.

(11) Damborský, P.; Švitel, J.; Katrlík, J. Optical biosensors. Essays in Biochemistry 2016, 60 (1), 91–100 https://doi.org/10.1042/ebc20150010.

(12) Vo-Dinh, T.; Cullum, B. M.; Stokes, D. L. Nanosensors and biochips: Frontiers in biomolecular diagnostics. Sensors and Actuators B: Chemical 2001, 74 (1-3), 2–11 https://doi.org/10.1016/s0925-4005(00)00705-x.

(13) Gupta, N.; Renugopalakrishnan, V.; Liepmann, D.; Paulmurugan, R.; Malhotra, B. D. Cell-based biosensors: Recent trends, challenges and future perspectives. Biosensors and Bioelectronics 2019, 141, 111435 https://doi.org/10.1016/j.bios.2019.111435.

(14) Oliveira Brett, A. M. Chapter 4 DNA-based biosensors. Biosensors and Modern Biospecific Analytical Techniques 2005, 179–208 https://doi.org/10.1016/s0166-526x(05)44004-0.

(15) Hamed, K.-K.; Vahideh, R.; Ali, E.; Fatemeh, S. DNA biosensors techniques and their applications in food safety, Environmental Protection and Biomedical Research: A mini-review. Journal of Cell and Developmental Biology 2020, 3 (1) https://doi.org/10.36959/596/446.

(16) Kumar, H.; Neelam. Enzyme-based electrochemical biosensors for Food Safety: A Review. Nanobiosensors in Disease Diagnosis 2016, 29 https://doi.org/10.2147/ndd.s64847.

(17) Sharma, S.; Byrne, H.; O'Kennedy, R. J. Antibodies and antibody-derived analytical biosensors. Essays in Biochemistry 2016, 60 (1), 9–18 https://doi.org/10.1042/ebc20150002.

(18) Rong, G.; Corrie, S. R.; Clark, H. A. In vivo biosensing: Progress and

perspectives. ACS Sensors 2017, 2 (3), 327–338 https://doi.org/10.1021/acssensors.6b00834.

(19) Dickert, F. Biomimetic receptors and sensors. Sensors 2014, 14 (12), 22525–22531 https://doi.org/10.3390/s141222525.

(20) Stortini, A. M.; Baldo, M. A.; Moro, G.; Polo, F.; Moretto, L. M. Bio- and biomimetic receptors for electrochemical sensing of heavy metal ions. Sensors 2020, 20 (23), 6800 https://doi.org/10.3390/s20236800.

(21) Syahir, A.; Usui, K.; Tomizaki, K.-ya; Kajikawa, K.; Mihara, H. Label and label-free detection techniques for protein microarrays. Microarrays 2015, 4 (2), 228–244 https://doi.org/10.3390/microarrays4020228.

(22) Wong, S.-F.; Khor, S. M. State-of-the-art of differential sensing techniques in Analytical Sciences. TrAC Trends in Analytical Chemistry 2019, 114, 108–125 https://doi.org/10.1016/j.trac.2019.03.006.

(23) Peveler, W. J.; Yazdani, M.; Rotello, V. M. Selectivity and specificity: Pros and cons in Sensing. ACS Sensors 2016, 1 (11), 1282–1285 https://doi.org/10.1021/acssensors.6b00564.

(24) Umali, A. P.; Anslyn, E. V. A general approach to differential sensing using synthetic molecular receptors. Current Opinion in Chemical Biology 2010, 14 (6), 685–692 https://doi.org/10.1016/j.cbpa.2010.07.022.

(25) Heller, A.; Feldman, B. Electrochemical glucose sensors and their applications in diabetes management. Chemical Reviews 2008, 108 (7), 2482–2505 https://doi.org/10.1021/cr068069y.

(26) Koczula, K. M.; Gallotta, A. Lateral flow assays. Essays in Biochemistry 2016, 60 (1), 111–120 https://doi.org/10.1042/ebc20150012.

(27) Kitamura, M.; Shabbir, S. H.; Anslyn, E. V. Guidelines for pattern recognition

using differential receptors and indicator displacement assays. The Journal of Organic Chemistry 2009, 74 (12), 4479–4489 https://doi.org/10.1021/jo900433j.

(28) He, X.-P.; Hu, X.-L.; James, T. D.; Yoon, J.; Tian, H. Multiplexed photoluminescent sensors: Towards improved disease diagnostics. Chemical Society Reviews 2017, 46 (22), 6687–6696 https://doi.org/10.1039/c6cs00778c.

(29) Baldini, L.; Wilson, A. J.; Hong, J.; Hamilton, A. D. Pattern-based detection of different proteins using an array of fluorescent protein surface receptors. Journal of the American Chemical Society 2004, 126 (18), 5656–5657 https://doi.org/10.1021/ja039562j.

(30) Lee, J. W.; Lee, J.-S.; Chang, Y.-T. Colorimetric identification of carbohydrates by a ph indicator/ph change inducer ensemble. Angewandte Chemie International Edition 2006, 45 (39), 6485–6487 https://doi.org/10.1002/anie.200602055.

(31) Wang, B.; Han, J.; Ma, C.; Bender, M.; Seehafer, K.; Herrmann, A.; Bunz, U. H. A simple optoelectronic tongue discriminates amino acids. Chemistry - A European Journal 2017, 23 (51), 12471–12474 https://doi.org/10.1002/chem.201702826.

(32) Phillips, R. L.; Miranda, O. R.; You, C.-C.; Rotello, V. M.; Bunz, U. H. F. Rapid and efficient identification of bacteria using gold-nanoparticle–poly(para-phenyleneethynylene) constructs. Angewandte Chemie International Edition 2008, 47 (14), 2590–2594 https://doi.org/10.1002/anie.200703369.

(33) Bajaj, A.; Rana, S.; Miranda, O. R.; Yawe, J. C.; Jerry, D. J.; Bunz, U. H.; Rotello, V. M. Cell surface-based differentiation of cell types and cancer states using a Gold Nanoparticle-GFP based Sensing Array. Chemical Science 2010, 1 (1), 134 https://doi.org/10.1039/c0sc00165a.

(34) Lavigne, J. J.; Anslyn, E. V. Sensing a paradigm shift in the field of molecular recognition: From selective to differential receptors. Angewandte Chemie International Edition 2001, 40 (17), 3118–3130 https://doi.org/10.1002/1521-

3773(20010903)40:17<3118::aid-anie3118>3.0.co;2-y.

(35) Jia, M.; Li, S.; Zang, L.; Lu, X.; Zhang, H. Analysis of biomolecules based on the surface enhanced Raman spectroscopy. Nanomaterials 2018, 8 (9), 730 https://doi.org/10.3390/nano8090730.

(36) Biomarkers and surrogate endpoints: Preferred definitions and Conceptual Framework. Clinical Pharmacology & Therapeutics 2001, 69 (3), 89–95 https://doi.org/10.1067/mcp.2001.113989.

(37) Varjani, S. J.; Binod, P.; Kumar, S.; Khare, S. K. Introduction to biosynthetic technology and environmental challenges. Biosynthetic Technology and Environmental Challenges 2017, 3–7 https://doi.org/10.1007/978-981-10-7434-9_1.

(38) Zhao, X.; Modur, V.; Carayannopoulos, L. N.; Laterza, O. F. Biomarkers in pharmaceutical research. Clinical Chemistry 2015, 61 (11), 1343–1353 https://doi.org/10.1373/clinchem.2014.231712.

(39) Afshari, R.; Pillidge, C. J.; Dias, D. A.; Osborn, A. M.; Gill, H. Biomarkers associated with cheese quality uncovered by integrative multi-omic analysis. Food Control 2021, 123, 107752 https://doi.org/10.1016/j.foodcont.2020.107752.

(40) Pan, Y.; Chen, H.; Shen, X.; Wang, X.; Ju, S.; Lu, M.; Cong, H. Serum level of long noncoding RNA H19 as a diagnostic biomarker of multiple myeloma. Clinica Chimica Acta 2018, 480, 199–205 https://doi.org/10.1016/j.cca.2018.02.019.

(41) Mohd Khair, S. Z.; Abd Radzak, S. M.; Mohamed Yusoff, A. A. The uprising of mitochondrial DNA biomarker in cancer. Disease Markers 2021, 2021, 1–20 https://doi.org/10.1155/2021/7675269.

(42) Landegren, U.; Hammond, M. Cancer diagnostics based on plasma protein biomarkers: Hard Times but great expectations. Molecular Oncology 2020, 15

(6), 1715–1726 https://doi.org/10.1002/1878-0261.12809.

(43) Ueda, K. Glycoproteomic strategies: From Discovery to clinical application of cancer carbohydrate biomarkers. Proteomics - Clinical Applications 2013, 7 (9-10), 607–617 https://doi.org/10.1002/prca.201200123.

(44) Zella, D.; Gallo, R. C. Viruses and bacteria associated with cancer: An overview. Viruses 2021, 13 (6), 1039 https://doi.org/10.3390/v13061039.

(45) Bajaj, A.; Miranda, O. R.; Kim, I.-B.; Phillips, R. L.; Jerry, D. J.; Bunz, U. H.; Rotello, V. M. Detection and differentiation of normal, cancerous, and metastatic cells using nanoparticle-polymer sensor arrays. Proceedings of the National Academy of Sciences 2009, 106 (27), 10912–10916 https://doi.org/10.1073/pnas.0900975106.

(46) Chen, X. H., Huang, S., & Kerr, D. Biomarkers in Clinical Medicine. IARC scientific publications, (163), 303–322, 2011.

(47) Patton, W. F. Detection technologies in Proteome Analysis. Journal of Chromatography B 2002, 771 (1-2), 3–31 https://doi.org/10.1016/s1570-0232(02)00043-0.

(48) Bradford, M. M. A rapid and sensitive method for the quantitation of microgram quantities of protein utilizing the principle of protein-dye binding. Analytical Biochemistry 1976, 72 (1-2), 248–254 https://doi.org/10.1016/0003-2697(76)90527-3.

(49) Shrivastaw, K. P.; Singh, S.; Sharma, S. B.; Sokhey, J. Quantitation of protein content by Biuret method during production of yellow fever vaccine. Biologicals 1995, 23 (4), 299–300 https://doi.org/10.1006/biol.1995.0048.

(50) Lowry, O. H.; Rosebrough, N. J.; Farr, A. L.; Randall, R. J. Protein measurement with the Folin phenol reagent. Journal of Biological Chemistry 1951, 193 (1), 265–275 https://doi.org/10.1016/s0021-9258(19)52451-6.

(51) Miranda, O. R.; Creran, B.; Rotello, V. M. Array-based sensing with nanoparticles: 'chemical noses' for sensing biomolecules and cell surfaces. Current Opinion in Chemical Biology 2010, 14 (6), 728–736 https://doi.org/10.1016/j.cbpa.2010.07.021.

(52) Hemmateenejad, B.; Shahrivar-kevishahi, A.; Shakerizadeh-Shirazi, F.; Rouhani, S.; Mohamadi-Gharaghani, F. A time-insensitive colorimetric sensor for the determination of total protein. RSC Advances 2016, 6 (57), 52026–52033 https://doi.org/10.1039/c5ra25234b.

(53) Leca-Bouvier, B.; Blum, L. J. Biosensors for protein detection: A Review. Analytical Letters 2005, 38 (10), 1491–1517 https://doi.org/10.1081/al-200065780.

(54) Falahi, S.; Rafiee-Pour, H.-A.; Zarejousheghani, M.; Rahimi, P.; Joseph, Y. Non-coding RNA-based biosensors for early detection of liver cancer. Biomedicines 2021, 9 (8), 964 https://doi.org/10.3390/biomedicines9080964.

(55) Akshaya, K.; Arthi, C.; Pavithra, A. J.; Poovizhi, P.; Antinate, S. S.; Hikku, G. S.; Jeyasubramanian, K.; Murugesan, R. Bioconjugated gold nanoparticles as an efficient colorimetric sensor for cancer diagnostics. Photodiagnosis and Photodynamic Therapy 2020, 30, 101699 https://doi.org/10.1016/j.pdpdt.2020.101699.

(56) Ackermann, S.; Mrowka, R. Cancer – an ongoing fight searching for reasons and therapies. Acta Physiologica 2019, 226 (1) https://doi.org/10.1111/apha.13275.

(57) Sung, H.; Ferlay, J.; Siegel, R. L.; Laversanne, M.; Soerjomataram, I.; Jemal, A.; Bray, F. Global cancer statistics 2020: Globocan estimates of incidence and mortality worldwide for 36 cancers in 185 countries. CA: A Cancer Journal for Clinicians 2021, 71 (3), 209–249 https://doi.org/10.3322/caac.21660.

(58) Kurmendra; Kumar, R. MEMS based cantilever biosensors for cancer detection

using potential bio-markers present in vocs: A survey. Microsystem Technologies 2019, 25 (9), 3253–3267 https://doi.org/10.1007/s00542-019-04326-1.

(59) Bellassai, N.; D'Agata, R.; Jungbluth, V.; Spoto, G. Surface plasmon resonance for Biomarker Detection: Advances in non-invasive cancer diagnosis. Frontiers in Chemistry 2019, 7 https://doi.org/10.3389/fchem.2019.00570.

(60) Rana, S.; Singla, A. K.; Bajaj, A.; Elci, S. G.; Miranda, O. R.; Mout, R.; Yan, B.; Jirik, F. R.; Rotello, V. M. Array-based sensing of metastatic cells and tissues using nanoparticle–fluorescent protein conjugates. ACS Nano 2012, 6 (9), 8233–8240 https://doi.org/10.1021/nn302917e.

(61) Feng, Y.; Mitchison, T. J.; Bender, A.; Young, D. W.; Tallarico, J. A. Multi-parameter phenotypic profiling: Using cellular effects to characterize small-molecule compounds. Nature Reviews Drug Discovery 2009, 8 (7), 567–578 https://doi.org/10.1038/nrd2876.

(62) Malek, A.; Catapano, C. V.; Czubayko, F.; Aigner, A. A sensitive polymerase chain reaction-based method for detection and quantification of metastasis in human xenograft mouse models. Clinical & Experimental Metastasis 2010, 27 (4), 261–271 https://doi.org/10.1007/s10585-010-9324-1.

(63) Wang, J.-W.; Peng, S.-Y.; Li, J.-T.; Wang, Y.; Zhang, Z.-P.; Cheng, Y.; Cheng, D.-Q.; Weng, W.-H.; Wu, X.-S.; Fei, X.-Z.; et al. Identification of metastasis-associated proteins involved in gallbladder carcinoma metastasis by proteomic analysis and functional exploration of chloride intracellular channel 1. Cancer Letters 2009, 281 (1), 71–81 https://doi.org/10.1016/j.canlet.2009.02.020.

(64) Hedegaard, M.; Krafft, C.; Ditzel, H. J.; Johansen, L. E.; Hassing, S.; Popp, J. Discriminating isogenic cancer cells and identifying altered unsaturated fatty acid content as associated with metastasis status, using k-means clustering and partial least squares-discriminant analysis of Raman maps. Analytical Chemistry 2010, 82 (7), 2797–2802 https://doi.org/10.1021/ac902717d.

(65) Szlasa, W.; Zendran, I.; Zalesińska, A.; Tarek, M.; Kulbacka, J. Lipid composition of the cancer cell membrane. Journal of Bioenergetics and Biomembranes 2020, 52 (5), 321–342 https://doi.org/10.1007/s10863-020-09846-4.

(66) Ma, Y.; Poole, K.; Goyette, J.; Gaus, K. Introducing membrane charge and membrane potential to T cell signaling. Frontiers in Immunology 2017, 8 https://doi.org/10.3389/fimmu.2017.01513.

(67) El Kirat, K.; Morandat, S. Cholesterol modulation of membrane resistance to Triton X-100 explored by atomic force microscopy. Biochimica et Biophysica Acta (BBA) - Biomembranes 2007, 1768 (9), 2300–2309 https://doi.org/10.1016/j.bbamem.2007.05.006.

(68) Tan, L. T.-H.; Chan, K.-G.; Pusparajah, P.; Lee, W.-L.; Chuah, L.-H.; Khan, T. M.; Lee, L.-H.; Goh, B.-H. Targeting membrane lipid a potential cancer cure?. Frontiers in Pharmacology 2017, 8 https://doi.org/10.3389/fphar.2017.00012.

(69) Bevers, E. M.; Comfurius, P.; Zwaal, R. F. A. Regulatory mechanisms in maintenance and modulation of transmembrane lipid asymmetry: Pathophysiological Implications. Lupus 1996, 5 (5), 480–487 https://doi.org/10.1177/096120339600500531.

(70) Adem, A.; Mattsson, M. E. K.; Nordberg, A.; Påhlman, S. Muscarinic receptors in human SH-SY5Y Neuroblastoma Cell Line: Regulation by Phorbol Ester and retinoic acid-induced differentiation. Developmental Brain Research 1987, 33 (2), 235–242 https://doi.org/10.1016/0165-3806(87)90156-8.

(71) Jobin, M.-L.; Alves, I. D. On the importance of electrostatic interactions between cell penetrating peptides and membranes: A pathway toward tumor cell selectivity? Biochimie 2014, 107, 154–159 https://doi.org/10.1016/j.biochi.2014.07.022.

(72) Alves, A. C.; Ribeiro, D.; Nunes, C.; Reis, S. Biophysics in cancer: The relevance of drug-membrane interaction studies. Biochimica et Biophysica Acta (BBA) - Biomembranes 2016, 1858 (9), 2231–2244 https://doi.org/10.1016/j.bbamem.2016.06.025.

(73) Le, W.; Chen, B.; Cui, Z.; Liu, Z.; Shi, D. Detection of cancer cells based on glycolytic-regulated surface electrical charges. Biophysics Reports 2019, 5 (1), 10–18 https://doi.org/10.1007/s41048-018-0080-0.

(74) Nishino, M.; Matsuzaki, I.; Musangile, F. Y.; Takahashi, Y.; Iwahashi, Y.; Warigaya, K.; Kinoshita, Y.; Kojima, F.; Murata, S.-ichi. Measurement and visualization of cell membrane surface charge in fixed cultured cells related with cell morphology. PLOS ONE 2020, 15 (7) https://doi.org/10.1371/journal.pone.0236373.

(75) Chen, B.; Le, W.; Wang, Y.; Li, Z.; Wang, D.; Lin, L.; Cui, S.; Hu, J. J.; Hu, Y.; Yang, P.; et al. Targeting negative surface charges of cancer cells by multifunctional nanoprobes. Theranostics 2016, 6 (11), 1887–1898 https://doi.org/10.7150/thno.16358.

(76) Rana, S.; Elci, S. G.; Mout, R.; Singla, A. K.; Yazdani, M.; Bender, M.; Bajaj, A.; Saha, K.; Bunz, U. H.; Jirik, F. R.; et al. Ratiometric array of conjugated polymers–fluorescent protein provides a robust mammalian cell sensor. Journal of the American Chemical Society 2016, 138 (13), 4522–4529 https://doi.org/10.1021/jacs.6b00067.

(77) Bajaj, A.; Miranda, O. R.; Phillips, R.; Kim, I.-B.; Jerry, D. J.; Bunz, U. H.; Rotello, V. M. Array-based sensing of normal, cancerous, and metastatic cells using conjugated fluorescent polymers. Journal of the American Chemical Society 2009, 132 (3), 1018–1022 https://doi.org/10.1021/ja9061272.

(78) Wang, G.; Han, R.; Su, X.; Li, Y.; Xu, G.; Luo, X. Zwitterionic peptide anchored to conducting polymer pedot for the development of antifouling and ultrasensitive electrochemical DNA sensor. Biosensors and Bioelectronics 2017,

92, 396–401 https://doi.org/10.1016/j.bios.2016.10.088.

(79) Gharatape, A.; Yari Khosroushahi, A. Optical biomarker-based biosensors for cancer/infectious disease medical diagnoses. Applied Immunohistochemistry & Molecular Morphology 2019, 27 (4), 278–286 https://doi.org/10.1097/pai.0000000000000586.

(80) Kaja, S. Detection of novel biomarkers for ovarian cancer with an optical nanotechnology detection system enabling label-free diagnostics. Journal of Biomedical Optics 2012, 17 (8), 081412 https://doi.org/10.1117/1.jbo.17.8.081412.

(81) Joseph, R. Pillar[n]arene derivatives as sensors for amino acids. ChemistrySelect 2021, 6 (14), 3519–3533 https://doi.org/10.1002/slct.202100098.

(82) Martins, J. N.; Lima, J. C.; Basílio, N. Selective recognition of amino acids and peptides by small supramolecular receptors. Molecules 2020, 26 (1), 106 https://doi.org/10.3390/molecules26010106.

(83) Hu, X.; Guo, F. Amino acid sensing in metabolic homeostasis and health. Endocrine Reviews 2020, 42 (1), 56–76 https://doi.org/10.1210/endrev/bnaa026.

(84) Walsh, C. T.; O'Brien, R. V.; Khosla, C. Nonproteinogenic amino acid building blocks for nonribosomal peptide and hybrid polyketide scaffolds. Angewandte Chemie International Edition 2013, 52 (28), 7098–7124 https://doi.org/10.1002/anie.201208344.

(85) Aerts, J.; Röling, W.; Elsaesser, A.; Ehrenfreund, P. Biota and biomolecules in extreme environments on earth: Implications for life detection on Mars. Life 2014, 4 (4), 535–565 https://doi.org/10.3390/life4040535.

(86) Berg, J. M.; Tymoczko, J. L.; Stryer, L.; Clarke. Biochemistry; Freeman: New York, 2002.

(87) Minami, T.; Esipenko, N. A.; Zhang, B.; Isaacs, L.; Anzenbacher, P. “turn-on” fluorescent sensor array for basic amino acids in water. Chem. Commun. 2014, 50 (1), 61–63 https://doi.org/10.1039/c3cc47416j.

(88) Gao, Y.; Gao, F.; Zhang, G.; Chen, L.; Wu, Q.; Liu, X. Sensor array based on single carbon quantum dot for fluorometric differentiation of all natural amino acids. Microchimica Acta 2019, 186 (12) https://doi.org/10.1007/s00604-019-3864-0.

(89) Qin, M.; Li, F.; Huang, Y.; Ran, W.; Han, D.; Song, Y. Twenty natural amino acids identification by a photochromic sensor chip. Analytical Chemistry 2014, 87 (2), 837–842 https://doi.org/10.1021/ac504121d.

(90) Huo, D.-Q.; Zhang, G.-P.; Hou, C.-J.; Dong, J.-L.; Zhang, Y.-C.; Liu, Z.; Luo, X.-G.; Fa, H.-B.; Zhang, S.-Y. A colorimetric sensor array for identification of natural amino acids. Chinese Journal of Analytical Chemistry 2010, 38 (8), 1115–1120 https://doi.org/10.1016/s1872-2040(09)60061-x.

(91) Ambade, A. V.; Sandanaraj, B. S.; Klaikherd, A.; Thayumanavan, S. Fluorescent polyelectrolytes as protein sensors. Polymer International 2007, 56 (4), 474–481 https://doi.org/10.1002/pi.2185.

(92) Jaiswal, M.; Menon, R. Polymer Electronic Materials: A Review of Charge Transport. Polymer International 2006, 55 (12), 1371–1384 https://doi.org/10.1002/pi.2111.

(93) Leclerc, M.; Faid, K. Electrical and optical properties of processable polythiophene derivatives: Structure-property relationships. Advanced Materials 1997, 9 (14), 1087–1094 https://doi.org/10.1002/adma.19970091404.

(94) Pak, Y. L.; Wang, Y.; Xu, Q. Conjugated polymer based fluorescent probes for metal ions. Coordination Chemistry Reviews 2021, 433, 213745 https://doi.org/10.1016/j.ccr.2020.213745.

(95) Najeeb, M. A.; Ahmad, Z.; Shakoor, R. A. Organic thin-film capacitive and resistive humidity sensors: A Focus Review. Advanced Materials Interfaces 2018, 5 (21), 1800969 https://doi.org/10.1002/admi.201800969.

(96) Coakley, K. M.; McGehee, M. D. Conjugated polymer photovoltaic cells. Chemistry of Materials 2004, 16 (23), 4533–4542 https://doi.org/10.1021/cm049654n.

(97) Bai, L.; Han, Y.; Lin, J.; Xie, L.; Huang, W. Intrinsically stretchable conjugated polymers for flexible optoelectronic devices. Science Bulletin 2021, 66 (21), 2162–2164 https://doi.org/10.1016/j.scib.2021.07.017.

(98) Pavase, T. R.; Lin, H.; Shaikh, Q.-ul-ain; Hussain, S.; Li, Z.; Ahmed, I.; Lv, L.; Sun, L.; Shah, S. B.; Kalhoro, M. T. Recent advances of conjugated polymer (CP) nanocomposite-based chemical sensors and their applications in Food Spoilage Detection: A comprehensive review. Sensors and Actuators B: Chemical 2018, 273, 1113–1138 https://doi.org/10.1016/j.snb.2018.06.118.

(99) Cevher, Ş. C.; Bekmezci, S. A.; SaniyeSoylemez; Udum, Y. A.; Toppare, L.; Çırpan, A. Indenoquinoxalinone based conjugated polymer substrate for laccase biosensor. Materials Chemistry and Physics 2021, 257, 123788 https://doi.org/10.1016/j.matchemphys.2020.123788.

(100) López Cabarcos, E.; Carter, S. A. Characterization of the photoluminescence quenching of mixed water-soluble conjugated polymers for potential use as biosensor materials. Macromolecules 2005, 38 (10), 4409–4415 https://doi.org/10.1021/ma050153c.

(101) Jaymand, M.; Hatamzadeh, M.; Omidi, Y. Modification of polythiophene by the incorporation of processable polymeric chains: Recent progress in synthesis and applications. Progress in Polymer Science 2015, 47, 26–69 https://doi.org/10.1016/j.progpolymsci.2014.11.004.

(102) Li, C.; Numata, M.; Takeuchi, M.; Shinkai, S. A sensitive colorimetric and

fluorescent probe based on a polythiophene derivative for the detection of ATP. Angewandte Chemie International Edition 2005, 44 (39), 6371–6374 https://doi.org/10.1002/anie.200501823.

(103) Fan, L.-J.; Zhang, Y.; Murphy, C. B.; Angell, S. E.; Parker, M. F. L.; Flynn, B. R.; Jones, W. E. Fluorescent conjugated polymer molecular wire chemosensors for transition metal ion recognition and signaling. Coordination Chemistry Reviews 2009, 253 (3-4), 410–422 https://doi.org/10.1016/j.ccr.2008.03.008.

(104) Huynh, T.-P.; Sharma, P. S.; Sosnowska, M.; D'Souza, F.; Kutner, W. Functionalized Polythiophenes: Recognition materials for chemosensors and biosensors of superior sensitivity, selectivity, and detectability. Progress in Polymer Science 2015, 47, 1–25 https://doi.org/10.1016/j.progpolymsci.2015.04.009.

(105) AL-Refai, H. H.; Ganash, A. A.; Hussein, M. A. Polythiophene and its derivatives –based nanocomposites in electrochemical sensing: A Mini Review. Materials Today Communications 2021, 26, 101935 https://doi.org/10.1016/j.mtcomm.2020.101935.

(106) Lee, O. P. Design Strategies for Controlling Optoelectronic Properties and Solid-State Order of Conjugated Materials in Organic Photovoltaics. Ph.D. Dissertation, University of California, United States of America, 2013.

(107) Rajwar, D.; Ammanath, G.; Cheema, J. A.; Palaniappan, A.; Yildiz, U. H.; Liedberg, B. Tailoring conformation-induced chromism of polythiophene copolymers for nucleic acid assay at Resource Limited settings. ACS Applied Materials & Interfaces 2016, 8 (13), 8349–8357 https://doi.org/10.1021/acsami.5b12171.

(108) Goto, H.; Yashima, E. Electron-induced switching of the supramolecular chirality of optically active polythiophene aggregates. Journal of the American Chemical Society 2002, 124 (27), 7943–7949 https://doi.org/10.1021/ja025900p.

(109) Maynor, M. S.; Deason, T. K.; Nelson, T. L.; Lavigne, J. J. Multidimensional response analysis towards the detection and identification of soft divalent metal ions. Supramolecular Chemistry 2009, 21 (3-4), 310–315 https://doi.org/10.1080/10610270802516658.

(110) Ho, H.-A.; Najari, A.; Leclerc, M. Optical detection of DNA and proteins with cationic polythiophenes. Accounts of Chemical Research 2008, 41 (2), 168–178 https://doi.org/10.1021/ar700115t.

(111) Li, C.; Shi, G. Polythiophene-based optical sensors for small molecules. ACS Applied Materials & Interfaces 2013, 5 (11), 4503–4510 https://doi.org/10.1021/am400009d.

(112) Feng, X.; Liu, L.; Wang, S.; Zhu, D. Water-soluble fluorescent conjugated polymers and their interactions with biomacromolecules for sensitive biosensors. Chemical Society Reviews 2010, 39 (7), 2411 https://doi.org/10.1039/b909065g.

(113) Ho, H. A.; Leclerc, M. New colorimetric and fluorometric chemosensor based on a cationic polythiophene derivative for iodide-specific detection. Journal of the American Chemical Society 2003, 125 (15), 4412–4413 https://doi.org/10.1021/ja028765p.

(114) Tu, M.-C.; Rajwar, D.; Ammanath, G.; Alagappan, P.; Yildiz, U. H.; Liedberg, B. Visual detection of Al3+ ions using conjugated copolymer-ATP supramolecular complex. Analytica Chimica Acta 2016, 912, 105–110 https://doi.org/10.1016/j.aca.2015.12.002.

(115) Liu, M.; Li, J.; Li, B. A colorimetric aptamer biosensor based on cationic polythiophene derivative as peroxidase mimetics for the ultrasensitive detection of thrombin. Talanta 2017, 175, 224–228 https://doi.org/10.1016/j.talanta.2017.07.003.

(116) Yildiz, U. H.; Sheng, C. W.; Mailepessov, D.; Xueqi, D. C.; Shochat, S. G.; Liedberg, B. Real-time determination of the activity of ATPase by use of a water-

soluble polythiophene. Analytical and Bioanalytical Chemistry 2012, 404 (8), 2369–2375 https://doi.org/10.1007/s00216-012-6341-8.

(117) Rubio-Magnieto, J.; Azene, E. G.; Knoops, J.; Knippenberg, S.; Delcourt, C.; Thomas, A.; Richeter, S.; Mehdi, A.; Dubois, P.; Lazzaroni, R.; et al. Self-assembly and hybridization mechanisms of DNA with cationic polythiophene. Soft Matter 2015, 11 (32), 6460–6471 https://doi.org/10.1039/c5sm01484k.

(118) Rajwar, D.; Ammanath, G.; Cheema, J. A.; Palaniappan, A.; Yildiz, U. H.; Liedberg, B. Tailoring conformation-induced chromism of polythiophene copolymers for nucleic acid assay at Resource Limited settings. ACS Applied Materials & Interfaces 2016, 8 (13), 8349–8357 https://doi.org/10.1021/acsami.5b12171.

(119) Ammanath, G.; Yeasmin, S.; Srinivasulu, Y.; Vats, M.; Cheema, J. A.; Nabilah, F.; Srivastava, R.; Yildiz, U. H.; Alagappan, P.; Liedberg, B. Flow-through colorimetric assay for detection of nucleic acids in plasma. Analytica Chimica Acta 2019, 1066, 102–111 https://doi.org/10.1016/j.aca.2019.03.036.

(120) Yucel, M.; Koc, A.; Ulgenalp, A.; Akkoc, G. D.; Ceyhan, M.; Yildiz, U. H. PCR-free methodology for detection of single-nucleotide polymorphism with a cationic polythiophene reporter. ACS Sensors 2021, 6 (3), 950–957 https://doi.org/10.1021/acssensors.0c02130.

(121) Mao, L.; Liu, Y.; Yang, S.; Li, Y.; Zhang, X.; Wei, Y. Recent advances and progress of fluorescent bio-/chemosensors based on aggregation-induced emission molecules. Dyes and Pigments 2019, 162, 611–623 https://doi.org/10.1016/j.dyepig.2018.10.045.

(122) Yeh, Y.-C.; Creran, B.; Rotello, V. M. Gold nanoparticles: Preparation, properties, and applications in Bionanotechnology. Nanoscale 2012, 4 (6), 1871–1880 https://doi.org/10.1039/c1nr11188d.

(123) Li, Y.; Schluesener, H. J.; Xu, S. Gold nanoparticle-based biosensors. Gold

Bulletin 2010, 43 (1), 29–41 https://doi.org/10.1007/bf03214964.

(124) Moyano, D. F.; Rana, S.; Bunz, U. H.; Rotello, V. M. Gold nanoparticle-polymer/biopolymer complexes for protein sensing. Faraday Discussions 2011, 152, 33 https://doi.org/10.1039/c1fd00024a.

(125) Kong, H.; Liu, D.; Zhang, S.; Zhang, X. Protein sensing and cell discrimination using a sensor array based on nanomaterial-assisted chemiluminescence. Analytical Chemistry 2011, 83 (6), 1867–1870 https://doi.org/10.1021/ac200076c.

(126) You, C.-C.; Miranda, O. R.; Gider, B.; Ghosh, P. S.; Kim, I.-B.; Erdogan, B.; Krovi, S. A.; Bunz, U. H.; Rotello, V. M. Detection and identification of proteins using nanoparticle–fluorescent polymer 'chemical nose' sensors. Nature Nanotechnology 2007, 2 (5), 318–323 https://doi.org/10.1038/nnano.2007.99.

(127) De, M.; Rana, S.; Akpinar, H.; Miranda, O. R.; Arvizo, R. R.; Bunz, U. H.; Rotello, V. M. Sensing of proteins in human serum using conjugates of nanoparticles and green fluorescent protein. Nature Chemistry 2009, 1 (6), 461–465 https://doi.org/10.1038/nchem.334.

(128) Shang, L.; Qin, C.; Wang, T.; Wang, M.; Wang, L.; Dong, S. Fluorescent conjugated polymer-stabilized gold nanoparticles for sensitive and selective detection of cysteine. The Journal of Physical Chemistry C 2007, 111 (36), 13414–13417 https://doi.org/10.1021/jp073913p.

(129) Wang, N.; Wang, L.; Yang, H.; Xiong, T.; Xiao, S.; Zhao, J.; Du, W. Fluorescent sensors based on organic polymer-capped gold nanoparticles for the detection of Cr(VI) in water. International Journal of Analytical Chemistry 2019, 2019, 1–10 https://doi.org/10.1155/2019/1756014.

(130) Qin, X.; Tong, Q.; Chang, M.; Liang, S. A hydrophilic polymer-based bifunctional nanosensor for sequential fluorescence sensing of Cu2+ and biothiols and constructing Molecular Logic Gate. Journal of Photochemistry and

Photobiology A: Chemistry 2020, 402, 112792 https://doi.org/10.1016/j.jphotochem.2020.112792.

(131) Zhang, H.; Wang, B.; Seehafer, K.; Bunz, U. H. Sensor array based determination of Edman degradated amino acids using poly(p-phenyleneethynylene)s. Chemistry – A European Journal 2020, 26 (35), 7779–7782 https://doi.org/10.1002/chem.202001262.

(132) Tawfik, S. M.; Abd-Elaal, A. A.; Lee, Y.-I. Selective dual detection of Hg2+ and TATP based on amphiphilic conjugated polythiophene-quantum dot hybrid materials. The Analyst 2021, 146 (9), 2894–2901 https://doi.org/10.1039/d1an00166c.

(133) Özenler, S.; Yucel, M.; Tüncel, Ö.; Kaya, H.; Özçelik, S.; Yildiz, U. H. Single chain cationic polymer dot as a fluorescent probe for cell imaging and selective determination of hepatocellular carcinoma cells. Analytical Chemistry 2019, 91 (16), 10357–10360 https://doi.org/10.1021/acs.analchem.9b02300.

(134) Turkevich, J.; Stevenson, P. C.; Hillier, J. A study of the nucleation and growth processes in the synthesis of colloidal gold. Discussions of the Faraday Society 1951, 11, 55 https://doi.org/10.1039/df9511100055.

(135) Facchi, D.; da Cruz, J.; Bonafé, E.; Pereira, A.; Fajardo, A. R.; Venter, S.; Monteiro, J.; Muniz, E.; Martins, A. Polysaccharide-based materials associated with or coordinated to gold nanoparticles: Synthesis and medical application. Current Medicinal Chemistry 2017, 24 (25) https://doi.org/10.2174/0929867324666170309123351.

(136) Schmidt-Böcking Horst; Reich, K.; Templeton, A.; Trageser, W.; Vill, V. Otto Sterns veröffentlichungen - band 2 sterns veröffentlichungen von 1916 bis 1926; Springer Berlin Heidelberg: Berlin, Heidelberg, 2016.

(137) Figueira, T. N.; Oliveira, F. D.; Almeida, I.; Mello, É. O.; Gomes, V. M.; Castanho, M. A.; Gaspar, D. Challenging metastatic breast cancer with the

natural defensinpvD1. Nanoscale 2017, 9 (43), 16887–16899 https://doi.org/10.1039/c7nr05872a.

(138) Karabatak, M.; Ince, M. C.; Avci, E. An expert sytem for diagnosis breast cancer based on Principal Component Analysis Method. 2008 IEEE 16th Signal Processing, Communication and Applications Conference 2008 https://doi.org/10.1109/siu.2008.4632642.

(139) Abdi, H.; Williams, L. J. Principal component analysis. Wiley Interdisciplinary Reviews: Computational Statistics 2010, 2 (4), 433–459 https://doi.org/10.1002/wics.101.

(140) Khalili, F.; Henni, A.; East, A. L. Pkavalues of some piperazines at (298, 303, 313, and 323) K. Journal of Chemical & Engineering Data 2009, 54 (10), 2914–2917 https://doi.org/10.1021/je900005c.

(141) Lee, M. H. Bis(naphthalimide-piperazine)-based off-on fluorescent probe for acids. Journal of Fluorescence 2016, 26 (3), 807–811 https://doi.org/10.1007/s10895-016-1767-6.

(142) Fu, Y.; Zhang, J.; Wang, H.; Chen, J.-L.; Zhao, P.; Chen, G.-R.; He, X.-P. Intracellular ph sensing and targeted imaging of lysosome by a galactosyl naphthalimide-piperazine probe. Dyes and Pigments 2016, 133, 372–379 https://doi.org/10.1016/j.dyepig.2016.06.022.

(143) Nilsson, K. P.; Andersson, M. R.; Inganäs, O. Conformational transitions of a free amino-acid-functionalized polythiophene induced by different buffer systems. Journal of Physics: Condensed Matter 2002, 14 (42), 10011–10020 https://doi.org/10.1088/0953-8984/14/42/313.

(144) Burns, C.; Spendel, W.; Puckett, S.; Pacey, G. Solution ionic strength effect on Gold Nanoparticle Solution Color Transition. Talanta 2006, 69 (4), 873–876 https://doi.org/10.1016/j.talanta.2005.11.038.

(145) Maciulevičius, M.; Vinčiūnas, A.; Brikas, M.; Butsen, A.; Tarasenka, N.; Tarasenko, N.; Račiukaitis, G. On-line characterization of gold nanoparticles generated by laser ablation in liquids. Physics Procedia 2013, 41, 531–538 https://doi.org/10.1016/j.phpro.2013.03.112.

(146) Saha, K.; Agasti, S. S.; Kim, C.; Li, X.; Rotello, V. M. Gold nanoparticles in chemical and biological sensing. Chemical Reviews 2012, 112 (5), 2739–2779 https://doi.org/10.1021/cr2001178.

(147) Guan, H.; Zhou, P.; Zhou, X.; He, Z. Sensitive and selective detection of aspartic acid and glutamic acid based on polythiophene–gold nanoparticles composite. Talanta 2008, 77 (1), 319–324 https://doi.org/10.1016/j.talanta.2008.06.040.

(148) Du, S.; Kendall, K.; Toloueinia, P.; Mehrabadi, Y.; Gupta, G.; Newton, J. Aggregation and adhesion of gold nanoparticles in phosphate buffered saline. Journal of Nanoparticle Research 2012, 14 (3) https://doi.org/10.1007/s11051-012-0758-z.

(149) Li, D. D.; Gu, X.; Timchenko, V.; Chan, Q. N.; Yuen, A. C.; Yeoh, G. H. Study of morphology and optical properties of gold nanoparticle aggregates under different ph conditions. Langmuir 2018, 34 (35), 10340–10352 https://doi.org/10.1021/acs.langmuir.8b01457.

(150) Fraiji, L. K.; Hayes, D. M.; Werner, T. C. Static and dynamic fluorescence quenching experiments for the Physical Chemistry Laboratory. Journal of Chemical Education 1992, 69 (5), 424 https://doi.org/10.1021/ed069p424.

(151) Ogunsipe, A.; Nyokong, T. Photophysicochemical consequences of bovine serum albumin binding to non-transition metal phthalocyanine sulfonates. Photochemical & Photobiological Sciences 2005, 4 (7), 510–516 https://doi.org/10.1039/b416304d.

(152) Tanwar, A. S.; Parui, R.; Garai, R.; Chanu, M. A.; Iyer, P. K. Dual “static and dynamic” fluorescence quenching mechanisms based detection of TNT via a

cationic conjugated polymer. ACS Measurement Science Au 2021, 2 (1), 23–30 https://doi.org/10.1021/acsmeasuresciau.1c00023.

(153) Moradi, S.; Shareghi, B.; Saboury, A. A.; Farhadian, S. The influence of cadaverine on the structure, stability, and activity of acid phosphatase. Journal of Molecular Structure 2022, 1247, 131372 https://doi.org/10.1016/j.molstruc.2021.131372.

(154) Zhang, Y.-F.; Zhou, K.-L.; Lou, Y.-Y.; Pan, D.-qi; Shi, J.-H. Investigation of the binding interaction between estazolam and bovine serum albumin: Multi-spectroscopic methods and molecular docking technique. Journal of Biomolecular Structure and Dynamics 2016, 35 (16), 3605–3614 https://doi.org/10.1080/07391102.2016.1264889.

(155) Lakowicz, J. R. Quenching of fluorescence. Principles of Fluorescence Spectroscopy 1983, 257–301 https://doi.org/10.1007/978-1-4615-7658-7_9.

(156) Hirayama, K.; Akashi, S.; Furuya, M.; Fukuhara, K.-ichi. Rapid confirmation and revision of the primary structure of bovine serum albumin by ESIMS and frit-FAB LC/MS. Biochemical and Biophysical Research Communications 1990, 173 (2), 639–646 https://doi.org/10.1016/s0006-291x(05)80083-x.

(157) Niamnont, N.; Mungkarndee, R.; Techakriengkrai, I.; Rashatasakhon, P.; Sukwattanasinitt, M. Protein discrimination by fluorescent sensor array constituted of variously charged dendritic phenylene–ethynylene fluorophores. Biosensors and Bioelectronics 2010, 26 (2), 863–867 https://doi.org/10.1016/j.bios.2010.07.096.

(158) Kim, I.-B.; Dunkhorst, A.; Bunz, U. H. Nonspecific interactions of a carboxylate-substituted PPE with proteins. A cautionary tale for biosensor applications. Langmuir 2005, 21 (17), 7985–7989 https://doi.org/10.1021/la051152g.

(159) Morawiecka, B. Białka Ziemniaka (solanum tuberosum) rozpuszczalne W Kwasie sulfosalicylowym [sulphosalicylic acid soluble proteins of the potato

{solanum tuberosum)]. Acta Societatis Botanicorum Poloniae 2015, 34 (2), 161–170 https://doi.org/10.5586/asbp.1965.010.

(160) Schenk, G.; Elliott, T. W.; Leung, E.; Carrington, L. E.; Mitić, N.; Gahan, L. R.; Guddat, L. W. Crystal structures of a purple acid phosphatase, representing different steps of this enzyme's catalytic cycle. BMC Structural Biology 2008, 8 (1), 6 https://doi.org/10.1186/1472-6807-8-6.

(161) Waratrujiwong, T.; Krebs, B.; Spener, F.; Visoottiviseth, P. Recombinant purple acid phosphatase isoform 3 from sweet potato is an enzyme with a diiron metal center. FEBS Journal 2006, 273 (8), 1649–1659 https://doi.org/10.1111/j.1742-4658.2006.05179.x.

(162) Schenk, G.; Carrington, L. E.; Hamilton, S. E.; de Jersey, J.; Guddat, L. W. Crystallization and preliminary X-ray diffraction data for a purple acid phosphatase from sweet potato. Acta Crystallographica Section D Biological Crystallography 1999, 55 (12), 2051–2052 https://doi.org/10.1107/s0907444999012597.

(163) Bortolato, M.; Besson, F.; Roux, B. Role of metal ions on the secondary and quaternary structure of alkaline phosphatase from bovine intestinal mucosa. Proteins: Structure, Function, and Genetics 1999, 37 (2), 310–318 https://doi.org/10.1002/(sici)1097-0134(19991101)37:2<310::aid-prot16>3.0.co;2-b.

(164) Besman, M.; Coleman, J. E. Isozymes of bovine intestinal alkaline phosphatase. Journal of Biological Chemistry 1985, 260 (20), 11190–11193 https://doi.org/10.1016/s0021-9258(17)39164-0.

(165) Fosset, M.; Chappelet-Tordo, D.; Lazdunski, M. Intestinal alkaline phosphatase. physical properties and quaternary structure. Biochemistry 1974, 13 (9), 1783–1788 https://doi.org/10.1021/bi00706a001.

(166) Vaganova, T. I.; Ivanova, N. M.; Klepikova, F. S. Isolation and properties of

aminopeptidase from Bacillus thuringiensis. Biochemistry 1984, 49 (11), 1899–1907.

(167) Neidhart, D. J.; Petsko, G. A. The refined crystal structure of Subtilisin Carlsberg at 2.5 Å Resolution. "Protein Engineering, Design and Selection" 1988, 2 (4), 271–276 https://doi.org/10.1093/protein/2.4.271.

(168) DeLange, R. J.; Smith, E. L. Subtilisin Carlsberg. Journal of Biological Chemistry 1968, 243 (9), 2134–2142 https://doi.org/10.1016/s0021-9258(18)93457-5.

(169) Chertkova, R. V.; Brazhe, N. A.; Bryantseva, T. V.; Nekrasov, A. N.; Dolgikh, D. A.; Yusipovich, A. I.; Sosnovtseva, O.; Maksimov, G. V.; Rubin, A. B.; Kirpichnikov, M. P. New insight into the mechanism of mitochondrial cytochrome c function. PLOS ONE 2017, 12 (5) https://doi.org/10.1371/journal.pone.0178280.

(170) Chen, P.; Andoy, N. M. Single-molecule fluorescence studies from a bioinorganic perspective. Inorganica Chimica Acta 2008, 361 (4), 809–819 https://doi.org/10.1016/j.ica.2007.08.012.

(171) Sandanaraj, B. S.; Demont, R.; Aathimanikandan, S. V.; Savariar, E. N.; Thayumanavan, S. Selective sensing of metalloproteins from nonselective binding using a fluorogenic amphiphilic polymer. Journal of the American Chemical Society 2006, 128 (33), 10686–10687 https://doi.org/10.1021/ja063544v.

(172) Hulko, M.; Hospach, I.; Krasteva, N.; Nelles, G. Cytochrome c biosensor—a model for gas sensing. Sensors 2011, 11 (6), 5968–5980 https://doi.org/10.3390/s110605968.

(173) Zhang, Y.; Liu, B.; Cao, Y. Synthesis and characterization of a water-soluble carboxylated polyfluorene and its fluorescence quenching by cationic quenchers and proteins. Chemistry – An Asian Journal 2008, 3 (4), 739–745

https://doi.org/10.1002/asia.200700294.

(174) Qin, C. J.; Tong, H.; Wang, L. X. Water-soluble phosphate-functionalized polyfluorene as fluorescence biosensors toward cytochrome c. Science in China Series B: Chemistry 2009, 52 (6), 833–839 https://doi.org/10.1007/s11426-009-0067-2.

(175) Fan, C.; Plaxco, K. W.; Heeger, A. J. High-efficiency fluorescence quenching of conjugated polymers by proteins. Journal of the American Chemical Society 2002, 124 (20), 5642–5643 https://doi.org/10.1021/ja025899u.

(176) Béra Abérem, M.; Najari, A.; Ho, H.-A.; Gravel, J.-F.; Nobert, P.; Boudreau, D.; Leclerc, M. Protein detecting arrays based on cationic polythiophene–DNA-aptamer complexes. Advanced Materials 2006, 18 (20), 2703–2707 https://doi.org/10.1002/adma.200601651.

(177) Yao, Z.; Ma, W.; Yang, Y.; Chen, X.; Zhang, L.; Lin, C.; Wu, H.-C. Colorimetric and fluorescent detection of protamines with an anionic polythiophene derivative. Organic & Biomolecular Chemistry 2013, 11 (38), 6466 https://doi.org/10.1039/c3ob41407h.

(178) Wang, J.; Li, Y.; Patel, N. G.; Zhang, G.; Zhou, D.; Pang, Y. A single molecular probe for multi-analyte (Cr3+, Al3+and Fe3+) detection in aqueous medium and its biological application. Chem. Commun. 2014, 50 (82), 12258–12261 https://doi.org/10.1039/c4cc04731a.

(179) Yang, Z.; Peng, H.; Wang, W.; Liu, T. Crystallization behavior of poly(ε-caprolactone)/layered double hydroxide nanocomposites. Journal of Applied Polymer Science 2010 https://doi.org/10.1002/app.31787.

(180) Rovati, L.; Fabbri, P.; Ferrari, L.; Pilati, F. Plastic optical fiber ph sensor using a sol-gel sensing matrix. Fiber Optic Sensors 2012 https://doi.org/10.5772/26517.

(181) Ma, F.; Rehman, A.; Liu, H.; Zhang, J.; Zhu, S.; Zeng, X. Glycosylation of quinone-fused polythiophene for Reagentless and label-free detection of E. coli. Analytical Chemistry 2015, 87 (3), 1560–1568 https://doi.org/10.1021/ac502712q.

(182) Kaji, Y.; Amano, S.; Usui, T.; Oshika, T.; Yamashiro, K.; Ishida, S.; Suzuki, K.; Tanaka, S.; Adamis, A. P.; Nagai, R.; et al. Expression and function of receptors for advanced glycation end products in bovine corneal endothelial cells. Investigative Opthalmology & Visual Science 2003, 44 (2), 521 https://doi.org/10.1167/iovs.02-0268.

(183) Bellosta, P.; Costa, M.; Lin, D. A.; Basilico, C. The receptor tyrosine kinase ark mediates cell aggregation by homophilic binding. Molecular and Cellular Biology 1995, 15 (2), 614–625 https://doi.org/10.1128/mcb.15.2.614.

(184) Torgersen, M. L.; Klokk, T. I.; Kavaliauskiene, S.; Klose, C.; Simons, K.; Skotland, T.; Sandvig, K. The anti-tumor drug 2-hydroxyoleic acid (minerval) stimulates signaling and retrograde transport. Oncotarget 2016, 7 (52), 86871–86888 https://doi.org/10.18632/oncotarget.13508.

(185) Datta, P. K. Neuronal Cell Culture. Methods in Molecular Biology 2013 https://doi.org/10.1007/978-1-62703-640-5.

(186) Lambert, D. G.; Ghataorre, A. S.; Nahorski, S. R. Muscarinic receptor binding characteristics of a human neuroblastoma SK-N-SH and its clones SH-SY5Y and SH-EP1. European Journal of Pharmacology 1989, 165 (1), 71–77 https://doi.org/10.1016/0014-2999(89)90771-1.

(187) Comşa Ş, Cîmpean AM, Raica M. The Story of MCF-7 Breast Cancer Cell Line: 40 years of Experience in Research. Anticancer research 2015 Jun;35(6):3147-54. PMID: 26026074. (değişen referans)

(188) Hegde, S. M.; Kumar, M. N.; Kavya, K.; Kumar, K. M.; Nagesh, R.; Patil, R. H.; Babu, R. L.; Ramesh, G. T.; Sharma, S. C. Interplay of nuclear receptors (ER,

PR, and GR) and their steroid hormones in MCF-7 cells. Molecular and Cellular Biochemistry 2016, 422 (1-2), 109–120 https://doi.org/10.1007/s11010-016-2810-2.

(189) Panjehpour, M.; Castro, M.; Klotz, K.-N. Human breast cancer cell line MDA-MB-231 expresses endogenous a2b adenosine receptors mediating a Ca2+ signal. British Journal of Pharmacology 2005, 145 (2), 211–218 https://doi.org/10.1038/sj.bjp.0706180.

(190) Selvi, R. B.; Chatterjee, S.; Jagadeesan, D.; Chaturbedy, P.; Suma, B. S.; Eswaramoorthy, M.; Kundu, T. K. ATP driven clathrin dependent entry of carbon nanospheres prefer cells with glucose receptors. Journal of Nanobiotechnology 2012, 10 (1) https://doi.org/10.1186/1477-3155-10-35.

(191) Zhang, Y.; Yang, M.; Portney, N. G.; Cui, D.; Budak, G.; Ozbay, E.; Ozkan, M.; Ozkan, C. S. Zeta potential: A surface electrical characteristic to probe the interaction of nanoparticles with normal and cancer human breast epithelial cells. Biomedical Microdevices 2007, 10 (2), 321–328 https://doi.org/10.1007/s10544-007-9139-2.

(192) Kier, A. B. Membrane properties of metastatic and non-metastatic cells cultured from C3H mice injected with LM fibroblasts. Biochimica et Biophysica Acta (BBA) - Biomembranes 1990, 1022 (3), 365–372 https://doi.org/10.1016/0005-2736(90)90287-x.

(193) Ballentine Carter, H.; Coffey, D. S. Cell surface charge in predicting metastatic potential of aspirated cells from the dunning rat prostatic adenocarcinoma model. Journal of Urology 1988, 140 (1), 173–175 https://doi.org/10.1016/s0022-5347(17)41521-7.

(194) Magarkar, A.; Dhawan, V.; Kallinteri, P.; Viitala, T.; Elmowafy, M.; Róg, T.; Bunker, A. Cholesterol level affects surface charge of lipid membranes in saline solution. Scientific Reports 2014, 4 (1) https://doi.org/10.1038/srep05005.

(195) Purdom, L.; Ambrose, E. J.; Klein, G. A correlation between electrical surface charge and some biological characteristics during the stepwise progression of a mouse sarcoma. Nature 1958, 181 (4623), 1586–1587 https://doi.org/10.1038/1811586a0.

(196) Riedl, S.; Leber, R.; Rinner, B.; Schaider, H.; Lohner, K.; Zweytick, D. Human lactoferricin derived di-peptides deploying loop structures induce apoptosis specifically in cancer cells through targeting membranous phosphatidylserine. Biochimica et Biophysica Acta (BBA) - Biomembranes 2015, 1848 (11), 2918–2931 https://doi.org/10.1016/j.bbamem.2015.07.018.

(197) Karabacak, S. Synthesis of polythiophene-polyurethane soft nanoparticles for bioimaging applications. Ph.D. Dissertation, Izmir Institute of Technology, Turkey, 2020.

(198) Pathak, R. K.; Dessingou, J.; Rao, C. P. Multiple sensor array of Mn2+, Fe2+, Co2+, Ni2+, Cu2+, and Zn2+ complexes of a triazole linked imino-phenol based Calix[4]arene conjugate for the selective recognition of Asp, Glu, Cys, and His. Analytical Chemistry 2012, 84 (19), 8294–8300 https://doi.org/10.1021/ac301821c.

(199) Guo, C.; Yang, X.; Yang, X.; Zhu, W.; Pei, M.; Zhang, G. Fluorescent probes for Cu2+, Hg2+ and amino acids in aqueous solutions based on two mechanisms. Sensors and Actuators B: Chemical 2014, 205, 345–351 https://doi.org/10.1016/j.snb.2014.08.075.

(200) Li, Z.; Lou, X.; Li, Z.; Qin, J. A new approach to fluorescence “turn-on” sensing of α-amino acids. ACS Applied Materials & Interfaces 2008, 1 (2), 232–234 https://doi.org/10.1021/am800093d.

(201) Guo, C.; Li, P.; Pei, M.; Zhang, G. A new polythiophene derivative-based fluorescent sensor for Co2+, Cu2+, Cd2+, and its complex with Cu2+ for sensing homocysteine and glutathione. Sensors and Actuators B: Chemical 2015, 221, 1223–1228 https://doi.org/10.1016/j.snb.2015.07.105.

(202) Liu, Y.; Li, H.; Pei, M.; Zhang, G.; Hu, L.; Han, J. A new fluorescence “off–on” chemodosimeter for L-cysteine based on water-soluble polythiophene. Talanta 2013, 115, 190–194 https://doi.org/10.1016/j.talanta.2013.04.030.

(203) Doyen, M.; Goole, J.; Bartik, K.; Bruylants, G. Amino acid induced fractal aggregation of gold nanoparticles: Why and how. Journal of Colloid and Interface Science 2016, 464, 160–166 https://doi.org/10.1016/j.jcis.2015.11.017.

(204) Ustunol, I. B.; Gonzalez-Pech, N. I.; Grassian, V. H. Ph-dependent adsorption of α-amino acids, lysine, glutamic acid, serine and glycine, on TiO2 nanoparticle surfaces. Journal of Colloid and Interface Science 2019, 554, 362–375 https://doi.org/10.1016/j.jcis.2019.06.086.

(205) Tomoaia, G.; Frangopol, P. T.; Horovitz, O.; Boboş, L.-D.; Mocanu, A.; Tomoaia-Cotisel, M. The effect of arginine on gold nanoparticles in colloidal solutions and in thin films. Journal of Nanoscience and Nanotechnology 2011, 11 (9), 7762–7770 https://doi.org/10.1166/jnn.2011.4734.

(206) Shellaiah, M.; Thirumalaivasan, N.; Sun, K. W.; Wu, S.-P. A ph cooperative strategy for enhanced colorimetric sensing of Cr(III) ions using biocompatible L-glutamic acid stabilized gold nanoparticles. Microchemical Journal 2021, 160, 105754 https://doi.org/10.1016/j.microc.2020.105754.

(207) Chen, Y.; Yao, L.; Deng, Y.; Pan, D.; Ogabiela, E.; Cao, J.; Adeloju, S. B.; Chen, W. Rapid and ultrasensitive colorimetric detection of Mercury(II) by chemically initiated aggregation of gold nanoparticles. Microchimica Acta 2015, 182 (13-14), 2147–2154 https://doi.org/10.1007/s00604-015-1538-0.

(208) Horovitz, O.; Mocanu, A.; Tomoaia, G.; Bobos, L.; Dubert D.; Daian, I.; Yupsanis T.; Tomoaia-Cotisel, M. Lysine Mediated Assembly of Gold Nanoparticles. Studia Univ. Babes-Bolyai Chem. 52 2007, 97–108.

(209) Ghisaidoobe, A.; Chung, S. Intrinsic tryptophan fluorescence in the detection and

analysis of proteins: A focus on Förster resonance energy transfer techniques. International Journal of Molecular Sciences 2014, 15 (12), 22518–22538 https://doi.org/10.3390/ijms151222518.

(210) Selvakannan, P. R.; Mandal, S.; Phadtare, S.; Gole, A.; Pasricha, R.; Adyanthaya, S. D.; Sastry, M. Water-dispersible tryptophan-protected gold nanoparticles prepared by the spontaneous reduction of aqueous chloroaurate ions by the amino acid. Journal of Colloid and Interface Science 2004, 269 (1), 97–102 https://doi.org/10.1016/s0021-9797(03)00616-7.

(211) Aryal, S.; B.K.C., R.; Dharmaraj, N.; Bhattarai, N.; Kim, C. H.; Kim, H. Y. Spectroscopic identification of S AU interaction in cysteine capped gold nanoparticles. Spectrochimica Acta Part A: Molecular and Biomolecular Spectroscopy 2006, 63 (1), 160–163 https://doi.org/10.1016/j.saa.2005.04.048.

(212) Sharma, B.; Rabinal, M. K. Biologically Active L-cysteine as a reducing/capping agent for controlled tuning of gold nanoparticles. Journal of Alloys and Compounds 2015, 649, 11–18 https://doi.org/10.1016/j.jallcom.2015.06.160.

(213) Mocanu, A.; Cernica, I.; Tomoaia, G.; Bobos, L.-D.; Horovitz, O.; Tomoaia-Cotisel, M. Self-assembly characteristics of gold nanoparticles in the presence of cysteine. Colloids and Surfaces A: Physicochemical and Engineering Aspects 2009, 338 (1-3), 93–101 https://doi.org/10.1016/j.colsurfa.2008.12.041.

(214) Brosnan, M. E.; Brosnan, J. T. Histidine metabolism and function. The Journal of Nutrition 2020, 150 (Supplement_1) https://doi.org/10.1093/jn/nxaa079.

VITA

Duygu ARSLANTAŞ

EDUCATION

- Ph.D. in Bioengineering, Izmir Institute of Technology (2022)
- M.Sc. in Medical Biology and Genetics, Dokuz Eylül University (2013)
- B.Sc. in Biochemistry, Ege University (2009)

SCHOLARSHIP

YOK 100/2000 PhD Scholarship Program, 2017-2021

CONFERENCE PRESENTATIONS

1. Arslantaş D., Sakızlı M., Tunca Z. (2019). Mutation/SNP Analysis of CALHM1 (Calcium Homeostasis Modulator Factor 1) Gene in Bipolar Disorder Patients. 1st International Medical Congress of Izmir Democracy University, pp 606-610. (Printed Full Paper-Oral Presentation)
2. Girgin B., Arslantaş D., Sözmen A., Arslan-Yıldız A. (2022). Green Synthesized Gold nanoparticle Sensory System for Heavy Metal Detection. 5th International Congress on Biosensors of Çanakkale Onsekiz Mart University. (Poster Presentation)

PROJECT INVOLVED

1. Bipolar Bozukluk (BD) Olgularında CALHM1 (Kalsiyum Homeostaz Düzenleyici Faktör) Geninin SNP (Mutasyon/Polimorfizm)'ler Yönünden İncelenmesi, 2009-2013.
DEÜ 2011.KB.SAG.022, Researcher
Project Coordinator: Prof. Dr. MERAL SAKIZLI
2. Protein Tayini için İletken Politiyofen Temelli pH Biyosensör
Geliştirilmesi, 2019-2020.
BAP- 20191YTE0250, Researcher
Project Coordinator: Assoc. Prof. Dr AHU ARSLAN YILDIZ